



HAL
open science

Structure and dynamics of DNA confined in-between non-cationic lipid membranes

Emerson Rodrigo Teixeira da Silva

► **To cite this version:**

Emerson Rodrigo Teixeira da Silva. Structure and dynamics of DNA confined in-between non-cationic lipid membranes. Biological Physics [physics.bio-ph]. Université Sciences et Technologies - Bordeaux I, 2011. English. NNT: . tel-00755050

HAL Id: tel-00755050

<https://theses.hal.science/tel-00755050>

Submitted on 20 Nov 2012

HAL is a multi-disciplinary open access archive for the deposit and dissemination of scientific research documents, whether they are published or not. The documents may come from teaching and research institutions in France or abroad, or from public or private research centers.

L'archive ouverte pluridisciplinaire **HAL**, est destinée au dépôt et à la diffusion de documents scientifiques de niveau recherche, publiés ou non, émanant des établissements d'enseignement et de recherche français ou étrangers, des laboratoires publics ou privés.

N° d'ordre : 4342

THÈSE EN COTUTELLE

PRÉSENTÉE À

L'UNIVERSITÉ BORDEAUX 1

ÉCOLE DOCTORALE DES SCIENCES PHYSIQUES ET DE L'INGÉNIEUR

avec **L'UNIVERSITÉ DE SÃO PAULO**

INSTITUTO DE FÍSICA

Par **Emerson Rodrigo TEIXEIRA DA SILVA**

Pour obtenir le grade de

DOCTEUR

Spécialité : **Lasers, matières et nanosciences**

Structure and dynamics of DNA confined in-between non-cationic lipid membranes

Directeurs de recherche : Mme. Elisabeth ANDREOLI DE OLIVEIRA / M.
Frédéric NALLET

Co-directeur : Mme. Laurence NAVAILLES

Soutenue à Sao Paulo, le 08/11/2011

Après l'avis de :

B. PANSU	Professeur	Univ. Paris-Sud XI	Rapporteur
C.R. SAFINYA	Professeur	Univ. of California (SB)	Rapporteur

Devant la commission d'examen formée de :

E. A. de OLIVEIRA	Professeur	Univ. de Sao Paulo	Président
F. NALLET	Professeur	Univ. Bordeaux 1	Directeur
L. NAVAILLES	Ch. de Recherche	CRPP - UPR 8641 CNRS	Co-Directeur
M. C. A. FANTINI	Professeur	Univ. de Sao Paulo	Examinateur
N. P. da SILVEIRA	Professeur	Univ. Fed. Rio Grande do Sul	Examinateur
Y. LEVIN	Professeur	Univ. Fed. Rio Grande do Sul	Examinateur

Université de Bordeaux 1

Les Sciences et les Technologies au service de l'Homme et de l'environnement

Notice



This thesis was carried out in the context of a binational collaboration between the University of Sao Paulo, Brazil, and the University Bordeaux 1, France. The experimental part of the work was entirely carried out at the Centre de Recherche Paul Pascal, CNRS, UPR 8641 (115 Avenue du Docteur Albert Schweitzer, 33600, Pessac, France), whereas the redaction of the manuscript as well as my theoretical education were conducted at the Instituto de Física da USP (Rua do Matão, n. 187, 05508-090, São Paulo, Brasil).

The original version of the text was written in English and delivered to the library of the University Bordeaux 1. In order to satisfy the rules of the University of Sao Paulo, a complete version of the work was translated to Portuguese and now is deposited at the library of the Institute of Physics at USP. The online Portuguese version can be found at www.teses.usp.br. To satisfy requirements of the University Bordeaux 1, an extended abstract was written in French and can be found at the appendix C of this volume.

RESUMÉ

STRUCTURE ET DYNAMIQUE D'ADN CONFINÉE ENTRE DES MEMBRANES LIPIDIQUES NON-CATIONIQUES

Une étude expérimentale sur la structure et la dynamique d'un complexe hydraté de fragments d'ADN (150 pb) et des phases lamellaires de lipides zwitterioniques est présentée. Par la variation de d'hydratation, il est possible de contrôler le *confinement* imposé par cette matrice hôte sur les nucléotides insérés dans les couches aqueuses. L'organisation supramoléculaire du complexe est suivie par diffraction des rayons-X et des techniques de microscopie optique et électronique. Un riche polymorphisme de mesophases est observé en fonction du confinement. Dans le régime plus hydraté, les fragments se distribuent selon une orientation nématique. Dans la mesure où la quantité de l'eau diminue, le confinement des bicouches sur les nucléotides monte et des corrélations transmembranaires donnent origine à des phases hautement organisées, avec de symétries rectangulaires et hexagonales (2D) d'ADN dans la phase lipidique. L'incorporation totale des nucléotides par la phase lamellaire est observée uniquement lorsque des grandes quantités d'ADN y sont présentes. Ce fait souligne une importance majeure des interactions de volume exclu. Une analyse du paramètre de Caillé montre que l'insertion des fragments diminue les fluctuations des membranes. À partir de ces observations, il est suggéré que la modification des interactions stériques entre des lamelles, associée à des effets interfaciaux ADN-membranes, est un mécanisme important dans le comportement de phases. Les propriétés dynamiques sont étudiées avec la technique de *retour de fluorescence après photoblanchiment* (FRAP). Un modèle développé récemment pour l'analyse de diffusion anisotrope est testé avec succès, démontrant une corrélation proche entre structure et dynamique.

Mots clés: complexes ADN-lipides, auto-assemblage, membranes, phases lamellaires .

ABSTRACT

STRUCTURE AND DYNAMICS OF DNA CONFINED IN-BETWEEN NON-CATIONIC LIPID MEMBRANES

An experimental study on the structural and dynamical properties of a hydrated DNA-zwitterionic complex is presented. By varying the water amount, it is possible to control the *confinement* imposed by this host matrix over the organization of the nucleotides inserted within the water layers. The supramolecular assembly is investigated by X-rays diffraction and techniques involving both optical and electron microscopy. A rich polymorphism of mesophases is observed in function of confinement. In the more hydrated regime, the fragments are distributed according to nematic orientation in-between lamellae. As the water amount decreases, the confinement of bilayers over the particles increases and transmembrane correlations appear, giving raise to highly-ordered phases, with 2D-rectangular and -hexagonal symmetries of DNA embodied in the lamellar phase. The full incorporation of nucleotides by the lamellar phase is observed only in the presence of large amounts of DNA. This finding points to major importance of excluded volume interactions. An analysis of the Caillé parameter shows that the insertion of DNA reduces the fluctuations of membranes. From these observations, it is suggested that changes in the interactions between bilayers, together with the appearance of interfacial effects between DNA and membranes, are a mechanism relevant for the phase behavior of these systems. The dynamical properties of nucleotides are investigated through the fluorescence recovery after photobleach (FRAP). A model recently developed for analyses of anisotropic diffusion is successfully tested, demonstrating a close relationship between structure and dynamics.

Key-words: DNA-lipid complexes, self-assembly, membranes, lamellar phases .

RESUMO

ESTRUTURA E DINÂMICA DE DNA CONFINADO ENTRE MEMBRANAS LIPÍDICAS NÃO-CATIÔNICAS

Um estudo experimental sobre aspectos estruturais e dinâmicos de um complexo hidratado de fragmentos de DNA (150 pb) e fases lamelares de lipídios zwitteriônicos é apresentado. Variando-se a hidratação, é possível controlar o *confinamento* imposto por essa matriz hospedeira sobre os nucleotídeos inseridos na camada aquosa. O arranjo supramolecular do complexo é investigado por difração de raios X e técnicas de microscopia óptica e eletrônica. Um rico polimorfismo de mesofases é observado em função do confinamento. No regime mais hidratado, os fragmentos se distribuem segundo uma orientação nemática entre as membranas. À medida que a quantidade de água diminui, o confinamento das bicamadas sobre os nucleotídeos aumenta e correlações transmembranares aparecem, dando origem a fases altamente organizadas, com simetrias retangulares e hexagonais 2D de DNA entre as lamelas. A incorporação completa de nucleotídeos é observada apenas quando grandes quantidades de DNA estão presentes. Esse fato aponta para importância maior de interações de volume excluído. Uma análise do parâmetro de Caillé mostra que as flutuações das membranas diminuem com a inserção de DNA. A partir dessas observações, é sugerido que a alteração das interações entre membranas, aliada à aparição de efeitos interfaciais entre DNA e membranas, é um mecanismo relevante no comportamento de fase. As propriedades dinâmicas dos nucleotídeos são investigadas através da técnica de FRAP (fluorescence recovery after photobleaching). Um modelo recentemente desenvolvido para análise de difusão anisotrópica é testado com sucesso, demonstrando estreita correlação entre estrutura e dinâmica.

Palavras-chaves: complexos DNA-lipídios, auto-organização, membranas, fases lamelares

To Elieste da Silva, my father, *in memoriam*.

“Today I understand my father. A man must travel. By his own, not through stories, pictures, books or TV. He’s got to travel by himself, with his eyes and feet, to understand what is his. To one day plant his own trees and give them value. Knowing the cold to enjoy the warmth. And the opposite. Feel the distance and the homelessness to be well under his own roof. A man must travel to places which he does not know to break this arrogance that makes us see the world as we imagine it, and not simply as it is. That makes us teachers and doctors of what we have not seen, when we should be students, just go and see”.

Amyr Klink, Brazilian sailor

ACKNOWLEDGEMENTS

The development of this thesis was shared between the Institute of Physics at the University of Sao Paulo and the Paul Pascal Research Center, a CNRS unit attached to the University Bordeaux 1. In this way, the number of contributors to its accomplishment, direct or indirectly, is large and spread over two continents. Any attempt to cite all them will be, therefore, incomplete and reductionist. However, even taking the risk to forget some relevant actors in this adventure, I must mention by name very important persons who helped me along the way. So, I want to thank in a special manner:

To God, for His continuous presence in my life.

To my family. Specially, to my dear wife, Karina Alves. Beyond myself, she is who more personal sacrifices made for this work. For this reason, she will have my gratefulness forever. My mother, “Dona” Odete, and my brother, Elieste, also take part in this “frontline” of my life. I have no words to address these people. I can just say that I love them and, independent on titles, positions and circumstances, they are a mainstay which I could always count on.

To my advisors. To Beth, for introducing me in this fantastic field of self-assembled systems. I deeply admire her tenacity in an academic environment that, for various reasons, is often unfavorable. Along my career, I will be forever grateful to her for the confidence placed in me to consolidate the exchange between the Complex Fluids Group at USP and the CRPP. To Frédéric, for his intellectual giantism as a scientist and for his humility as a person. These qualities make him the physicist who I aspire to be. To Laurence, for having been the major engine driving this work. I can say with conviction that, among all mentors I had the fortune to meet during my academic career, she is the one who has invested more of herself in my guidance. Surely, their examples will follow me throughout my journey, even if, sometimes, I have to fight against “windmills”.

To the colleagues from the A^2B team (*Auto-Assemblage et Biomolécules - Self-assembly and biomolecules*), for the wonderful scientific environment. To Annie Février, for the help with protocols and the preparation of the components used in the samples. To Eric Grelet, for the fruitful discussions. To Gilles Sigaud, for the help to interpretate the TEM images. To François Dole, for discussions during the seminars. To Emile Pouget, for the help during the TEM observations. To Isabelle Ly, for the preparation of cryofracture replicas. To Jens Dobrindt who, even I never met “face to face”, was continuously present in the studies related to dynamics, either by proposing the theoretical model for analyzing anisotropic diffusion or by constructing the software for data treatment.

To the colleagues I did at CRPP, for the atmosphere of conviviality. To its permanent staff: Alain Pénicaut, Harald Bock, Carlos Drummont, Marie-France Achard, Corinne Amengual, Maryse Joli, Maryse Maugey, Jean-Yves Juanico, Jean-Luc Laborde, Jean-Cristophe Loudet, Philippe Barboteau, Ahmed Bentaleb, Brigitte Delord, Anne Facq, Sandrine Maillet, Joanna Giermanska... among others. To its non-permanent members: Antonin Prévotau, Nessim Arazam, Sylvain (Dauphin) Lannebere, Victoria Flexer, Miriam Materna, Andreas Schoepach, Nadja Mebner, Sonia Souakri, Frédéric Mondiot, Pratap Chandran, Giovanni Tonelli... among others. To the CRPP Director, Philippe Richetti, I specially thank for the welcome and for the conditions for carrying out the work, besides allowing my wife and me to live in the studio of the lab during a considerable part of our stay in France.

To my colleagues from the Complex Fluids Group at USP. To Renata Bicev, Vivian Vieira, Carlos Bayer, Cássio Alves and Bruno Honda, who shared office with me during the last four years. The first two became my day-by-day at IFUSP “ten fold happier” whereas, from the last three, I will take some of the funniest memories of my days as a doctoral student. Cássio, besides having become a great friend, shared several hours in confocal experiments and pleasant moments in Bordeaux, so that I can say that the southwest of France was never the same after his stay at CRPP. To Barbara Gerbelli, I thank for discussions and help with the fits of scattering curves. To Sandra Nakamatsu, for teaching me to prepare samples in the beginnings of my doctorate. Rafael Rubim, Pedro Oseliero and Eraldo Sales also provided an extra motivation and a great atmosphere on my return to Brazil. To Prof. Cristiano L. P. de Oliveira, I am grateful for enriching discussions and various clarifications. I mention also Fernando Batalioto, Alexander Duarte, Odair Gimenes, Igino Martins, Edneuma Oliveira, Ellen Binotto, Diogo Soga, Sara Alves, Amarildes Dantas, Cleidilane Sena, Messias de Souza, Thiago Gualberto, Celso Risi, Luiz Henrique da Silva, Prof. Suhaila Shibili and Prof. Antônio Figueiredo. All of them contributed, in many ways, to a good stay at GFCx-IFUSP.

To the administrative staff at both universities. In France, I mention Mmle. Brigitte Bordes who worked for the documentation follow its normal route in Bordeaux, even with the Atlantic separating us. In Brazil, I thank to Cristiano Chaves and Maria Izabel Cav-

alcante. I am aware that, without them, my problems with the archaic bureaucracy of USP would have been much greater.

To those ones who were willing to read this manuscript and contribute with suggestions and corrections. I thank to Professor Brigitte Pansu, from the University Paris-Sud XI, and to Professor Cyrus R. Safynia, from the University of California, Santa Barbara, for being the referees of the thesis. To Professor Márcia Fantini, from the University of Sao Paulo, to Professor Yan Levin and to Professor Nadya Pesce da Silveira, both from the Federal University of Rio Grande do Sul, I thank kindly for participating in the thesis jury and for the precious contributions for the final version of the text.

At last (but not at least!), I thank those ones who ensured my daily bread: to CAPES, to program CAPES-COFECUB (project n. 558/07) and to program Eiffel-EGIDE, for fellowships and grants during my doctorate.

To all of you, and those who were eventually forgotten, my many thanks.

Sao Paulo, november 17, 2011.

CONTENTS

Resumé	iii
Abstract	v
Resumo	vii
Acknowledgements	xiii
Contents	xvii
General introduction	21
1 Background	25
1.1 Phospholipids	25
1.2 Self-assembly phenomena	26
1.3 Lyotropic lamellar phases	28
1.3.1 Elasticity and interactions in lamellar phases	30
1.4 DNA molecule: few physical properties	32
1.4.1 Interactions between DNA molecules	35
1.5 DNA-lipid complexes: state of the Art	36
1.5.1 Counterion release	39
1.5.2 DNA-neutral lipids complexes	41
1.6 X-rays scattering by lamellar phases	42
1.6.1 The model of <i>Nallet et al.</i>	42
1.6.2 Effects of disorder on $\tilde{S}(q)$	46
1.7 DNA dynamics in lamellar phases	48
1.7.1 Anisotropic Brownian diffusion	49
1.7.2 Spatially-resolved FRAP	50
1.8 Dobrindt's model	51

1.8.1	Difficulties on analyzing diffusion within lamellar phases	52
1.8.2	Modified form of the spatial bleaching profile	53
2	Materials and methods	57
2.1	Constituents of the system	57
2.1.1	DNA fragments	57
2.1.2	Lipid part	58
2.1.3	Solvent	59
2.2	Samples preparation	59
2.2.1	Equilibration procedure	61
2.3	X-rays experiments	61
2.3.1	SWING-SOLEIL synchrotron line	62
2.3.2	Conventional sources	64
2.3.3	Data treatment	66
2.4	Polarized-light and epifluorescence microscopies	72
2.5	Freeze-fracture and electron microscopy	74
2.6	FRAP experiments	74
2.6.1	Analysis software	76
3	Structural results	79
3.1	Lipid-water system: host phase	79
3.1.1	Membranes with 70:30 PC-to-Simulsol ratio	79
3.1.2	Membranes with 50:50 PC-to-Simulsol ratio	100
3.1.3	Discussion	106
3.2	DNA-lipids complexes: structural polymorphism	109
3.2.1	Membranes with 70:30 PC-to-Simulsol ratio	109
3.2.2	Membranes with 50:50 PC-to-Simulsol ratio	141
3.3	Discussion	144
3.3.1	Varying the DNA amount	144
3.3.2	Effects of DNA on the smectic ordering of L_α phases	145
4	Dynamical results	149
4.1	Simulations	149
4.1.1	Isotropic case	149
4.1.2	Anisotropic case	150
4.2	Experiments	153
4.2.1	Isotropic DNA-water system	153
4.2.2	Ternary DNA-lipid complex	154
	Conclusions and perspectives	163

A	Protocols	167
A.1	DNA desalting and sonication	167
A.2	DNA labeling	168
A.3	Preparation of lipids	168
B	Correlation length	169
C	Résumé en Français	173
C.1	Motivations et objectives	173
C.2	Bases	174
C.2.1	Complexes d'ADN et lipides: état de l'Art	174
C.2.2	Diffusion des rayons X par des phases lamellaires	176
C.2.3	Diffusion de l'ADN dans des phases lamellaires	177
C.3	Matériaux et méthodes	179
C.3.1	Constituants du système	179
C.3.2	Expériences de rayons X	179
C.3.3	Microscopie d'épifluorescence et à lumière polarisée	180
C.3.4	Microscopie électronique et cryo-fracture	180
C.3.5	La technique de FRAP	180
C.4	Résultats structuraux	180
C.4.1	Système lipides-eau : la phase hôte	180
C.4.2	Complexes lipides-ADN : polymorphisme structural	185
C.5	Résultats dynamiques	192
C.5.1	Expériences de FRAP	192
C.6	Conclusions et perspectives	195
	Bibliography	205

GENERAL INTRODUCTION

Scientific context

Under proper conditions, surfactants can be used for preparing nanostructured materials thanks to their ability to self-assemble into a variety of liquid crystalline phases. Lamellar phases are particularly attractive for preparing layered composite structures because colloidal particles can be intercalated within or between surfactant bilayers. The final properties of the composite can be controlled by varying the bending rigidity of bilayers or their separation. The design and preparation of a variety of new composite materials open a broad horizon for several technological applications, covering fields from materials science to biomedicine [1] and offer new challenges in understanding self-assembly in soft-confined geometries [2, 3].

DNA is a semi-flexible biopolymer that can be complexed with lipid mesophases. In the particular case in which nucleic acids and surfactants are mixed to form complexes, such systems appear as a synthetic alternative to engineered viral vectors used in gene therapy. Essentially, the idea consists in the encapsulating of nucleotides by lipid phases in order to protect the genetic material against damages from the extracellular medium [4–6]. Obviously, the structure of these vectors also plays a crucial role in the release of DNA inside cells, which must occur in a progressive and controlled manner. Therefore, their efficiency depends on the precise understanding of the mechanisms responsible for the formation of the complexes and their dynamical properties either to optimize the quantity of material to be encapsulated or to provide the proper delivery into the targeted cells [7].

Over the past two decades, research activities around these systems have experienced vigorous growth. Experimentally, the structure of DNA-lipid compounds has been successfully elucidated by X-ray diffraction and electron microscopy [8–13]. These studies have shown a wide diversity of supramolecular assemblies with a intricate interplay between organization and several parameters involved in preparation protocols such as quantity of material, incubation time and mixing conditions [14]. Thanks to the role played by electrostatic interactions, cationic lipids have been the preferred choice for the creation

of such vectors [15]. However, in spite of good results obtained *in vitro*, these complexes have shown some degree of cytotoxicity, limiting their *in vivo* applications [16]. Therefore, the research for a system based on neutral lipids, in which electrostatic interactions are not an obvious candidate to drive complexation, appears as an attractive subject either for fundamental science or for technological applications. On a such complex, where DNA fragments were mixed to non-cationic membranes in order to form a model system and evaluate its structural and dynamical properties.

Motivations and goals

From the above described scenario, the reasons of the interest around DNA-lipid complexes are now clear. The present thesis contributes to the state of the Art by presenting an experimental study on a hydrated complex obtained from the mixing between DNA fragments and non-cationic lamellae. It is a work on basic Science, which focuses on the fundamental properties of the complex, studying its phase diagram.

The lack of *a priori* opposite charge attraction between DNA and membranes opens a promising experimental window to probe the role of other interactions, especially those ones of thermodynamic origin (fluctuation and hydration forces, for instance), in the formation and phase behavior of DNA-neutral lipids complexes [17]. Since the system deals with confinements at the scale of few nanometers, this also provides a nice opportunity to explore short-range interactions, such as hydration forces, not yet completely understood [18, 19]. The main goals were to investigate the structural features and identify the mesophases as function of composition and hydration. The originality of the approach consisted in the use of the swelling properties of a lyotropic lamellar phase to control the size of the aqueous layers in between lipid bilayers. In other words, by controlling the hydration of the complex, we tuned the *confinement* exerted by the host phase over the nucleotides [20, 21]. In order to gain some insight on the mechanisms involved on the stabilization of the complex, the ionic strength of the solvent as well as the elastic properties of membranes were modulated by the respective addition of monovalent salt and co-surfactants to the system.

A set of techniques was used to address these goals. The principal experimental tool was X-rays diffraction, performed either by using conventional sources or synchrotron radiation facilities. In order to complement diffraction data, optical and electron microscopies were used to obtain direct-space visualization of the aggregates. Some modelisation, describing the structure and the form factors of the lipid/water host phase, was carried out to furnish subsidies to discussion on the role of intermembrane forces in complexation and phase behavior.

Another contribution from the current study concerns dynamical properties. Reports on mobility of DNA-amphiphile complexes are very rare in the literature [22] and, as far as we know, studies measuring the diffusion of nucleotides between the bilayers of

lipid lamellar phases have never been conducted outside the groups where this thesis was developed [23, 24]. A possible explanation for this absence may be related to difficulties in the analysis of anisotropic diffusion at molecular scale. Here, the *fluorescence recovery after photo bleaching* is used to test a theoretical method recently proposed at CRPP to describe the Brownian motion of cylinders in the particular constraints imposed by lyotropic lamellar phases.

The manuscript is structured as follows: the next chapter is dedicated to the presentation of the backgrounds. Informations available in the literature are presented in order to give a brief review and present the state of the Art. Special attention is paid to the models used in the description of X-rays scattering from lamellar phases and to the approach of anisotropic diffusion. In chapter 3, the structural results are presented. Chapter 3 starts with the characterization of the host phase, that is, the binary lipids/water system. Three different ratios between lecithin and co-surfactants are evaluated as well as the behavior of the phase under two ionic strength conditions. It is found that the host phase is stabilized by a hybrid interplay between van der Waals, hydration and fluctuation forces, as attested by a careful analysis of the parameter of Caillé. In following, the phase behavior of the ternary DNA-lipid-water complex is presented. A rich polymorphism of mesophases is found and the full incorporation of nucleotides to the lipid part is observed to be dependent on the amount of DNA in the system. In addition, the insertion of rods in-between bilayers is found to increase the smectic ordering, suggesting a major role of steric forces in complexation and phase behavior. In all the above described analysis, X-rays, electron microscopy and optical observations are used in a complementary way. Chapter 4 brings the experimental results related to dynamical properties. Here, “dynamical properties” mean the diffusion of DNA fragments within the water gaps of the host phase. Anisotropic diffusion coefficients, parallel and perpendicular to the orientation of local nematic director, were successfully extracted showing a close relationship between structure and dynamics. Finally, the main results of the work are presented together with the conclusions.

CHAPTER 1

BACKGROUND

1.1 Phospholipids

Lipids are a wide class of organic materials, generally obtained from oils and fats, which has not a precise or consensual definition. An attempt in order to classify these substances is to describe them in terms of their solubility properties. For instance, we can denote as lipids those substances which are highly soluble in apolar liquids and virtually not soluble in water [25]. Most of these compounds are endowed with amphiphilic properties, although some important types, such as cholesterol, have not this characteristic. Lipids of biological interest, including those ones used in this manuscript, belong mostly to the group of **phospholipids**, which are formed around a common structure composed by a phosphate group and a glycerol.

Fatty acids bind to both ends of the glycerol through ester bonds. These acids have a long hydrocarbon chain, typically composed of 14 to 24 atoms, which may have one or more unsaturations [26]. At the other end of the molecule, the phosphate group joins other polar groups, usually nitrogenated, constituting the hydrophilic part of the lipid. Essentially, it is this polar head which determines the properties of the molecule and thus differentiates the various classes of these compounds.

Among the fatty acids commonly involved in the formation of phospholipids, we found oleic and palmitic acids as well as their derivatives. One of the most common polar groups is the group **choline**. Phospholipids composed of cholines are also called **phosphatidylcholines** (PCs) or **lecithins**. These molecules have a packing factor $p \approx 1$ —more details given below, see Sec. 1.2—, and appear frequently self-associated in bilayers. Lecithins share the same head group and differ among themselves according to the fatty acids of their tails [25].

Depending on the electrical properties of the hydrophilic group, phospholipids can be divided in cationic, anionic and **zwitterionics**. In the first two types, the net electric charge is nonzero. Zwitterionics are globally neutral, but the spatial arrangement of differ-

ent ionized functions within the head group gives rise to a weak dipole moment. Some of the most abundant lipids are zwitterionic PCs, where the dipole $P^- - N^+$ is oriented almost parallel to the plane of membranes [27]. The general structure of phosphatidylcholines, the main lipid used in this work, is exhibited in figure 1.1.

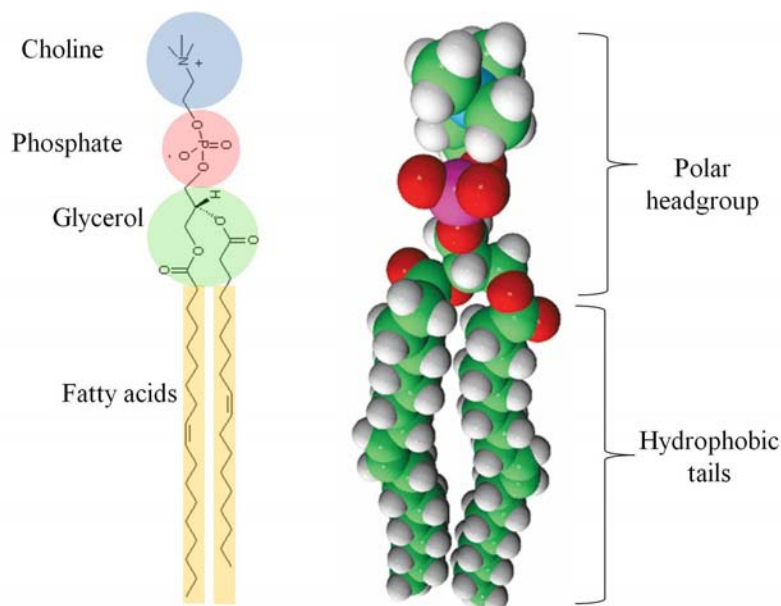


Figure 1.1: General structural formula (left) and a space filling model of phosphatidylcholines. Carbons and hydrogens, designed by green and white balls in 3D picture, were omitted in 2D representation.

1.2 Self-assembly phenomena

Self-assembly phenomena have crucial importance in a variety of biological processes, including the formation of membranes. At the basis of such phenomena, one finds the *amphiphiles*. The word “amphiphilic” finds its roots in the Greek *amphi*, which means *both*, and *philos*, which means *friendship*. This nomenclature explicits the ambiguous nature of these molecules, which have both hydrophilic and hydrophobic (or lipophilic) properties simultaneously [28]. This dual behavior related to water plays a primordial role in self-organizing properties of these substances in solution. In figure 1.2, the scheme of an amphiphilic molecule is shown.

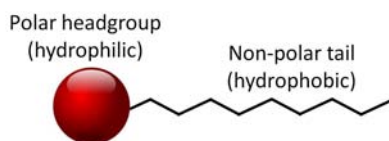


Figure 1.2: Schematic draw of an amphiphilic molecule.

The molecule can be divided in two distinct parts: a polar head and a carbonic tail. In the presence of water (or other polar solvent), the contact between the polar hydrophilic

group and the medium is thermodynamically favored, whereas the aliphatic tail suffers intense **hydrophobic** effect minimizing the surface contact with the surrounding. This property makes amphiphilic molecules able to form interfaces separating polar and non polar environments. For that reason, this class of materials is also known as *surfactants* (surface active agents) [3].

At very low concentrations, these molecules can be found dispersed in the solvent. However, above a certain concentration of surfactant, the critical micelle concentration (CMC), the formation of molecular aggregates gives rise to a variety of stable structures. The form of such aggregates depends, apart from the chemical composition of amphiphilics, on thermodynamic variables such as temperature and concentration. The thermodynamic mechanism involved in the formation of self-assembled structures in aqueous solutions is the hydrophobic effect. The presence of hydrocarbons induces the formation of cavities in the vicinity of the non polar tails, causing the structuration of water. This increase in the ordering near the chains implies a decrease in local entropy. When molecules meet together, a fusion of the cavities occurs and expulsion of the water located at the interface, leading to increasing of entropy and to the appearance of highly stable arrays [29].

In figure 1.3, the most commonly found structures in surfactants/water mixtures are shown. In order to proceed further, it is useful to define the packing parameter $p = \nu/a_0l_c$, where ν is the volume of hydrophobic part, a_0 is the area of polar head and l_c is the length of the tail. Simple geometric considerations about the packing of the molecules allows to predict the final conformation of the formed aggregates [26]. The packing parameter determines whether the amphiphiles will form spherical micelles ($p < 1/3$), non-spherical micelles ($1/3 < p < 1/2$), vesicles or bilayers ($1/2 < p < 1$) or inverted structures ($p > 1$) [26]. Obviously, the boundaries of these domains are not precisely defined and are given only in an indicative context.

Micelles and bilayers are fundamental types of amphiphilic aggregates. In function of concentration (or temperature), these entities can rearrange and form superstructures at larger scales. Among the many possible arrangements, we found the **lamellar** and the **hexagonal** phases. Lyotropic lamellar phases (L_α , $L_{\beta'}$ e $P_{\beta'}$) are made from one-dimensional stacking of bilayers, where carbonic tails remain facing the inner membrane and polar heads are in contact with the intercalated solvent (fig. 1.4(a)). This configuration has greater importance for this study, because the lipid part of the complex consisted of a lyotropic lamellar phase whose aqueous layers hosted DNA fragments.

Hexagonal arrangements, in turn, are composed by cylindrical micelles. The H_I phase is formed by direct micelles organized in a columnar phase along z-axis and forming a two-dimensional triangular structure in the xy-plane. The H_{II} phase is formed from tubular reverse micelles with the aqueous solvent located inside cylinders formed by the hydrophilic groups (fig. 1.4(b)).

Other anisotropic molecules also self-assemble in a variety of liquid-crystalline phases.


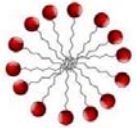





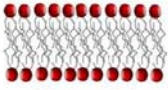

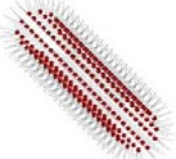
$p < \frac{1}{3}$			Spherical micelles
$\frac{1}{3} < p < \frac{1}{2}$			Non-spherical micelles
$\frac{1}{2} < p < 1$			Vesicles
$p \sim 1$			Bilayers
$p > 1$			Inverted micelles

Figure 1.3: Structures formed from self-assembly of amphiphiles. In the first column, the values of the packing parameter are presented. In the second column, the geometric form of the molecules are shown. In the last column, structures of large scale aggregates are exhibited.

Solutions containing these molecules usually present lyotropic behavior with mesophases depending on concentration. A typical example concerns rod-like molecules such as the DNA fragments used in this work. In diluted aqueous solutions, the particles are isotropically distributed. Nevertheless, above a certain concentration, $C_{DNA} > 160\text{mg/ml}$ for the DNA fragments studied in this work, the cylinders acquire orientational order. The axis appear then aligned around a preferred direction and, in a narrow range of concentrations, they form a cholesteric phase characterized by a helically-wound director vector \hat{n} [31,32].

Due to chirality, solutions containing high amounts of DNA, self-organize in a rich polymorphism of highly-ordered phases, where, besides the orientational ordering, the particles have positional correlation. Among the mesophases found in concentrated solutions, one can highlight the cholesteric phases, where the rods form a supramolecular arrays in a helicoidal structure. Hexagonal columnar phases and orthorhombic symmetries are also observed for extremely concentrated solutions [31,33].

1.3 Lyotropic lamellar phases

Lyotropic lamellar phases are liquid-crystalline systems doted of singular physical properties. Along the direction perpendicular to the plane of membranes (so called **z-axis**

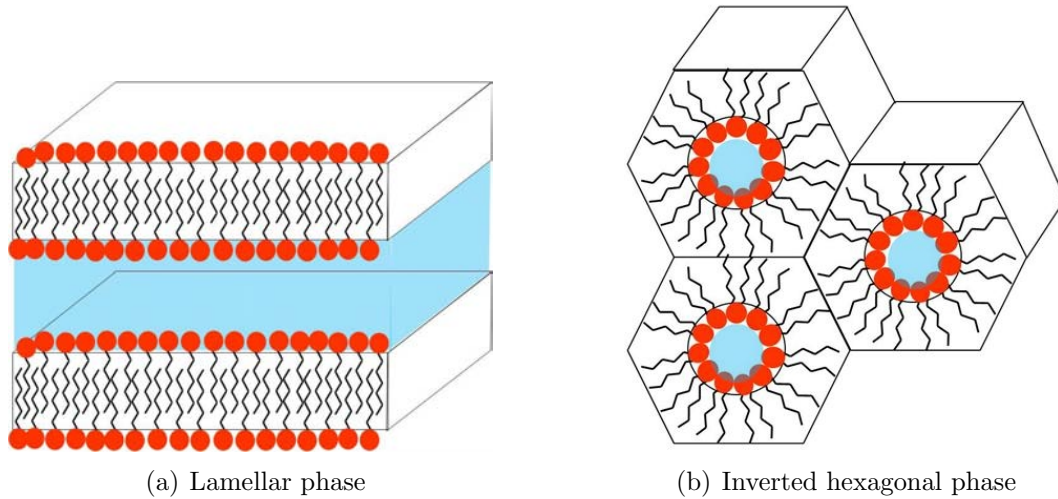


Figure 1.4: Superstructures of surfactants. (a) multilamellar phase formed from the stacking of bilayers and (b) H_{II} phase formed from hexagonal-columnar arrays of inverted cylindrical micelles (adapted from [30]).

throughout the manuscript), there is long-range positional order in a periodic structure with alternating lipid bilayers and solvent layers. Along the other two directions (**xy-plane**), the degree of order depends on thermodynamic variables, specially temperature and concentration. According to the ordering of monomers within membranes, such phases can be classified as L_{α} , $L_{\beta'}$ ou $P_{\beta'}$ [34].

For membranes in the L_{α} state, molecules have behavior similar to a two-dimensional liquid. Bilayers are flat on average and fluctuate around a defined equilibrium position. This means that, in directions **xy**, molecules have high degree of freedom without positional ordering in the plane of membranes. Although molecules may change of monolayer within bilayers (a phenomenon known as *flip-flop*), there is little transfer of monomers from one bilayer to another across the aqueous medium. In addition, aliphatic tails are highly disordered with no defined distance from one lipid molecule to other. At macroscopic scale, the system has great fluidity at room temperature. For that reason, this phase is often (although improperly) referred to as *fluid phase* or *liquid phase*.

In $L_{\beta'}$ and $P_{\beta'}$ phases, molecules keep positional order within bilayers. The membranes are also flat, in average, and present fluctuations lower than those ones found for L_{α} phases. The polar head groups form a 2D triangular lattice in the plane **xy**, forming 2D hexatic phases. According to the inclination of the tails within the bilayers, this domain can be classified in three sub-types: $L_{\beta F}$, $L_{\beta L}$ and $L_{\beta I}$ [35]. Compared to L_{α} , $L_{\beta'}$ phases are viscous at room temperature and, for that reason, they are often called *gel phases*.

Finally, the $P_{\beta'}$ phase presents the higher level of ordering among the three types of lamellar phases described here. Molecules have positional correlation within bilayers, wherein their tails keep regular distances between themselves. Unlike the two phases previously detailed, in $P_{\beta'}$, membranes are not flat and have periodic corrugations (see fig. 1.5).

From the point of view of this manuscript, the more relevant of these phases is the L_{α} .

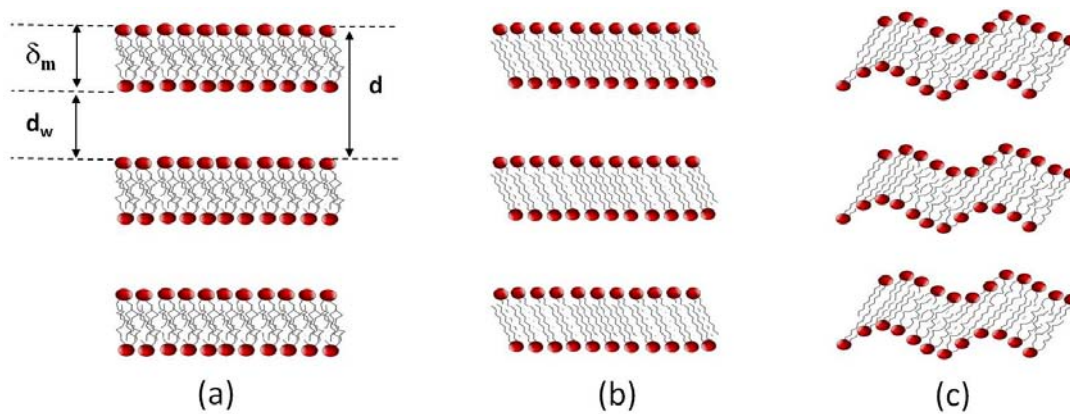


Figure 1.5: Lyotropic lamellar phases. (a) L_α , (b) $L_{\beta'}$ and (c) $P_{\beta'}$. Conventions indicated for lamellar periodicity d and the thicknesses of membranes and aqueous layer, δ_m and d_w , will be used throughout the manuscript.

This is because the lipid phase employed here is self-organized in this kind of arrangement. A fundamental property of L_α phases is its capability to incorporate solvent. As the system is hydrated, the thickness of aqueous layers (d_w in fig. 1.5-a) increases, leading to the swelling of the structure. From simple geometrical considerations, the **lamellar periodicity** $d = \delta_m + d_w$ is obtained by using the relationship:

$$d = \frac{\delta_m}{1 - \phi_{wt}} \quad (1.1)$$

where ϕ_{wt} corresponds to the water volume fraction and δ_m to the thickness of membranes. From 1.1, we see that the lamellar periodicity increases upon hydration. This process occurs until a maximum hydration limit, above which the system phase-separate with excess water.

Since lyotropic lamellar phases are 1-D ordered systems, obtained from sheet-like entities, the bilayers, their physical description is analogous to that one of smectic-A liquid crystals. Detailed considerations about this description, as well as the intermolecular forces involved in the stabilization of the system, are carried out below.

1.3.1 Elasticity and interactions in lamellar phases

Elasticity plays a major role on the formation and stabilization of self-assembled surfactant systems. The structural form acquired by amphiphile aggregates is the result of a close interplay between elasticity and thermodynamics [3]. In the previous section, lyotropic lamellar phases were treated as stacks of flat rigid bilayers. However, in real systems, thermal effects lead to *fluctuations* on membranes with drastic consequences over structure [36–38].

In this work, we will assume lamellae subjected to two kinds of membrane deformations: curvature stress and compression. The schematic representation of these deformations is exhibited in fig. 1.6.

In the harmonic approximation, the deformation energy per unit volume of smectics-A

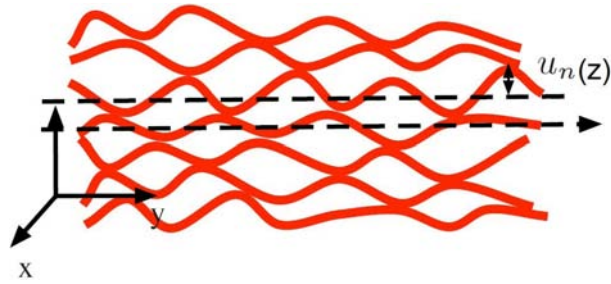


Figure 1.6: Schematic drawing of lipid bilayers confined in a multilamellar phase. The equilibrium positions are indicated by dotted lines. Thermal effects induce either fluctuations around the mean separations (compression) or curvatures on membranes. (Adapted from [39]).

is given by [40, 41]:

$$f_{def} = \frac{1}{2}K (\nabla_{\perp}^2 u)^2 + \frac{1}{2}B \left(\frac{\partial u}{\partial z} \right)^2 \quad (1.2)$$

where u are displacements around the equilibrium positions (defined in fig. 1.6) and K is the splay constant, which is related to the membrane bending curvature modulus of an isolated membrane through the relationship:

$$K = \frac{\kappa}{d} \quad (1.3)$$

Since the bilayers are treated as oscillating sheets, the periodicity d in 1.3 is the average smectic step.

The constant B is the compression modulus of the stack of lamellae. It should be noted that this coefficient is related to the interactions between membranes and, therefore, it is an interaction constant. For single (isolated) membranes, B has no meaning.

The total **interaction energy** per unit surface of multilamellar arrays of **non-charged and flexible** bilayers is given by [3]:

$$f_{int} = f_{vdW} + f_{hyd} + f_{und} \quad (1.4)$$

The first term in the right side of 1.4 represents the *attractive* van der Waals forces. The other two energies, f_{hyd} and f_{und} , are associated to *repulsive* hydration (solvation) and undulation forces, respectively.

The van der Waals interaction is given by [42]:

$$f_{vdW} = -\frac{H}{12\pi} \left[\frac{1}{d^2} + \frac{1}{(d + 2\delta_m)^2} - \frac{2}{(d + \delta_m)^2} \right] \quad (1.5)$$

where H is the Hamaker constant.

The hydration energy per unit area corresponds to a short-range interaction acting at very small surface separations, $d_w \lesssim 10 \text{ \AA}$. The physical origin of this force is still unclear and remains an object of debate in the literature [43, 44]. A very first attempt to explain

these interactions was to associate them to the structuration of water molecules at the interface with polar heads [45,46]. More recently, a new mechanism based on polarization effects in vicinity of membranes has been proposed [19]. A consensual point, however, is that hydration energy per unit surface is empirically described by an exponential decay expression of the kind:

$$f_{hyd} = P_h e^{-\frac{d'_w}{\lambda_h}} \quad (1.6)$$

where P_h is a scaling constant and λ_h is the decay interaction length. The typical values of these constants are around $4k_B T / \text{\AA}^2$ and 2\AA , respectively, at room temperature [47].

The last term in 1.4 refers to thermally induced out of plane fluctuations. They are long-range repulsive forces, arising from the difference in entropy between a fluctuating “free” membrane and a “bound” membrane [42]. Since these steric interactions are thermally induced, the bending curvature modulus, κ , must be of the order of $k_B T$ in order they are effective in the system. An analytical form for this energy was first derived by Helfrich [41, 48, 49]:

$$f_{und} = \frac{3\pi^2 (k_B T)^2}{128} \frac{1}{\kappa} \frac{1}{d'_w{}^2} \quad (1.7)$$

1.4 DNA molecule: few physical properties

DNA, or **deoxyribonucleic acid**, is a semi-flexible biopolymer whose monomers, the nucleotides, are formed from a **phosphate group**, a pentose sugar (the **deoxyribose**) and a nitrogen base [25]. The bases involved in the formation of nucleotides are the purines **adenine** (A) and **guanine** (G), and their complementary pyrimidines **thymine** (T) and **cytosine** (C). In figure 1.7, the structural formulas of these constituents are exhibited. By combining these four types of heterocyclic bases, DNA encodes, together with RNA, all information contained in genome. Besides being the reservoir of genetic information, this molecule is also a fascinating system that places challenges of great complexity for its description in physical basis [50].

The three-dimensional structure of DNA was elucidated in 1953, in one of the most controversial episodes of the History of Science. Based on X-rays data obtained by Maurice Wilkins and Rosalind Franklin, James Watson and Francis Crick determined, without Franklin’s knowledge, that DNA chain is organized in an anti-parallel right-handed double helix [51]. The discovery earned to Watson, Crick and Wilkins the Nobel Prize in medicine and physiology in 1962. According to this model, pentose and phosphate groups form the backbone of the chain, with the nitrogen bases joined at the center, through hydrogen bonds, forming the “steps” of a spiral staircase.

According to environmental conditions (pH, hydration or ionic strength, for example), the double helix can assume different conformations. In solution, the most common form of DNA is the B-form. In this configuration, the nitrogen bases are aligned perpendicularly

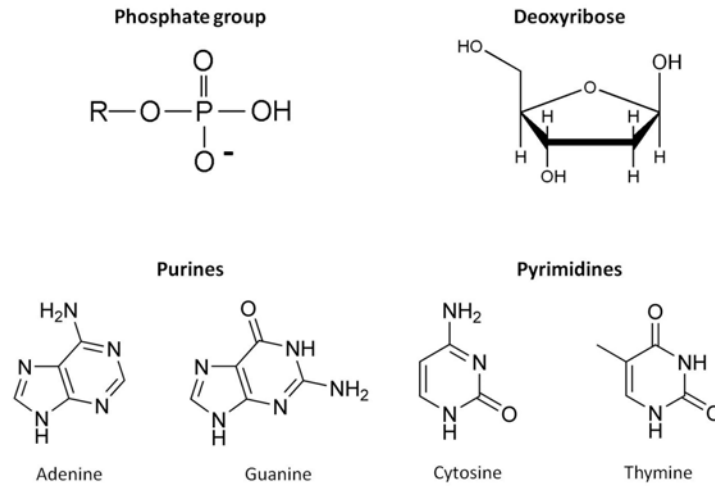


Figure 1.7: Structural formulas of DNA constituents. The phosphate group and the pentose sugar form the backbone of the molecule. The permutation of the four heterocyclic bases allows the coding of all genetic information.

to the helical axis, with ten base pairs (bp) per helical pitch. The distance between base pairs is $\approx 3.4 \text{ \AA}$ and every turn has length of $\approx 34 \text{ \AA}$. The diameter of the chain is $\approx 20 \text{ \AA}$ [52].

In figure 1.8, the double helix structure of DNA is outlined with its most relevant dimensions. The persistence length, that is, the part of the molecule wherein it is rigid, has size of $\approx 500 \text{ \AA}$, or 150 bp. The polymeric chain can reach very long lengths, exceeding 2 meters, resulting in highly packaged structures when polynucleotides are confined within the nucleus of eukaryotic cells. In addition, another remarkable aspect of the double helix is its chirality. This leads to particular liquid-crystalline properties with a complex set of mesophases in confined geometries [31].

From the point of view of electrostatics, DNA can be treated as a polyelectrolyte [50, 53]. When placed in water, phosphate groups release a proton regardless of pH conditions. Therefore, every nucleotide remains with an excess negative charge. Assuming that these anions are uniformly distributed along the chain, the charge separation is $l_D \approx 1.7 \text{ \AA}$. This leads to a surface density of $\sigma_D \approx -e/110 \text{ \AA}^2$ [54]. These values make DNA the most charged system in the nature [25].

Solubility properties also play an important role in DNA structure. The pentose and phosphate groups are extremely soluble in water whereas the nitrogen bases are not. This implies the presence of strong hydrophobic effect in the core of the chain, driving the bases to turn to each other, in a self-assembly phenomenon similar to that one observed in surfactants. Still in this way, the insolubility of the bases has direct consequences on the hydration properties of the molecule, preventing water from penetrating the core [52]. This feature, combined with the stiffness of the chain within its persistence length, allows us to describe DNA fragments as rigid massive cylinders. In the process of hydration, water molecules bind to the backbone of the chain, covering only the outside of the double helix. A monolayer of hydration is formed when the amount of water reaches ≈ 30

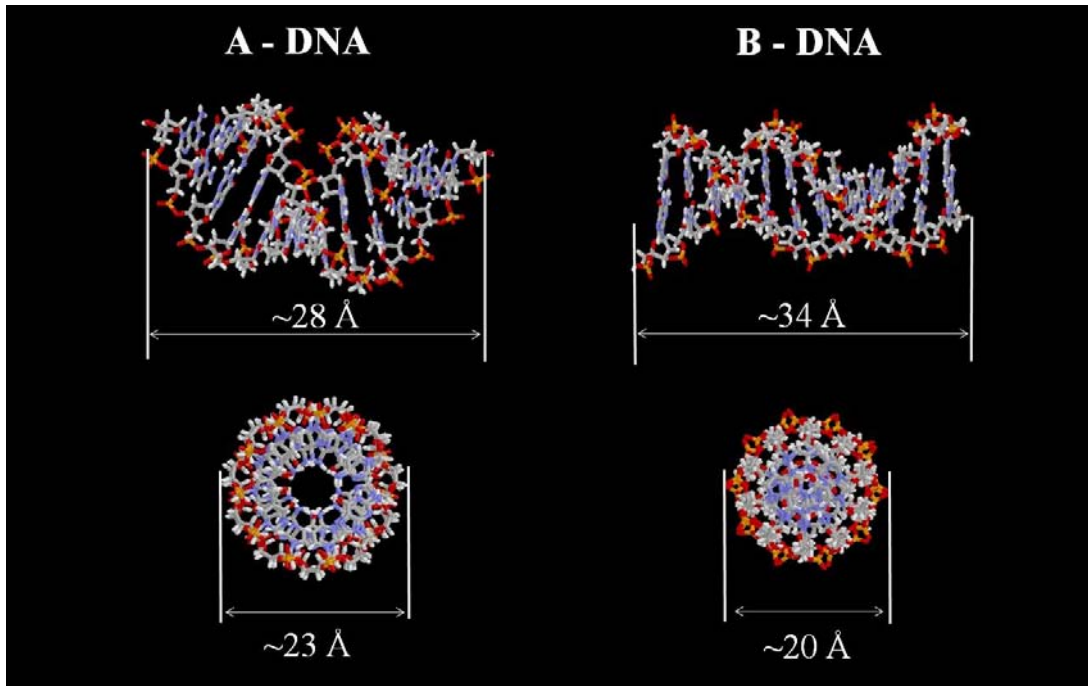


Figure 1.8: Tridimensional models showing one helical pitch of A- and B-DNA forms. Changes on diameter and longitudinal size between the two conformations are evidenced.

H_2O molecules per base pair [55].

Depending on environmental conditions, the presence (or not) of ionic salts and, especially, hydration, DNA can assume different conformations. Besides the B-form, other common configurations are A and Z-form. The Z-form is more rare, having rotation axis in the counterclockwise direction (left-handed), and will not be treated here. The A-form is frequent in situation of low hydration and keeps the same rotation direction of B-form. It is a more compact structure in the longitudinal direction, where the distance between nucleotides decreases to $\approx 2.5 \text{ \AA}$ and every helical pitch has $\approx 28 \text{ \AA}$, or 11 bp. The transition from B to A-form occurs when hydration decreases to less than 20 water molecules per base pair [56]. In table 1.1, the main properties of DNA relevant to this work are summarized.

Table 1.1: DNA features relevant to this work.

Persistence length	150 bp or $\approx 500 \text{ \AA}$
Diameter	$\approx 20 \text{ \AA}$ (B-form) $\approx 23 \text{ \AA}$ (A-form)
Distance between base pairs	$\approx 3.4 \text{ \AA}$ (B-form) $\approx 2.5 \text{ \AA}$ (A-form)
Helical pitch	10 bp or $\approx 34 \text{ \AA}$ (B-form) 11 bp or $\approx 28 \text{ \AA}$ (A-form)
Electric charge	$1e^-$ /nucleotide
Density	1.7 g/cm^3
Molar mass	330 g/mol (of nucleotides)

1.4.1 Interactions between DNA molecules

As mentioned above, the DNA is a very strong polyelectrolyte. For the purposes of this work, we can consider the fragments as negatively charged rigid cylinders. Isolated DNA molecules always appear associated to counterions which neutralize the global charge. When nucleotides are put in water, a fraction of their counterions dissociates and is released to the bulk solution. In the context of the Manning's theory [57], when the charge separation along the polyelectrolyte is less than the Bjerrum length of the medium, part of the counterions remains condensed at the surface in order to renormalize the charge density parameter to unity:

$$\zeta = \frac{\lambda_B}{l_D} \quad (1.8)$$

The fraction of condensate counterions (CC) is then given by:

$$\phi_{CC} = 1 - \frac{1}{\zeta} \quad (1.9)$$

For B-DNA aqueous solutions, at room temperature, $\lambda_B = 7.1 \text{ \AA}$ and $l_D = 1.7 \text{ \AA}$, leading to $\zeta = 4.2$ and $\phi_{CC} = 0.76$ [58]. This means that only $\approx 24\%$ of the counterions are released to the bulk in DNA solutions.

Direct force measurements between DNA chains have been performed through osmotic stress methods [59–61]. These experiments show the existence of two types of repulsive interactions: at interaxial separations less than 30 \AA (surface separations less than 10 \AA), an exponential decaying force is found to drive the interplay. This force behaves in the same fashion as the hydration forces observed for small membrane separations in lipid lamellae [46]. This repulsion has been attributed to the partial ordering of water molecules in the vicinity of the nucleotides, however, the exact mechanism also remains unclear. The second kind of interaction occurs for interaxial spacing greater than 30 \AA . In this case, the interplay is driven by double-layer electrostatic repulsions, presumably due to the phosphate charges in the DNA structure [47]. Attractive interactions have been theoretically predicted, where its origin would be associated to short-range correlations between charges on the phosphate groups [62]. However, attractive forces have been observed only in solutions containing multivalent ions [47, 50, 53, 63].

These studies have been also carried out under different ionic strengths. The very important conclusion from these researches is that **the short-range intermolecular interactions appear to be insensitive to the amount of added salt**, which has been taken as an evidence that these interactions have no electrostatic origin [60]. As it will be discussed in chapter 4, this result has direct consequences in the system evaluated in this thesis because, since the DNA fragments are constrained by the lamellar matrix, these forces appear as a major actor in the self-assembly of DNA-non cationic systems.

1.5 DNA-lipid complexes: state of the Art

The interest around DNA-lipids complexes dates back to the late of years 1980 [4–6]. Although these early studies have emphasized therapeutic applications, without an immediate concern with structural aspects, it was soon demonstrated that the understanding of the mechanism of transfection (the transfer of DNA followed by expression) would be impossible without the full knowledge of the arrangement of biomolecules within the vector. Moreover, the potential of these systems for the study of self-assembly phenomena was early realized so much that the issue has attracted attention from both theoretical and experimental researchers. Due to the primordial role played by electrostatic interactions, cationic lipids (CLs) were the prime choice for the complexation with very anionic polynucleotides. Since then, these complexes have been widely referred in the literature as *lipoplexes* [7]. Only more recently, studies reporting on zwitterionic- and anionic-based complexes have appeared in the literature [16, 64].

The first attempts to assess the organization of lipoplexes at nanoscopic scale were carried out by using electron microscopy techniques. Inspired on their visual appearance, the aggregates were baptized with somewhat exotic nomenclatures like “beads on a string” [5], “spaghetties” or “meatballs” [11, 12].

The first accurate description of the structure of lipoplexes was carried out by *Radler et al.* in 1997. Using synchrotron radiation and polarizing microscopy, they demonstrated that a DNA/DOTAP-DOPC system is self-organized in a L_{α}^c phase wherein the nucleotides are inserted in the aqueous layers in-between bilayers¹ such as depicted in figure 1.9. In the plane of membranes (xy), DNA is condensed in a 2D smectic lattice where the interaxial spacing, d_{DNA} , depends on a delicate balance between positive charges of lipids and negative charges of hosted macromolecules. When the number of charges introduced by nucleotides exceeds the number of cationic charges, an aqueous phase containing naked DNA appears. Conversely, when positive charges exceeds the number of anions, a non-complexed lipid phase appears. Complexation is optimized at the isoelectric point, when the system is globally neutral. A little latter, it was also demonstrated that the ionic strength of solvent, modulated by introduction of divalent salts in solution, plays a relevant role in compactation and adhesion of biomolecules to membranes [63]. Typically, the distance between DNA rods varies in the range $25 \text{ \AA} < d_{DNA} < 70 \text{ \AA}$, with correlation lengths extending to over ≈ 10 molecules.

Since these pioneering works, X-ray scattering has been used as the standard technique in structural investigations on numerous other lipoplexes. For some systems, it was observed that the emergence of intermembrane correlations leads to the formation of structures with higher levels of organization [13]. Exploring the thermotropic properties of DMPC/DMTAP mixtures, the authors of Ref. [65] revealed the formation of a

1. The index “c”, in the symbol L_{α}^c , means that the fluid lamellar phase “contains” DNA. Inspired by names given in electron microscopy studies, this conformation was early referred to as “sandwich-like” structure.

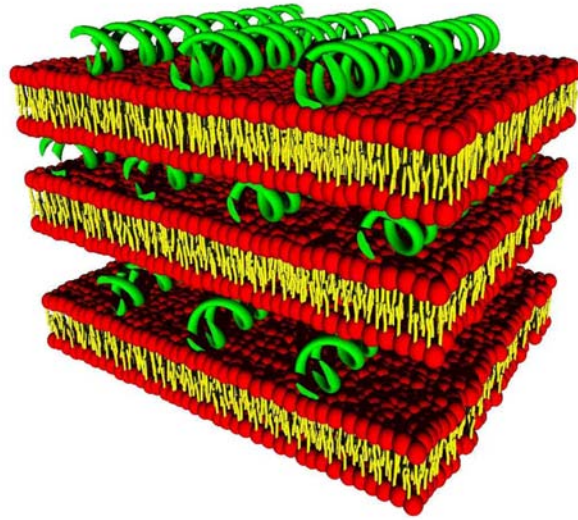


Figure 1.9: Schematic drawing of the L_α^c “sandwich-like” structure found by Rädler et al. [8]. The lipids form a multilayered array with the DNA molecules inserted in the aqueous gaps in-between lamellae (figure kindly provided by G. Tresset).

centered-rectangular columnar phase of DNA rods embedded in a L_β^c lipid phase. More recently, a two-dimensional structure of simple rectangular symmetry was also reported in a thermotropic DNA-CL system [66].

Although lyotropic lamellar phases are the more frequent structures in lipoplexes, they are not the only type of aggregates found in these systems. Hexagonal arrays of lipids, “honeycomb-like” structures, have also been often observed. In the study reported in Ref. [9], mixtures of DOPE / DOTAP formed an inverse hexagonal columnar phase, H_{II}^c , wherein linear DNA fragments were lodged inside cylinders of water (fig. 1.10(a)). $L_{\alpha}^c \rightarrow H_{II}^c$ transitions were obtained in this system either by reducing the bending constant κ or by inducing a spontaneous curvature in membranes through the introduction of co-surfactants. In another recent work [10], lipids formed a micellar hexagonal phase, with the nucleotides accommodated in the interstice of the phase, forming, themselves, a honeycomb structure (H_I^c , see fig. 1.10(b)). In general, lipids which spontaneously form lamellar phases tend to form lamellar lipoplexes and lipids which form hexagonal phases tend to form hexagonal lipoplexes [2]. Other rarer types of organization have also been found in DNA-CLs arrays. In particular, the crystallographic groups $Im\bar{3}m$, $Ia\bar{3}d$ and $Pn\bar{3}m$, corresponding to bicontinuous cubic phases, have appeared in systems based on phosphatidylcholines [2, 67, 68].

Theoretical studies have been developed in order to bring some insight on the mechanisms involved on the formation of lipoplexes. Several models have been proposed to address this issue and explain the above-described polymorphism [30]. These works have been conducted at different scales, both microscopic and macroscopic, using methods ranging from computer simulations, at atomic level, to the elastic theory of liquid crystals [69, 70].

The large majority of these models deals with complexes based on CLs. Despite the

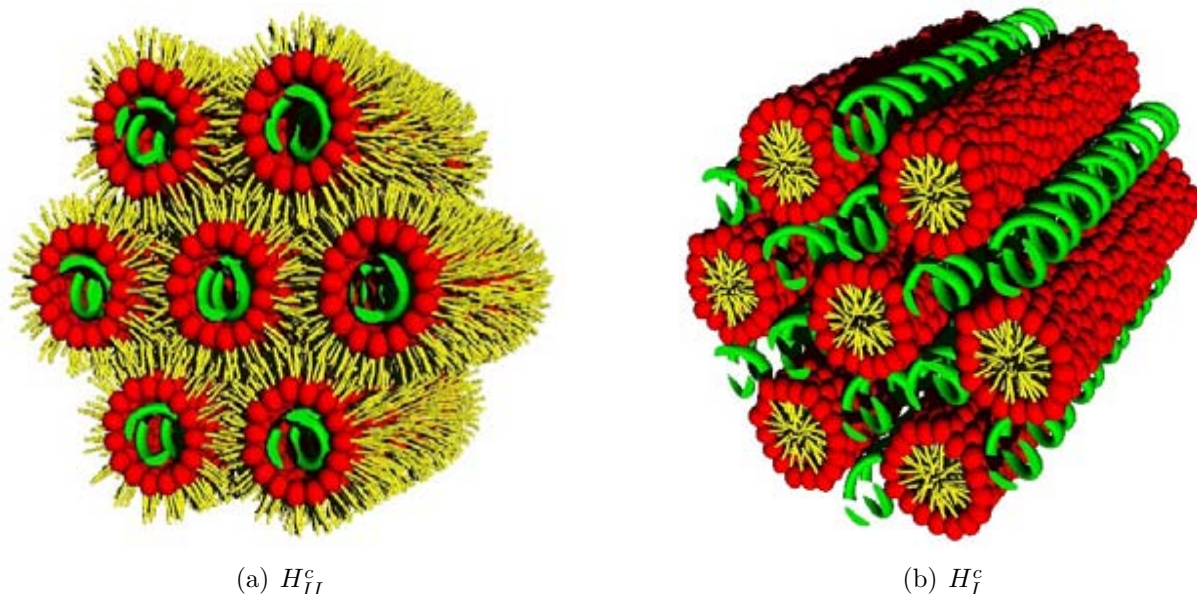


Figure 1.10: Schematic drawing of hexagonal, “honeycomb-like”, lipid phases containing DNA strands inside water tubes (a) and in the interstice (b) (figures kindly provided by G. Tresset).

fact that lipids employed in this thesis are zwitterionic, it is instructive to outlook the main results derived from these approaches. They employ mean field theories and highlight the electrostatic interactions between nucleotides and membranes as well as the thermodynamical variables implied in the stabilization of the structures. A variety of mesophases in equilibrium have been predicted, some of which not yet found experimentally [15, 71–74].

In the current work, our efforts were concentrated around lipid lamellar phases containing DNA strands, the “sandwich-like” structure exhibited in figure 1.9. As pointed out in Ref. [70], assuming the lamellar phase is not disrupted by typical smectic defects as dislocations or rips, the following equilibrium phases have been predicted:

Columnar phase. In this configuration, the DNA fragments are aligned along the direction parallel to the helical axis, forming columnar phases in the plane of membranes (x,y). In the plane (y,z), their centers form 2D crystal lattices. Due to Coulomb repulsion, centered rectangular lattices are the normally expected arrangements [65]. However, if the effective interaction between nucleotides in different layers is attractive, simple rectangular structures are also predicted.

Nematic phase of DNA rods inside a lamellar phase of lipids. In this phase the rods lose positional ordering and the columnar phase is destroyed. The orientational ordering, in turn, is kept with the rods aligning in average around a director vector in the plane of bilayers, forming a nematic-like array. **There is no correlation across the bilayers** in such a way that the nematic directors are randomly distributed along the stacking direction. As it will be discussed below, this characteristic has strong consequences on the behavior of FRAP spots in the studies of anisotropic diffusion conducted in this thesis.

Sliding columnar phase. This phase was not experimentally detected yet. It has in-

intermediate properties between the above described nematic and columnar phases. The major characteristic is a weak coupling between orientation across different bilayers. This correlation falls exponentially according to the number of layers. In the plane of membranes, the correlation between DNA galleries obeys a more complex law, decaying as $\exp\{-const \times \ln^2(a)\}$, where a is the interaxial distance between DNA rods.

Isotropic phase of DNA inside lamellar phase of lipids. This phase is predicted for very low concentration of nucleotides in the system. The particles have no preferential direction and are randomly distributed within the aqueous layers forming a bidimensional liquid.

Although the diversity of approaches, a common result from these theoretical efforts is the consensual conclusion that the phase behavior depends on an intricate interplay between elastic forces, electrostatic interactions and thermodynamics. In addition, for DNA-CLs systems, the complexation has been found to be optimized at the isoelectric point, in agreement with experimental findings.

Results from coarse-grained simulations show the appearance of columnar hexagonal superlattices of DNA embodied between lipid lamellae, as shown in figure 1.11 [75, 76]. According to these predictions, the self-assembly depends strongly on the stiffness of the lipid membranes. For very soft membranes, $\kappa \ll k_B T$, the system tends to form the H_{II}^c phase depicted in figure 1.10(a). For rigid membranes, $\kappa \gg k_B T$, the L_α^c phase is privileged. At intermediate stiffness, and depending on the membrane composition, the complex would incorporate features from both symmetries with a hexagonal phase of DNA inside a lamellar lipid array. This symmetry was experimentally found in a recent work from the group where this thesis has been developed [21]. It should be noted that the prediction from Ref. [75] concerns cationic lipids complexed with DNA into a bulk solution. The case approached in this work is quite different, since we have used non-charged lipids hydrated below the dilution limit. The membranes have been obtained by mixing soya-lecithin and ethoxylated fatty acids. Lecithins form very rigid bilayers, however, the addition of single-chain co-surfactants reduces the stiffness, which could lead to intermediate values of κ , satisfying the elasticity condition derived from the simulations in [75].

1.5.1 Counterion release

Complexation between DNA and cationic lipids involves two mechanisms, one of electrostatic nature and a second one of thermodynamic origins. The electrostatic mechanism corresponds to attraction between opposite charges of nucleotides and CLs. However, opposite attraction, alone, is not sufficient to promote the condensation of DNA on the surface of membranes. This is because, when the fragments adhere to membranes, both nucleotides and surfactants suffer penalties on translational entropy.

This problem is overcome by the counterions. When put into solution, either DNA or CLs are found together with their respective counterions neutralizing the overall charge.

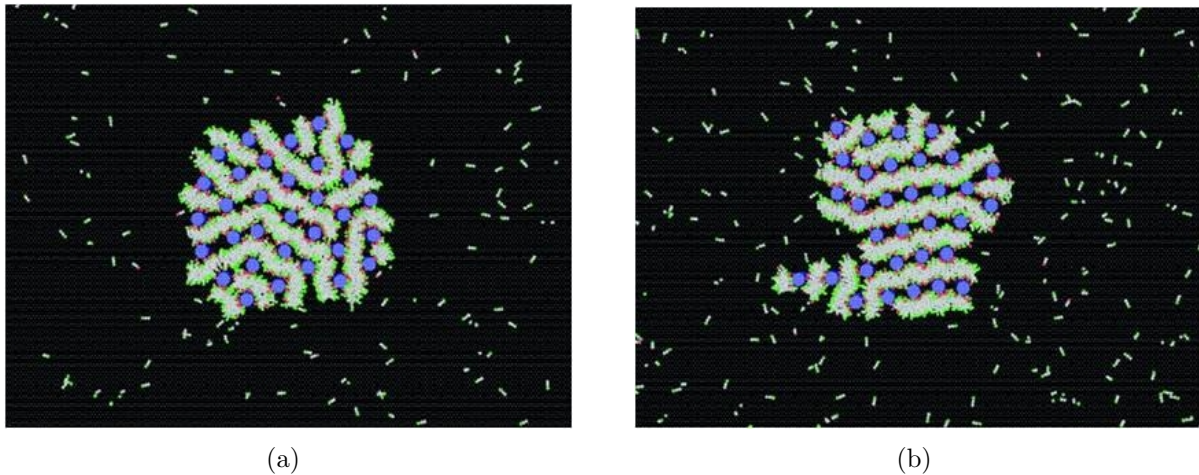


Figure 1.11: Simulation predictions extracted from figure 6 of the Ref. [75]. The structural arrangement is strongly dependent on the membrane stiffness. In (a), at intermediate stiffness, the structure incorporates features from both inverted hexagonal and lamellar lipid phases. As the membranes rigidity is increased (b), the DNA rods form a centered rectangular structure where the aspect ratio between the lattice basis vectors is quite close to unity (which is the aspect ratio between the basis vectors of the hexagonal lattice).

During adhesion, these counterions are released to the solvent promoting the gain on entropy of these ions [77]. The result is the increasing of the global entropy, making the system to become thermodynamically stable (fig. 1.12). This second mechanism is much more important for the formation of lipoplexes than opposite attraction. For this reason, the complexation is often stated to be “entropically driven” [15, 47, 72, 77].

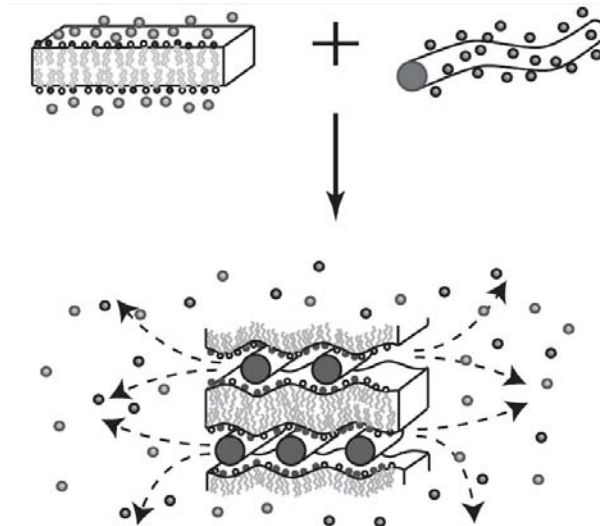


Figure 1.12: Counterion release mechanism. The adhesion of opposite charged macromolecules promotes the release of their respective counterions in solution leading to increase on the global entropy. (Extracted from [47]).

The description in terms of free energy represents a compromise between these two mechanisms and its minimization leads to the formation of stable complexes [50, 53]. It should be noted that the counterions referred to above do not correspond to added salts. The addition of salt changes the thermodynamic behavior of the solution and

the adsorption free energy mainly because it lowers the entropic gain associated to the counterion release [63].

1.5.2 DNA-neutral lipids complexes

Complexes formed between CLs and DNA have found strong receptivity in the scientific community due to high transfection efficient within a relatively large domain of concentrations, ensuring a safer use [78–80]. Nevertheless, as observed for all exogenous materials in live organisms, these compounds also present cytotoxicity under certain conditions and doses [81,82]. For this reason, the search for new compounds based on neutral lipids (NLs) emerges as a natural step in researches on lipoplexes. On one hand, certain NLs have the advantage of being completely biocompatible. On the other hand, they do not rely on electrostatic interactions to drive the complexation with anionic macromolecules. In fact, for a long time it was thought that the formation of hybrid systems involving nucleotides and NLs was not possible precisely due to the absence of intense attraction between opposite charged particles [83].

In the majority of studies on DNA-NLs complexes available in the literature divalent salts are used as mediators of electrostatic interactions between polynucleotides and lipids [68, 83, 84]. The first works on complexes entirely based on neutral lipids, without any other mediators, appeared only recently [16, 85, 86]. Although the complexation does not occur immediately, requiring often a time scale much higher than the one observed in cationic systems, these studies have shown that it is possible to formulate compounds with zwitterionic lipids. These investigations have also revealed that such complexes behave in liquid-crystalline polymorphism mesophases as rich as that one seen in cationic lipoplexes.

Due to the lack of direct (strong) electrostatic interactions between nucleotides and membranes, theoretical models approaching DNA-NLs complexes are necessarily different of the traditional methods employed in cationic systems. In this case, not only the phase behavior, that is, the organization of the rods in-between bilayers, is relevant, but the main question is **how** DNA can enter in the host phase even in absence of electrostatic attraction. Roux et al. [17] have proposed a steric model in the context of a Flory-like framework. They started by addressing the coupling between the isotropic/nematic transition in solution and the incorporation of rods to the lamellar phase. The host phase was considered as a lattice of sites which could be (or not) occupied by lattice rods. Cross overs between rods and between rods and membranes were forbidden. Four types of configurations were evaluated: an isotropic and nematic phase of rods in solution, and an isotropic and a nematic phase of rods in-between lamellae. The free energies were then calculated for the different phases in competition as function of the volume fraction of rods and surfactants. Their results demonstrated that, for large amounts of rods, a 2D nematic lattice inside the aqueous layers of the lamellar stacking is more stable than the separate DNA solution. For compositions diluted in rods, however, an isotropic phase of DNA in the bulk is energetically favored in comparison to a complexed phase in-between bilayers.

They have raised, still, theoretical phase diagrams which have qualitative agreement with experimental ones.

In this thesis, we partially reproduce the experimental data of Roux et al. [17, 86] and expand their results by exploring the low hydration region of the phase diagram. We demonstrate also that the insertion of DNA enhances the smectic ordering of the lamellar phase. In addition, we evaluate the behavior of the system under different membrane compositions and different ionic strengths and conclude that fluctuations and short-range hydration forces play a fundamental role on complexation and phase behavior.

1.6 X-rays scattering by lamellar phases

Since X-rays have electromagnetic nature, their interaction with matter occurs at the level of the electron clouds surrounding the atomic nuclei. Therefore, the X-rays scattering profiles carry information on the electron density of the sample. The schematic picture of the diffraction by evenly-spaced membranes is shown in figure 1.13. Two distinct cases are represented in this figure. In 1.13(a), the situation corresponds to oriented samples where the bilayers are aligned perpendicularly to the X-ray beam. In this scenario, the diffraction pattern at the reciprocal space is composed by a set of equally separated spots along the axis z . The peak positions obey the Bragg condition: $|\vec{q}_z| = 2\pi n/d$, where $\vec{q} = \vec{k}_r - \vec{k}_i$; \vec{k}_r and \vec{k}_i , respectively, the reflected and the incident wave vectors [87].

In 1.13(b), the situation is quite different. In this case, we have a non-oriented (or powder) sample. Inside the irradiated volume, the membranes are found distributed over the three spatial directions and the resulting diffraction pattern has circular symmetry, with concentric rings. The positions of the circles also follows the above-described Bragg condition, that is, they appear to be equally-spaced. Along this work, the samples were X-rayed according to this last configuration. The reduction of the 2-D pattern, which is obtained through an azimuthal integration of the diffracted intensities, leads to scattering profiles of $I(q)$ vs. q .

1.6.1 The model of *Nallet et al.*

From the positions of the Bragg peaks, it is easy to determine the periodicity d , the main structural parameter of lyotropic lamellar phases. However, X-rays diffractograms contain much more information than simply the repetition distance. The shape of the peaks as well as the diffuse scattering, that is, the scattering out from Bragg maxima, allow to probe the scatterer structure in more detail. Several models have been proposed in order to describe the diffusion of radiation by lyotropic lamellar phases [89–91]. The aim of these models is to get information either at supramolecular level, through the extraction of parameters such as the Caillé index and the number of correlated layers, or at the fine structure of the system, by determining the electron density profile of the surfactant bilayers. Nevertheless, one of the most important results derived from

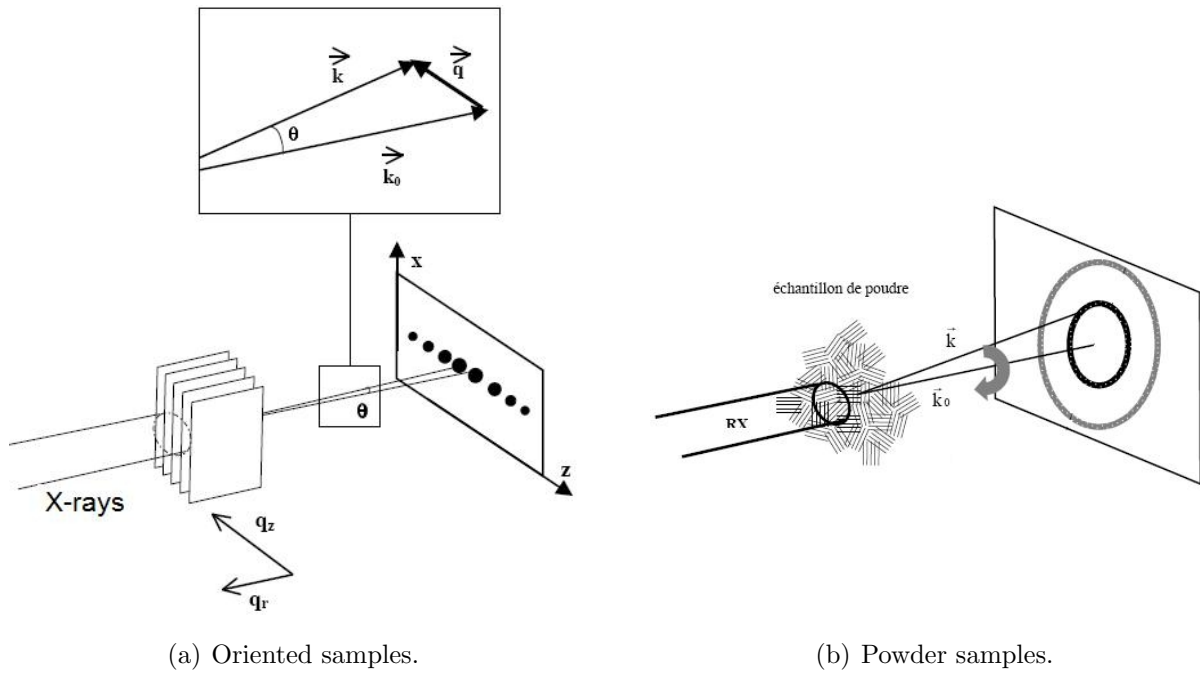


Figure 1.13: Schematic pictures of X-rays diffraction by regular stacks of bilayers. In (a), the situation corresponds to oriented samples where membranes are oriented perpendicular to the X-ray beam. The diffraction pattern is composed by a set of equally spaced spots along q_z . In (b), the situation corresponds to powder samples where several orientations are found within the irradiated volume. In this case, the diffraction pattern has circular symmetry (adapted from [88]).

these models is not directly related to structural determinations: since they are powerful methods to measure fluctuations, they are also suitable tools to extract information on thermodynamic properties of smectic phases [42, 92].

In this work, we have used a model developed by Nallet et al. This model has been chosen due to its relative simplicity and ease for computational implementation [93]. In addition, it has been successfully used by others in similar contexts [94–97]. Below, the main features of the Nallet’s approach are reproduced. The complete framework can be found in the Ref. [93].

The intensity scattered by an irradiated volume, at a wave vector \vec{q} , is given by:

$$I_{id}(\vec{q}) = \left\langle \left| \int_V \rho(\vec{x}) e^{i\vec{q}\cdot\vec{x}} d^3\vec{x} \right|^2 \right\rangle \quad (1.10)$$

where the brackets $\langle \dots \rangle$ corresponds to a thermal averaging and $\rho(\vec{x})$ to the scattering length density. The most intuitive way to describe the function $\rho(\vec{x})$ is based on purely *geometrical assumptions*. According to these assumptions a finite-size crystal of the smectic structure is seen as a regular stacking of N identical plaquettes with thickness δ_m and lateral extension L_{\perp} , **all oriented normally to z** [93]. In this case, $\rho(\vec{x})$ is defined as:

$$\rho(\vec{x}) = \sum_0^{N-1} \rho_0(z - n \cdot d), \quad |x_\perp| < L_\perp \quad (1.11a)$$

$$\rho(\vec{x}) = 0, \quad \textit{otherwise} \quad (1.11b)$$

where $\rho_0(z)$ is the scattering length density profile of one plaquette with non-zero values only when $0 \leq z \leq \delta_m$. Combining 1.10 and 1.11, one observes that the intensities of the Bragg peaks are modulated by a factor of the bilayer:

$$P(q) = \left| \int_0^{\delta_m} \rho_0(z) \exp\{iqz\} dz \right|^2 \quad (1.12)$$

It should be noted that at 1.11 the stacks were assumed to be composed by flat and rigid layers, with well defined positions along the axis z . This situation is clearly an ideal picture since, in real systems, thermal disorder and fluctuations on membrane positions must be taken into account. In order to overcome the drawbacks of this simplest approach, the Nallet's model takes advantage of some features of the Caillé's description for smectic-A phases [87]. In the context of this modified approach, the scattering length density represented in 1.11 is re-written in the form:

$$\rho(\vec{x}) = \sum_0^{N-1} \rho_0(z - nd + u_n), \quad |\vec{x}_\perp| < L_\perp \quad (1.13a)$$

$$\rho(\vec{x}) = 0, \quad \textit{otherwise} \quad (1.13b)$$

where the function u_n represents random thermal fluctuations of the n^{th} layer around an equilibrium position $n \cdot d$.

The displacements in different layers are related through the smectic correlation function [87]:

$$\langle (u_n - u_0)^2 \rangle = \frac{\eta n^2 d^2}{8}, \quad n \textit{ small} \quad (1.14a)$$

$$\langle (u_n - u_0)^2 \rangle = \frac{\eta}{2\pi^2} [\ln(\pi n) + \gamma] d^2, \quad n \gg 1 \quad (1.14b)$$

where $\gamma = 0.5772$ is the Euler's constant and η is the Caillé parameter, which is defined in terms of the elastic constants \bar{B} and K by:

$$\eta = \frac{q_0^2 k_B T}{8\pi \sqrt{K \bar{B}}} \quad (1.15)$$

In equation 1.15, the coefficient \bar{B} is the compressibility modulus *at constant chemical potential* [34]. Combining equations 1.13 and 1.10, the scattered intensity assumes the form:

$$I_{id}(\vec{q}) = N \cdot P_{\perp}(q_{\perp}) \cdot P(q_z) \cdot S(q_z) \quad (1.16)$$

where N is the number of correlated layers and P_{\perp} is the transverse form factor (in the plane xy), related to the finite lateral size of the membranes. $P(q_z)$, the form factor of the bilayers along the axis z , is given by 1.12 and S is the *structure factor* of the stacking given by:

$$S(q) = 1 + 2 \sum_{n=1}^{N-1} \left(1 - \frac{n}{N}\right) \cos(nqd) \exp \left\{ \frac{-q^2}{2} \langle (u - u_0)^2 \rangle \right\} \quad (1.17)$$

The above-derived expression 1.17 does not take into account the finite resolution of the measuring system. The *real* intensity is given by:

$$\tilde{I}(\vec{q}) = \int I_{id}(\vec{q}') R(q - q') d^3 q' \quad (1.18)$$

where the resolution function $R(\vec{q})$ is chosen as a Gaussian profile of width Δq :

$$R(\vec{q}) = (2\pi\Delta q^2)^{-3/2} \exp \left\{ \frac{-q^2}{2\Delta q^2} \right\} \quad (1.19)$$

Considering an irradiated volume large enough, so much that the lateral extension of bilayers is much larger than the instrumental resolution ($L_{\perp}\Delta q \gg 1$), the transversal form factor P_{\perp} becomes:

$$\tilde{P}_{\perp} = 2\pi \frac{L_{\perp}^2}{\Delta q^2} \exp \left\{ \frac{-q_{\perp}^2}{2\Delta q^2} \right\} \quad (1.20)$$

In the direction perpendicular to the bilayers plane, the function $P(q_z)$ has soft variations, so much that the structure factor can be convoluted alone with the resolution. This convolution process re-writes the structure factor in its resolution-limited form:

$$\begin{aligned} \tilde{S}(q_z) = & 1 + 2 \sum_1^{N-1} \left(1 - \frac{n}{N}\right) \cos \left(\frac{q_z dn}{1 + 2\Delta q^2 d^2} \alpha(n) \right) \times \\ & \times \exp \left\{ \frac{-2q_z^2 d^2 \alpha(n) + \Delta q^2 d^2 n^2}{2(1 + 2\Delta q^2 d^2 \alpha(n))} \right\} \times \\ & \times \frac{1}{\sqrt{1 + 2\Delta q^2 d^2 \alpha(n)}} \end{aligned} \quad (1.21)$$

where $\alpha(n)$ is the correlation function $\langle (u_n - u_0)^2 \rangle / 2d^2$.

The above-derived form and structure factors are obtained assuming that the bilayers are oriented. In order to contemplate randomly-oriented domains, one needs to powder-average 1.18. For large scattering wave vectors, $q \gg \Delta q$, the final form for the scattered intensity is:

$$I(q) = \frac{2V\pi P(q)\tilde{S}(q)}{dq^2} \quad (1.22)$$

In order to compare the prediction stated in 1.22 with real X-rays data, one needs still to define the form factor of bilayers, $P(q)$. The model of Nallet et al. proposes a two-square profile for the electron density, which is exhibited in the figure 1.14.

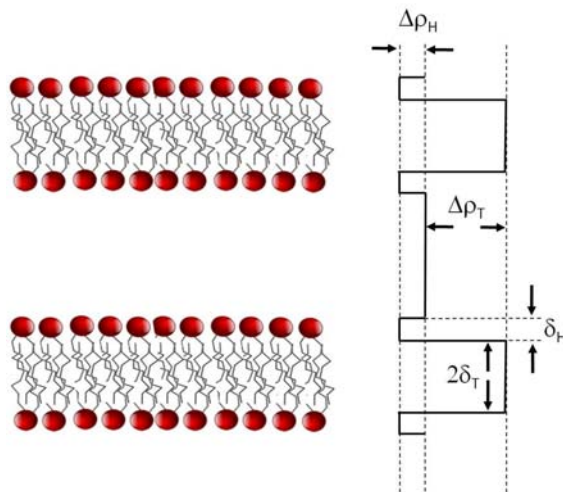


Figure 1.14: Schematic electron density profile ρ_0 for lipid bilayers according to the model of Nallet et al.

According to this proposition, $\rho_0(z) = \Delta\rho_H$ for $0 \leq z \leq \delta_H$ or $(\delta_H + 2\delta_T) \leq z \leq 2(\delta_H + \delta_T)$ and $\rho_0(z) = \Delta\rho_T$ for $\delta_H \leq z \leq (\delta_H + 2\delta_T)$. The thickness of bilayers is $2(\delta_H + \delta_T)$. This form leads to:

$$P(q) = \frac{4\Delta\rho_H^2}{q^2} \left\{ \sin(q(\delta_H + \delta_T)) - \sin(q\delta_T) + \frac{\Delta\rho_T}{\Delta\rho_H} \sin(q\delta_T) \right\}^2 \quad (1.23)$$

1.6.2 Effects of disorder on $\tilde{S}(q)$

Part of the analyses which will be presented in chapter 3 concerns the smectic ordering of lyotropic lamellar phases. In the model presented in the previous section, the information on this ordering is contained on $\tilde{S}(q)$. Therefore, now we focus our interest in a more detailed evaluation of the behavior of the structure factor as a function of the parameters N and η . It should be noted that these two variables are closely related to the ordering of the stacking since they are associated, respectively, to the *number of correlated layers* and to *membrane fluctuations* [90, 98].

The structure factor from an infinite and periodic stack of membranes, where the distance between bilayers is always the same and there is no fluctuations on the system, is composed by a set of Bragg peaks of equal intensity, independent on the diffraction order. These peaks are well represented by delta functions and their width is only limited by the instrumental resolution. Solid crystals have a behavior near to this ideal picture. In smectic phases, however, disorder effects have major importance. The appearance of disorder has two direct consequences on the structure factor: the parameter of Caillé increases and the number of correlated layers decreases.

In figure 1.15, it is shown the behavior of $\tilde{S}(q)$ for three distinct values of η . The number of correlated layers was chosen to be large ($N = 10000$), the periodicity was $d = 62.8 \text{ \AA}$ and the instrumental resolution was fixed at $\Delta q = 0.006 \text{ \AA}^{-1}$. We observe that, for $\eta = 0$, the structure factor is identical to that one expected for unperturbed solid crystals. As the value of η is increased, however, the intensity of the peaks decreases dramatically. Moreover, the width of the peaks broaden slightly.

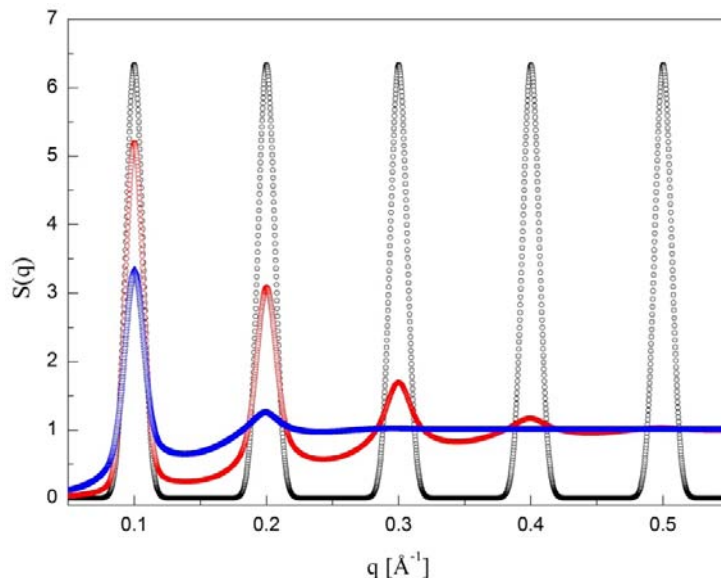


Figure 1.15: Simulated structure factors for three different values of Caillé number: $\eta = 0$ (black), $\eta = 0.1$ (red) and $\eta = 0.35$ (blue). The other parameters were fixed at $d = 62.8 \text{ \AA}$, $\Delta q = 0.006 \text{ \AA}^{-1}$ and $N = 10000$ (adapted from [93]).

In figure 1.16, the behavior of $\tilde{S}(q)$ is evaluated as a function of the number of correlated layers. The other parameters were fixed at $d = 62.8 \text{ \AA}$, $\eta = 0.1$ and $\Delta q = 0.006 \text{ \AA}^{-1}$. Here again, we observe changes on the intensities of the Bragg reflections. The lower the value of N , the lower the peak intensities. In comparison to the effect introduced by non-zero values of η , we note that decreasing the number of correlated layers does not destroy the higher orders. Instead, the peaks become rounded and lose the delta-like behavior. On the other hand, the broadening phenomenon is more noticeable and, for very low values of N (blue curve, $N = 3$), oscillations due to beating effects appear convoluted on the structure factor.

The more important consequence of these disorder effects on the structure factor is that, for large wave vectors, it tends asymptotically to unity:

$$\lim_{q \rightarrow \infty} \tilde{S}(q) = 1 \quad (1.24)$$

This finding is a very important result because it means that, for large values of q in diffractograms from lyotropic lamellar phases, the intensity profiles will be dominated by the form factor $P(q)$.

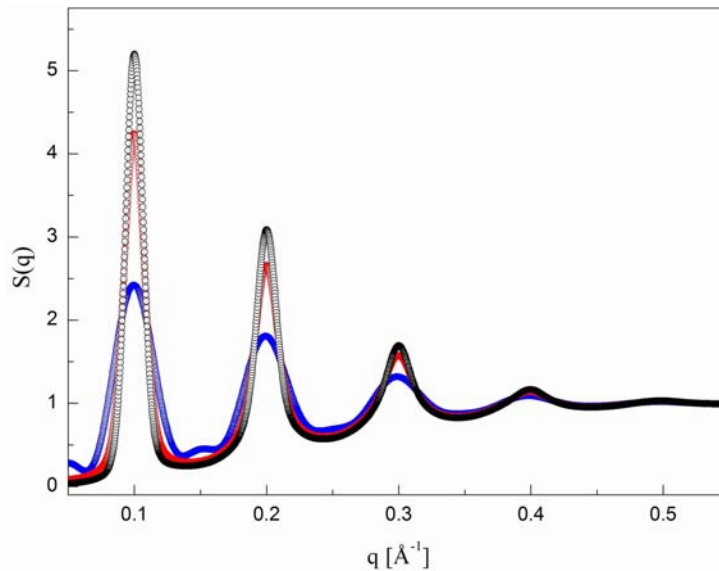


Figure 1.16: Simulated structure factors for three different numbers of correlated layers: $N = 10000$ (black), $N = 10$ (red) and $N = 3$ (blue). The others parameters were fixed at $d = 62.8 \text{ \AA}$, $\eta = 0.1$ and $\Delta q = 0.006 \text{ \AA}^{-1}$.

1.7 DNA dynamics in lamellar phases

The knowledge about the dynamical properties of DNA fragments within lipid phases is an important matter for two main reasons: first, considering the potential of these systems in gene therapy, the controlled release of nucleotides inside the nucleus requires the precise determination of the time scale in which they are expelled from the complex. Secondly, the motion of anisotropic macromolecules in confined geometries is found in a variety of fundamental biological phenomena such as transport of proteins across membranes and DNA replication, among others [99–102].

In addition, there is a very close relationship between the structure of the aggregates and the way how their particles diffuse. Therefore, in the context of this thesis, dynamical studies also complement the structural analyses carried out by X-rays diffraction and microscopy. By “dynamical properties”, we mean the **diffusion** of nucleotides in the water channels of a lamellar phase. As discussed in previous sections, DNA self-organizes into ordered phases. It should be noted that, for sandwich-like complexes, the rods are constrained by lipid walls restraining their motion to the plane of the bilayers. This structural characteristic gives anisotropic properties to the mobility of the particles inside the stacking. Special attention must be paid to the size scales involved in the processes analyzed here. The cylinders and the intermembrane spacing wherein diffusion occurs have only few nanometers. These dimensions do not allow to track the displacement of individual particles nor to visualize their motion inside an unique aqueous layer. In this situation, the analysis is made by following the average diffusion of a large population of molecules across thousands of layers.

1.7.1 Anisotropic Brownian diffusion

The displacement of cylindrical particles in solution is conveniently described in terms of two independent translational friction coefficients (see figure 1.17(a)), for motions parallel and perpendicular to the cylinder long axis, respectively [103,104]. Experimentally, two regimes of Brownian motion have been observed in isotropic suspensions of rod-like particles. The first regime, corresponding to low volume fractions, is characterized by a diffusion coefficient independent of concentration that is also well described by properly averaging the two basic friction coefficients [105–107]. For rods with aspect ratio ≈ 25 , such as the DNA fragments used in this work, this diffusion coefficient has been determined in the order of $D \approx 30\mu\text{m}^2/s$ when the particles are dispersed in aqueous solutions [32,106,108–110]. In the second, more concentrated regime when the particles start to interact, the diffusion coefficient D becomes dependent on the particle volume fraction [105,108,111], and various theoretical models or numerical simulations [32] relevant in this regime have been proposed. At still higher concentrations, the cylinders become orientationally correlated as the nematic phase is reached (figure 1.17(b)). The long-time mean square displacement of a single particle is anisotropic [111] which explicitly reflects the broken symmetry of the nematic phase.

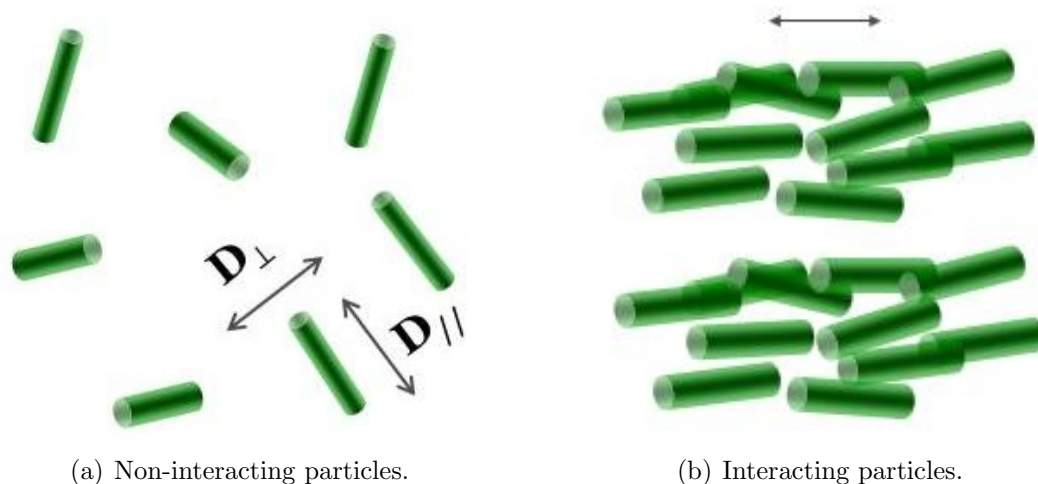


Figure 1.17: Schematic drawing of aqueous DNA dispersions: (a) Non-interacting particles: the displacement of rods is characterized in terms of two independent friction coefficients, parallel and perpendicular to the long axis. Diffusion is isotropic, with total D given by the proper average of D_{\perp} and D_{\parallel} [103]. (b) Interacting particles: the rods have local nematic order and diffusion is anisotropic, reflecting the broken symmetry.

The anisotropic diffusion of DNA rods, moving within a given slice at height z , is properly described by the second Fick’s law in the form:

$$\partial_t C = D_{\parallel} \partial_x^2 C + D_{\perp} \partial_y^2 C \quad (1.25)$$

There exist a large number of solutions for 1.25 depending on the initial boundary conditions [112]. In the context of this work, the relevant initial condition is given by a

Dirac delta function. This assumption leads to the bidimensional Gaussian solution given by:

$$C(x, y, z, t) = \frac{C_0(z)}{4\pi t \sqrt{D_{\parallel} D_{\perp}}} \exp \left\{ - \left(\frac{x^2}{4D_{\parallel} t} + \frac{y^2}{4D_{\perp} t} \right) \right\} \quad (1.26)$$

where C_0 is the initial concentration. D_{\parallel} and D_{\perp} are the respective diffusion coefficients along the axis parallel and perpendicular to the long axis of the rods.

1.7.2 Spatially-resolved FRAP

A standard technique for evaluation of dynamics at molecular level is the *fluorescence recovery after photo bleaching* (FRAP). The operation principle of FRAP is to label, with a fluorescent dye, a small quantity of the particles whose diffusion we desire to study. An intense and focused light beam, in the excitation wavelength of the dye, is irradiated over a small region of the sample, causing the irreversible loss of the local fluorescence. In following, the illumination beam is strongly attenuated and the sample is observed in the emission spectrum. The lateral migration of unbleached molecules from surrounding regions causes the recovery of the fluorescence into the bleached area (see fig. 1.18). The time behavior of this process depends on the mobility rate of particles, from whose analysis diffusion coefficients are obtained [110, 111, 113–115].

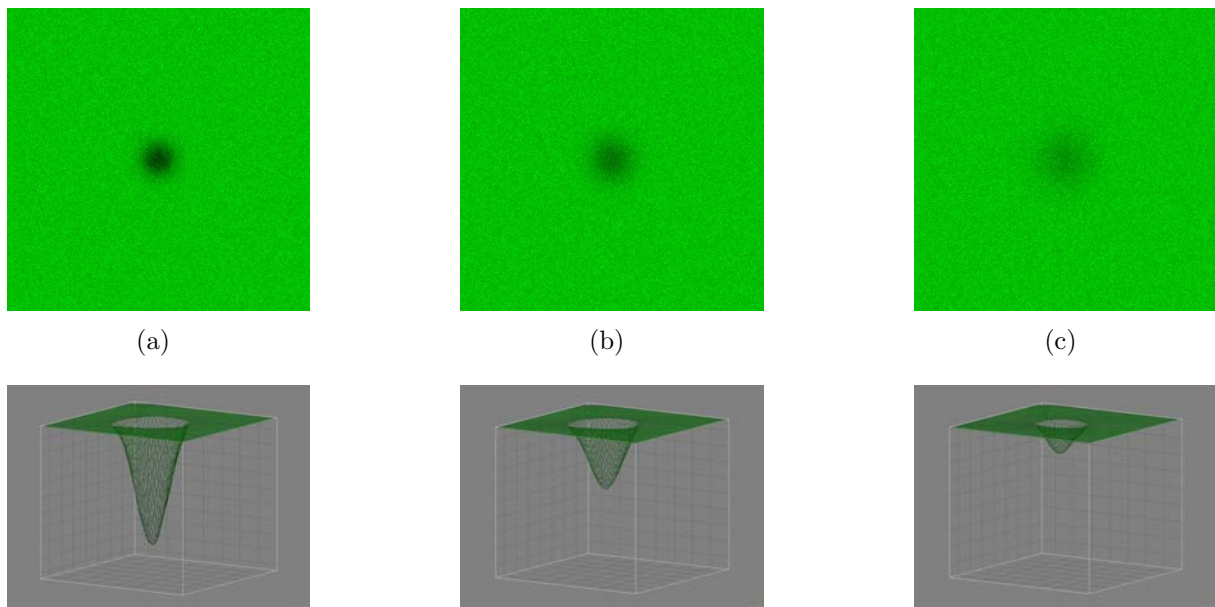


Figure 1.18: Typical FRAP images with their respective 3D profiles. (a) Soon afterwards the bleach, the fluorescence inside the bleached spot is virtually extinct. In time, the width of the bleached zone increases and the migration of fluorophores from surrounds gives raise to the recovery of brightness (b and c).

In a FRAP experiment, the intensity of fluorescence is assumed to be proportional to the concentration of fluorophores. Assuming two dimensional diffusion, one has $f_0 \propto$

$C(x, y, t)$. Using polar coordinates, the fluorescence profile at a given time t is described by:

$$f_0(r, \theta, t) = I_0 + f_0(t) \exp \left[-\frac{r^2}{2} \left(\frac{\cos^2 \theta}{w_{\parallel}^2} + \frac{\sin^2 \theta}{w_{\perp}^2} \right) \right] \quad (1.27)$$

In 1.27, w_{\parallel}^2 and w_{\perp}^2 correspond to the components of variance at time t . Comparing 1.27 and 1.26, it is easy to determine the relationships:

$$w_{\parallel}^2 = 2D_{\parallel}t \quad (1.28a)$$

$$w_{\perp}^2 = 2D_{\perp}t \quad (1.28b)$$

Equations 1.28 were obtained by assuming a sharp delta function as the initial condition. In practice, however, such situation is not reached. Due to the finite width of the laser beam and a certain time duration of the bleaching pulse, the real case is different of the ideal condition.

Nevertheless, since the beam has Gaussian profile, we can interpret the first image as a shift in the experimental time scale. In other words, this first record is assumed to be the state of a point-like spot, after a time t_0 . Thus, equations 1.28 can be corrected [113]:

$$w_{\parallel}^2 = 2D_{\parallel}t + w_0^2 = 2D_{\parallel}(t + t_0) \quad (1.29a)$$

$$w_{\perp}^2 = 2D_{\perp}t + w_0^2 = 2D_{\perp}(t + t_0) \quad (1.29b)$$

In 1.29, w_0^2 corresponds to the size of the bleaching beam. It is not difficult to connect the temporal behavior of the spatial profile, the variances w_{\parallel}^2 and w_{\perp}^2 , to the respective diffusion coefficients.

1.8 Dobrindt's model

The analysis of isotropic diffusion is largely referred to in the literature [111, 113, 114]. On the other hand, the extraction of information when diffusion occurs in anisotropic media requires specific approaches according to the kind of symmetry. In the case of the system evaluated here, two difficulties must be overcome: the anisotropy imposed by the lamellar phase and the anisotropy related to the self-assembly of DNA molecules in-between bilayers. Recently, a theoretical model dealing with the specific characteristics of our systems was developed by Jens Dobrindt at CRPP [23]. Below, we present a brief description of this model and, in chapter 4, few experimental evidences for its validation are given. A more accurate discussion is found in Ref. [24], where the treatment is extended to the motion of rods in cholesteric phases.

1.8.1 Difficulties on analyzing diffusion within lamellar phases

First, let us start with few considerations about diffusion inside ONE aqueous layer of a lamellar phase. If the concentration of particles is low, so much that interactions are not strong enough to form ordered phases, the rods are found to be isotropically distributed in the plane. As mentioned above, in this case, diffusion is characterized by only one properly averaged coefficient, D . From equation 1.27, it is easy to conclude that, for a delta initial condition, the time evolution of a FRAP spot follows a circular geometry. Moreover, still according to 1.27, the spatial profile across a longitudinal section is Gaussian.

On the other hand, if the concentration of particles is sufficiently high to give rise to a 2D nematic phase, diffusion is characterized by two mobility coefficients: a fast one, D_{\parallel} , and a slow one, D_{\perp} . In this case, since the speeds are different along the axis parallel and perpendicular to the director vector, the bleach spot evolves according to an elliptic geometry. Along the two main axis, the spatial profile is also Gaussian, characterized by the variances w_{\parallel}^2 and w_{\perp}^2 .

Now, consider a set of **homeotropically oriented** bilayers, with DNA fragments inserted in the intermembrane aqueous layers. For convenience, the polar coordinate system (r, θ) is chosen with the origin of the azimuthal angles taken along the local nematic director. In addition, we assume **the director vectors of the nematic phases in different layers are independent and uniformly sample the interval $[0, \pi]$** . In other words, there is no correlation between particles across membranes. In a FRAP experiment, the observations are made along the optical axis of the microscope, the same direction of the homeotropic orientation. Therefore, the registered frame carries information about a large number of layers along the optical axis².

The superposition of several layers leads to different spatial profiles for the observed bleached spot, depending on the symmetry of diffusion inside the individual slices. In the case of isotropic diffusion, the final image correspond to the convolution of several circular spots with Gaussian spatial profiles (see figure 1.19(a)). The result is a circular spot whose profile is also Gaussian and is well described by 1.27.

For anisotropic diffusion, however, the case is quite different. Since the nematic directors are randomly distributed, the superposition of many elliptic spots leads to a resulting spot with circular geometry (see figure 1.19(b)). In contrast to the spatial profile observed in the case of isotropic diffusion, here, the shape is not Gaussian. This means that equation 1.27 is not appropriate to deal with the spatial distribution of fluorescence for anisotropic diffusion and a new model is required.

2. In this work, a confocal microscope was used. However, the pinhole was kept entirely open, so much that it worked such as a wide-field conventional microscope (see the chapter Materials and Methods for further details).

1.8.2 Modified form of the spatial bleaching profile

In order to describe the spatial profile of the bleached spot resulting from anisotropic diffusion within the intermembrane spacing, figure 1.19(b), we need to modify the equation 1.27 to take into account the azimuthal averaging of the several convoluted ellipses. Since the orientations at different heights are uniformly distributed in the interval $[0, \pi]$, a first step in order to obtain the appropriate formula is to perform the average of 1.27 in the angular interval [23]:

$$\begin{aligned} F_0(r, t) &= \frac{1}{\pi} \int_0^\pi f_0(r, \theta) d\theta \\ &= y_0 + A(t) \exp \left[\frac{-r^2}{4} \left(\frac{1}{w_{\parallel}^2} + \frac{1}{w_{\perp}^2} \right) \right] \mathbf{I}_0 \left[\frac{r^2}{4} \left(\frac{1}{w_{\parallel}^2} - \frac{1}{w_{\perp}^2} \right) \right] \end{aligned} \quad (1.30)$$

where the term \mathbf{I}_0 is a **modified Bessel-function of first kind and order 0**. Equation 1.30 corresponds to an idealized situation, which does not account for deviations introduced by the experimental conditions.

In a more realistic description, the width of the beam is not constant along the optical axis. Indeed, if the objective has low numerical aperture, as typically used in spatially-resolved FRAP experiments [107, 115], the paraxial approximation is appropriate to describe the Gaussian light intensity profile. The beam in-plane half-width at e^{-2} becomes then:

$$w(z) = w_0 \sqrt{1 + \left(\frac{z}{z_R} \right)^2} \quad (1.31)$$

where z_R is related to the beam waist w_0 and to the wavelength of the light by $z_R = \pi w_0^2 / \lambda$. The beam axial intensity is given by:

$$I(z) = I_0 \left[\frac{w_0}{w(z)} \right]^2 \quad (1.32)$$

Assuming the integration range Z along the optical axis small enough in comparison with Rayleigh range z_R (as usual in standard experiments), the final formula to the depletion in fluorescence is given by [24]:

$$F_0(r, t) = F_0'(t) \exp \left[\frac{-r^2}{4} \left(\frac{1}{w_{\parallel}^2} + \frac{1}{w_{\perp}^2} \right) \right] \times I_0 \left[\frac{r^2}{4} \left(\frac{1}{w_{\parallel}^2} - \frac{1}{w_{\perp}^2} \right) \right] \quad (1.33)$$

The variances w_{\parallel}^2 and w_{\perp}^2 are now related to the mobility coefficients through the relationships:

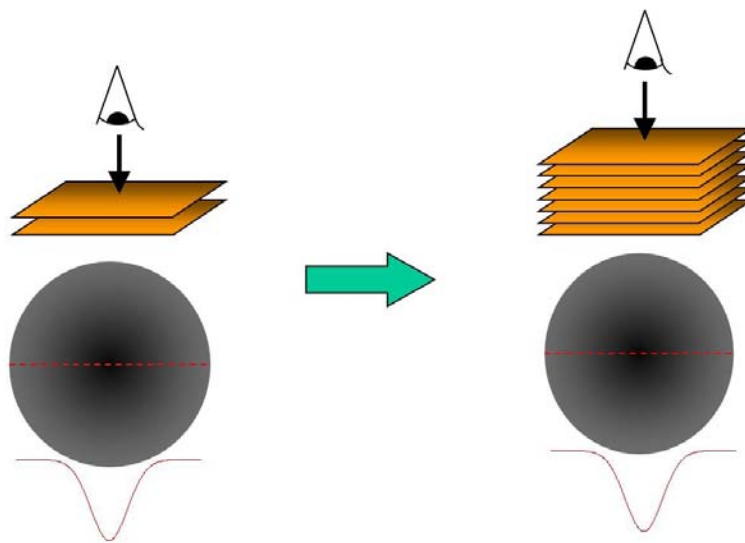
$$w_{\parallel}^2 = w_0^2 + 8D_{\parallel}t \quad (1.34a)$$

$$w_{\perp}^2 = w_0^2 + 8D_{\perp}t \quad (1.34b)$$

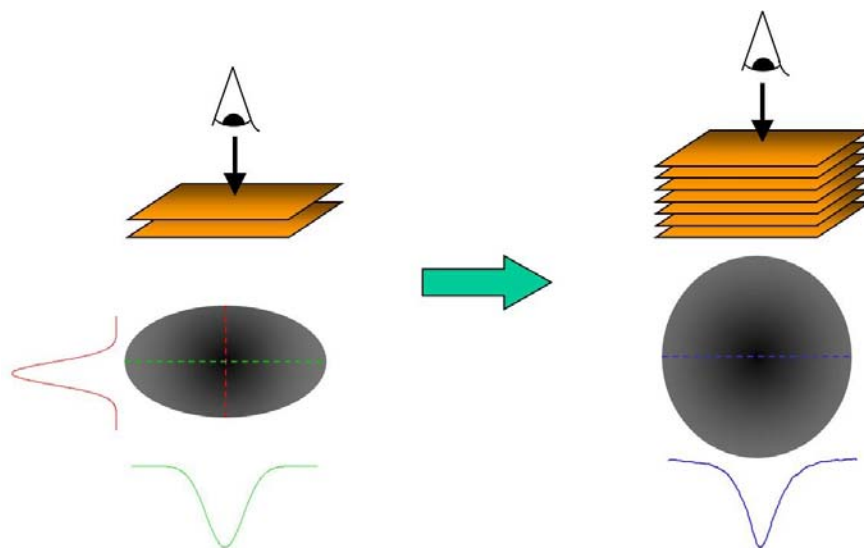
The normalizing factor $F'_0(t)$ appearing in 1.33 is given by:

$$F'_0(t) = \frac{2ZC_0}{\pi\sqrt{(w_0^2 + 8D_{\parallel}t)(w_0^2 + 8D_{\perp}t)}} \quad (1.35)$$

For long-time scales, the diffusion length, *i. e.* the smaller of $D_{\parallel}t$ and $D_{\perp}t$, is much larger than the Gaussian beam intrinsic scales (w_0 , λ and z_R). In this case, the form described in 1.30 is *asymptotically* recovered. For extraction of anisotropic diffusion coefficients in this work, the form described in 1.33 has been used. It should be noted, however, that this form is possibly non rigorous at short times due to approximations used in account the experimental conditions. The observable *non* Gaussian shape of the profile at (and close to) $t = 0$ is then attributed to imperfections of the model [24].



(a) Isotropic diffusion within aqueous layers.



(b) Anisotropic diffusion within aqueous layers.

Figure 1.19: Schematic picture of the diffusion process in two situations: (a) when the concentration of nucleotides is low and diffusion between bilayers is isotropic, the convolution of several circular spots results in a circular spot whose spatial shape is also Gaussian. (b) When diffusion within individual layers is anisotropic, the superposition of several uncorrelated elliptic spots results in a circular spot whose spatial profile is not described by a simply Gaussian function. (Adapted from [116]).

CHAPTER 2

MATERIALS AND METHODS

2.1 Constituents of the system

2.1.1 DNA fragments

Calf thymus DNA was purchased from Sigma-Aldrich and undergone desalinization with buffer solution (sodium acetate 0.3 M, *pH* adjusted to 7) and pure ethanol¹. After freezing overnight, at -80°C , the mixture was centrifuged several times and the supernatant was removed. The precipitate was then subjected to lyophilization providing salt-free nucleotides to be sonicated.

The ultrasound treatment lead to pieces with ≈ 150 bp and contour length of ≈ 50 nm. Temperature control was reached by introducing a mixture of water and ice into the ultrasound reservoir. The dimensions of the fragments were systematically inspected by electrophoresis techniques. The sizes roughly corresponded to the persistence length of the biopolymer and, without taking into account hydration shells, allowed to describe the particles as rigid rods with $500 \text{ \AA} \times 20 \text{ \AA}$ in size.

In order to make possible further observations in fluorescence microscopy, and in view of FRAP experiments, the fragments were marked with a fluorescent dye. The chosen fluorophore was YOYO, purchased from Molecular Probes. The labeling ratio was 1 molecule per 5000 base pairs. In aqueous solution, the dye is virtually not fluorescent, however, when bound to nucleotides, its fluorescence intensity increases by a factor 3500. The excitation spectrum has peak at $\lambda_{exc} = 491$ nm, whereas the maximum emission wavelength is at $\lambda_{em} = 508$ nm. The molecule has planar geometry and binds the end of the fragments, assuming an orientation parallel to the long axis of the base-pair pocket [117]. This conformation makes an angle of almost 90 degrees between the excitation dipole of YOYO and the DNA axis. For that reason a light beam polarized parallel to DNA

1. All pretreatment stages on DNA and lipids were carried out by Annie Février, lab technician, at the Centre de Recherche Paul Pascal, Bordeaux, France.

axis will not excite YOYO and hence fluorescence intensity carries information about the orientation of the rods [118]. The cycle of preparation of DNA is outlined in figure 2.1. Further details on the protocols used in the treatment of the particles can be found in the Appendix A.

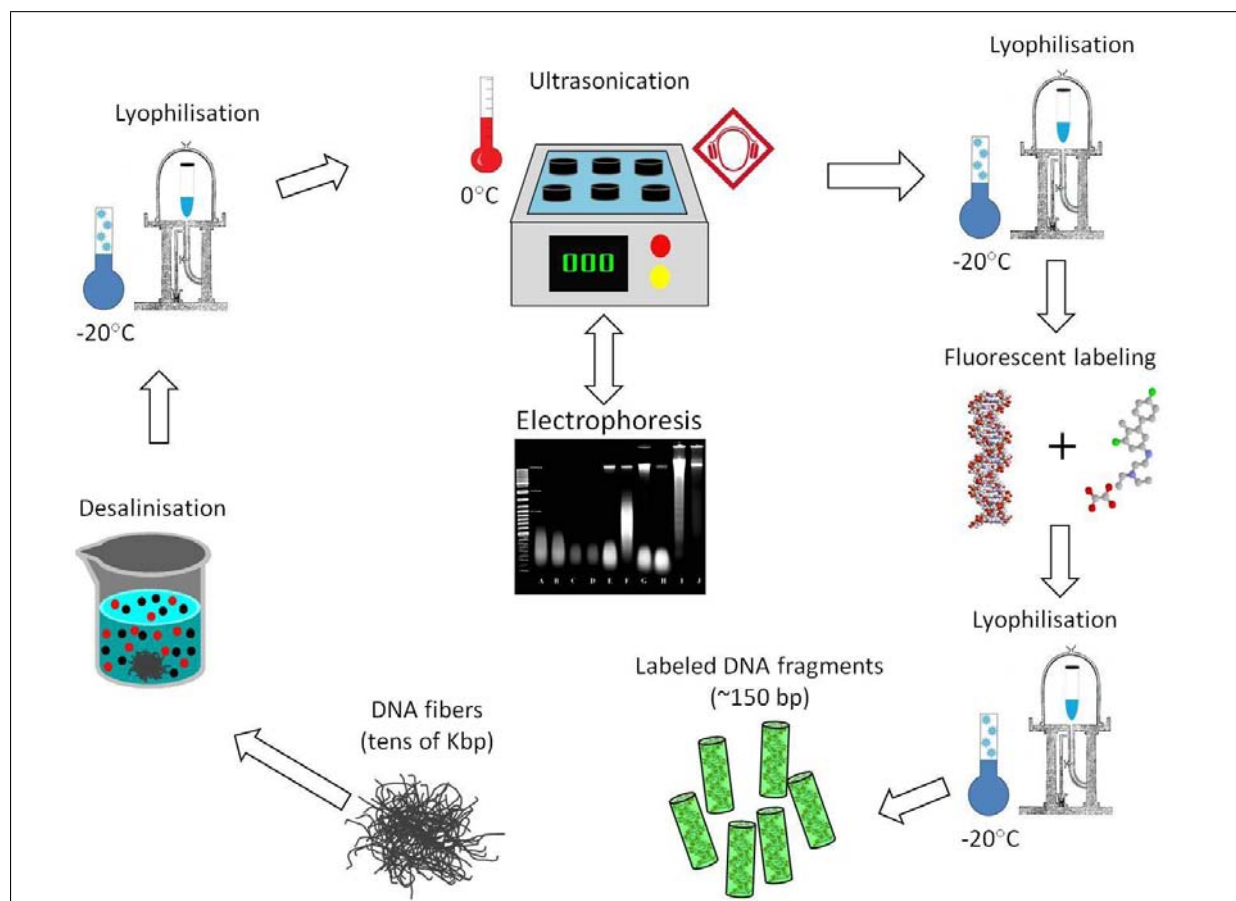


Figure 2.1: Summary of DNA treatment: the cycle starts with size-polydispersed fibers. In following, they are submitted to desalination process, releasing cations and anions to solution. In the next step, the precipitate is ultrasonicated leading to rod-like fragments with 150 bp. During sonication, the size of the particles is systematically inspected by electrophoresis. The last stage is the labeling with YOYO-fluorophores. Between different steps, solutions are submitted to freeze-drying. At the end of a cycle, one has lyophilized fluorescent fragments with a size corresponding to the DNA persistence length.

2.1.2 Lipid part

The lipid part was obtained by mixing soy lecithin-phosphatidylcholine (PC) and Simulsol 2599 PHA, a non-ionic co-surfactant. These products were purchased from Sigma-Aldrich and Seppic, respectively, and used without further purification.

The major constituents of soybean lecithin are double-chained phosphatidylcholines whose chains are composed by C18:2 linoleic acid (64%)². C16:0 palmitic acid (13%),

2. Lipids are often referred to in terms of the number of carbons and unsaturations in their chains. In this notation, with general form $CN_1 : N_2$, N_1 represents the number of carbons and N_2 , the number of

C18:1 oleic acid (10%), C18:3 linoleic acid (6%) and C18:0 stearic acid (4%) also appear in important amounts in lecithin. The average molar mass is ≈ 776 g/mol and specific mass is around 1.02 g/cm³ [119]. The predominance of unsaturated lipids gives to lecithins a low melting point in such a way that, at room temperature, their chains are found in the fluid state (L_α) [120].

Simulsol 2599 PHA is the trade name for a blend of ethoxylated fatty acids. Sometimes, this product is also referred to by its chemical name *macrogol oleate*. The major constituent is oleic acid (around 72%). Palmitic and stearic acids also appear in important quantities (11% and 3%, respectively). Among the minors compounds we find palmitoleic, linoleic and myristic acids. A little percentage of $C > 18$ fatty acids, which does not exceed 2.5 %, is also found. The resulting calculated molar mass is ≈ 278 g.mol⁻¹ and the specific mass is 1.02 g/cm³, according to Seppic products catalog [121].

A “premix” of these two groups of lipids was prepared. They were cosolubilized in cyclohexane and desiccated under lyophilization overnight in order to evaporate the solvent. The role of co-surfactant is to increase the flexibility of the lipid layers, enlarging the dilution domain of the host phase. The results presented in the next chapter were obtained from two distinct types of membranes prepared at PC-to-Simulsol mass ratios of 7:3 and 1:1. Due to the zwitterionic character of lecithin head groups, and non-ionic character of Simulsol, the overall charge of the resulting membrane was neutral. Henceforth, the preparation PC+Simulsol will be referred just as *lipids*.

2.1.3 Solvent

For most of samples, the used solvent was ultra pure water obtained from a *Millipore* system. In order to evaluate the role of ionic strength, several formulations were also prepared using a solution of *ammonium acetate*, at concentration of 0.25M. This salt solution was obtained from dissolution of dry CH_3COONH_4 powder in pure water.

Ammonium acetate is a monovalent salt formed from a weak acid, the acetic acid CH_3COO^- , and a weak base, the ammonia NH_4^+ . The respective dissociation constants are $pK_a = 4.75$ and $pK_b = 9.25$. Because of this, it can be used as buffer solution, providing a medium with $pH = 7.0$.

2.2 Samples preparation

Samples were prepared by mixing the above described constituents into clean Eppendorf tubes. The mass of each compound was chosen according to the desired volume fraction, which was calculated through the relation:

$$\phi_i = \frac{m_i}{P_i V_T} \quad (2.1)$$

unsaturations.

where ϕ_i is the volume fraction of the constituent (ϕ_{DNA} , ϕ_{lip} or ϕ_{wt}), P_i is its specific mass and V_T is the total volume of the sample. In a general way, V_T was chosen to be $100 \mu L$, performing a good compromise between material availability and accuracy on weighting ($\pm 0.1 mg$).

Two types of samples were studied: the first group was prepared from (pseudo) binary mixtures of lipids and solvent. The purpose of these series was to evaluate the behavior of the host lipid phase and to determine the dilution domain, the thickness of formed membranes and the hydration limit. The second group of formulations was obtained from DNA-lipids-solvent mixtures. In both cases, studies involving changes in the ionic conditions were carried out by using solutions of ammonium acetate.

Formulations can be graphically represented in a ternary diagram as that one exhibited in Fig. 2.2. The sides of the triangle correspond to the axis of the graph where the volume fractions are represented for each component. These fractions can be varied between 0 and 1. Binary mixtures are represented on the axis whereas ternary formulations are indicated by points inside the triangle.

For ternary systems, it is convenient to define the parameter ρ corresponding to lipid-to-DNA volume ratio:

$$\rho = \frac{\phi_{lip}}{\phi_{DNA}} \quad (2.2)$$

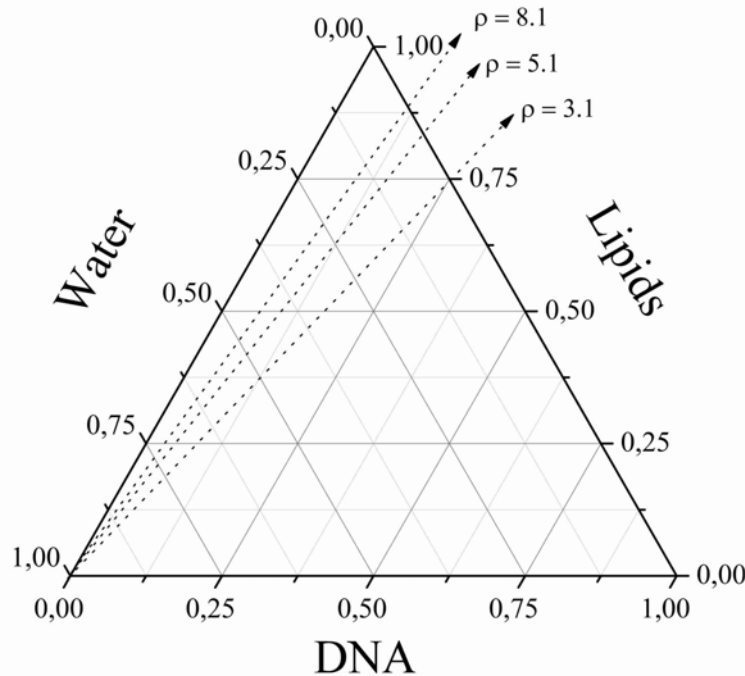


Figure 2.2: Ternary diagram for graphical representation of formulations. By keeping ρ constant, dilution lines are established on the diagram. Dotted lines indicate the main dilution lines followed in this work.

Small values of ρ mean DNA-richer complexes. Conversely, larger values of ρ imply lipid-richer formulations. Keeping ρ constant, and varying the water amount ϕ_w , dilution lines are established on the diagram. Most of the samples studied in this thesis were

prepared along three dilution lines: $\rho = 3.1$, $\rho = 5.1$ and $\rho = 8.1$ (represented by dashed lines in Fig. 2.2). Moreover, for a few samples, the hydration degree was fixed and ρ was varied.

After the preparation of the tubes, they were centrifugated and stored under refrigeration at 4 °C for 24 hours before starting the equilibration procedure.

2.2.1 Equilibration procedure

Since the system is entirely based on neutral lipids, it cannot rely on the help of electrostatic interactions to drive the complexation. So, in this case, adhesion of DNA to the lipid part occurs in time scales significantly larger than those observed for DNA-CLs complexes [86]. In order to boost this process and promote homogenization, the samples were submitted to mechanical agitation. Shortly after being removed from refrigerator, the tubes were incubated for about half an hour at temperature of 30 °C. In following, they were regularly subjected to alternate cycles of head up / upside down centrifugation. The speed of rotation was carefully chosen depending on the viscosity of the samples. For hydrated formulations, which were typically fluid, the cycles were performed using 1000-2500 revolutions per minute (rpm). On the other hand, for samples with high viscosity, the rotational velocity reached values around 12000 rpm. The rule of thumb was to chose the minimum speed enough to displace the sample inside the tube. This care on the choice of velocity is an important issue because, when the rotation is excessive, a separation of phases can occur. The time of centrifugation was a few minutes. In general, times around 3 minutes were enough to promote the complete displacement of the mixtures inside the tubes. This treatment was daily carried out, for at least 4 weeks, before any further analysis.

2.3 X-rays experiments

Once having reached equilibrium, samples were carefully placed into flame sealed glass capillaries, which yielded randomly oriented domains. The procedure to achieve this also depended on the viscosity of the formulations. Lipid/water mixtures, for instance, generally were very fluid and could be easily accommodated by simple centrifugation inside glass tubes with diameter of 1 mm. For ternary diluted preparations, *e.g.* $\phi_w > 0.35$, this also could be done. Metallic frames were used to put concentrated samples inside capillaries with diameter of 2 or 3 mm.

The total number of formulations analyzed in this work was somewhat around 250. One-third of them was evaluated by using synchrotron radiation (SR) and the remainder ones were analyzed with conventional sources at the Centre de Recherche Paul Pascal (Bordeaux, France). Experiments consisted in recording the scattered intensities in function of the wave vector $q = \frac{4\pi}{\lambda} \sin \theta$, where θ is the angle between the scattering vector and the direct beam.

Synchrotron studies were carried out at SWING station at SOLEIL, near Paris, France. We made two SOLEIL trips (project numbers: 20080568 and 20100052), performing ≈ 48 hours of beam time. The classical sources were a Bruker Nanostar machine and a homemade set-up based on a rotating anode and a MAR1200 detector. Below, the main features of these devices are detailed.

2.3.1 SWING-SOLEIL synchrotron line

Synchrotron radiation (SR) has several advantages over classical sources. Among these conveniences, we can point out high resolution, high flux of photons, wavelength tunability, polarization and coherence. From the point of view of this work, the most important of the above-mentioned characteristics are high brilliance and high resolution. Elevated flux allows to bring out weak reflections which can be crucial to discriminate between different structures. In addition, the time scale of experiments can be greatly reduced, making possible to run a large number of samples in a few hours. In turn, high resolution allows to observe and resolve certain reflections which would be not distinguishable with conventional devices.

The SWING station is an “easy-to-use” beam line at SOLEIL, specially designed for experiments involving either *small- or wide- angle X-rays scattering (SAXS and WAXS)*. *Grazing incidence- SAXS*, or *GISAXS*, is another technique also feasible in this facility. These capabilities open an experimental window for studies covering scales from tens of \AA to few $\mu\text{ m}$. In Fig. 2.3, it is shown a schematic representation of the beamline.

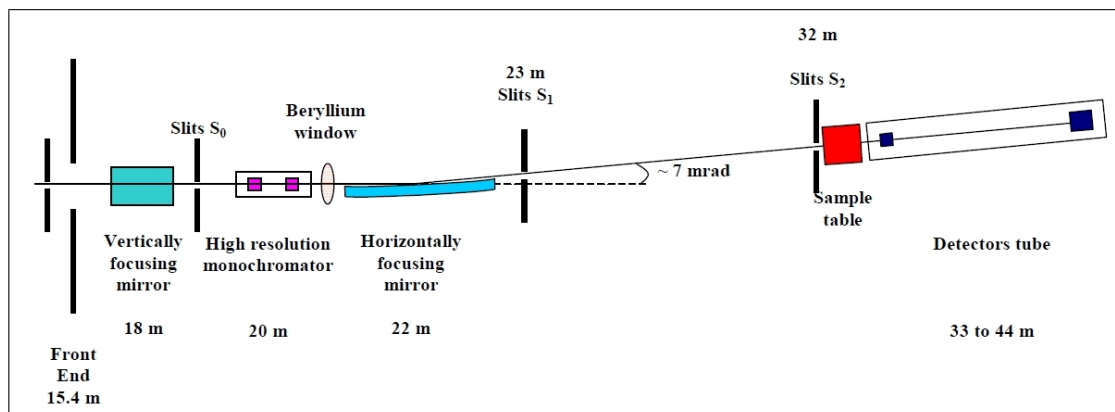


Figure 2.3: General scheme of SWING-SOLEIL beam line drafting the main components and devices. (Extracted from ref. [122]).

The available energies are situated in the interval 5–17 keV, covering from soft to hard X-rays domains. Equivalently, the corresponding wavelengths range from $\lambda_{min} = 0.729 \text{ \AA}$ to $\lambda_{max} = 2.48 \text{ \AA}$. The flux of photons is expected to be of the order of 10^{13} ph/s, when the current in the storage ring is 500 mA. The beam is provided by an U20 in-vacuum undulator and a Si_{111} double-crystal mirror is the optical component responsible by the selection of wavelengths. Sample-to-detector distance ranges from 0.6 m to 8 m. The

beam has a rectangular geometry, with dimensions of $400 \mu\text{m}$ (H) \times $100 \mu\text{m}$ (V). The maximum divergences are $14.5 \mu\text{rad}$ (H) \times $4.6 \mu\text{rad}$ (V) [122].

One strong point of the station is its detection system: a $170 \times 170 \text{ mm}^2$ CCD detector (PCCD170170, from Avix) is positioned inside a cylindrical chamber with 7 m for length and 2 m for diameter (see fig. 2.4(a)). The ensemble is kept under evacuated atmosphere, at 10^{-5} bar. Motorized trucks move the piece through 6 m in longitudinal shifts and 40 cm in transversal displacements (in the plane perpendicular to the beam). The detection array is composed by 1024×1024 pixels, each one corresponding to a single square with sides $\approx 166 \mu\text{m}$. A second 2D detector (Princeton), dedicated to WAXS registers, is also installed allowing simultaneous analysis of small- and wide- angles scattering.

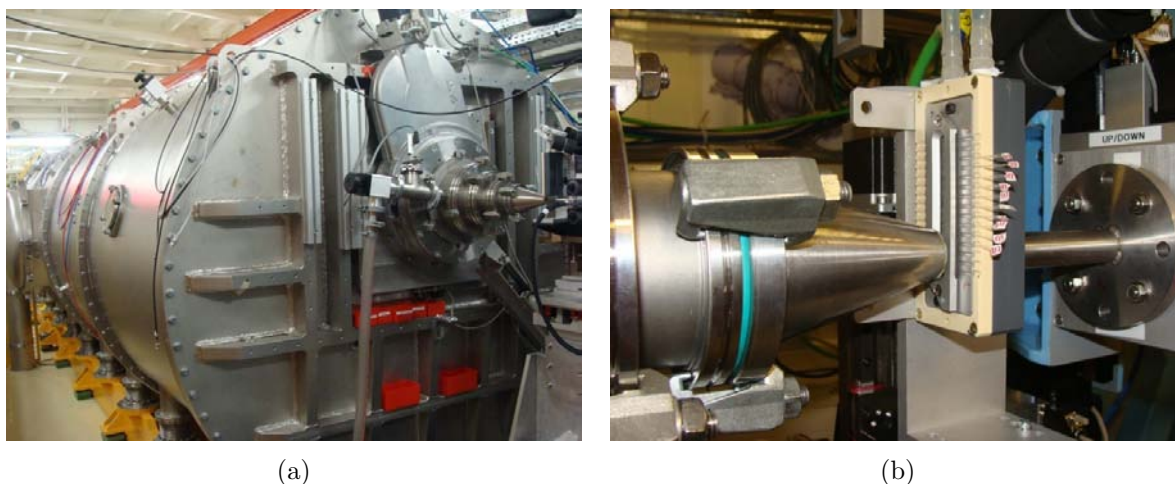


Figure 2.4: Experiments at SWING-SOLEIL beam line. In the left, the perspective view of the detection tunnel. In the right, detailed view of the sample holder showing the entry of the detection chamber, the sample capillaries, the water circulation system (hoses above the holder) and part of the beam delivery setup.

Experiments at SWING-SOLEIL beam line were performed in two different runs. In the first round of analysis, emphasis was given to studies of the host phase. In particular, the aim of this run was to verify the fluidity of membranes and search for possible $L_{\alpha} \rightarrow L_{\beta'}$ transitions. From data available in the literature, it is known that the typical distances between carbonic tails in phospholipids are located in the range of 3 to 6 Å. In order to access this region in the reciprocal space, the sample-to-detector distance was set at $D_{SD} = 608 \text{ mm}$. The beam energy was chosen to be $E = 12 \text{ keV}$, which is equivalent to wavelength $\lambda = 1.03 \text{ Å}$. In this configuration, the spatial resolution was estimated to be $\Delta q \approx 0.0038 \text{ Å}^{-1}$ (see section 2.3.3). Furthermore, the detector was set off-axis in a such a way that the range of wave vectors accessible to our experiment was between $q_{min} = 0.0310 \text{ Å}^{-1}$ and $q_{max} = 1.7450 \text{ Å}^{-1}$.

In the second run, both binary and ternary mixtures were evaluated. Special attention was given to DNA-containing samples. This time, the objective was to evaluate the phase behavior of the system at mesoscopic scale, which means that the expected distances were typically in the range of 10–100 Å. Moreover, for DNA-free complex, we were interested in

probing the diffuse scattering in order to do further considerations about the form factor of the system. In order to reach an optimal configuration for these analyses, the sample-to-detector distance was set in $D_{SD} = 1575.6$ mm. Again, the energy of radiation was set at the standard value of $E = 12$ keV. The resolution estimated for such a configuration was $\Delta q = 0.0017 \text{ \AA}^{-1}$ and range of accessible q vectors was $q_{min} = 0.0060 \text{ \AA}^{-1}$ – $q_{max} = 0.7000 \text{ \AA}^{-1}$.

For both experiments, water circulation was used to keep the sample holder temperature at 25°C . A set of ≈ 15 capillaries was gently loaded in a holder which was remotely driven (see fig. 2.4(b)). Calibration frames were taken using AgBe (silver behenate) standard for each configuration. These control images were used latter to precisely determine the position of direct beam as well as to establish the exact sample-to-detector distance. Before each round of samples, previous nanography analysis were performed in order to determine the best positioning for capillaries. After this, frames were taken with exposure times varying between 5 and 1500 ms depending on the transmittance and scattering of the sample.

Data reduction was made by a Java-written routine called *FoxTrot*, provided by the SWING staff. This software introduced the appropriate distortion and homogeneity corrections, as well as normalizations by time and transmittance. At the end of experiments, we obtained *.dat* files containing columns with scattered intensities in function of the wave vector q . The associated uncertainties were also contained in these files.

2.3.2 Conventional sources

Nanostar-Bruker device

Most of data used in this thesis was obtained at the *Bruker NanoStar* machine (see Fig. 2.5(a)) installed at the Centre de Recherche Paul Pascal, CRPP. This device is entirely dedicated to X-rays diffraction and specially designed for studies of structures in the range 1 nm – 100 nm. The beam is provided by a conventional source wherein radiation raises from the characteristic spectrum of a copper target. The acceleration voltage was 40 kV and the filament current was 35 mA (1400 W). The radiation came from the $\text{Cu}K_\alpha$ transitions³ whose wavelength was $\lambda = 1.5418 \text{ \AA}$. The flux at the sample was estimated to be somewhat of the order of 10^7 ph/s. The geometry of the beam was circular and its size is determined by a set of pinholes, with a final diameter of $450 \mu\text{m}$.

The trajectory of the photons inside the machine is fully under primary vacuum ($\approx 10^{-4}$ bar), thereby effects of spurious scattering due to air are avoided. The detector is based on a gas system for which the noise level is very low, less than one count per second per pixel. The array of detection totalizes 1024×1024 pixels, each one with $100 \mu\text{m}$ for side. Inhomogeneities of detector response, as well as spatial distortions are appropriately

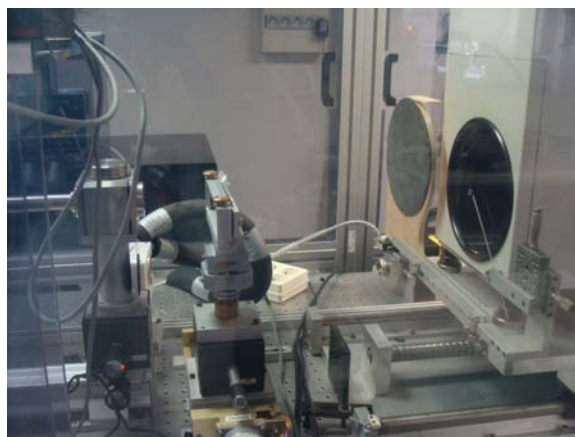
3. A Ni filter was used in order to extinguish photons from K_β transitions. However, there was no separation between $K_{\alpha 1}$ and $K_{\alpha 2}$. This nominal wavelength is the weighted average of $\text{Cu}K_\alpha$ transitions [123].

corrected by calibration files. Beam stopper was made by a small lead piece suspended in the center of the detector by very thin wires made of a material transparent to X-rays.

The procedure to perform experiments involving Nanostar, in a general way, was very similar to that one used at SWING-SOLEIL beam line. Around 10 or 15 capillaries were placed in a metallic holder and nanography was previously carried out in order to determine the best positions for the beam with respect to samples. A system for circulation of water was used to control the temperature and to keep the sample holder at 25 °C. In following, depending on the transmittance of the sample, the frames were registered with exposure times ranging from 2 to 5 hours. The sample-to-detector distance was usually 25 cm, although few experiments have been conducted at $D_{SD} = 105$ cm. For such distances, the accessible regions in reciprocal space were, respectively, $0.040\text{\AA}^{-1} < q < 0.825\text{\AA}^{-1}$ and $0.010\text{\AA}^{-1} < q < 0.200\text{\AA}^{-1}$. The machine was driven remotely by an appropriate software, *SAXS-BRUKER*, which provided 2D diffractograms in the format *.gfrm*. This software also allowed data reduction, giving 1D curves in the form of $I(q)$ vs. q columns. These two types of files could be further manipulated by using other analysis tools as *Fit 2D* or *Origin*.



(a) Nanostar-Bruker



(b) Rotating-anode

Figure 2.5: Conventional X-rays sources used in this work. At Nanostar-Bruker device, experiments are performed under vacuum and detection is made by a 2D gas detector. At rotating-anode, samples are kept under air at atmospheric pressure and data is recorded by an image plate system.

Rotating-anode setup

In addition to experiments carried out at synchrotron beam line and Nanostar, several analysis were performed at a home-made machine, whose source was a rotating anode. The wavelength of the radiation was $\lambda = 1.5418 \text{\AA}$. The flux at the sample could not be precisely determined. However, the total power of the source was 1500 W, divided into two beam lines. In addition, the pathway of the beam is taken at atmospheric pressure, implying spurious scattering due to air.

This device was used because of its capability to access wide-angle scattering regions. Data obtained from this machine were usually used to check the state of the carbonic tails, requiring q wave vectors at the range from 1 to 2 \AA^{-1} . This capability results from the detector, based on an image plate device MAR1200, which can be placed at the short sample-to-detector distance of 13 cm. In addition, the detection matrix is composed by 1200×1200 pixels, each pixel having $150 \mu\text{m}$ in size, allowing to reach wave vectors up to $q = 2.2 \text{ \AA}^{-1}$. The sample-holder and the detection system are exhibited in Fig. 2.5(b).

The machine is controlled by a computational routine developed by the technical staff at CRPP. Before recording the X-rays diffraction data, a photodiode was used to scan the samples in order to find the best position for the capillaries. As said above, most experiments carried out in this machine used sample-to-detector distance of 13 cm. Few studies were performed with $D_{SD} = 38$ cm. The exposure times were of the order of 2.5 hours. After irradiation, the image plate was scanned by a laser system and data were stored in 2D images in the format *.mar1200*. These files were reduced further by using *Fit 2D*.

2.3.3 Data treatment

Calibration

Data treatment was started with the precise determination of the sample-to-detector distances and the position of the direct beam. To accomplish this task, reference frames from silver behenate, AgBe, were recorded before every experiment. The distances between the crystallographic planes of the AgBe are known with high accuracy, being widely used as standard for calibration in X-ray diffraction [124]. The diffraction pattern from this monocrystal is composed by a series of concentric rings situated at regularly-spaced positions corresponding to integer multiples of 58.38 \AA .

The beam center coordinates were determined by marking several points along one of the diffraction rings from AgBe, usually the third or fourth order (see fig. 2.6(a)). In following, an averaging circle was traced and its center corresponded to the origin of the diffractogram. In order to evaluate the goodness of this determination, polar representations of the concentric rings were performed. In cases where the center was correctly determined, the pattern obtained was a set of parallel and vertical bars (Fig. 2.6(b), top). Small deviations, less than 2 pixels, introduced strong sinuosities allowing the quick identification of misalignments.

The sample-to-detector distances were determined from the peak positions of silver behenate. When the distances were correctly defined, these reflections are situated at $q_n = 2n\pi/58.38 \text{ \AA}^{-1}$.

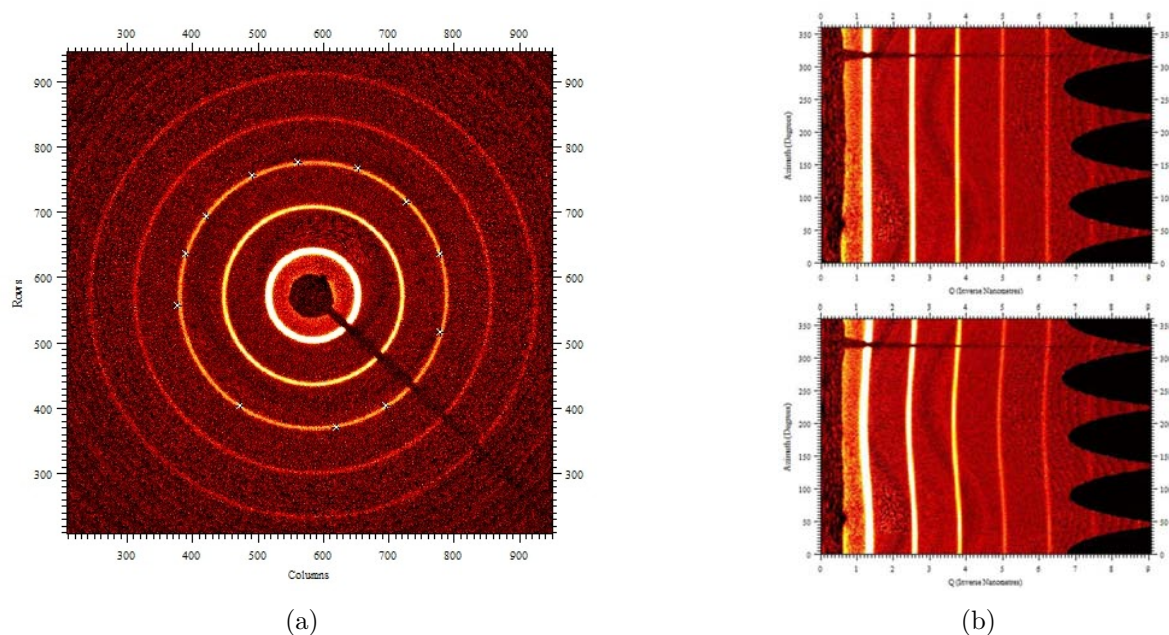


Figure 2.6: Diffraction pattern from silver behenate. (a) Five orders of concentric, evenly-spaced rings ($d = 58.38 \text{ \AA}$): On the third order, crosses show the points used in order to determine the beam center. (b) Polar representation of the pattern. When the center is correctly localized, concentric rings transform into a set of vertical lines (top). Conversely, when the center is slightly misaligned (just 2 pixels in this case), sinusoidies appear on the pattern.

Subtraction of background

According to the facility used in data collection, different background and noise corrections were carried out. In particular, the detection system employed in each case played a major role in how such subtractions and normalizations were made.

The values of q relevant for this work are placed in the region between $q \approx 0.0500 \text{ \AA}^{-1}$ and $q \approx 2.2000 \text{ \AA}^{-1}$. This means that they are predominantly at the middle- and wide-angles range. In addition, the complexes studied here are analyzed below their hydration limit being, therefore, strong scattering centres. These two elements together imply high signal-to-noise ratios because, on one hand, effects related to spurious scattering are usually concentrated in the vicinity of the direct beam (small-angle region) and, on the other hand, the signal from the sample is intense compared to noise sources. The random noise introduced by synchrotron and Nanostar detectors does not cause significant changes in the scattering curves, except for the WAXS region, wherein the scattering intensities from the samples can rather decay. This region carries specially form factor informations and the proper background subtraction is indispensable to extract the electronic density profile of the system.

For experiments carried out at synchrotron line, almost the entire beam path is in vacuum. This minimizes strongly the effects due to scattering from the air. Moreover, the detector, based on CCD technology, has low level of electronic noise. Because of construction reasons, along the detection matrix, there are some inhomogeneities which

must be taken into account in the analysis procedure. In order to correct them, the background intensities were registered and further subtracted from the sample intensities. In order to compare different curves, the obtained profiles were also normalized by their exposure times. Mathematically, the correction procedure is summarized as follows:

$$I_{corr} = \frac{I_S}{T_S \times t_S} - \frac{I_{BG}}{T_{BG} \times t_{BG}} \quad (2.3)$$

where I , T and t refer, respectively, to scattering intensity, transmission and exposure time. Indexes ‘‘S’’ and ‘‘BG’’ refer, respectively, to sample and background⁴.

For experiments carried at Nanostar, spurious scattering due to air is virtually absent because the trajectory of the photons is entirely covered under evacuated atmosphere. The detector, based on a gas system, also has low level of electronic noise. Since the device works with a limited number of configurations (λ and D_{SD} are fixed), previous calibration files are used and the only correction necessary during our experiments was the subtraction of a uniform background. The corrected and normalized intensities are then given by:

$$I_{corr} = \frac{I_S}{t_S} - BG \quad (2.4)$$

The value of the constant BG was defined in a relatively arbitrary way. As rule of thumb, the subtracted value was chosen in such a way that few zero values were observed at wide-angle region.

For data collected at the rotating anode, the analysis required more corrections. Besides the background scattering, it was necessary to subtract the remanence of the detector. In order to do this, a record of the unexposed image plate was made. This frame was subtracted from all further diffractograms obtained at this machine. The procedure used to correct data from rotating anode is summarized as follows:

$$I_{corr} = \frac{I_S - I_R}{T_S \times t_S} - \frac{I_{BG} - I_R}{T_{BG} \times t_{BG}} \quad (2.5)$$

where I_R correspond to the remanence on the detection system.

Estimations on resolution

An important point for the studies carried out here is the instrumental resolution $\Delta q/q$. This parameter is crucial, for instance, for the appropriate use of the models describing the X-rays scattering curves (see sec. 1.6.1). In addition, it is also relevant for indexing Bragg peaks because it determines the minimum distance between two reflections.

The accurate determination of the instrumental resolution is not a trivial task because it depends on several parameters which are not always known in detail. Some analytical expressions and numerical methods have been proposed in order to predict the intrinsic

4. At SWING, the application *Foxtrot* provided data files normalized by exposure times and transmissions.

broadening on X-rays peaks due to the instrumental apparatus [125]. Here, however, due to the lack in ensuring the exact values of certain parameters ($\Delta\lambda$, size of pinholes and slits, etc.), we have chosen to estimate the resolutions by using a purely experimental approach based on the silver behenate standard. Since our samples are soft systems, the disorder on its liquid-crystalline arrangements is much larger than that one observed in the crystalline structure of the silver behenate. In addition, for the purposes of our studies, we consider that the widths of the AgBe peaks are resolution-limited. In this case, the measurement of the broadness of reflections from AgBe allows to reasonably estimate the total resolution $\Delta q/q$.

In general, resolution functions are adequately described by Gaussians or Lorentzians [93,125]. For data obtained at Nanostar and rotating anode setup, we were able to fit the silver behenate peaks by equations of type:

$$I(q) = A_0 + I_0 \cdot \exp \left\{ \frac{-(q - q_n)^2}{2(\Delta q)^2} \right\} \quad (2.6)$$

where A_0 is the off-set constant, I_0 is the amplitude of the peak and q_n is its position. The parameter Δq is the standard deviation of the Gaussian function and is related to the half width at half maximum (HWHM) through the relationship $\Delta q = HWHM/\sqrt{2 \ln 2}$.

On the other hand, in the case of SWING station experiments, fits were not possible with Eq. 2.6. Suitable fits of such peaks could be carried out by using Lorentzians functions of type:

$$I(q) = A_0 + \frac{I_0}{1 + \frac{(q - q_n)^2}{\Delta q^2}} \quad (2.7)$$

where $\Delta q = HWHM$.

It should be noted that the values of Δq given by equations 2.6 and 2.7 carry also an intrinsic broadening from the crystalline disorder of the AgBe and correspond, therefore, to over-estimations of the resolution, specially for synchrotron-raised data. In Fig. 2.7, it is showed the comparison among the widths of the second-order peak from AgBe for the three facilities used in this work. The sample-to-detector distances are those ones more often employed. Differences on resolution for each device are clearly observed. The quality of the resolution for synchrotron data is outlined by the narrowness of the peak obtained at SWING-SOLEIL beamline. In table 2.1, the values of $\Delta q/q$ are exhibited for all configurations used along the manuscript. A clear effect of the sample-to-detector distance on resolution appears.

Indexation procedure

After the appropriate corrections on background and detector inhomogeneities, extraction of information from diffraction patterns was initiated by determining the positions of Bragg peaks. This procedure was manually carried out with traditional softwares for viewing and data processing (Origin, Kaleidagraph, GNU plot, etc.). In following, these

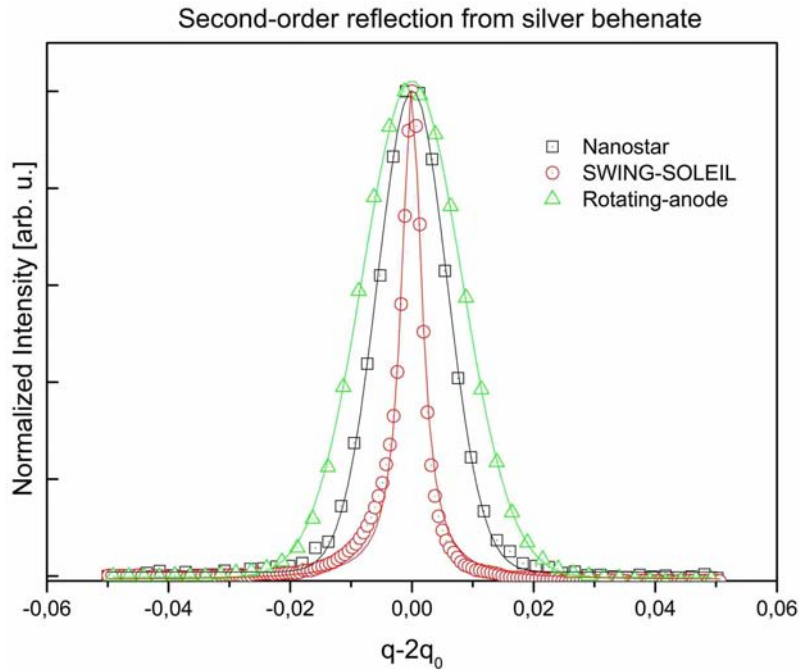


Figure 2.7: Comparison of widths for the second-order peak from AgBe. Data were recorded at sample-to-detector distances of 133 mm (rotating-anode), 250 mm (Nanostar) and 1575.6 mm (SWING-SOLEIL). Solid lines correspond to Gaussian fits (green and black lines) and to a Lorentzian function (red).

positions were introduced in a Matlab routine specially designed for this purpose. The principle of this computational tool was to test three types of symmetries: lamellar, 2D hexagonal and 2D rectangular (Fig. 2.8). Biphasic combinations of these three basic structures were also evaluated and the choice of the correct indexation was based on the minimization of the sum of square differences between predicted and experimental peaks.

Lamellar symmetries were indexed according to the expression:

$$q_n = (n + 1) \times q_0 \quad (2.8)$$

where n is an integer and q_0 is the position of the first order peak. Smectic periodicities

Table 2.1: Estimations of the total resolution $\Delta q/q$, for all configurations used in this work, at $q = 0.215 \text{ \AA}^{-1}$. The actual values for resolutions are slightly lower than the ones showed here (see text for details).

Facility	Sample-to-detector distance (mm)	q range (\AA^{-1})	$\Delta q/q$ (\AA^{-1})
SWING-SOLEIL	1575.6	$0.0600 < q < 0.7000$	1.7×10^{-3}
	608.0	$0.0300 < q < 1.7450$	3.8×10^{-3}
Nanostar-Bruker	1060	$0.0100 < q < 0.2000$	1.5×10^{-3}
	250	$0.0400 < q < 0.8250$	6.3×10^{-3}
Rotating-anode	383	$0.0660 < q < 0.8200$	5.1×10^{-3}
	133	$0.190 < q < 2.200$	8.1×10^{-2}

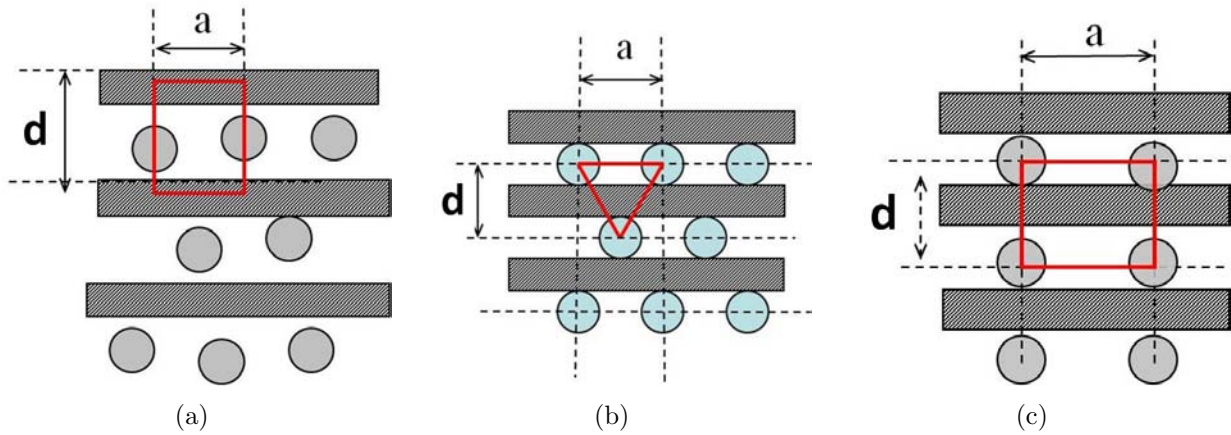


Figure 2.8: Unit cells indexed in this work. (a) Lamellar phase containing rods organized according to a nematic symmetry. (b) Lamellar phase of lipids containing a 2D hexagonal arrangement of rods and (c) lamellar phase of lipids containing a 2D rectangular structure of rods.

could be then easily extracted from the relationship:

$$d = \frac{2\pi}{q_0} \quad (2.9)$$

When a diffuse peak appeared convoluted between the lamellar peaks (usually between the second and the third), its position, here called q_{DNA} , was determined separately through Lorentzian fits (see Eq. 2.7). This reflection was attributed to in-plane DNA-DNA correlations (fig. 2.8(a)). The average distance between rods, henceforth designed by a , was determined by using the relationship $a = 2\pi/q_{DNA}$. The correlation length of the rods was estimated by (see appendix B for details):

$$\xi = \frac{2.783}{\Delta q} \quad (2.10)$$

For 2D rectangular symmetries, the positions of the peaks were predicted to be at:

$$q_{hk} = 2\pi \times \sqrt{\left(\frac{h}{a_{rect}}\right)^2 + \left(\frac{k}{b}\right)^2} \quad (2.11)$$

where a_{rect} and b are the sides of unit cell (fig. 2.8(c)).

For 2D hexagonal symmetries, the peaks were predicted to be at the following positions [126]:

$$q_{hk} = \frac{4\pi}{a_{hex}} \times \sqrt{\frac{h^2 + hk + k^2}{3}} \quad (2.12)$$

Which leads to peaks at relative positions $1 : \sqrt{3} : \sqrt{4} : \sqrt{7} : \sqrt{9} : \sqrt{12} : \sqrt{13} : \sqrt{16} : \dots$. The lattice parameter a , corresponding to the side of the unit cell, was then obtained from:

$$a_{hex} = \frac{4\pi}{q_0\sqrt{3}} \quad (2.13)$$

For samples with ambiguous indexation, for which the above described procedure did not find physically meaningful parameters, the cubic groups $Pn3m$ (relative peak positions at $\sqrt{2} : \sqrt{3} : \sqrt{4} : \sqrt{6} : \sqrt{8} : \sqrt{9} : \sqrt{10} \dots$) [127], $Im3m$ ($\sqrt{2} : \sqrt{4} : \sqrt{6} : \sqrt{8} : \sqrt{10} : \sqrt{12} : \sqrt{14} \dots$) [128] and $Ia3d$ ($\sqrt{3} : \sqrt{4} : \sqrt{7} : \sqrt{8} : \sqrt{10} : \sqrt{11} : \sqrt{12} \dots$) [68] were also checked by using another routine. For all indexations, the maximum difference tolerated between predicted and experimental peaks was equal to the instrumental resolution.

Fitting process

Data from binary (lipids/water) and ternary (DNA/lipids/water) mixtures were also fitted according to the model of Nallet et al. The main goal of such analysis was to evaluate the smectic ordering of the host lamellar phases as well as the effects of the insertion of nucleotides on the stacking of bilayers. This was achieved through the study of behavior of the parameter of Caillé as a function of the thickness of aqueous layers in-between membranes. In order to reach this purpose, equations from the model were written in the *Curve Fitting* MatLab toolbox which performed minimizations using Levenberg-Marquardt algorithms.

Due to the complexity of the parameter space, which had several local minima, the fitting process was very sensitive to starting values. In order to minimize this drawback, the number of free parameters was diminished by previous determination of the size of polar heads and carbonic tails. These last ones were obtained by fitting Eq. 1.23 to data from highly-hydrated samples in the range $0.300 \text{ \AA}^{-1} < q < 0.500 \text{ \AA}^{-1}$. As discussed in section 1.6.1, for diluted lamellar phases, the structure factor rapidly tends to $S(q) \rightarrow 1$, which results in the predominance of the form factor $P(q)$ at WAXS region.

In following, full range fits were carried out using Eq. 1.22. Four parameters were left free to be adjusted: the scaling factor $A_0 = \frac{8\pi}{D} \Delta\rho_H^2$, the periodicity d , the Caillé number η and the ratio between electronic contrasts $\Delta\rho_T/\Delta\rho_H$. Since the model has some limitations to describe the wide angle region, the q - range was truncated at $q = 0.500 \text{ \AA}^{-1}$. This same procedure was adopted before in similar contexts [95,96].

Uncertainties on parameters were estimated from several repetitions using different set of initial values which converged to the same final values.

2.4 Polarized-light and epifluorescence microscopies

Preparations were also systematically submitted to visual inspection. The used techniques were polarized-light (POM) and epifluorescence microscopies. The main objective of these observations was to evaluate the optical birefringence of the samples and get informations about uniformity of DNA distribution inside the complex. The instrument

employed in both analysis was a microscope *Leica* model *CTR Mic*. It is an inverted microscope, where the illumination can be made either by using a filament lamp or a mercury source. This device is very similar to that one showed in Fig. 2.10.

Sample drops were deposited onto glass slides and rapidly covered with glass cover slides. A gentle shearing was manually performed for a few seconds. The cells were then sealed with a UV-curing glue to prevent solvent evaporation. Owing to this procedure, the cell thickness along the microscope optical axis was not precisely known, but lied in the range $5 - 15 \mu\text{m}$. The favored anchoring corresponded to bilayers being parallel to the glass flat sides (or “homeotropic” anchoring). In homeotropically-oriented domains, the stacking axis was therefore also parallel to the setup optical axis. The number of stacked solvent layers across the height of the cell was typically of the order of 10^3 or more.

A pair of crossed polarizers, placed along the optical axis, allowed analysis of textures. According to observed patterns, information on anisotropy of the complex was obtained. This was possible because the birefringence pattern depends on the symmetry of the system. An isotropic phase, for instance, does not introduce modifications on the axis of polarization, and through crossed polarizers, the observed pattern is a dark stain. A lyotropic lamellar phase, in turn, is strongly anisotropic appearing like a chaotic, but characteristic texture of alternating bright and dark areas. A hexagonal symmetry also changes the axis of polarization giving rise to a mosaic picture. Typical examples of these three kinds of texture are shown in Fig. 2.9.

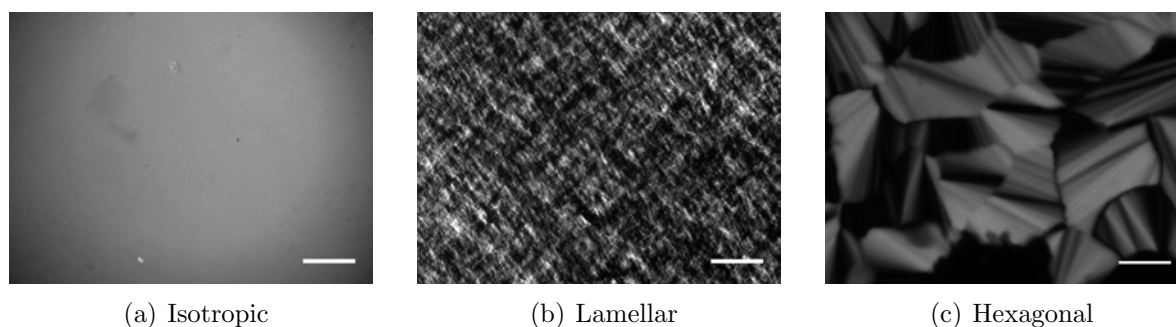


Figure 2.9: Typical optical textures found under crossed polarizers microscopy. Scale bars correspond to $100 \mu\text{m}$ for (a) and (b) and to $20 \mu\text{m}$ for (c).

Fluorescence studies were performed by using mercury lamp as light source and a pair of filters. The illumination was made in the range of blue while observations were achieved in the range of green. The associated wavelengths fall, respectively, in the excitation and emission spectra of YOYO. POM and fluorescence analysis were carried out on the same region of the sample which allowed co-locating areas of fluorescence with their local orientation.

2.5 Freeze-fracture and electron microscopy

Replicas for transmission electron microscopy (TEM) were prepared following standard freeze-fracturing protocols⁵ [129]. Two distinct procedures were used in order to prepare specimens for TEM observations: for hydrated samples, small quantities of the complex were sandwiched between copper plates and, for water-poor formulations, they were accommodated in the holes of gold stubs. In following, the sets were plunged in liquid propane cooled to -190°C by liquid nitrogen. The process of fracture and coating with platinum and carbon was made inside a BALTEC machine BAF060 wherein atmosphere reached 10^{-9} bar and temperature was -150°C . When samples were lodged on sandwich holders, fractures was obtained just by separating the plates. In the case where gold stubs were used, fracture was made by the passage of cold microtome knife through the frozen specimen preserving the internal structures of samples. In both cases, the system was replicated by shadowing a 4 nm platinum/carbon film sputtered at 45° angle. A second carbon layer, with thickness 30 nm, was finally deposited normal to the surface. The replicas were mounted on copper grids after being removed from the holders by successive baths in ethanol/water and chloroform/ethanol mixtures.

Observations were carried out in a Hitachi H600 transmission electron microscope. The acceleration tension was 75 kV and filament current was $100\ \mu\text{A}$. Magnification varied between 5000X and 300000X. In order to extract quantitative information about distances in the observed patterns, Fourier transforms, using *Image J* software, were performed over the TEM images.

2.6 FRAP experiments

Samples cells were prepared and sealed in the same manner described in Sec. 2.4. The bleaching and imaging were performed at CRPP with the Leica DMIRE *confocal laser scanning microscope* (CLSM) showed in Fig. 2.10. The objective lenses were chosen to be x10 or x40, with numerical apertures NA 0.3 and NA 0.6, respectively. In order to ensure a satisfactory azimuthal averaging across the height of the observed domains, the pinhole was kept at its maximal aperture, $600\ \mu\text{m}$. This is a very particular characteristic of the experiments conducted here because, at contrast with many studies reported in the literature [113–115, 130], the confocality property of the microscope, that is, the accurate resolution along optical axis z , is not used. Instead, our needs concern rather to the scanning capabilities of CLSMs, which allow to get high in-plane resolutions and to proceed surgical bleaches. Moreover, the detection system, based on photomultipliers synchronized with the illuminating beam, enables to follow the fluorescence recovery at specific wavelengths leading to very good signal-to-noise ratios.

The 488 nm line from an Argon laser was used as illuminating source. This wavelength

5. The preparation of replicas was made with the invaluable help of Isabelle Ly, lab technician at CRPP.



Figure 2.10: Leica DMIRE confocal laser scanning microscope used at CRPP for FRAP experiments in this work.

is very close to the excitation peak of YOYO, namely 491 nm. The detection range was set in the interval between 500 nm and 600 nm, ensuring that only emitted light was recorded. Before every bleach, the samples were observed under crossed polarizers and a squared zone, with size $\approx 80 \mu\text{m}$, was selected inside an extended dark zone to ensure homeotropic orientation. This same region was observed in fluorescence in order to inspect the homogeneity of DNA distribution. A quarter-wave plate was then placed in the beam path in order that the laser light striking the samples had circular polarization⁶.

FRAP experiments were divided in two parts. The first one is related to the *pre-bleach* stage. A set of 10 images of the region of interest was recorded previously to the bleach pulse. These images were further averaged and a background picture was obtained. The second stage is related to recording the images after the bleaching burst. The total number of records, as well as the interval between images, depended strongly on the speed of the diffusion process. For our samples, these times were situated between 5, for the more diluted binary DNA-water solution, and 20 seconds, for the more concentrated ternary DNA-lipid-water system. The total number of records was situated respectively between 20 and 80 images. The bleaching pulse was used at maximum power of the laser, estimated to be of the order of 50 mW at the sample. The illuminating beam, used to record images before and after bleach, was attenuated by a factor ≈ 20 . The state of the main microscope parameters used in the experiments described here are summarized in table 2.2.

6. This step is very important because, as discussed before, the fluorescence intensity depends on the orientation of the DNA rods.

Table 2.2: Experimental settings used in the FRAP experiments.

Objective	x10 (NA 0.3) or x40 (NA 0.6)
Scan mode	xyt
Scan speed	800 Hz
Illuminating λ	488 nm
Emission range	500-600 nm
Format (pixels)	512×512
Bleach power	Estimated in 50 mW
Beam diameter	$\approx 8\mu m$
Bleach pulse duration	500ms
Pinhole size	$600\mu m$

2.6.1 Analysis software

Analysis was carried out by using a MatLab routine developed by Jens Dobrindt and improved by others⁷. The code was based on a previous software developed by S. Seiffert and co-workers [113, 114, 131]. The treatment is divided as follows:

Normalization. In this step, the set of pre-bleach images is averaged and one background image is obtained. The records are imported by Matlab and stored into 512×512 objects whose entries are fluorescence intensities coded in integer levels between 0 and 255 (8-bits). All images taken after the bleach are divided by the background image in order to perform normalization.

Rotational center and averaging. The center of rotation is found through a specific algorithm developed by the authors of Ref. [113] and detailed therein. The image is then divided in 180 angular intervals and the fluorescence profiles across the center are obtained in the interval $[0, \pi]$. In following, these profiles are averaged and a mean radial contour is obtained (see figs. 2.11(a) and 2.11(b)).

Fitting of Eq. 1.33. In following, the modified anisotropic function 1.33 is fitted to the experimental fluorescence data. Since the elapsed time is known, a collection of $w_{\parallel}^2, w_{\perp}^2$ vs. t is obtained (fig. 2.11(c)).

Obtaining diffusion coefficients. Finally, linear fits using equations 1.34 are carried out and, from the slope of these straight lines, diffusion coefficients are extracted.

The data treatment is summarized in Fig. 2.11, where its main steps are sketched.

7. The final form of the code used here received improvements from C. L. Pinto de Oliveira (University of São Paulo), E. R. Teixeira da Silva, C. Alves (University of São Paulo) and A. Schoöppach (CRPP).

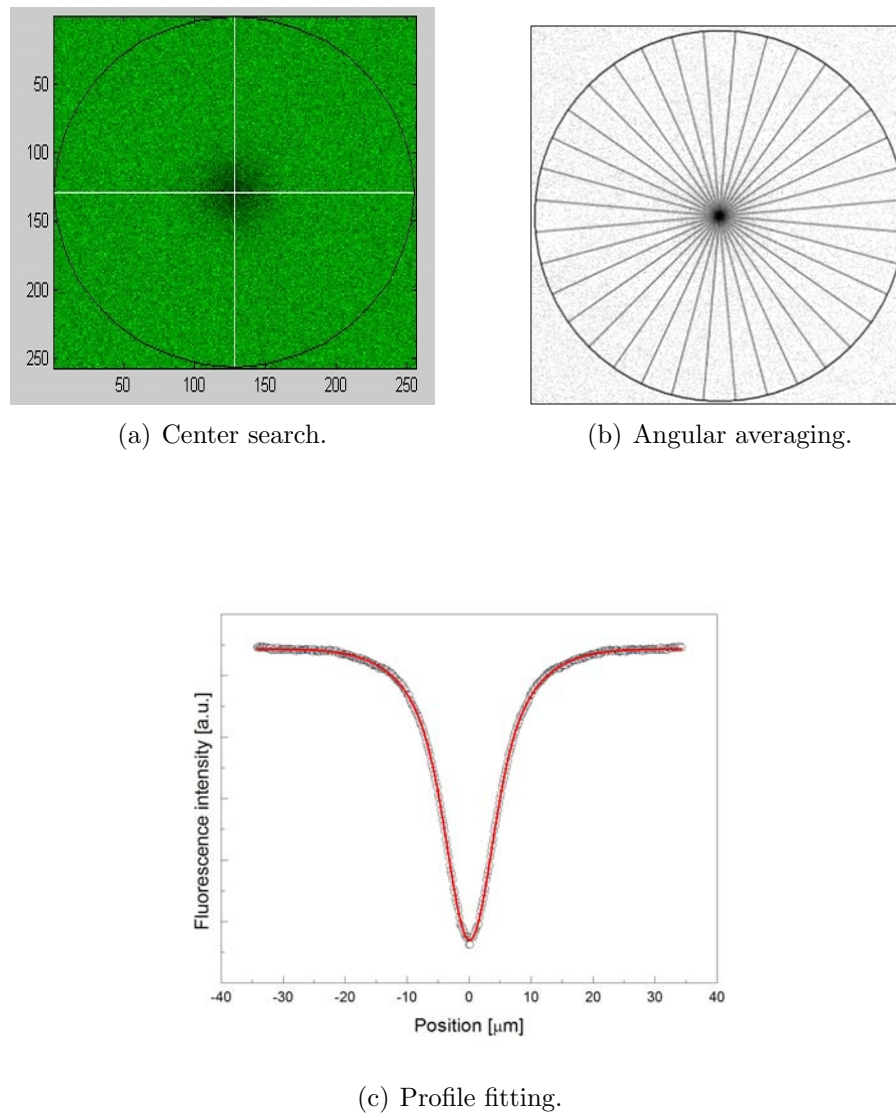


Figure 2.11: Main steps of the data analysis process: (a) The center of the bleaching spot is found. (b) In following, fluorescence intensities are averaged over 180 angular sectors passing by the center—note that, for clarity, only 18 sectors are shown here. (c) Eq. 1.33 is fitted to the average fluorescence profile.

CHAPTER 3

STRUCTURAL RESULTS

In this chapter we describe the structural results obtained throughout this work. In a first stage, analyses were carried out on the host phase, that is, the system formed by hydrated lipid lamellar phases. Two membrane compositions were evaluated, containing 70:30 or 50:50 PC-to-Simulsol ratios. The ionic strength was also modulated by introducing monovalent salt in the system. Quantitative analyses were performed by fitting the model of Nallet et al. to X-rays data and by studying the behavior of the Caillé parameter as a function of periodicity. An approach proposed by Petrache et al. [132–134] was used and allowed to determine that, for the intermembrane spacing of interest for introducing DNA rods, the attractive van der Waals interactions are equilibrated by an interplay of mixed hydration and Helfrich’s repulsive forces.

In a second stage, DNA fragments (150 bp) were added to prepare the complex. Series of data were obtained with the above-mentioned membrane compositions. For membranes with 70% of lecithin, three dilution lines were scanned: $\rho = 3.1$, $\rho = 5.1$ and $\rho = 8.1$. For the other composition, only samples with $\rho = 3.1$ were prepared. A rich polymorphism of mesophases driven by confinement is found and the full incorporation of nucleotides is observed to be closely dependent on the amount of DNA in the system. Electrostatic interactions appear to have a secondary role on the phase behavior whereas the increase on the proportion of Simulsol seems to favor the formation of single phase domains.

3.1 Lipid-water system: host phase

3.1.1 Membranes with 70:30 PC-to-Simulsol ratio

Structural analysis started with the study of host phases prepared from membranes with 70:30 PC-to-Simulsol ratio. Samples were formulated using pure water as solvent and left to equilibrate according to the procedure described in chapter 2. Water volume fractions ranged from $\phi_w = 0.25$ to $\phi_w = 0.75$ and X-rays experiments were carried out, in

different times, at the Nanostar-Bruker machine or/and at the SWING-SOLEIL station. The main goals were to evaluate the dilution domain of the system and to determine the hydration limit as well as the thickness of the formed membranes. Moreover, another important task was to establish the state of carbonic tails, L_α or $L_{\beta'}$, at room temperature for several concentrations.

Selected diffractograms from these samples are exhibited in Fig. 3.1. The diffraction patterns, as expected, are composed by concentric equally-spaced rings whose radii depend on the amount of water. This is the classical X-ray signature of lyotropic lamellar phases, where the repetition distances increases upon hydration. For few samples the scattering intensities do not appear homogeneously distributed along the rings. This is due to the formation of semi-oriented domains during the centrifugation procedure to place the product inside the glass capillaries.

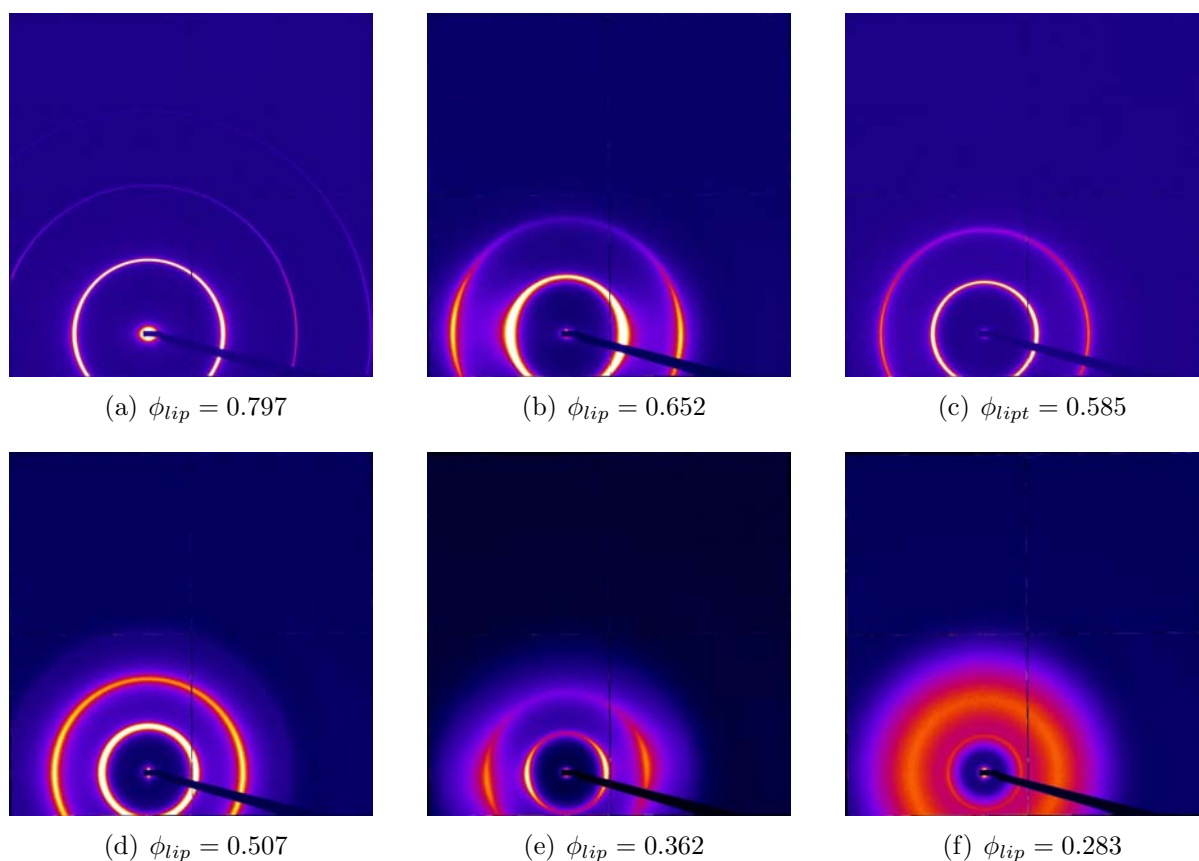


Figure 3.1: Diffraction patterns of lamellar phases containing different water amounts.

The reduced $I(q)$ vs. q data from all formulations with this membrane composition are exhibited in figs. 3.2 and 3.3.

Multilamellar stacks of regularly-spaced bilayers are found throughout the studied domain. As the water amount increases, the Bragg peaks shift towards the small angle region in a clear indication of the swelling of the lipid phase. For concentrated samples, *e.g.* $\phi_{lip} \approx 0.75$, one observes up to four narrow Bragg reflections attesting strong ordering and large number of correlated bilayers. On the other hand, for more diluted samples, *e.g.* $\phi_{lip} \approx 0.50$, the number of Bragg reflections decreases whereas the peaks become broader,

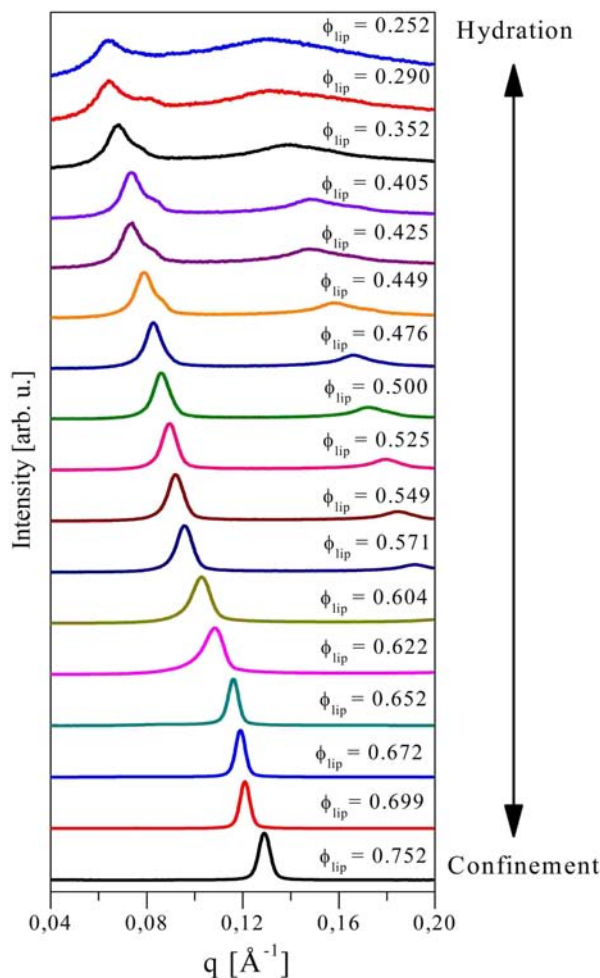


Figure 3.2: SAXS plots from binary lipids/water mixtures obtained at Nanostar-Bruker machine.

showing the decay of the smectic ordering.

Repetition distances are determined from first order peak positions by using Eq. 2.9. The behavior of the lamellar periodicity d as a function of the inverse lipid volume fraction $1/\phi_{lip}$ is shown in fig. 3.4. Two distinct regimes are identified. The first one is driven by an usual swelling law until water volume fraction $\phi_w \approx 0.60$. In this interval, lamellar periodicities range from $\approx 47 \text{ \AA}$ to $\approx 85 \text{ \AA}$. A relationship between the smectic period and hydration of the form $d = \delta_m/\phi_{lip}$, is found. Performing a linear fit over data from this domain, one determines the thickness of bilayers to be $\delta_m = 36.5(3) \text{ \AA}$.

In the second domain, for $1/\phi_{lip} \gtrsim 2.5$, the system presents excess of water and the repetition distances remain approximately constant, around $92(5) \text{ \AA}$. It should be noted that data used in fig. 3.4 were obtained from independently prepared samples, X-rayed at distinct facilities and configurations. Hence, the reproducibility of d points to the strong robustness of the data.

The knowledge of δ_m enables to obtain the size of the aqueous layers $d_w = d - \delta_m$. This parameter is very important concerning ternary complexes because it permits to establish the available space for nucleotides within the host phase. On the other hand, it is also convenient to know the intermembrane spacing as a function of the lipid volume fraction

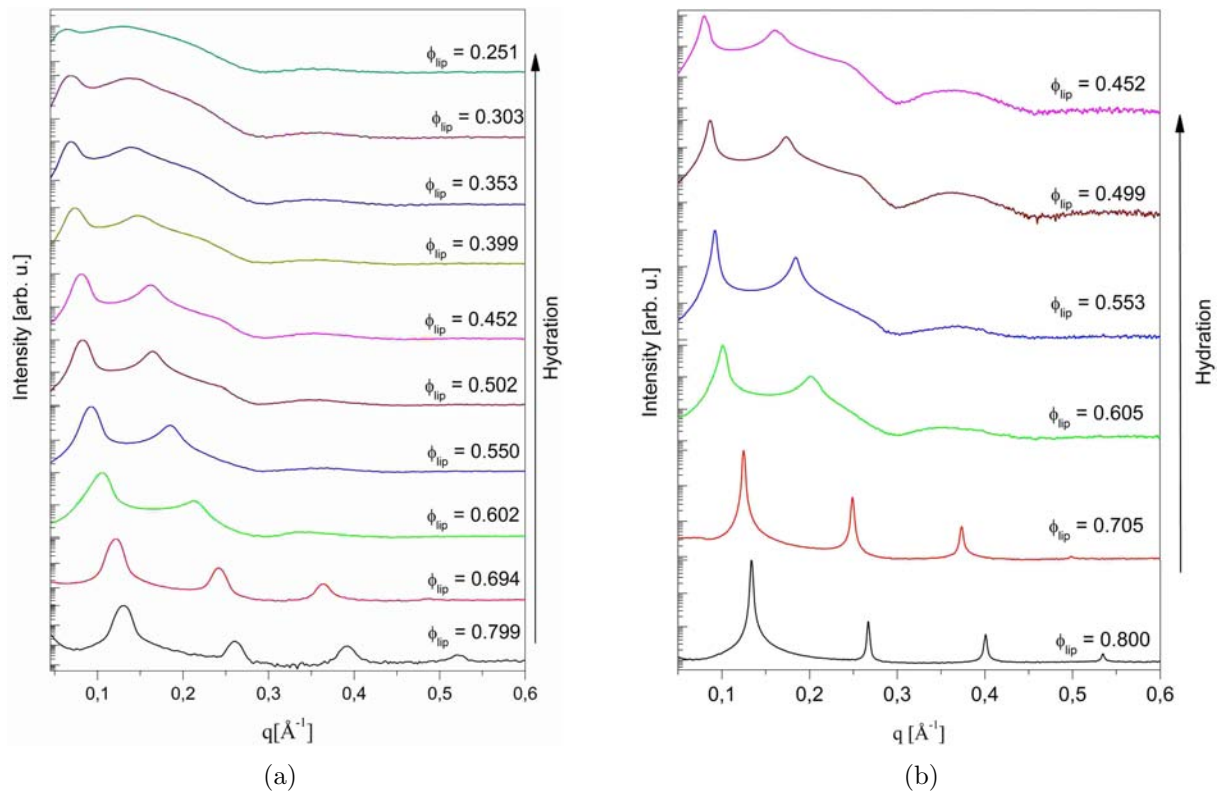


Figure 3.3: Plots of $I(q)$ vs. q from binary lipids/water mixtures obtained at (a) Nanostar-Bruker and (b) SWING-SOLEIL beamline. For concentrated samples it was possible to observe up to four Bragg reflections. Higher orders become unobservable with increasing hydration.

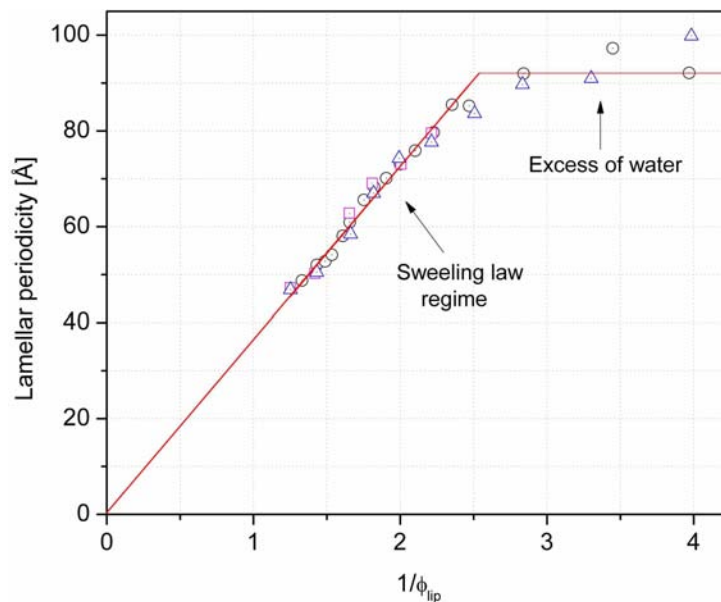


Figure 3.4: Behavior of the lamellar periodicity d as a function of $1/\phi_{lip}$. Two domains are identified: the first one is driven by an usual swelling law leading to membrane thickness $\delta_m = 36.5(3)$ Å. The second one is dominated by water excess, with $D_{max} = 92(5)$ Å. Black \circ are the data shown in fig.3.2, blue \triangle are the data shown in fig.3.3(a) and pink \square are the data shown in fig. 3.3(b).

because it allows to compare binary and ternary formulations with equivalent ϕ_{lip} . In fig. 3.5, we present the behavior of the separation between bilayers as a function of the lipid amount. Dashed lines indicate the dilution limit and the DNA size below which the thickness of aqueous layers are not enough to accommodate rods with diameter = 20 Å. It is found that the system is able to incorporate nucleotides in-between lamellae when the lipid volume fraction ranges from $\phi_{lip} \approx 0.35$ to $\phi_{lip} \approx 0.64$. In order to probe the state

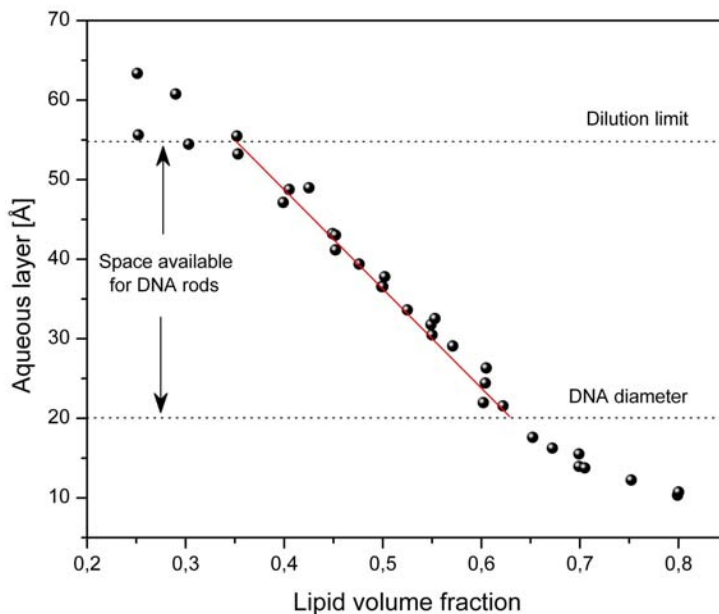


Figure 3.5: Behavior of intermembrane spacing as a function of lipid volume fraction. The region indicated by arrows corresponds to distances for which the host phase is able to incorporate nucleotides.

of the carbonic tails, and bring out informations on the fluidity of membranes, diffraction experiments were also carried out looking at high values of q . The results of these trials are showed in fig. 3.6. The systematic presence of a broad peak at the WAXS region evidences the fluid state of bilayers along the whole dilution domain. Fitting these reflections with Gaussian functions (solid red lines in the first row of Fig. 3.6), the peak position is found around $q = 1.38 \text{ \AA}^{-1}$ with $\Delta q = 0.50 \text{ \AA}^{-1}$. These values correspond to average distance between carbonic chains equal to 4.5 Å and correlation length $\xi \approx 12.5 \text{ \AA}$ (or about 3 molecules). In fig. 3.7, it is shown a 2D diffractogram from a sample where the loading process into the capillary induced semi-oriented domains. Intensities in the external wider ring are concentrated along the horizontal axis whereas, in the circles situated close to the beam stopper, they are stronger ahead the vertical direction. As discussed above, the circles at the small angle region arise from diffraction by the lipid bilayers whereas the wide-angle ring originates from diffraction by the aliphatic tails, perpendicular on average to the membranes.

Parallel to X-rays analysis, we carried out observations under polarizing microscopy. Lamellar textures were found for most of the samples (Fig.3.8) with chaotic birefringent patterns being observed for samples with $\phi_{lip} > 0.42$. In formulations containing higher amounts of water, isotropic droplets appeared surrounding birefringent lipid vesicles (*e.g.*

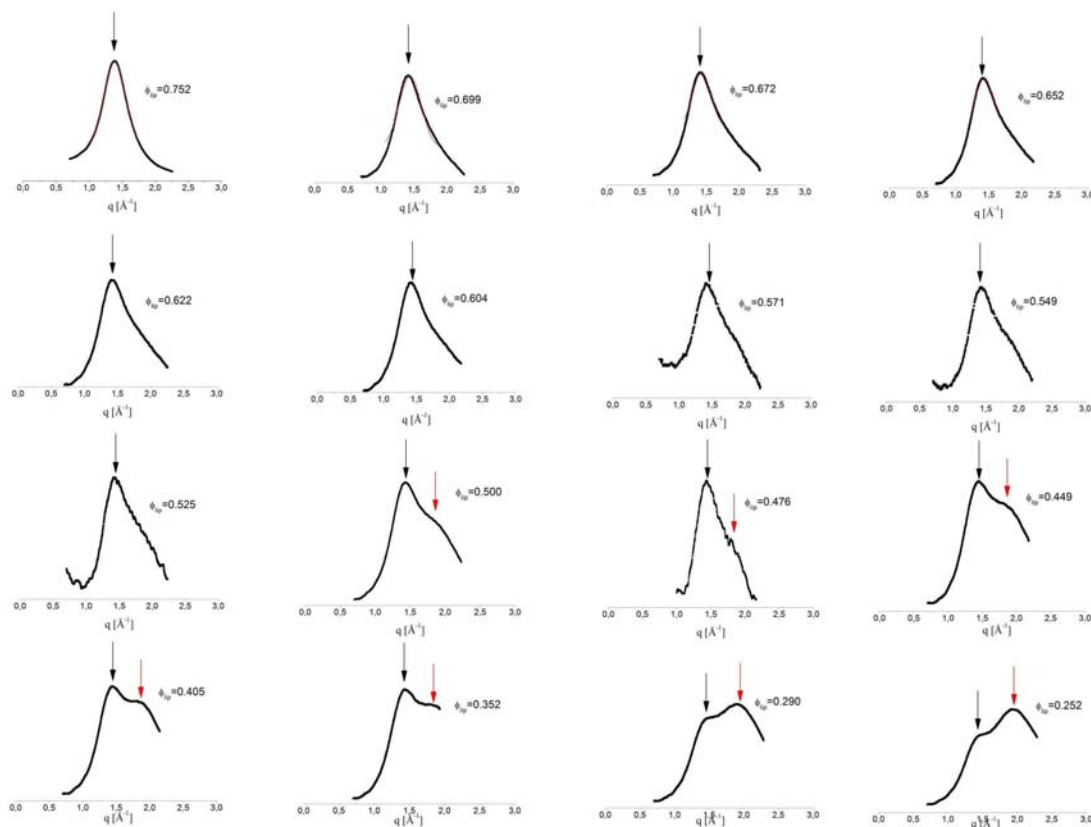


Figure 3.6: WAXS $I(q)$ vs. q profiles from lipids/water mixtures. The presence of a diffuse peak around 1.38 \AA^{-1} (black arrows) was found for all formulations, pointing to the L_α state of membranes along the whole dilution domain. For very hydrated samples, $\phi_{wt} < 0.50$, the peak associated to the water molecules becomes significant and is observed around 1.9 \AA^{-1} (red arrows).

fig.3.8(e)). These findings are in close agreement with data obtained from X-rays since lamellar textures are observed for samples belonging to the swelling domain, whereas the coalescence of droplets appeared in formulations above the hydration limit.

Transmission electron microscopy observations were also carried out to complement X-rays data with direct-space visualization. Few formulations were selected and replicated according to the procedure presented in Sec. 2.5. Five compositions were selected for cryofracture. Inside the swelling domain, the formulations with $\phi_{lip} = 0.752$, $\phi_{lip} = 0.604$, $\phi_{lip} = 0.500$ and $\phi_{lip} = 0.449$ were chosen. Above the dilution limit, the sample with $\phi_{lip} = 0.290$ was selected.

Low-magnification images from these replicas are exhibited in figures 3.9-3.11. The large-scale topology can be visualized and few vesicles, incrustated in a colloidal lipid matrix, are observed along the whole hydration range. The frequency and the size of such structures depend on concentration. For lipid-richer samples, *e.g.* $\phi_{lip} = 0.752$, vesicles are found to be larger in size and rarer in frequency. On the other hand, for diluted samples, *e.g.* $\phi_{lip} = 0.290$, the number of vesicles increases significantly whereas their sizes decrease. A possible reason for this observation is the decay on the smectic ordering upon hydration. As mentioned in Sec. 1.6.1, the lower the distance between bilayers, the lower the amplitude of undulations of membranes. Therefore, small thermal fluctuations,

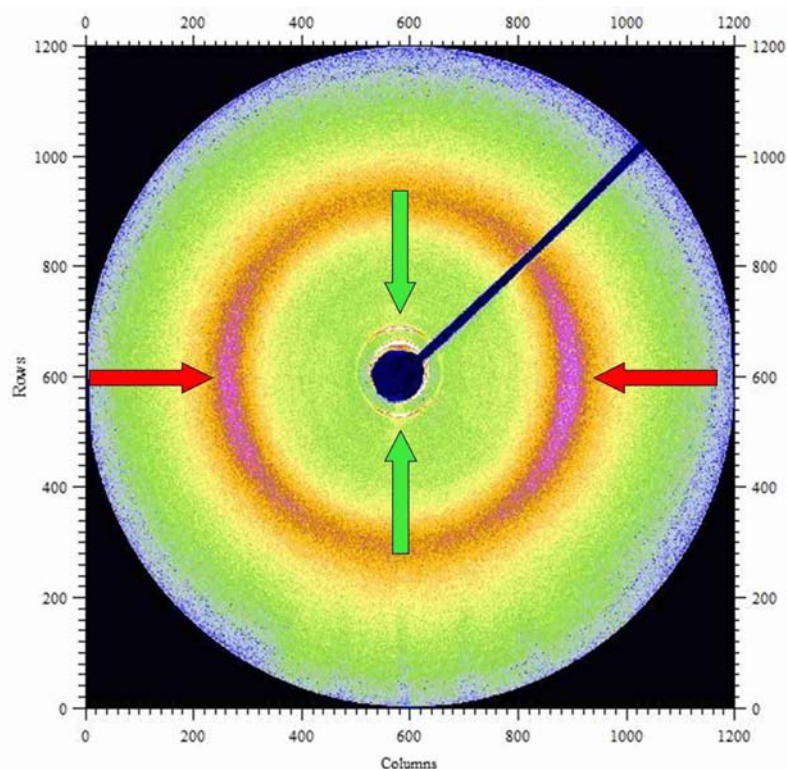


Figure 3.7: Diffractogram from a lamellar phase with $\phi_{lip} \approx 0.30$ showing simultaneously the SAXS and WAXS regions. The distribution of scattered intensities, indicated by red and green arrows, shows the perpendicularity between the corresponding structures in the direct space.

together with a high number of correlated layers, would be able to favor the appearance of more stable structures, allowing the coalescence of larger vesicles. On the other side, for strongly fluctuating membranes, there is no sufficient stability to keep the self-assembly of large structures.

In fig. 3.12, the replicas are exhibited in more detail. Fractures occurred parallel to the planes of membranes. Large defect-free terraces can be visualized providing spectacular pictures of the layered structures. For very concentrated samples, fig. 3.12(a), hundreds of correlated layers are observed. On the other hand, for diluted formulations, only few layers appear to be correlated. Furthermore, it is possible to see few corrugations on the borders of fractures (see fig. 3.12(c)). These findings are consistent with X-rays observations for which it was found a widening of Bragg peaks for hydrated samples.

In fig. 3.13, high magnification pictures show perpendicular fractures of lamellae. Images were taken from a concentrated sample for which $\phi_{lip} = 0.752$. Again, hundreds of lamellae are observed as well as the high degree of order. In 3.13(a), it is possible to see dislocations and disclinations, typical defects in smectic-A liquid crystals (indicated by red arrows) [28]. Fourier image analysis (inset in Fig. 3.13(b)) reveals strong one-dimensional anisotropy with lamellar periodicity equal to 50 \AA , in excellent agreement with the X-rays measurement, $d = 49 \text{ \AA}$.

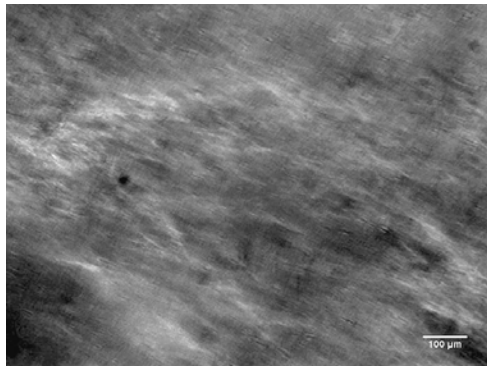
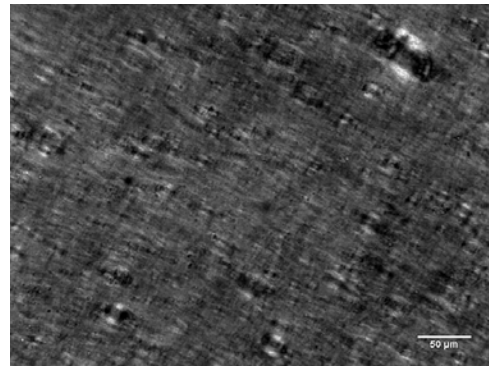
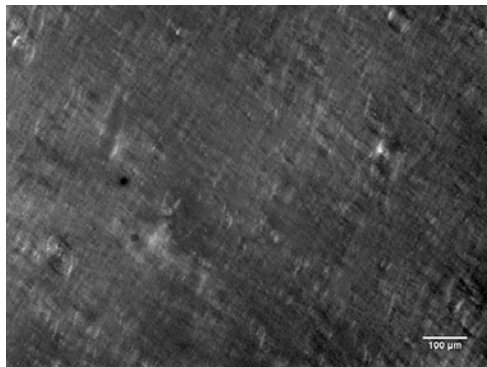
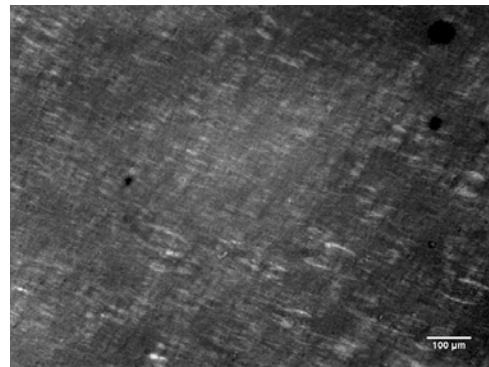
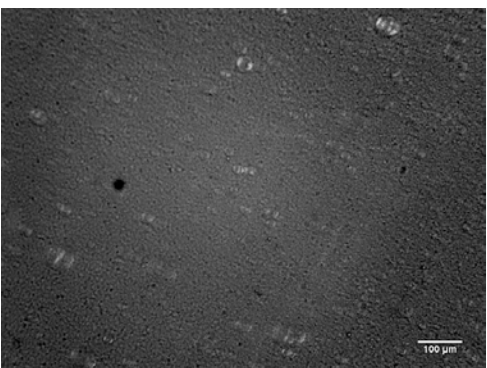
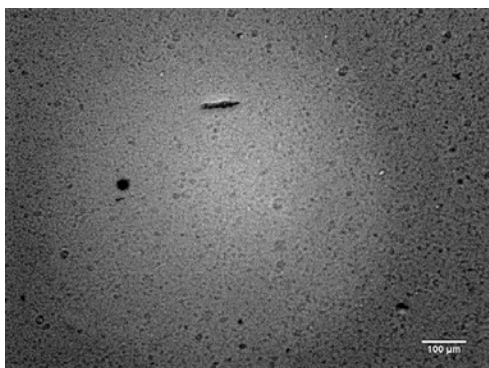
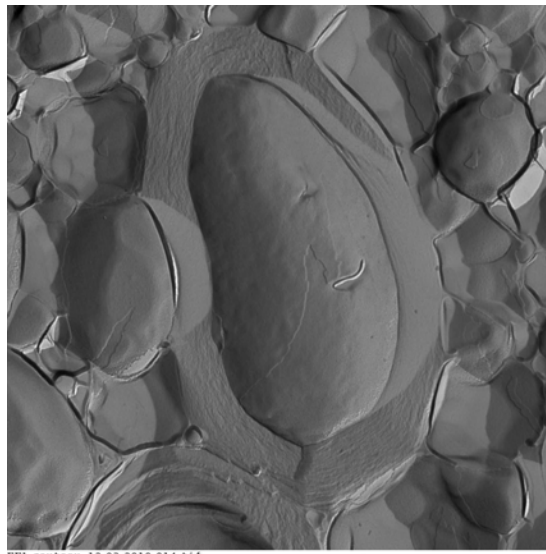
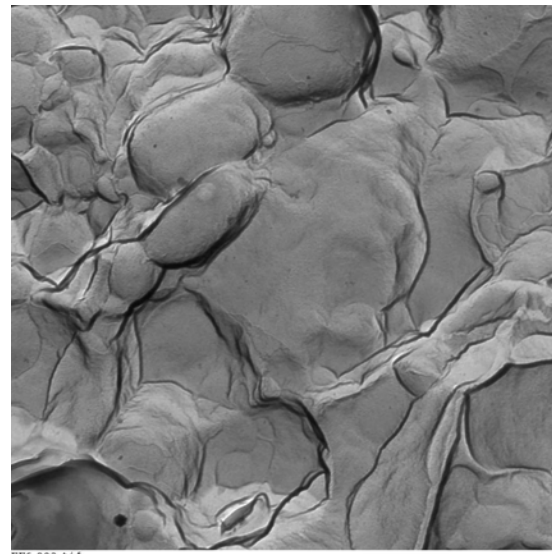
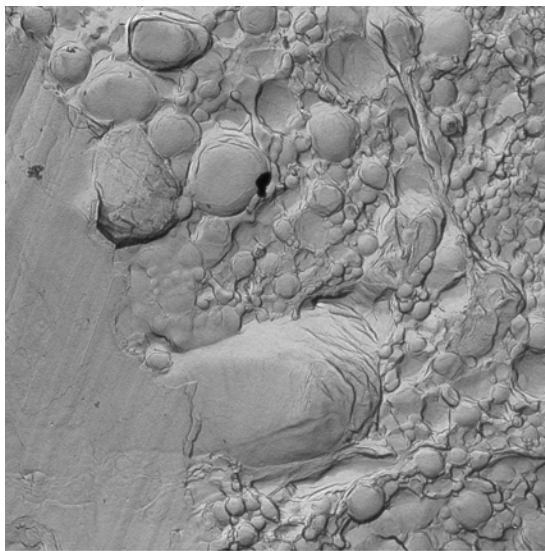
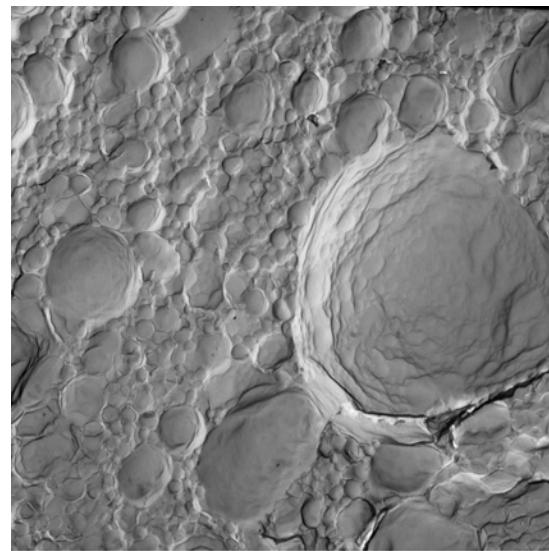
(a) $\phi_{lip} = 0.752$ (b) $\phi_{lip} = 0.650$ (c) $\phi_{lip} = 0.571$ (d) $\phi_{lip} = 0.500$ (e) $\phi_{lip} = 0.352$ (f) $\phi_{lip} = 0.252$

Figure 3.8: POM images from lipids/water mixtures with 70:30 PC-to-Simulsol ratio.

(a) $\phi_{lip} = 0.752$ (b) $\phi_{lip} = 0.604$ Figure 3.9: Replicas from concentrated samples observed at magnifications of 25000 \times and 30000 \times .(a) $\phi_{lip} = 0.500$ (b) $\phi_{lip} = 0.449$ Figure 3.10: Replicas from samples from the middle dilution domain observed at magnifications of 10000 \times .

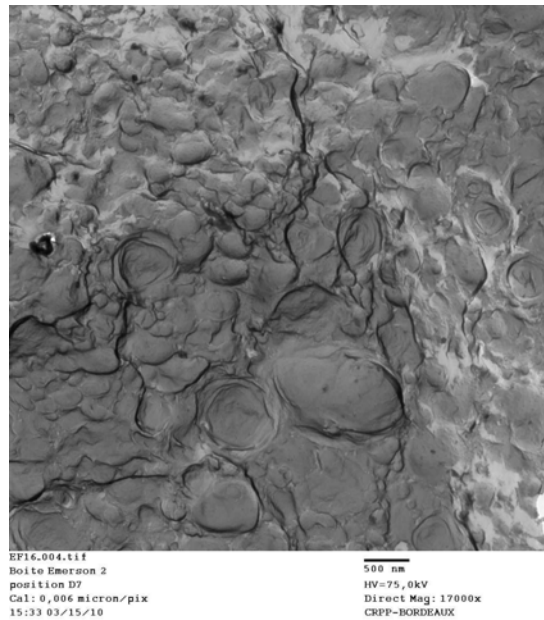


Figure 3.11: Replica from sample with $\phi_{lip} = 0.290$, beyond the hydration limit. Observation was made at a magnification of $17000\times$.

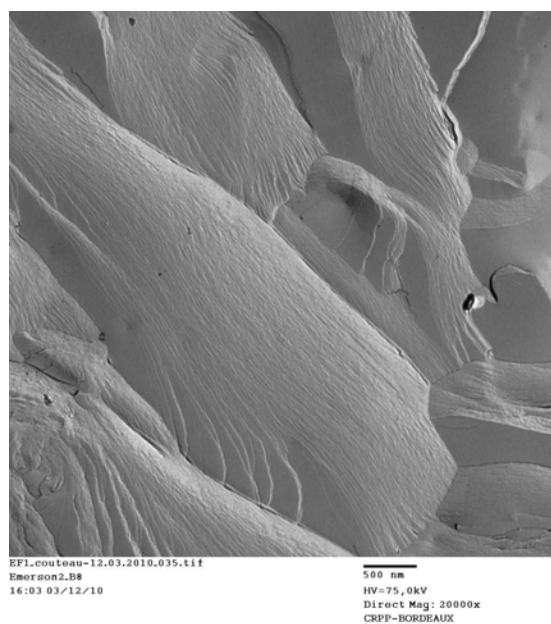
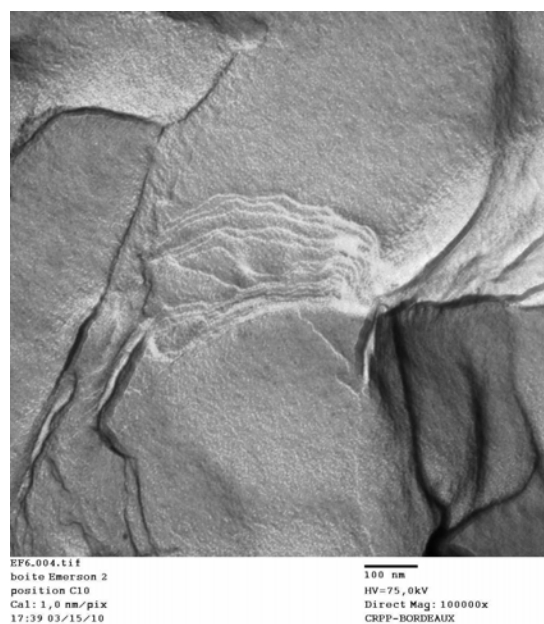
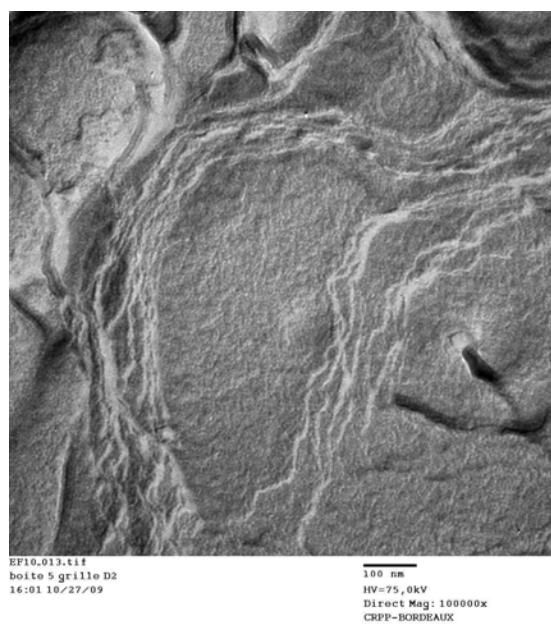
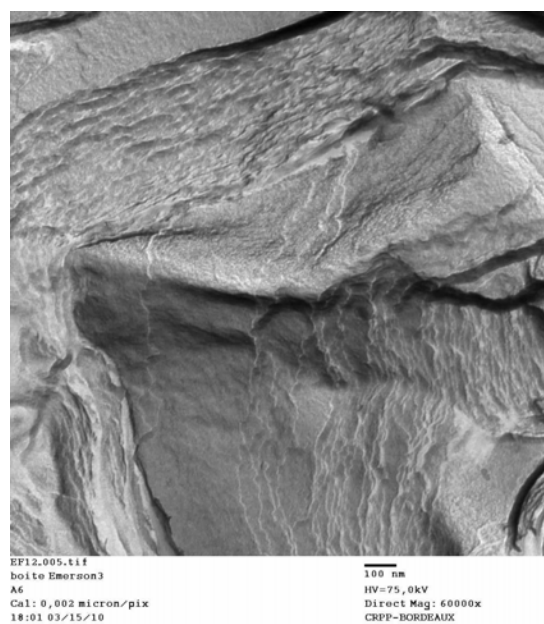
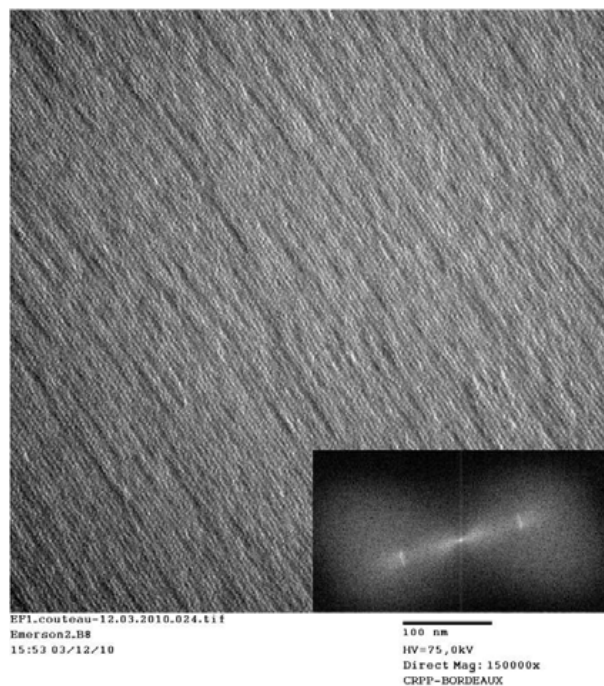
(a) $\phi_{lip} = 0.752$ (b) $\phi_{lip} = 0.604$ (c) $\phi_{lip} = 0.500$ (d) $\phi_{lip} = 0.449$

Figure 3.12: TEM replicas from binary lipids-water mixtures observed at magnifications between $20000\times$ and $100000\times$. The appearance of large free-defect terraces visually attested the lamellar behavior of the host phases. It should be noted the large difference on the smectic ordering between concentrated and diluted samples.



(a)



(b)

Figure 3.13: Perpendicular fractures of lamellae $\phi_{lip} = 0.752$. (a) Arrows indicate dislocations and disclinations, typical smectic-A defects. (b) Fourier image analysis reveals strong 1-D anisotropy with repetition distance $d = 50 \text{ \AA}$, in excellent agreement with 49 \AA from X-rays data.

Effects of salt addition

Two series of samples were prepared using brine solutions and pure water as solvent. The salt used in brine solutions was ammonium acetate at 0.25 M. The resulting behavior of the lamellar periodicities, as a function of the inverse lipid volume fraction, is shown in Fig. 3.14. No noticeable distinctions are observed between data from salt-containing or salt-free formulations.

Again, two domains are found. One of them is clearly governed by a swelling law, whose analysis leads to membrane thickness $\delta_m = 36.0(3) \text{ \AA}$ and dilution limit $D_{max.} = 89.3(6.5) \text{ \AA}$. These values are very close to the one found before.

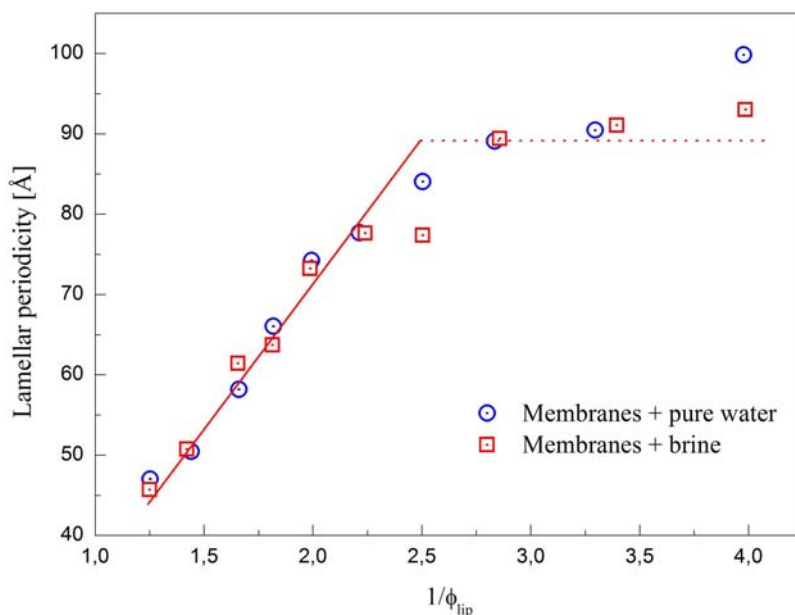


Figure 3.14: Lamellar periodicity as a function of $1/\phi_{lip}$ for salt-containing and salt-free host phases. The straight lines correspond to a linear fit with slope $\delta_m = 36.0(3) \text{ \AA}$ and a dilution limit $D_{max} = 89.3(6.5) \text{ \AA}$.

The study of the Bragg positions is useful to get information on the swelling properties of the lamellar phases as well as to determine the thickness of membranes and the dilution limit of the system. However, a more detailed analysis of the diffuse scattering, that is, of the intensities situated out from Bragg maxima, also reveals other interesting characteristics either at molecular or at supramolecular scales. Among the variables relevant for the studies conducted here, one can outline the smectic ordering given by the parameter of Caillé. This parameter is convoluted in the midst of the structure factor of the X-rays diffractograms. The model of Nallet et al., presented in sec. 1.6.1, is a suitable tool which allows to address this kind of investigation. Such procedure, combined with other frameworks available in the literature [18, 132], brings valuable insights on the intermolecular forces involved on the stabilization of the host phase being, thus, a first step to treat the question of which mechanisms are relevant for the complexation between DNA and neutral lipids complexes.

Following the above-described guidelines, diffractograms from DNA-free lipid phases

were fitted according to the model of Nallet et al. In order to assess any changes introduced by the screening of electrostatic interactions, curves obtained from salt-containing preparations were also fitted with this model.

For the reasons detailed in sec.2.3.3, the analysis started by fitting only the form factor $P(q)$ to the large wave vector region ($q > 0.20 \text{ \AA}^{-1}$) of a diluted sample. The fits were performed with four free parameters: a scaling factor, $A_0 = \frac{8\pi}{d} \Delta\rho_H^2$, the length of polar headgroups, δ_H , the length of carbonic tails, δ_T , and the ratio between electronic contrasts of tails and heads, $\Delta\rho_T/\Delta\rho_H$. In order to take into account background effects that may remain even after empty capillary and solvent scattering corrections, a second-order polynomial of form $BG + BG1 \times q + BG2 \times q^2$ was added to $P(q)$. Since $S(q) \rightarrow 1$ for $q \gg q_0$, it was assumed that the structure factor reaches its asymptotic value when $q > 0.2 \text{ \AA}^{-1}$. The resulting plots are presented side-by-side in Fig. 3.15.

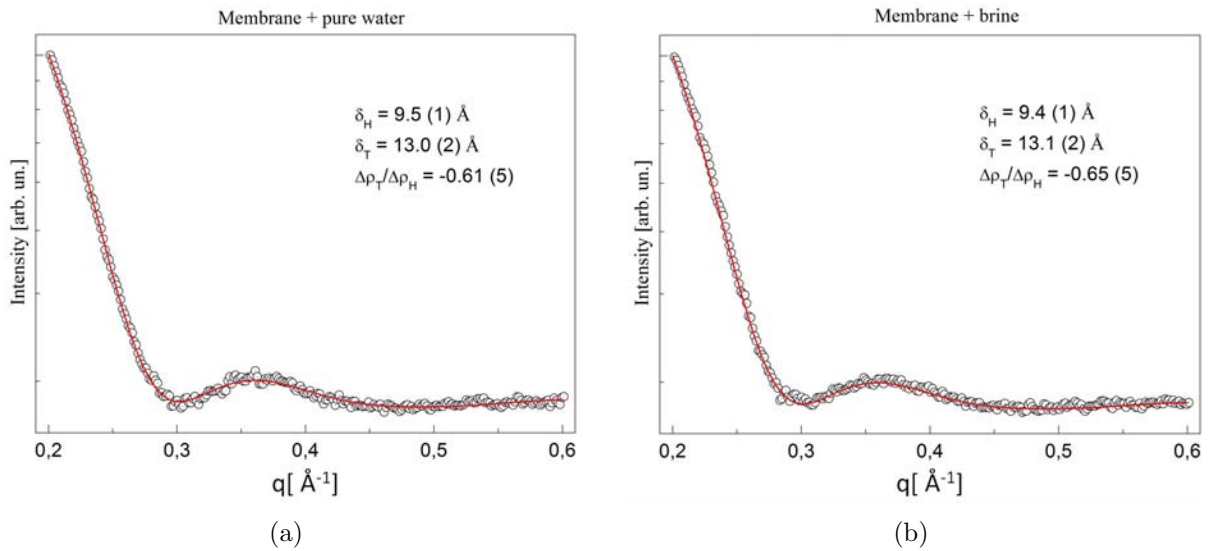


Figure 3.15: Diluted samples, both with $\phi_{lip} = 0.251$, fitted only with the form factor $P(q)$ (Eq. 1.23). The fitting parameters are the length of polar headgroups, δ_H , the length of carbonic tails, δ_T , and the ratio between the electronic contrasts of tails and heads, respectively.

No noticeable differences between salt-containing and salt-free preparations are observed. The lengths of polar headgroups and hydrophobic tails are, respectively, around $\delta_H \approx 9.5 \text{ \AA}$ and $\delta_T \approx 13.0 \text{ \AA}$ for both cases, with very small deviations. The ratio between the electronic contrasts, $\Delta\rho_T/\Delta\rho_H$, presents a more robust change upon salt addition that presumably result from the presence of salt in the water channels. Nevertheless, such variation occurs within the uncertainty range.

In the following, the obtained parameters δ_H , δ_T and $\Delta\rho_T/\Delta\rho_H$ were used as initial values for the full-range fitting, including the structure factor $S(q)$. Since important changes on the size of molecules are not expected upon dehydration, δ_H and δ_T were constrained in the range of $\pm 1 \text{ \AA}$ around the values exhibited in Fig. 3.15. On the other hand, appreciable variations on the electronic contrasts may occur for different dilutions due to variations in lipids concentration. Thus, the parameter $\Delta\rho_T/\Delta\rho_H$ was left free,

noting only that it should necessarily be negative. The scaling constant A_0 , was also left free in order to contemplate the modifications of the lamellar periodicity and $\Delta\rho_H$. In order to estimate the number of correlated layers, the following values for N were systematically tested: 3, 4, 5, 6, 7, 8, 9, 10, 12, 15, 20, 25, 30, 35, 40, 50, 60, 75 and 100.

The obtained parameters are summarized in table 3.1. The plots resulting from the full-range fits are shown in figs. 3.16–3.18. Again, no significant differences between salt-containing and salt-free preparations are found. This behavior points to the fact that direct electrostatic interactions do not play a major role on the stabilization of the lamellar phases, in agreement with the expectations for complexes entirely based upon neutral lipids.

The thickness of bilayers, extracted from the average of $2(\delta_H + \delta_T)$ on table 3.1, is found to be $\delta'_m = 44.9(7)$ Å. This value is $\approx 25\%$ higher than the “geometric” thickness obtained before from the swelling law, namely $\delta_m = 36.5$ Å. This discrepancy is often reported for membranes, especially in their fluid state (where molecules also oscillate along z-direction), because there are several ways to define the bilayer thickness [134]. The value of δ_m derived before is the so-called *Luzzati thickness* which is relevant for the determination of the water amount in membranes [135]. On the other hand, the value of δ'_m extracted from the electron density profiles corresponds to the so-called *steric thickness* and is defined as the maximum distance between two headgroups in the opposite monolayers of a membrane. Careful discussions on such definitions have been conducted by McIntosh [136] and Nagle and Tristram-Nagle [135]. In any case, both the Luzzati and steric thicknesses found here are in close agreement with values reported in literature for fully-hydrated membranes formed from lecithins [134, 137, 138].

The parameter of Caillé as a function of the smectic periodicity is presented in Fig. 3.19. The close similarity between the two series of data is now immediately clear. As discussed previously, η is an index of ordering on lamellar phases and its behavior upon intermembrane spacing is well known to be dependent on the origin of the repulsive interactions preventing the collapse of membranes by van der Waals forces. When unscreened electrostatics dominates this interplay, η is given by [34, 94]:

$$\eta_{elec} = \sqrt{\frac{\pi k_B T L_B (d - \delta_m)^3}{2\kappa d^4}} \quad (3.1)$$

where L_B is the Bjerrum length of the solvent (≈ 7 Å for water) and κ the bilayer bending modulus.

When the system is dominated by the entropically-driven mechanism of undulations interactions, η follows Helfrich’s universal prediction [42, 49, 92]:

$$\eta_{helf} = 1.33 \left(1 - \frac{\delta_m}{d}\right)^2 \quad (3.2)$$

The solid lines in fig. 3.19 correspond to the predictions from equations 3.1 and 3.2.

Table 3.1: Parameters obtained from the fit of the model of Nallet et al. to X-rays data showed in Figs. 3.16-3.18. Formulations marked with a * correspond to salt-containing samples.

ϕ_{lip}	d [Å]	δ_H [Å]	δ_T [Å]	$-\Delta\rho_H/\Delta\rho_T$	N	η
0.799	47.0(1)	10.2(1)	12.4(2)	-0.25(5)	100	0.02(1)
0.800*	45.7(1)	9.8(1)	13.7(2)	-0.42(5)	100	0.05(1)
0.694	50.5(1)	10.5(1)	12.8(2)	-0.22(5)	50	0.06(1)
0.703*	50.8(1)	10.0(1)	11.5(2)	-0.32(5)	60	0.03(1)
0.602	58.2(1)	9.4(1)	13.1(2)	-0.33(5)	10	0.18(2)
0.604*	61.4(1)	9.3(1)	13.2(2)	-0.31(5)	12	0.13(2)
0.550	66.1(1)	9.7(1)	12.2(2)	-0.39(5)	15	0.13(2)
0.551*	63.7(1)	9.4(1)	12.9(2)	-0.36(5)	12	0.12(2)
0.502	74.3(1)	9.7(1)	13.0(2)	-0.39(5)	12	0.14(2)
0.503*	73.2(1)	9.6(1)	13.3(2)	-0.39(5)	12	0.14(2)
0.452	77.7(1)	9.9(1)	11.6(2)	-0.37(5)	10	0.28(3)
0.447*	77.7(1)	9.6(1)	13.4(2)	-0.38(5)	5	0.18(2)
0.399	84.1(1)	9.8(1)	12.4(2)	-0.41(5)	10	0.22(2)
0.399*	77.4(1)	9.9(1)	12.9(2)	-0.39(5)	6	0.14(2)
0.353	89.1(1)	9.9(1)	12.4(2)	-0.42(5)	5	0.28(3)
0.350*	89.4(1)	9.8(1)	12.5(2)	-0.41(5)	5	0.25(3)
0.303	90.5(1)	10.0(1)	12.1(2)	-0.44(5)	5	0.30(3)
0.295*	91.1(1)	9.8(1)	12.6(2)	-0.41(5)	3	0.29(3)
0.251	99.8(1)	9.8(1)	12.4(2)	-0.43(5)	3	0.54(5)
0.251*	93.0(1)	9.8(1)	12.6(2)	-0.41(5)	3	0.36(5)

For the electrostatic prediction, the parameter corresponding to the bending rigidity, κ , was left free to be fitted.

It is found that both models fail in adjusting the data. The inability of a theory based on electrostatics to explain the behavior of non-charged membranes is expected since there is no *strong* electrostatic repulsions between polar groups [49]. Moreover, the adjusted value of $\kappa = 0.36(12) k_B T$ is too small, around two orders of magnitude lower than typical values found for similar PC lipids referred to in literature [138, 139].

On the other side, undulation forces are presumably involved in the mechanism of stabilization of lyotropic lamellar phases formed from soft membranes [135]. Therefore, since eq. 3.2 is not able to describe the data, the repulsive interaction between adjacent bilayers cannot be understood in terms of a single interaction. In this case, we try a hybrid mechanism, combining steric and hydration forces together.

An approach proposed by Petrache et al. [132] has provided a such hybrid model and has been widely used elsewhere [140–142]. Here, this approach will be only partially developed because, from the point of view of this manuscript, we are interested in evidencing that repulsive intermembrane interactions are governed by a mixing of hydration and steric undulation forces. The determination of elastic parameters, scaling constants, etc., is beyond the scope of this work.

According to the Petrache’s proposition, the parameter of Caillé can be expressed in

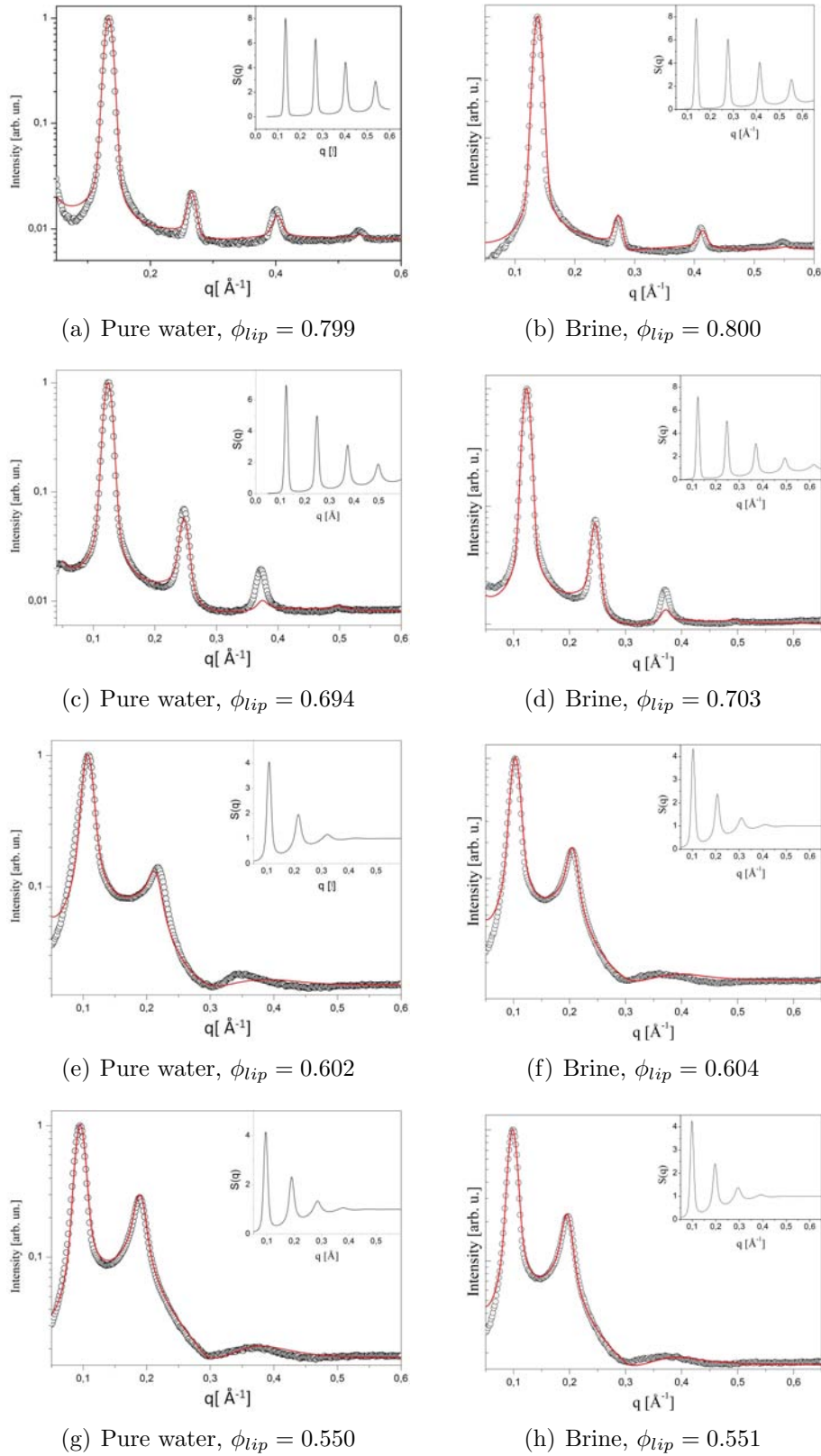


Figure 3.16: Full-range X-rays scattering and structure factors (insets) from L_α phases fitted with the model of Nallet et al.

terms of the *mean square of amplitude fluctuations*, σ^2 , through the relationship:

$$\sigma^2 = \eta \frac{d^2}{\pi^2} \quad (3.3)$$

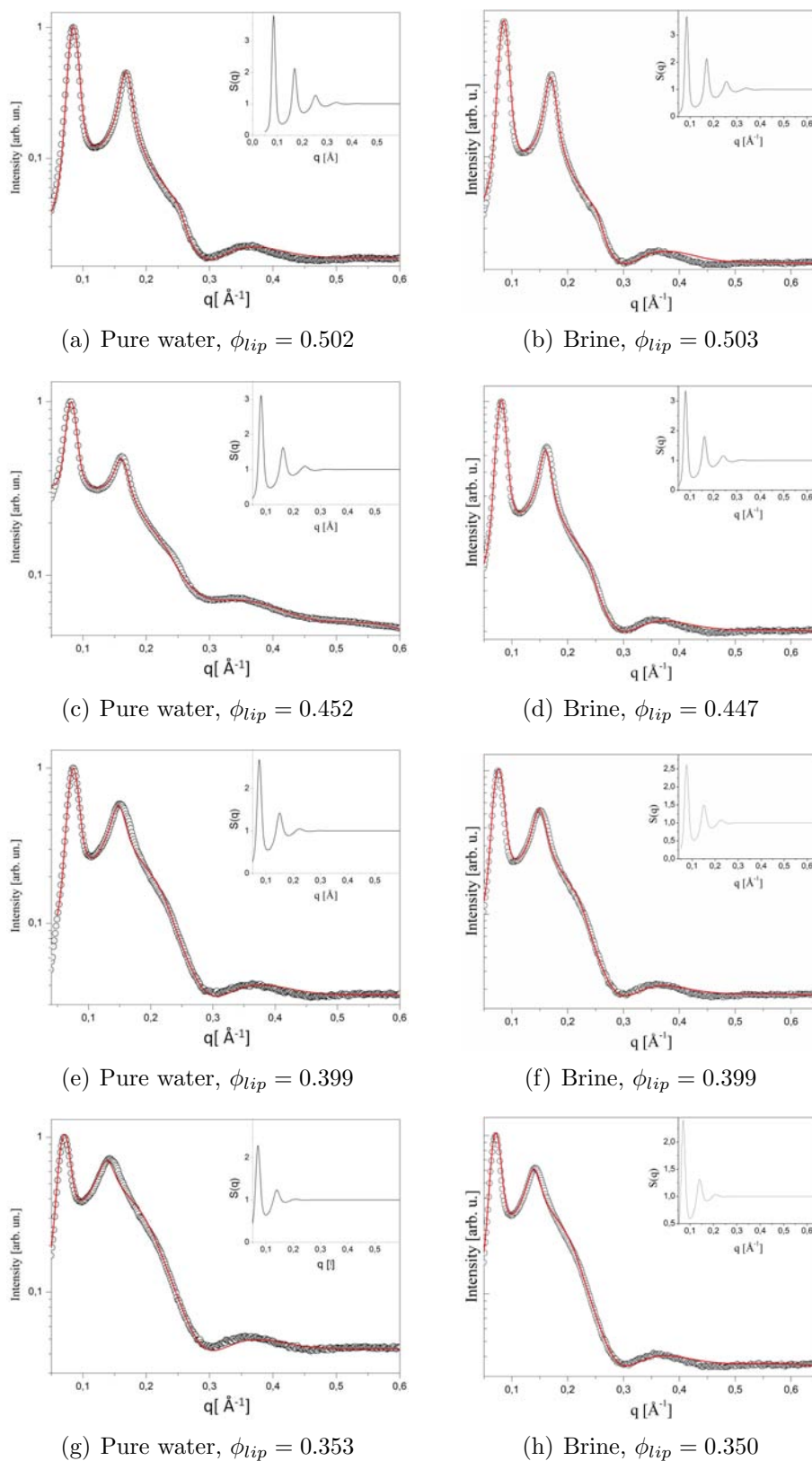


Figure 3.17: Full-range X-rays scattering and structure factors (insets) from L_α phases fitted with the model of Nallet et al.

Still according to the Petrache's approach, when hydration forces appear mixed with undulation interactions, the free energy associated to fluctuations themselves is given by [132, 133]:

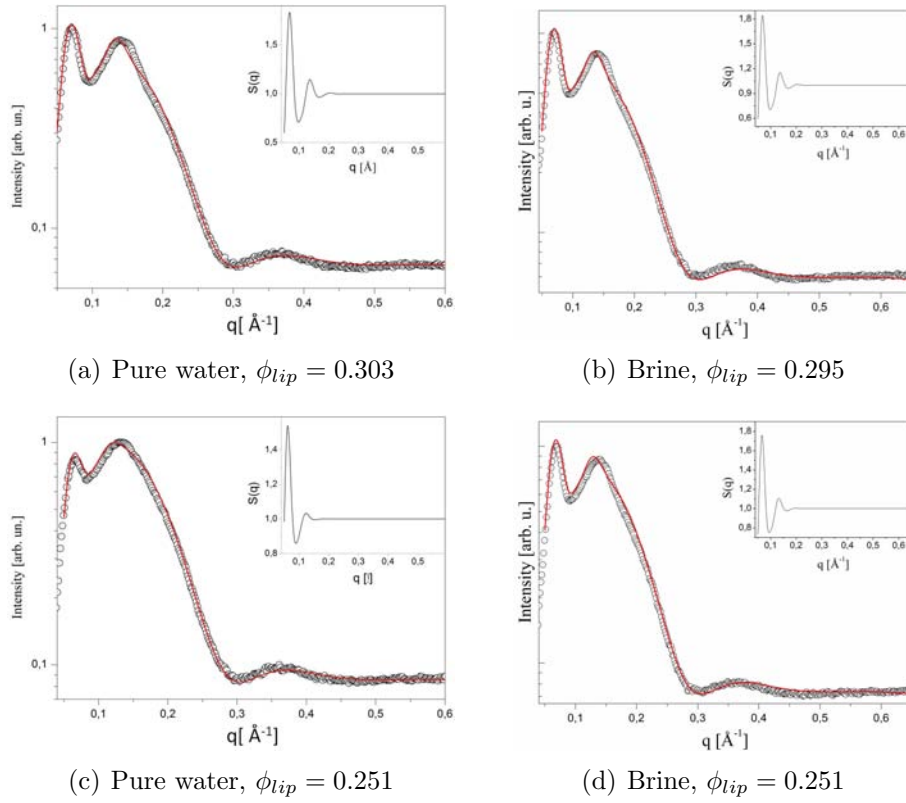


Figure 3.18: Full-range X-rays scattering and structure factors (insets) from L_α phases fitted with the model of Nallet et al.

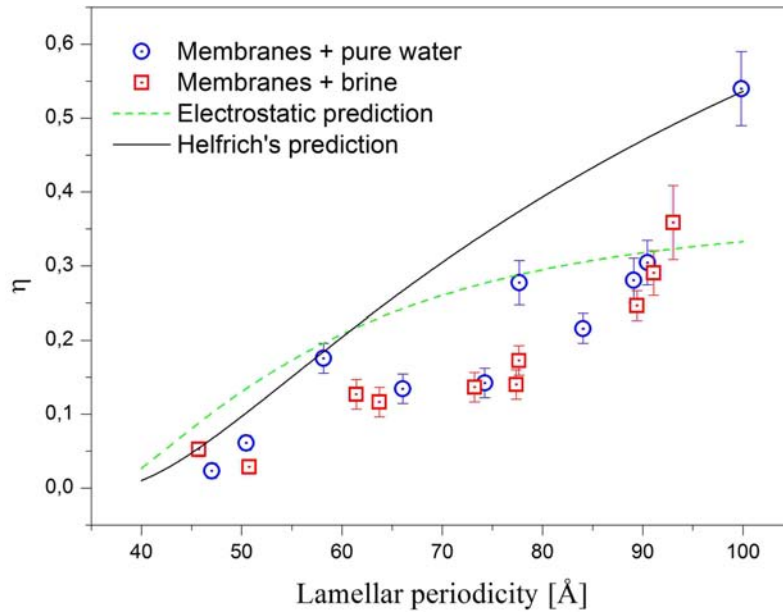


Figure 3.19: Behavior of η for both, salt-containing and salt-free, series. The universality of the smectic ordering is clear even upon significant ionic strength variations. Dotted and dashed lines correspond to Helfrich's and unscreened electrostatic predictions, see equations 3.2 and 3.1. For the electrostatic model, the fitted rigidity constant, κ , is found to be $0.36(12) k_B T$, an unreasonably small value.

$$F_{fl} = \left(\frac{k_B T}{2\pi} \right)^2 \frac{1}{\kappa} A_{fl} \exp \left(-\frac{d'_w}{\lambda_{fl}} \right) \quad (3.4)$$

where λ_{fl} is the decay length of interaction and A_{fl} is the inverse square amplitude of undulations. The water spacing, d'_w , is obtained by subtracting the steric thickness, δ'_m , from the smectic periodicity.

On the other hand, it is also possible to connect the fluctuational free energy to σ^2 :

$$F_{fl} = \left(\frac{k_B T}{2\pi} \right)^2 \frac{1}{K_c} \sigma^{-2} \quad (3.5)$$

Comparing eqs. 3.4 and 3.5, it is easy to obtain a direct relationship for σ^{-2} as a function of (d'_w) :

$$\sigma^{-2}(d'_w) = A_{fl} \exp\left(-\frac{d'_w}{\lambda_{fl}}\right) \quad (3.6)$$

The plot of σ^{-2} versus d'_w is presented in fig. 3.20 on logarithmic scale. Apart from data for small intermembrane separations, $d'_w \lesssim 13 \text{ \AA}$, σ^{-2} behaves according to an exponential decay law agreeing with the above-derived expectation. The solid line corresponds to the fit of 3.6 to the data with the following values for the parameters: $\lambda_{fl} = 16.3(1.2)\text{\AA}$ and $A_{fl} = 0.06(1) \text{ \AA}^{-2}$. This result for λ_{fl} is around three times higher than typical values available in the literature for pure DMPC, EPC, DPPC and DOPC [132–134,139]. In turn, the value of A_{fl} is one order of magnitude lower than the typical ones. Such differences are consistent with the addition of Simulsol to soya-lecithin membranes, suggesting that the introduction of ethoxylated fatty acids softens the formed bilayers and increases the range of the fluctuation forces.

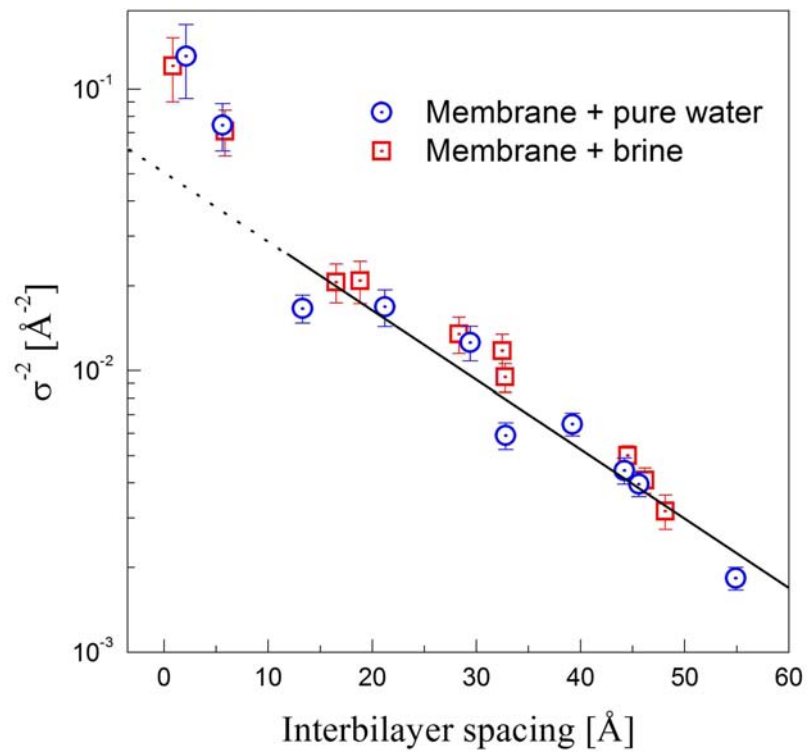


Figure 3.20: Plot of σ^{-2} in function of the separation between membranes, defined as $d'_w = d - \delta'_m$. The solid line is the fit of eq. 3.6 to data with the following parameters: $\lambda_{fl} = 16.3(1.2)$ Å and $A_{fl} = 0.06(1)$ Å⁻².

3.1.2 Membranes with 50:50 PC-to-Simulsol ratio

The addition of ethoxylated fatty acids to lecithin presumably changes the elastic properties of the formed membranes [16, 86]. To verify such effects, a second membrane composition, prepared from the mixing of PC and Simulsol at 50:50 ratio, was investigated. Samples were prepared with lipid concentrations ranging from $\phi_{lip} = 0.159$ to $\phi_{lip} = 0.797$. In order to evaluate in this case also the role of the ionic strength, some formulations were hydrated with ammonium acetate solutions, in the same fashion as for the studies conducted in Sec. 3.1.1. The behavior of the lamellar periodicity as a function of the inversed lipid volume fraction is shown in Fig. 3.21.

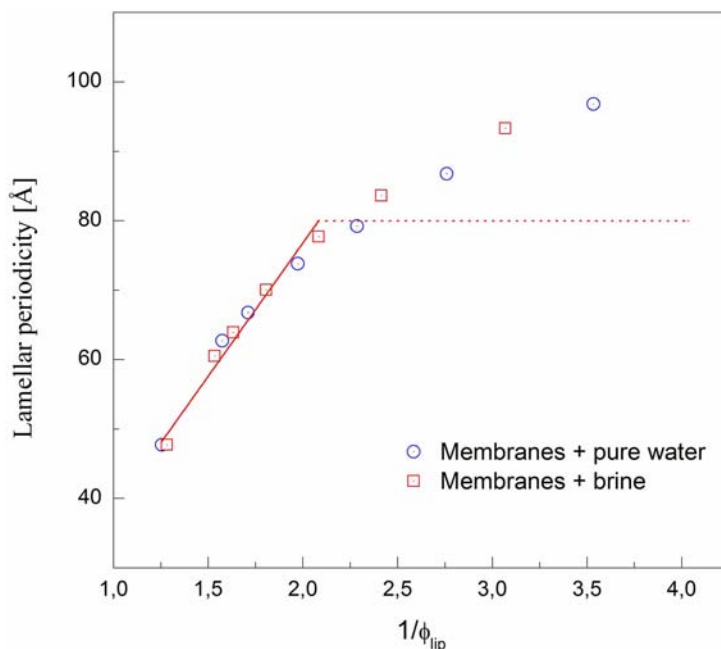


Figure 3.21: Lamellar periodicity as a function of $1/\phi_{lip}$ for membranes with 50:50 PC-to-Simulsol ratio. The dotted red line is a guide for the eyes representing a rough boundary of the swelling law regime. The solid red line is a linear fit which gives $\delta_m = 38.4(6)$ Å.

Similarly to the behavior observed for the previous membrane composition, there is no noticeable differences between salt-containing and salt-free samples. Again, two distinct regimes can be identified: the first one, with repetition distances ranging from $d \approx 45$ Å up to $d \approx 80$ Å, is driven by an usual dilution law. The slope of the data in this domain leads to the value of $\delta_m = 38.4(6)$ Å. It should be noted that this value is ≈ 2 Å higher than the one found for bilayers with 70:30 PC-to-Simulsol ratio. A possible reason for this observation is the increase in the proportion of surfactants containing 18 carbons in their tails, which probably gives rise to an expansion of the hydrophobic core of bilayers. On the other hand, the second regime, found when $d > 80$ Å, differs from the one observed previously. Here, the smectic periodicities do not reach a saturation value and the dilution limit is not clearly discerned.

Complementary observations with polarizing microscopy reveal the presence of solvent droplets when the lipid volume fraction is lower than 0.480. For samples above this lipid

concentration, it appears the classical birefringent textures expected for lamellar phases. Selected polarizing images from these formulations are exhibited in fig. 3.22, where the differences between textures of samples from the two domains are evidenced.

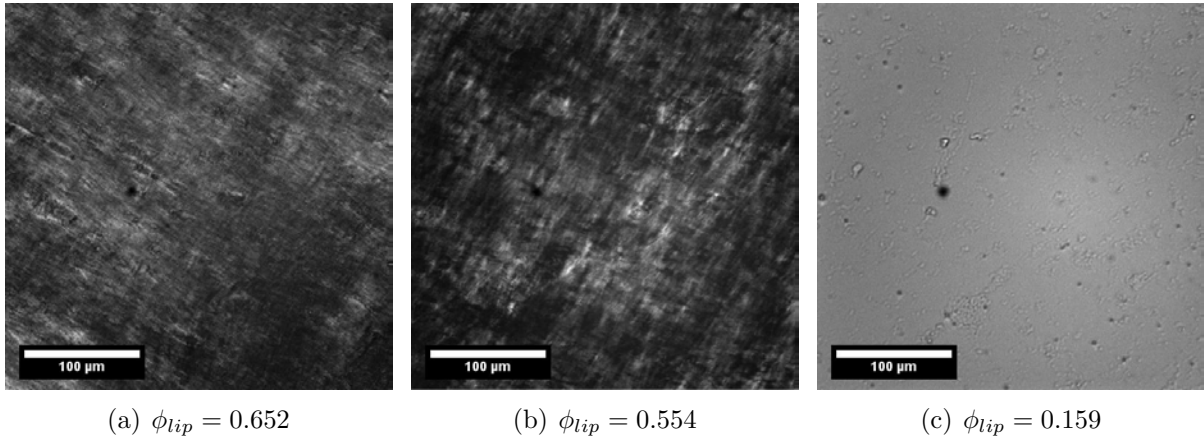


Figure 3.22: POM images from lipids/water mixtures with 50:50 PC-to-Simulsol ratio. Samples from the first domain, $\phi_{lip} \approx 0.50$, show birefringent textures, whereas in the second domain the presence of solvent droplets is observed.

Analyses using the model of Nallet et al. were also carried out for this membrane composition. The first step consisted in the fit of the form factor $P(q)$ to the large wave vector region of a diluted sample. In fig. 3.23, the plots arising from this preliminary procedure are shown. Comparing these results to those obtained with the other bilayers, see fig. 3.15, only small changes are noticed for δ_H , δ_T and $\Delta\rho_T/\Delta\rho_H$.

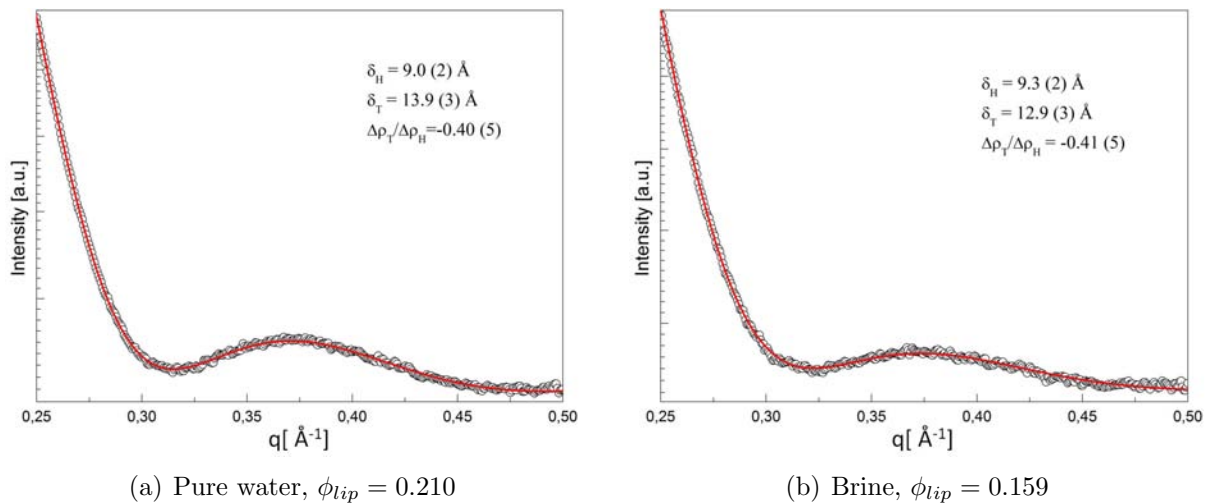


Figure 3.23: Diluted samples prepared from lamellae with 50:50 PC-to-Simulsol ratio. Red lines are fits to the form factor $P(q)$, eq. 1.23.

The parameters obtained for the large angle region were used as initial values for full-range fits, including the structure factor $S(q)$. The values obtained for d , δ_H , δ_T , $\Delta\rho_H/\Delta\rho_T$, N and η are summarized in table 3.2. The plots of the data, together with the respective fits, are shown in Figs. 3.24 and 3.25¹.

Table 3.2: Parameters obtained from the fit of the model of Nallet et al. to X-rays data from lamellar phases prepared with 50:50 PC-to-Simulsol ratio. Salt-containing samples are marked with a *. When a — appears, it means that the respective spectrum was fitted only to the form factor, Eq. 1.23.

ϕ_{lip}	d [Å]	δ_H [Å]	δ_T [Å]	$-\Delta\rho_H/\Delta\rho_T$	N	η
0.797	47.7(2)	10.0(2)	10.5(3)	-0.20(5)	100	0.03(3)
0.780*	47.7(2)	10.0(2)	9.7(3)	-0.20(5)	100	0,03(3)
0.652*	60.5(2)	9.0(2)	13.4(3)	-0.29(5)	35	0,12(3)
0.635	62.7(2)	9.0(2)	12.4(3)	-0.39(5)	75	0,14(3)
0.613*	63.9(2)	9.3(2)	13.3(3)	-0.33(5)	35	0,10(3)
0.585	66.(2)	9.3(2)	12.8(3)	-0.32(5)	75	0.11(3)
0.554*	70.0(2)	9.2(2)	13.0(3)	-0.33(5)	30	0.11(3)
0.507	73.(2)	9.2(2)	12.9(3)	-0.35(5)	75	0.15(3)
0.480*	77.7(2)	9.4(2)	12.6(3)	-0.38(5)	30	0.17(3)
0.437	79.2(2)	9.2(2)	13.2(3)	-0.37(5)	15	0.19(3)
0.414*	83.6(2)	9.7(2)	11.8(3)	-0.40(5)	30	0.23(4)
0.362	86.8(2)	9.4(2)	13.6(3)	-0.43(5)	15	0.31(4)
0.326*	93.3(3)	9.2(2)	13.1(3)	-0.39(5)	25	0.62(5)
0.283	96.8(3)	9.2(2)	13.9(3)	-0.41(5)	3	0.62(5)
0.261*	—	9.3(2)	12.9(3)	-0.40(5)	—	—
0.210	—	9.0(2)	13.9(3)	-0.40(5)	—	—
0.159*	—	9.3(2)	12.9(3)	-0.41(5)	—	—

The comparison of the parameters presented in table 3.2 with the one exhibited in table 3.1 shows only small differences between data with the two compositions. The ratio between electronic contrasts, for instance, remains around -0.35 . The average steric thickness, obtained from $2(\delta_H + \delta_T)$, is found to be $\delta'_m = 44.1(4)$ Å, in close agreement with the previous value. A significant exception is related to the behavior of the Caillé parameter for very hydrated formulations: for separations above ≈ 87 Å, one notices a sudden increase in η , which leads to the *quasi* complete disappearance of the structure factor features, as observed in Figs. 3.25(g) and 3.25(h). The behavior of the Caillé parameter as a function of the lamellar periodicity is presented in Fig. 3.26.

The lines in 3.26 are fits according to Eqs. 3.1 and 3.2. Similarly to the behavior observed in Fig. 3.19, both the electrostatic and the purely Helfrich's models fail in adjusting the data. Performing the analysis in the context of the Petrache's approach presented in Sec. 3.1.1, one obtains the behavior of σ^{-2} vs. d'_w exhibited in Fig. 3.27.

Unlike the behavior for bilayers containing 70% of lecithins, here σ^{-2} does not follow an exponential decaying law throughout the full range of intermembrane separations (dotted black line). Eq. 3.6 is able to adjust the data only in the range of d'_w situated between ≈ 15 Å and ≈ 40 Å (solid red line). These findings agree with the change in the slope of the dilution law, fig. 3.21, which is a sign that the membranes are affected.

The parameters resulting from the fit of eq. 3.6 lead to values of $\lambda_{fl} = 16.9(1.3)$

1. The fits exhibited in figs. 3.24 and 3.25 were carried out with the invaluable help of Barbara B. Gerbelli, MsC. student at IFUSP.

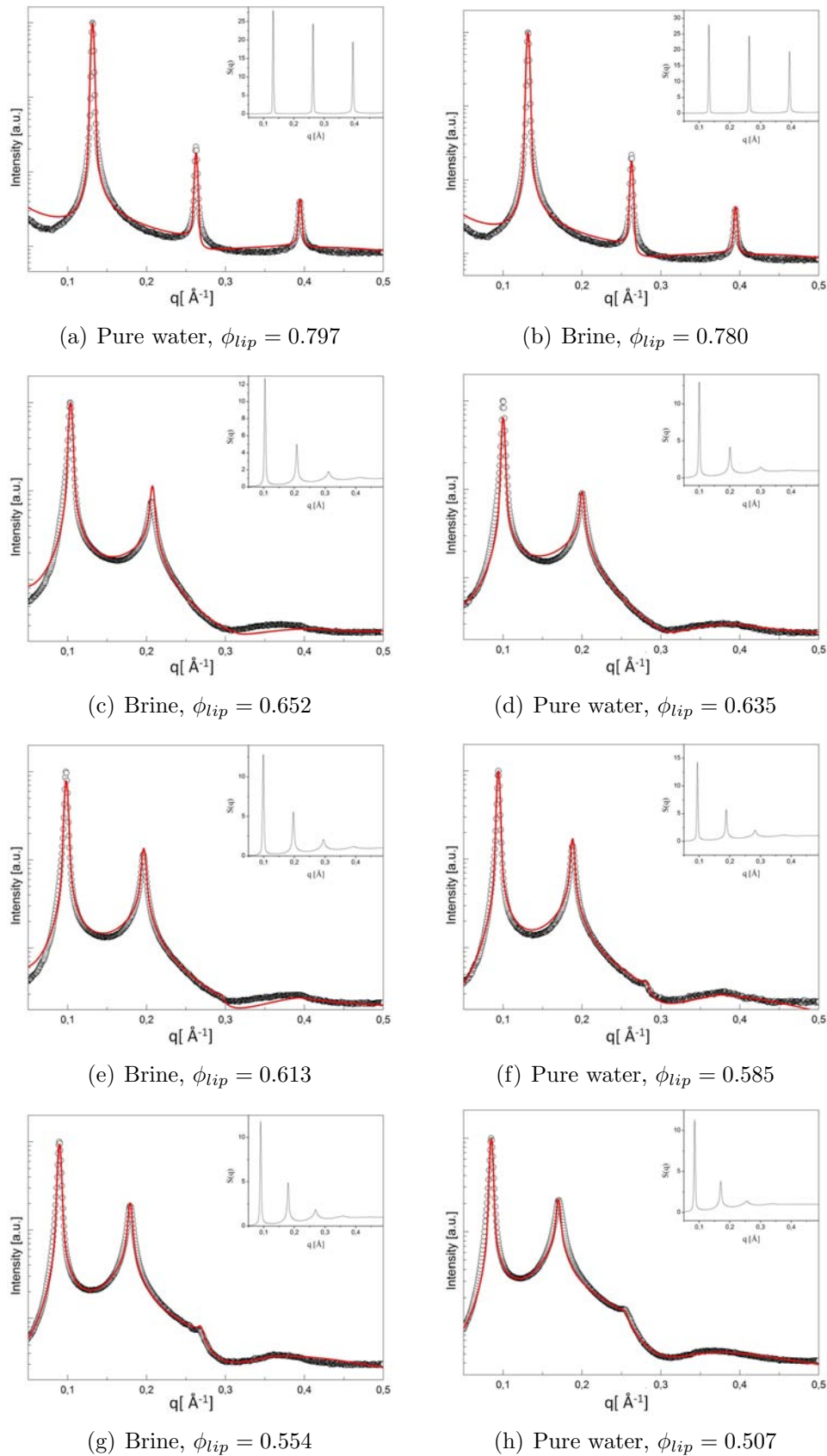


Figure 3.24: Full-range X-rays scattering and structure factors (insets) from L_α phases fitted with the model of Nallet et al.

\AA and $A_{fl} = 0.07(1) \text{\AA}^{-2}$, very close to the values obtained for membranes with 70:30 PC-to-Simulsol ratio.

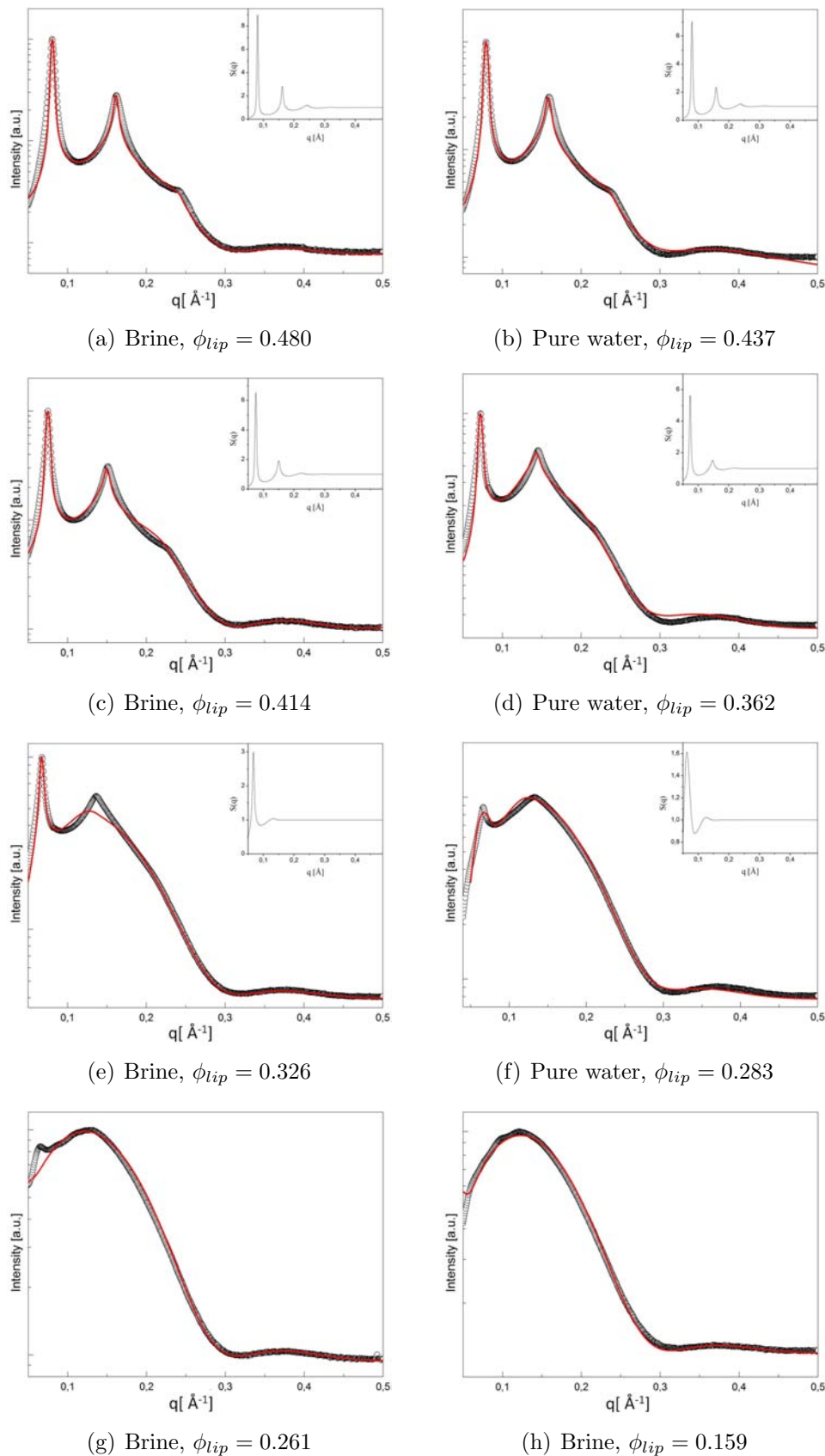


Figure 3.25: Full-range X-rays scattering and structure factors (insets) from L_α phases fitted with the model of Nallet et al.

The state of the carbonic tails of these membranes was also inspected by wide angle X-rays scattering. The diffuse broad peak, corresponding to the classical signature of chains

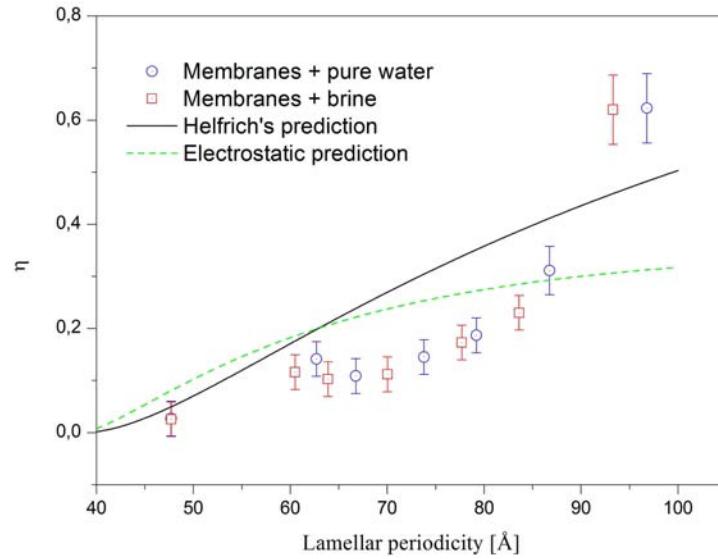


Figure 3.26: Behavior of η for both, salt-containing and salt-free, series. Dotted and dashed lines correspond to Helfrich's and unscreened electrostatic predictions, see equations 3.2 and 3.1. For the electrostatic model, the fitted rigidity constant, κ , is found to be $0.26(10) k_B T$.

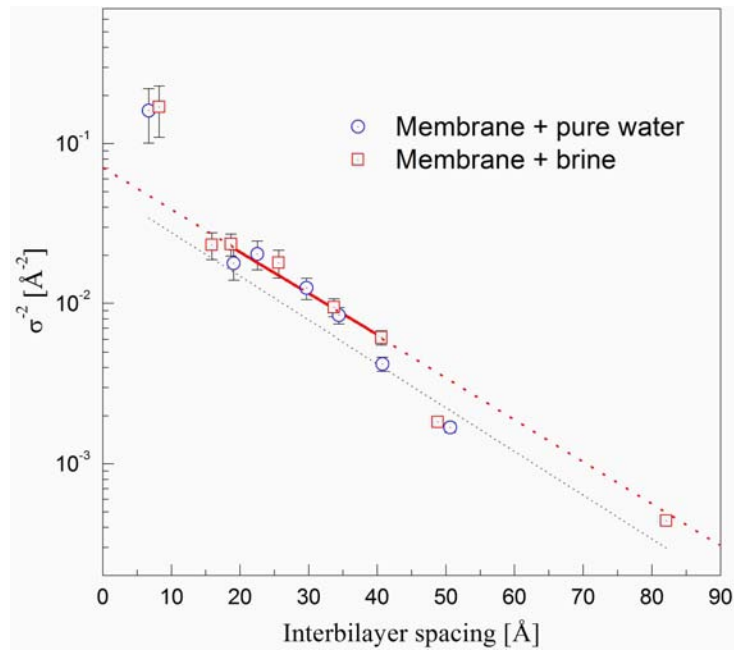


Figure 3.27: Plot of σ^{-2} as a function of d'_w , for membranes with 50 : 50 PC-to-Simulsol ratio. The solid red line is the fit of Eq. 3.6 to the linear region of data lying between $d'_w \approx 15 \text{ \AA}$ and $d'_w \approx 40 \text{ \AA}$. The red dotted line is an extrapolation of the linear fit. The obtained parameters are $\lambda_{fl} = 16.9(1.3) \text{ \AA}$ and $A_{fl} = 0.07(1) \text{ \AA}^{-2}$. The dotted black line is the fit of Eq. 3.6 to the full range of the data.

in their fluid state, was found for all formulations in the very same fashion as observed for samples with 70:30 PC-to-Simulsol ratio (see Fig. 3.6).

3.1.3 Discussion

From the above-described results, we can conclude that the host phases used in this work self-organizes into smectic arrays of stacked membranes across a large dilution domain. For both bilayer compositions, it is possible to obtain intermembrane spacings higher than 20 Å, presumably the minimal separation required for the introduction of DNA fragments. In addition, it is also observed that the swelling behavior follows a classical linear relationship between d and $1/\phi_{lip}$, at least within a certain range of the dilution domain. Therefore, by controlling the lipid concentration of the host phase, one can control the confinement exerted by the lamellar matrix over particles inserted in the water gaps.

The hydration limit is found to be around 92 Å, for bilayers with 70:30 PC-to-Simulsol whereas, for the other membrane composition, this limit can not be accurately determined. This finding evidences the changes introduced by the addition of ethoxylated fatty acids to lecithin membranes. In fact, the maximum periodicity in lamellar phases prepared from pure lecithins (EPC, DMPC or DPPC, for instance) is typically around 60 Å. Subtracting the usual values of membrane thicknesses, in such phases the maximum aqueous spacing remains around 24 Å [132–135]. This value is already close to the minimum spacing required to accommodate DNA rods and does not allow a convenient systematic study of the confinement over the supramolecular assembly of the hosted particles. Hence, in the context of this thesis, the addition of ethoxylated fatty acids to soya-lecithin is fundamental to enlarge the range of water spacings available for the nucleotides.

The analysis of the parameter of Caillé brought some informations about the intermembranar interactions. It revealed that the interactions preventing the bilayers from collapsing by the attractive van der Waals forces are not based on electrostatic repulsion. On the other hand, this same analysis showed that Helfrich's interactions are not the only repulsive forces between membranes. These findings show the need for a hybrid model to describe the balance of forces between bilayers. The Petrache's approach proved to be adequate for such analysis, showing that a mix between hydration and undulation forces is responsible for repulsive interactions within the lamellar phases. In addition, still according to this methodology, the decaying length of this hybrid force is $\lambda_{fl} \approx 17$ Å, a value around 3 times higher than those typically found for pure lecithins bilayers [134, 137, 138]. This is a quantitative measurement of the effect of Simulsol on the elastic properties of the membranes used here.

This hybrid regime, where the interactions are driven by a mix between hydration and Helfrich's forces, depends on the range of intermembranar separations. This statement is confirmed by the comparison between data from the two distinct compositions studied above. For both compositions, Eq. 3.6 does not describe the behavior of σ^{-2} at small separations (see Figs. 3.20 and 3.27). In this region, the interactions are dominated by short-range hydration forces and undulation interactions have a minor role in the system [3, 46]. On the other extremity, eq. 3.6 does not describe the behavior of σ^{-2}

for large membrane separations, when the lecithin amount is 50%. This observation can be interpreted as a direct consequence of the softening of the bilayers, caused by the introduction of ethoxylated fatty acids. Since the fluctuations become more relevant in softer systems, Helfrich interactions dominate the interplay for separations larger than 40 Å in the second case [42,92]. As it will be seen in next sections, the region of interest for incorporation of DNA to the lamellar phase is situated inside the separation range where the mix between hydration and Helfrich's forces drive the interactions.

3.2 DNA-lipids complexes: structural polymorphism

3.2.1 Membranes with 70:30 PC-to-Simulsol ratio

Dilution line $\rho = 3.1$

For samples prepared along the dilution line $\rho = 3.1$, the amount of water ranged from $\phi_{wt} = 0.156$ to $\phi_{wt} = 0.578$. Equivalently, these hydrations correspond to lipid volume fractions in the interval $0.318 < \phi_{lip} < 0.637$, covering the whole swelling domain. In Fig. 3.28, plots of $I(q)$ vs. q are shown for very diluted compositions where ϕ_{lip} varied from 0.318 to 0.379.

At the small and middle angle scattering regions, $0.040\text{\AA}^{-1} < q < 0.600\text{\AA}^{-1}$, several Bragg peaks arising from diffraction by smectic phases are found. For data obtained under synchrotron radiation (black and blue curves in 3.28), one can identify up to seven Bragg peaks. A set of four or five evenly-spaced reflections, indicated by stars in fig. 3.28, states the presence a long-range order structure in the complex. The repetition distances remain roughly constant upon hydration, oscillating around an average value of 77\AA .

In coexistence with this structure, it is found a second lamellar phase whose periodicities are lower compared to the first one. Similarly to the behavior of the first phase, the smectic periods remain approximately unchanged around an average value of 57\AA . In addition, only one or two reflections, pointed by arrows in fig. 3.28, are observed, demonstrating a low degree of order in the stacking. In the wide angle region (inset in fig. 3.28), the broad peak arising from diffraction by disordered tails appears at $q \approx 1.38\text{\AA}^{-1}$. Therefore, the aliphatic tails are in their fluid state. Convoluted with this peak, it is also detected a typical peak associated to water at $q \approx 1.9\text{\AA}^{-1}$.

Under polarizing microscopy, the characteristic birefringent texture of lamellar phases is clearly observed, fig. 3.29(a). This image shows no excess of water, leading to the assumption that the solvent is completely incorporated to the lamellae. Fluorescence microscopy, fig. 3.29(b), reveals the presence of nucleotides in limited regions surrounded by dark zones which suggests the addition of DNA to only *one* lamellar structure whereas the coexisting phase remains uncomplexed.

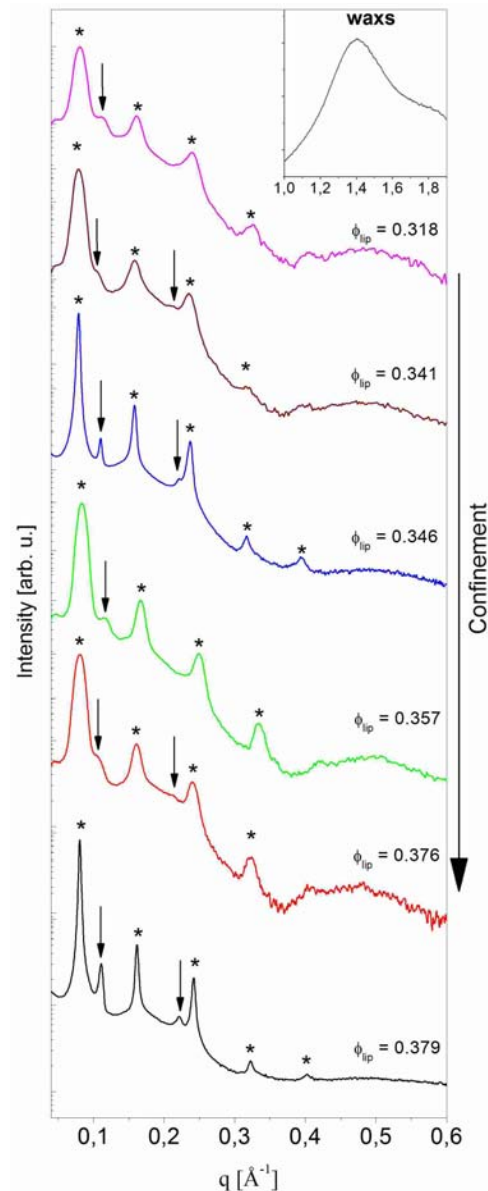


Figure 3.28: Scattered intensities from diluted samples prepared with lipids-to-DNA ratio $\rho = 3.1$. Regularly spaced peaks from lamellar phases, indicated by stars, were found jointly with a coexisting lamellar phase whose reflections are pointed by arrows. The curves in black and blue were obtained using synchrotron whereas the other ones arise from Bruker Nanostar. Inset: the presence of a broad peak at $q \approx 1.4 \text{ \AA}^{-1}$ states the fluid state of membranes. The WAXS signal from water molecules is also visible around 1.9 \AA^{-1} for such diluted systems.

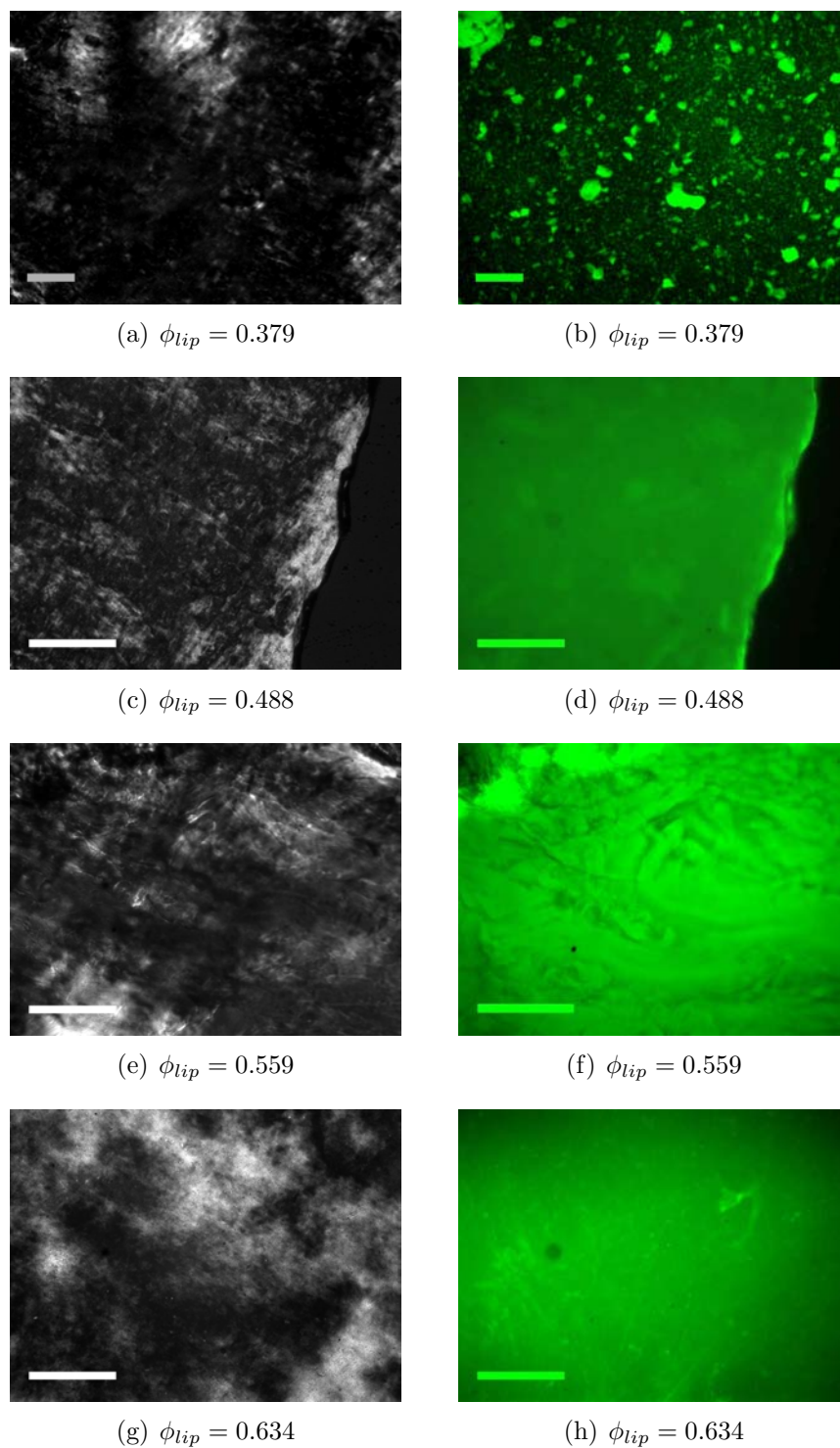


Figure 3.29: Polarized-light and fluorescence microscopies of representative samples observed along the dilution line $\rho = 3.1$. Scale bars = $100 \mu m$.

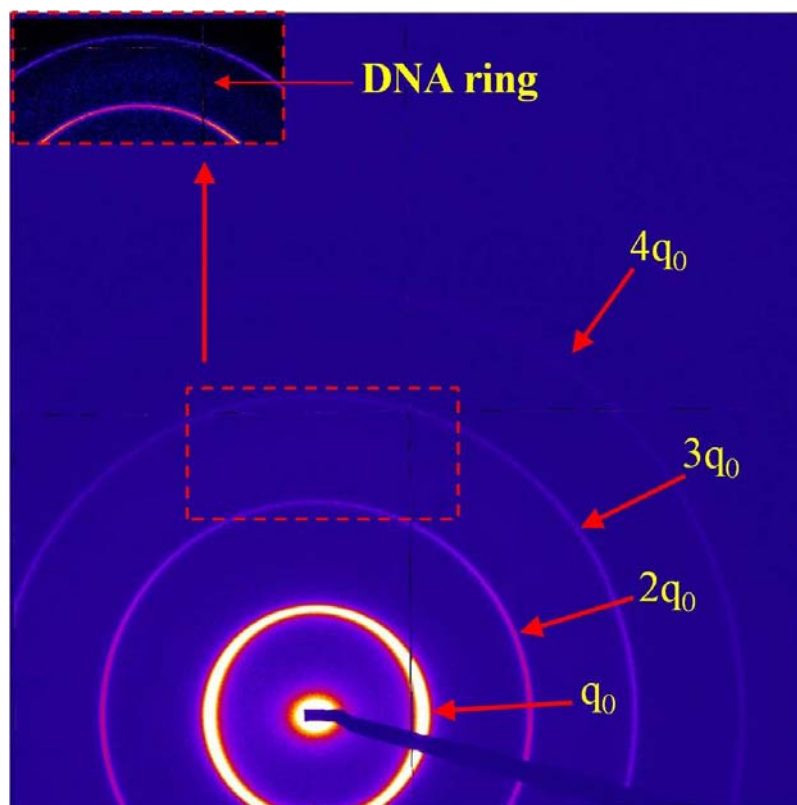


Figure 3.30: Diffractogram from a sample with $\phi_{lip} = 0.488$. Four intense rings, from a lamellar phase, appear. Inset: details presented within a color scale optimized to show the weak scattering due to DNA.

Proceeding along the dilution line towards lower water amounts, a new domain is found for concentrations situated between $\phi_{lip} = 0.404$ and $\phi_{lip} = 0.529$. A typical SAXS pattern from this region is presented in fig. 3.30. The pattern is very similar to the one obtained with DNA-free lamellar phases, except for few formulations when a diffuse ring appears convoluted between the second and the third smectic orders. In figs. 3.31 the reduced $I(q)$ vs. q profiles for samples from this domain are presented. As observed before, Bragg peaks associated to lamellar stacks can be identified. Unlike the plots shown in fig. 3.28, here we can not distinguish the presence of coexisting phases. Furthermore, a clear dependence of the lamellar periodicity upon hydration appears. As the water volume fraction increases, the peaks shift towards the SAXS region, attesting the growth of the interbilayer spacing. The repetition distances range from $d = 68.2 \text{ \AA}$ up to $d = 74.4 \text{ \AA}$ and the presence of four or five regularly-spaced reflections states the presence of highly ordered smectic phases in the complex. In the WAXS region (insets in 3.31), the fluid state of the membranes is demonstrated by the broad peak from carbonic tails. The peak related to water molecules is no longer observable as a consequence of the decreasing degree of hydration.

The appearance of a diffuse peak between the second and the third lamellar orders for most of the samples, indicated by black arrows in fig. 3.31, is another remarkable feature of this domain. These reflections arise from DNA-DNA in-plane correlations within the aqueous layers. The accurate positions of the peaks, as well as their widths, were determined from Lorentzian fits (red curves in 3.31). The corresponding distances

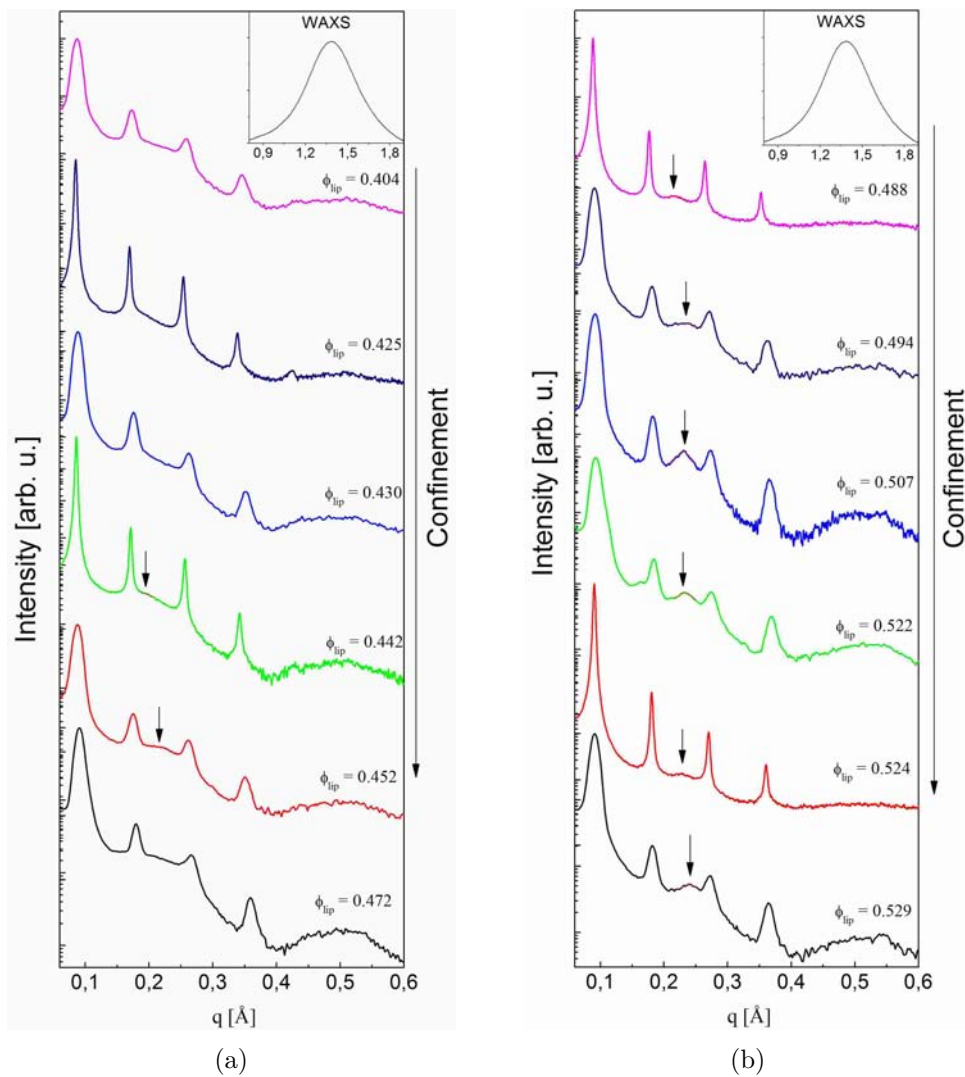


Figure 3.31: Scattered intensities from samples with $\rho = 3.1$ and ϕ_{lip} ranging from 0.404 to 0.529. Bragg reflections arising from lamellar phases can be easily identified. Arrows point diffuse peaks from DNA-DNA in-plane correlation. Inset: WAXS shows the L_α state of membranes.

in the direct space has been obtained from the relationship $d_{DNA} = 2\pi/q_{DNA}$. The values of d_{DNA} range from 26.3 Å to 34.3 Å. Such separations correspond to one DNA molecule plus a few hydration shells.

Polarizing and fluorescence microscopy, as it is shown in figs. 3.29(c) and 3.29(d), reveals the characteristic birefringent pattern of lamellar textures and homogeneity of the distribution of DNA, in rather good agreement with the picture of a full complexation between nucleotides and membranes.

The question of how the nucleotides are organized in-between lamellae is an interesting one. For samples which do not present the diffuse peak between lamellar orders, one could, in principle, state that DNA is isotropically distributed in the intermembrane space. Nevertheless, this hypothesis is not consistent with our experiments since these formulations appear intercalated by other ones where the DNA reflection indeed emerges. Thus, a possible organization to explain the observed data is to consider an orientational

ordering of the biomolecules in the plane of membranes, forming L_α^N structure. In this case, owing to in-plane rod-rod and out-of-plane rod-membrane excluded-volume interactions the rods form a nematic bidimensional mesophase, without positional ordering or transmembrane correlations. Another satisfactory hypothesis, however, places DNA molecules into regular galleries forming a 2D smectic structure in the plane of bilayers without transmembrane correlations [143]. A third possible interpretation is to consider, besides in-plane correlations, some degree of layer-to-layer orientational ordering. This last case could imply the presence of the so-called “sliding phase”, theoretically predicted but not experimentally found yet (L_α^S) [71]. Unfortunately, none of these ambiguities can be excluded from an analysis of SAXS diffractograms obtained with powder samples (the case of the present study). In order to overcome this difficulty, an alternative insight could be the modeling of $I(q)$ vs. q curves taking into account variations of electron density profiles for distinct types of orientational and positional ordering of the DNA molecules inside the host lamellar phase. Such models would allow the deconvolution of the form factors for different organizations, making it possible to distinguish the different structures. However, as far as we know, such studies have not been successfully realized to date.

Measuring the half width at half maximum ($\Delta q/2$) of diffuse peaks fitted with Lorentzians functions, the correlation length of the nucleotides, $\xi = 2\pi/HWHM$, can be estimated. For data obtained at SWING-SOLEIL beamline, where intrinsic resolution has a negligible influence on the peak width, the typical values of ξ are placed in the range between 200 Å and 400 Å. These values are equal to 6 to 15 aligned DNA molecules, yielding weak correlations between particles, which reinforces the hypothesis of nematic arrangement for nucleotides [86]. We were able to develop a simple geometric model in order to better ascertain the validity of this hypothesis. In fig. 3.32(a), we present a schematic drawing of the proposed 2D unit cell for the DNA organization in hydrated, single-phase domains. The model is constructed taking into account the structural parameters from X-ray data (lamellar periodicity and average distance between rods) and the previously known membrane thickness and DNA diameter. From simple geometric considerations (assuming flat bilayers, *i.e.* neglecting undulation fluctuations or the presence of defects), we derive eqs. (3.7)–(3.9) which allow us to predict the relevant volume fractions describing the composition of the system:

$$\phi_{DNA} = \frac{\pi\Phi_{DNA}^2}{4Da} \quad (3.7)$$

$$\phi_{lip} = \frac{\delta_m}{d} \quad (3.8)$$

$$\phi_w = 1 - \phi_{DNA} - \phi_{lip} \quad (3.9)$$

where ϕ_{DNA} , ϕ_{lip} and ϕ_w are the volume fractions for DNA, lipids and water, respectively. Φ_{DNA} is the diameter of rods and δ_m , the thickness of the membranes. d and a are the lamellar periodicity and the average distance between cylinders.

As the experimentally formulated volume fractions are *a priori* known for water, lipids

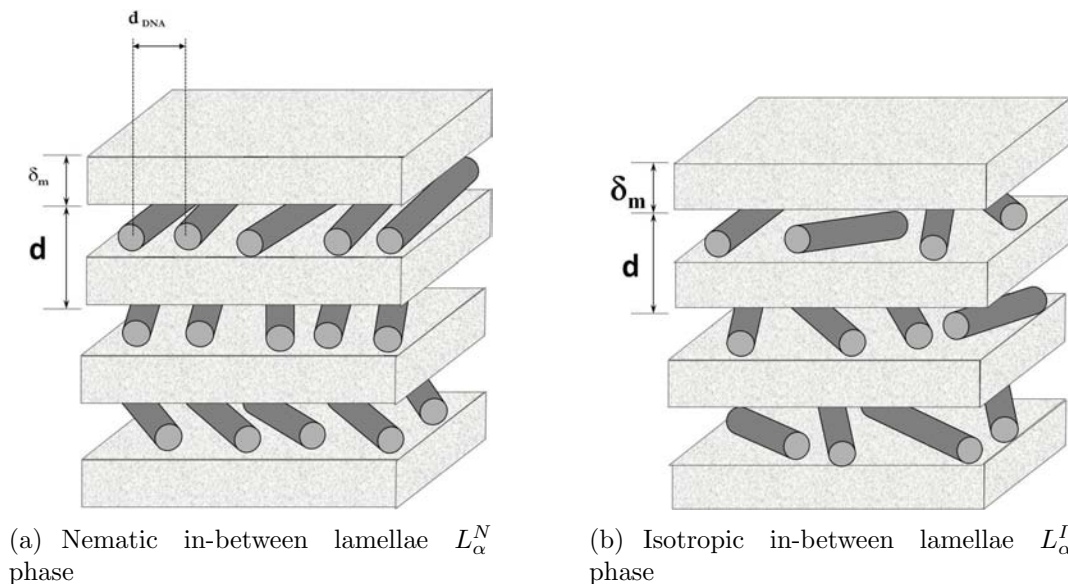


Figure 3.32: Schematic representations of lamellae hosting DNA rods. d represents the smectic periodicity of bilayers and a is the average distance between DNA molecules.

and DNA, it is possible to compare the geometrical predictions with formulated quantities. In Fig. 3.33, we present a comparison between the experimental and predicted volume fractions for all the samples exhibiting the (nematic) DNA peak. Lines represent theoretical predictions from expressions (3.7)–(3.9), while symbols indicate the experimentally formulated volume fractions for lipids, water and DNA. As is clear from the graph, there is a very good match between experimental data and theoretical predictions, underlining the reliability of the model.

It should be noted that the predictions from equations (3.7)–(3.9) are general for lamellar structures of bilayers hosting DNA in their aqueous layers, regardless of the arrangement of nucleotides inside bilayers (nematic, smectic, etc.). Our interpretation that, in this domain, the symmetry is L_{α}^N arises from the weak correlations between rods revealed by Lorentzians fits.

Despite the lack of knowledge about the average distance between rods, the predictions derived from eqs. (3.7)–(3.9) allow us to do some considerations about the organization of DNA even when the diffuse peak is not observed. Suppose that, for such formulations, the nucleotides are distributed in-between lamellae in the same manner as sketched in fig. 3.32(b). According to this sketch, the cylinders are distributed isotropically in the plane of membranes. In order to allow the free rotation of each particle around its center of mass, the minimum (average) distance between rods must be larger than half of their length. Taking as representative example of these samples the more hydrated formulation of the domain, see the pink curve in Fig. 3.31(a), whose lamellar periodicity is found to be $d = 74.1 \text{ \AA}$. Using the separation between DNA rods as $a = 250 \text{ \AA}$ (the half of the length), the theoretical volume fractions derived from (3.7)–(3.9) are: $\phi_{DNA} = 0.017$, $\phi_{lip} = 0.493$ and $\phi_{wt} = 0.490$. These values lead to a predicted lipids-to-DNA ratio $\rho = 29$, quite different from the experimental one $\rho = 3.1$. Therefore, we conclude that an isotropic

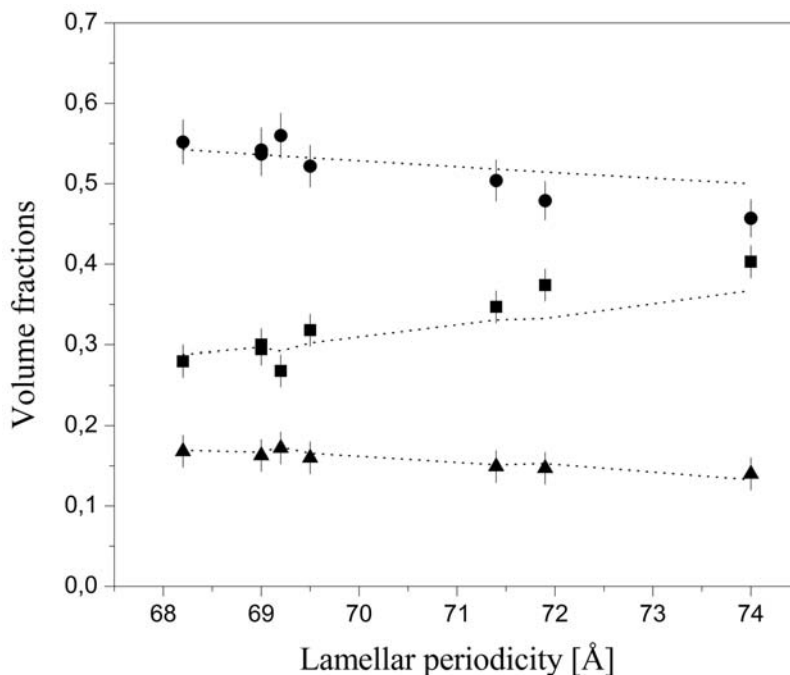


Figure 3.33: Experimental and predicted volume fractions for all the samples exhibiting the (nematic) DNA peak. Lines represent theoretical predictions from expressions (3.7)–(3.9) and filled symbols (circles for lipids, squares for water, triangles for DNA) indicate the experimentally formulated volume fractions.

distribution of DNA in this domain is highly unlikely.

Continuing along the dilution line in the direction of lower hydrations, we find a new coexistence domain whose diffractograms are shown in fig. 3.34. The corresponding lipid volume fractions of these samples are placed in the range between 0.545 and 0.586. A set of equally spaced peaks, indicated by red arrows, reveals the presence of smectic structures in the complex. The lamellar periodicities are nearly constant around 66 Å showing little variations upon hydration. For two samples, at $\phi_{lip} = 0.586$ and $\phi_{lip} = 0.545$, the typical DNA peak appears flanked by the second and the third lamellar orders. In addition to these lamellar peaks, a second set of peaks, pointed by black arrows in fig. 3.34, is observed in coexistence and can be perfectly indexed to 2D hexagonal symmetries (see eq. 2.12). The lattice parameter a also remains practically unchanged around 66 Å presenting an approximate identity with the periodicity of the coexisting lamellar phase. This epitaxiality is also found elsewhere [9] and remains unexplained. Experiments carried out in the WAXS region reveal the usual diffuse peak near to 1.4Å^{-1} showing, thus, the fluid state of membranes (inset in fig. 3.34).

Polarizing and fluorescence microscopy were also carried out and representative images from this double-phase domain are showed in figures 3.29(e) and 3.29(f). Despite the presence of 2D hexagonal symmetry revealed by X-rays, **fan-shape textures, characteristic for lipid hexagonal phases, were not observed**. Only chaotic birefringent patterns, typical for lamellar textures, are found in **all** samples.

In the driest region of the dilution line, *i.e.* for $\phi_{wt} \leq 0.200$, a new single-phase

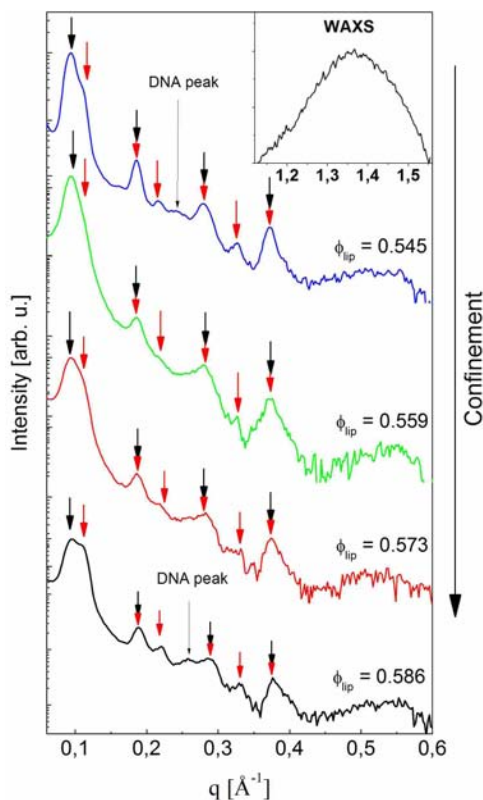


Figure 3.34: Diffractograms from samples with ϕ_{lip} in the range 0.545 to 0.586 and overall lipids-to-DNA ratio $\rho = 3.1$. Red arrows point peaks corresponding to lamellar phases whereas black pointers indicate reflections indexed to a 2D hexagonal symmetry.

domain appears. A typical SAXS pattern from this domain is exhibited in Fig. 3.35. The reduced 1-D diffractograms arising from these samples are presented in Fig. 3.36. The corresponding lipid volume fractions are situated in the interval $0.604 < \phi_{lip} < 0.638$. All Bragg reflections are perfectly indexed to a single 2D hexagonal lattice, without need for a coexisting structure. The system is highly organized such that, for concentrated samples ($\phi_{lip} = 0.634$ and $\phi = 0.638$), reflections at positions $q = \sqrt{12}q_0$ and $q = \sqrt{13}q_0$ can easily be identified. Inspection under polarizing microscopy, Fig. 3.29(g), shows only the presence of *lamellar* textures, while fluorescence microscopy, Fig. 3.29(h), reveals a homogeneous distribution of the DNA within the lipid phase. The lattice parameter a associated to this phase decreases very little as the lipid concentration increases reaching a minimum value of $a = 64.8 \text{ \AA}$.

The Bragg peak component of the X-ray scattering again allows multiple interpretations. In Fig. 3.37, we present two candidate structures which adequately describe the 2D hexagonal symmetry of the observed diffraction pattern. In the first one, Fig. 3.37(a), DNA rods form a hexagonal lattice inserted inside the water layers of a (direct) lamellar phase of lipid membranes (L_{α}^H). In the second sketch, fig. 3.37(b), the lipid component forms an inverted hexagonal structure, where DNA fragments are inserted into cylinders of water (H_{II}^c phase). The expressions deduced in equations (3.7)–(3.9) are general for platelet structures hosting cylinders and are valid to describe the scheme drawn in fig. 3.37(a). For the H_{II} symmetry, the prediction for ϕ_{DNA} also remains the same. The

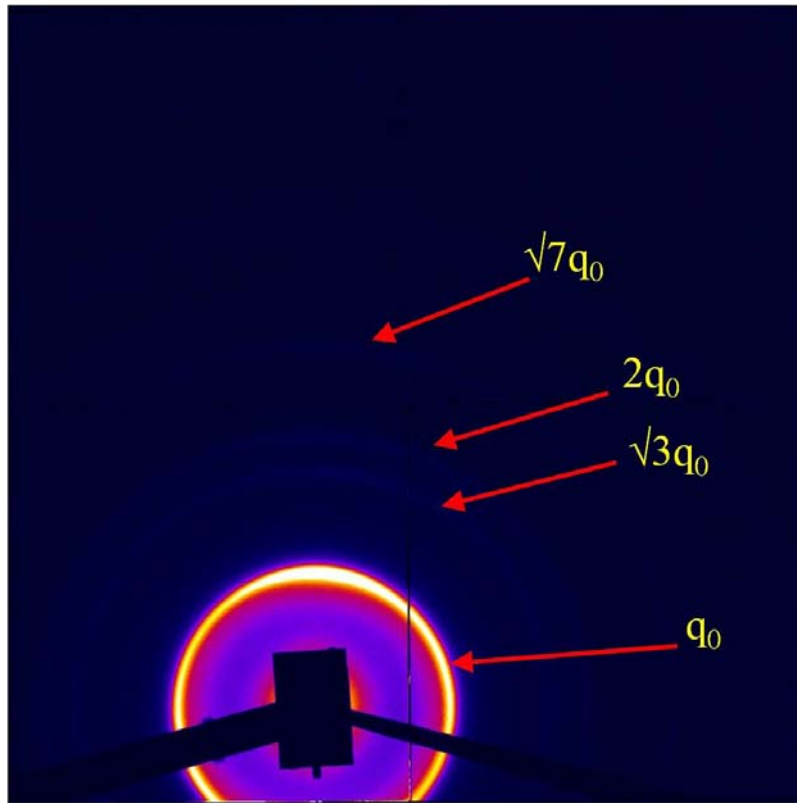


Figure 3.35: SAXS pattern from a sample with $\phi_{lip} = 0.634$. A typical signature from 2D hexagonal symmetries appears, as stated by the presence of rings at positions $\sqrt{3}q_0$ and $\sqrt{7}q_0$.

expressions for ϕ_w and ϕ_{lip} are quite different, however, and read:

$$\phi_w = \frac{\pi(a - \delta_m)^2}{4aD} - \phi_{DNA} \quad (3.10)$$

$$\phi_{lip} = 1 - \phi_w - \phi_{DNA} \quad (3.11)$$

Note that, in writing Eq. (3.10), we add a (presumably non restrictive) hypothesis, namely that the membrane thickness δ_m is identical to the size of the lipid domains along the natural hexagonal directions.

In fig. 3.38 we plot the geometrical predictions derived from equations (3.8)–(3.11) and compare them with the experimental lipid and water volume fractions. In spite of some deviations in both cases, we observe a better agreement between experimental data and theoretical predictions for the L_α^H hypothesis. This result is in good agreement with those published previously on oriented supported films [21]. The obtained lattice parameters a are around 65 Å which corresponds to lamellar periodicities of $d = \sqrt{3}a/2 \approx 56$ Å. Subtracting the geometrical thickness of the bilayers, the available space for DNA is *ca.* 19 (1) Å, slightly below the geometrical limit and thus requiring small deformations of the membranes. It should also be noted that here the bilayers were considered to be completely flat, which could explain deviations from the model.

In fig. 3.39 we show the behavior of structural parameters, as a function of the lipid

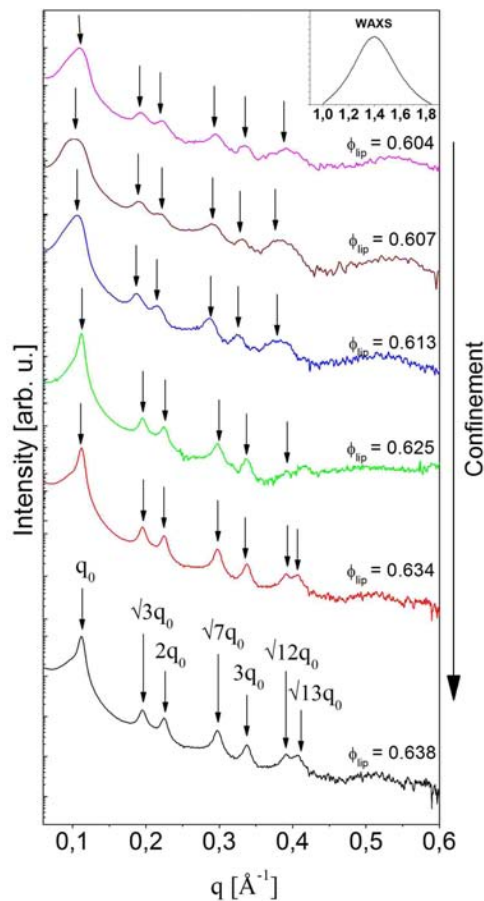


Figure 3.36: Diffractograms from the hexagonal single-phase domain.

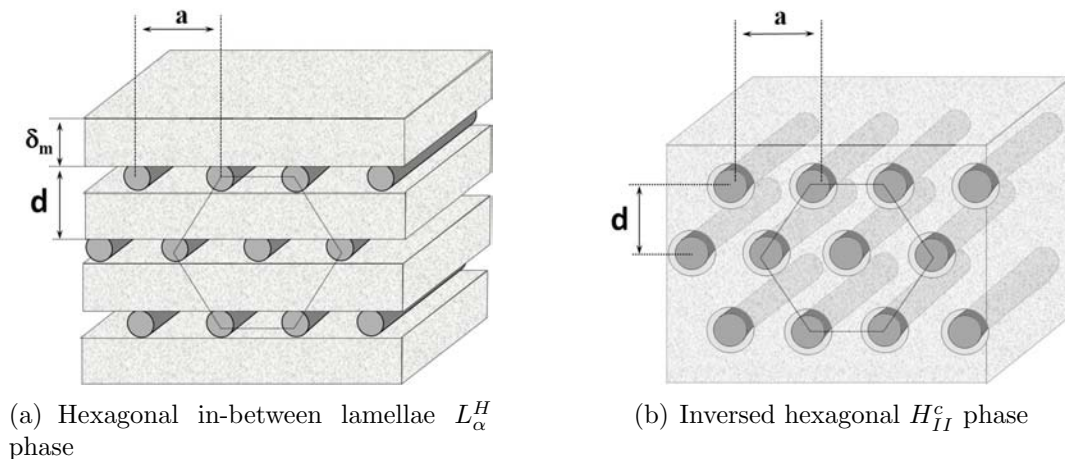


Figure 3.37: Schematic representations corresponding to (a) L_{α}^H hypothesis and (b) H_{II} symmetry, both compatible with the sets of Bragg peaks observed in the dehydrated region of the phase diagram.

volume fraction along the whole dilution line with $\rho = 3.1$. The lamellar repeat distance is represented by squares, whereas circles are associated to the distance between DNA rods. The approximate boundaries between different domains are indicated by vertical lines. In the more hydrated domain I , we have two sets of repetition distances, associated to coexisting lamellar phases, oscillating around 77 \AA and 57 \AA . In domain II , the periodicity of the host phase presents a quasi-linear dependence on hydration, quite similar to the

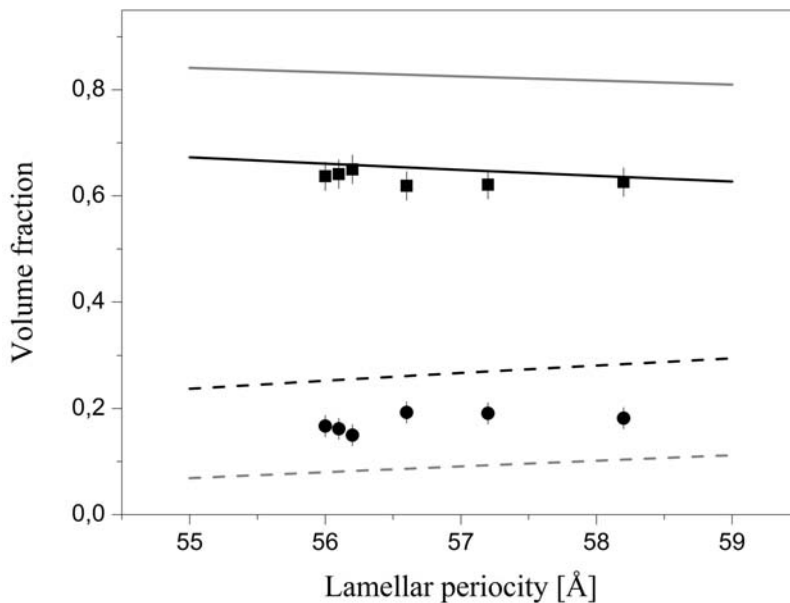


Figure 3.38: Comparison of ϕ_{lip} (filled circles: experimental values) and ϕ_w (filled squares) for the 2D hexagonal structures sketched in fig. 3.37. Solid lines indicate predictions for lipid volume fractions, and dashed lines for water volume fractions. L_α^H predictions are represented in black, whereas H_{II}^c are showed in gray.

behavior observed for the DNA-free system. It is possible to identify lamellar spacings between 68.2 \AA and 74.4 \AA leading to aqueous layers between 31.7 \AA and 37.9 \AA . This space is sufficiently large to accommodate DNA rods without need for deforming the lipid bilayers. In turn, the interaxial spacing between DNA molecules, obtained from the position of the diffuse peak between the second and third lamellar orders, is found to decrease slightly with the confinement imposed by the host phase until it reaches a minimum value around 26 \AA . Such a value, somewhat larger than the DNA diameter, appears to be large enough to accommodate a few hydration shells around the DNA rods. In domain *III*, we have a coexistence between a lamellar phase containing DNA organized in a nematic lattice in-between bilayers and a 2D hexagonal phase of DNA embedded within a lipid lamellar phase. An epitaxiality match is found between the parameter a of the hexagonal lattice and the periodicity d of the coexisting lamellar phase. Two samples from this domain, $\phi_{lip} = 0.545$ and $\phi_{lip} = 0.586$, show clearly the typical diffuse peak arising from DNA in-plane correlations. The distances between rods, d_{DNA} , are 26.0 \AA and 24.3 \AA , respectively.

In the highly-ordered domain *IV* (ϕ_{lip} larger than *ca.* 0.60), both lamellar periodicity and DNA-DNA distances became nearly constant, around $d = 56.0 \text{ \AA}$ and $a = 65.0 \text{ \AA}$ respectively. These values seem to be characteristic of the more compact structure allowed in the system. It is also interesting to note that the distance between DNA molecules is significantly larger than the one observed in the dilute regime (L_α^N) and also in the hexagonal phase of the DNA-water binary system studied by Livolant and co-workers [144]. These observations suggest the existence of repulsive interactions between DNA molecules when the layer to layer orientational correlations appear in the L_α^H phase. These

findings point to strong excluded volume interactions between DNA and membranes, as will be discussed in next sections.

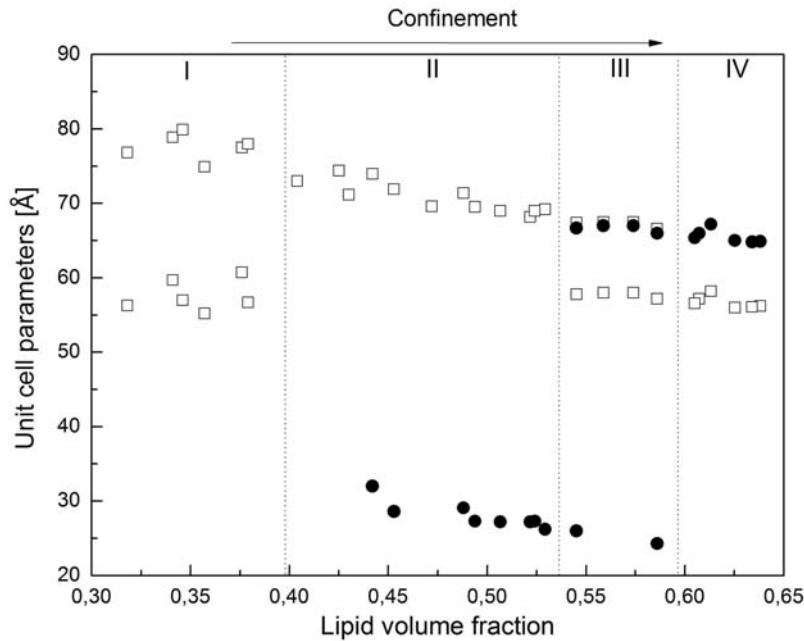
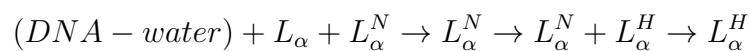


Figure 3.39: Behavior of the structural parameters as a function of the lipid volume fraction. Squares represent the smectic spacing of the lipid host phase, circles the separation between DNA rods. Dotted lines: guide for the eyes representing the approximate location of the boundaries between domains.

The self-assembly of DNA into the aqueous layers of the lamellar phases depends strongly on the (soft) **confinement** exerted by the bilayers. According to the above described interpretations, we can summarize the phase behavior upon confinement along the dilution line $\rho = 3.1$ as follows:



Replicas from the single-phase L_{α}^N and L_{α}^H domains were also observed in TEM. In fig. 3.40, it is shown the large-scale appearance of such domains. A remarkable feature is that, compared to binary systems with similar ϕ_{lip} (see figs. 3.9(b) and 3.10(a)), vesicles are not observed. In addition, fractures were observed only along the plane of membranes which can be a sign of how the elastic properties of the phase are changed by the incorporation of particles. The reason of this observation can be related to an increase of the smectic ordering. A more detailed discussion about this phenomenon will be conducted in Sec. 3.3.2.

Analyzing the L_{α}^N domain in more details, we find some interesting results. In fig. 3.41, a picture from a sample containing $\phi_{lip} = 0.488$ is shown at magnification of $150000\times$. The sputtering direction is indicated by a yellow arrow, near to a step allowing determination of the sense of platinum deposition. As expected from X-rays data and POM data, we observe large extensions of defect-free terraces forming a layered structure. In the inset, the Fourier transform, performed over one of the layers, shows an isotropic pattern, slightly

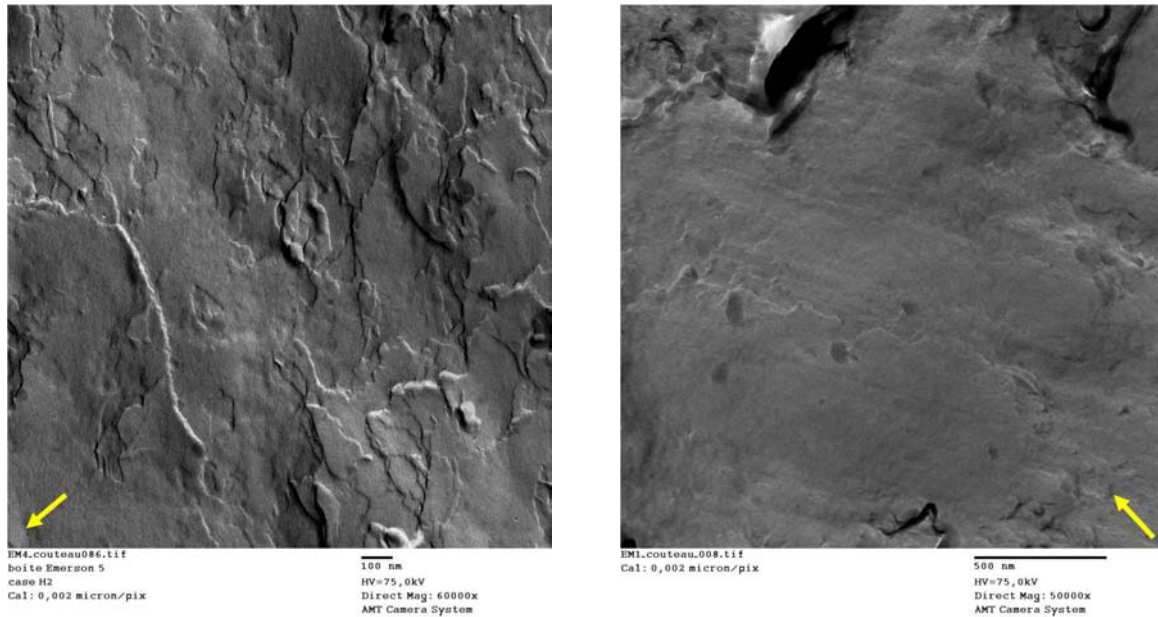
(a) L_{α}^N , $\phi_{lip} = 0.488$ and $\rho = 3.1$.(b) L_{α}^H , $\phi_{lip} = 0.634$ and $\rho = 3.1$.

Figure 3.40: Large scale view of replicas from single-phase domains with $\rho = 3.1$. Unlike the behavior found in binary mixtures with similar concentration, vesicles appear to be very rare.

elongated in the direction of the shadowing jet. Since the fracture process tends to cleave membranes through the central hydrophobic core [145], it is not possible, **in this case**, to see anisotropies introduced by DNA molecules, however, the membrane surfaces exhibit corrugations that were not present in the binary system.

High-magnification pictures from the L_{α}^H sample reveals interesting results. Smectic steps are observed across the replica as indicated by white arrows in fig.3.42(a). Nevertheless, these steps are smoother than the one observed in replicas from the L_{α}^N domain. In the plane of the layers, we identify a large number of anisotropic structures whose layer-to-layer orientation is conserved, in agreement with the expected behavior for columnar hexagonal lattices of DNA in-between lamellae. In fig. 3.42(c), the Fourier transforms performed over two consecutive layers confirm both the strong anisotropy of the particles and the persistence of their orientation.

In fig. 3.42(b), it is possible to observed the rod-like shape of the particles in detail. These structures are typically $530 \text{ \AA} \times 30 \text{ \AA}$ in size, in rather good agreement with the expected size of 150 bp DNA molecules taking into account the shadowing layer. The resolution limit of the freeze-fracture technique, which is estimated to be *ca.* 20 \AA for **periodical structures** [12], does not allow accurate measurements of the DNA diameter. However the shape of the particles is outlined as observed in similar contexts [146–148]. In addition, the separations between rods, after statistical analysis in a few pictures, is found to be *ca.* 61 \AA , again in rather good agreement with the DNA-DNA separation equal to 65 \AA obtained from X-rays.

The question of why we were able to outline DNA molecules in replicas from the L_{α}^H

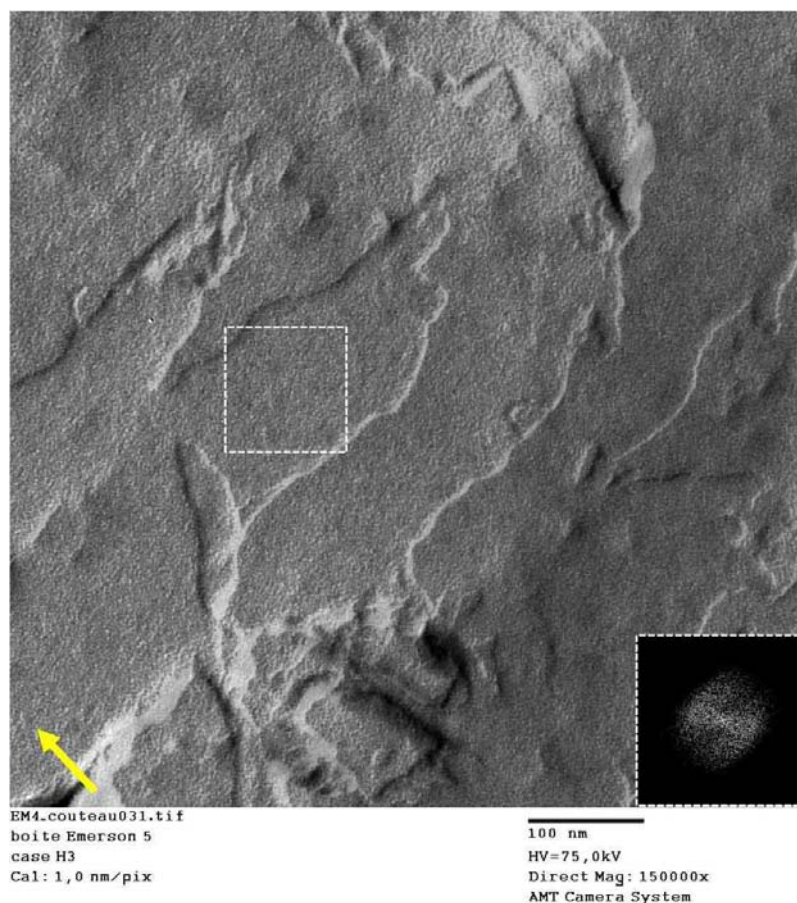


Figure 3.41: TEM image over freeze-fractured replica from the single-phase domain L_{α}^N . Large smectic terraces can be easily identified. The direction of the shadowing jet is indicated by the yellow arrow. Inset: Fourier transform carried out over the dotted white square reveals isotropy in the plane of the fractures (see text for details).

domain, whereas for the L_{α}^N domain this is not possible, deserves to be discussed here. In the shadowing process, platinum and carbon atoms or aggregates from the vapor phase arriving to the surface have a mobility after adsorption to the substrate. The binding energies are different for each site on the surface and nucleation occurs around certain centers forming more stable aggregates. The growth of Pt-C grains occurs then in some preferred sites [149]. If the substrate has periodic structure, the distribution of the coating is also periodical. This phenomenon is the so-called *decoration*. The sample replicated from the L_{α}^N domain has periodicity $d = 71.3 \text{ \AA}$. This means that the interbilayer spacing is large enough to accommodate the rods without need for deformations in membranes. Therefore, the lamellar phase is composed by flat bilayers and the fracture in the hydrophobic core gives rise to flat (and amorphous) monolayers covering the nucleotides. Nevertheless, the lamellar periodicity of the L_{α}^H sample is $d = 56.3 \text{ \AA}$, smaller than the one found in the above described L_{α}^N , and the confinement imposed to DNA strands is more severe, probably leading to membrane deformations. Hence, we could expect that the lipid monolayer coating the rods follows the reliefs of the particles, thus providing a periodic substrate for shadowing. While the grain size of Pt-C replicas prepared under

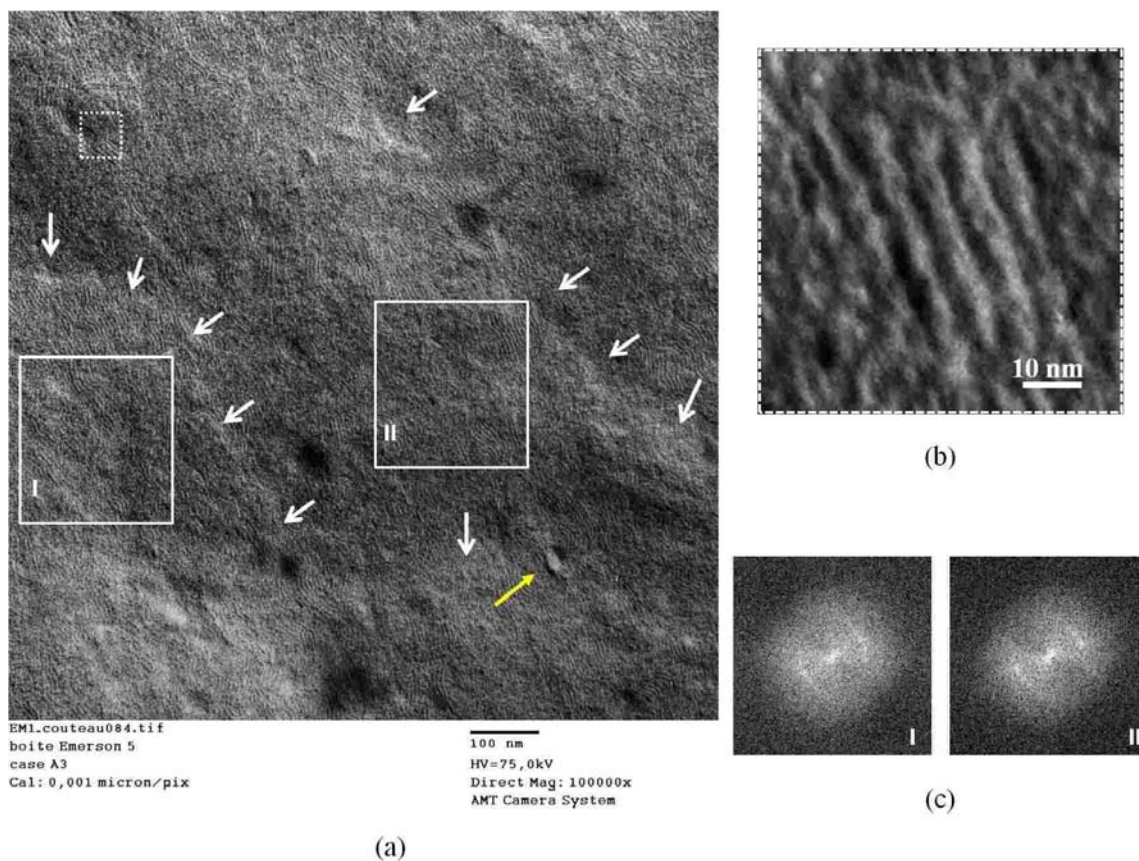


Figure 3.42: Electron microscopy images over freeze-fractured replica from L_{α}^H phase. (A) White arrows point smectic steps delimitating planes along which rod-like structures appear to be highly oriented. Yellow arrow point the illumination direction. (B) Zoom over the dashed square in Fig. A showing the rod-like structures in detail. (C) Fourier transforms over solid squares indicated in Fig. A, revealing the persistence of layer-to-layer orientation, as predicted for L_{α}^H phases.

the same conditions as employed here is estimated to be *ca.* 50 \AA [150], decoration allows the visualization of finer details than those observable on amorphous surfaces [151].

Ionic strength

The results obtained in sec. 3.1.1 show that electrostatics has not a strong influence on the stabilization of the host lamellar phases used here. On the other hand, since the net electric charge of the lipid part is thought to be zero, it is also reasonable to suppose that Coulomb forces between nucleotides and bilayers are not directly involved on complexation. However, even if electrostatic effects have a minor role on direct DNA-membrane interactions, one cannot neglect the release of the sodium counterion neutralizing the DNA phosphate groups. As mentioned in Sec. 1.5.1, the introduction of salt (ammonium acetate in our case) changes the thermodynamic behavior because it lowers the entropic gain associated to the counterion release [63]. In order to address this matter, after the study of the behavior of binary lamellar phases swollen with brine solutions, some effort was concentrated on analyzing the ternary DNA-containing system under a different ionic condition resulting from the addition of a monovalent salt to the system.

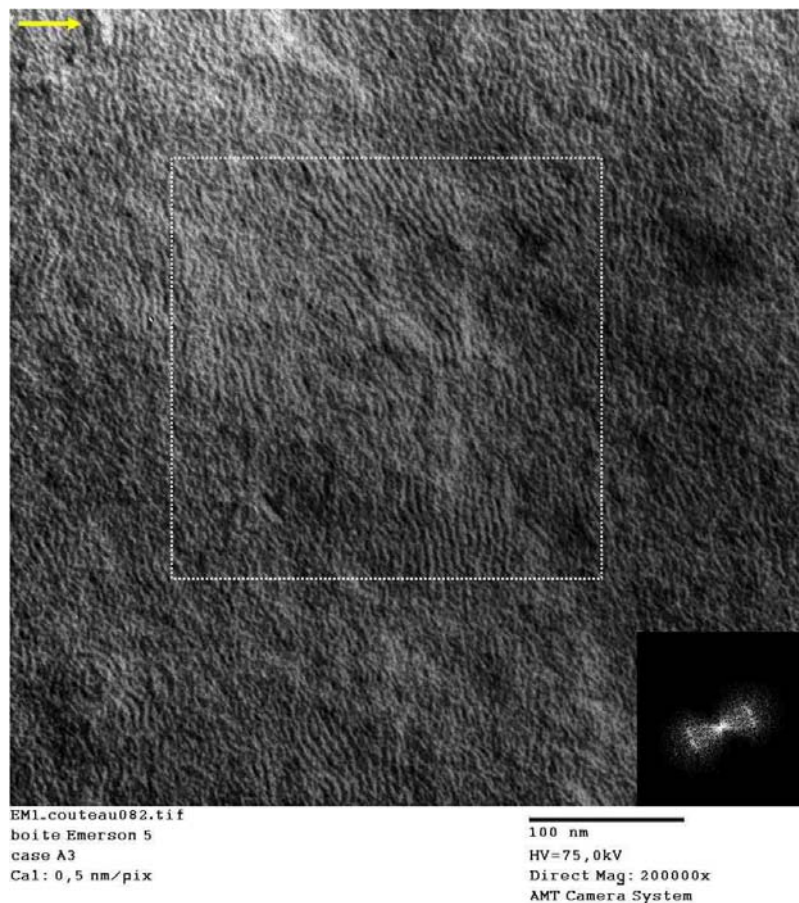


Figure 3.43: TEM image of replica from single-phase domain L_{α}^H at highest magnification available, $300000\times$. The presence of anisotropic rod-like structures is highlighted and their dimensions are found to agree with the DNA ones. The yellow arrow shows the direction of vaporization and the inset corresponds to FFT of the area indicated by white square.

For the ternary DNA-lipid-water complex studied in this manuscript, the molar concentration of **nucleotides in the aqueous phase** (in mol/L units) is given in terms of ρ and ϕ_w through the following relationship:

$$C(\rho, \phi_w) = \frac{1.7 \times 10^3}{330} \frac{1}{(1 + \rho)} \left[\frac{1}{\phi_w} - 1 \right] \quad (3.12)$$

From eq. 3.12, it is easy to derive that, for hydrations studied along the dilution line $\rho = 3.1$, the molar concentration of phosphate groups is comprised between ≈ 1 M and ≈ 5 M. Taking into account the Manning's renormalization constant, we conclude that the amount of Na^+ ions released to the aqueous phase ranges from ≈ 0.24 M to ≈ 1.25 M. Therefore, the introduction of extra monovalent salt, at concentration of 0.25 M, represents a strong change in the ion balance of the complex.

Few salt-containing samples, prepared with $\rho = 3.1$, were analyzed by X-rays diffraction. The resulting $I(q)$ vs. q curves are exhibited below, in fig. 3.44.

Again, a rich polymorphism of mesophases is found across the dilution line. For hydrated samples, with $\phi_{lip} < 0.45$, two lamellar phases appear in coexistence. In the

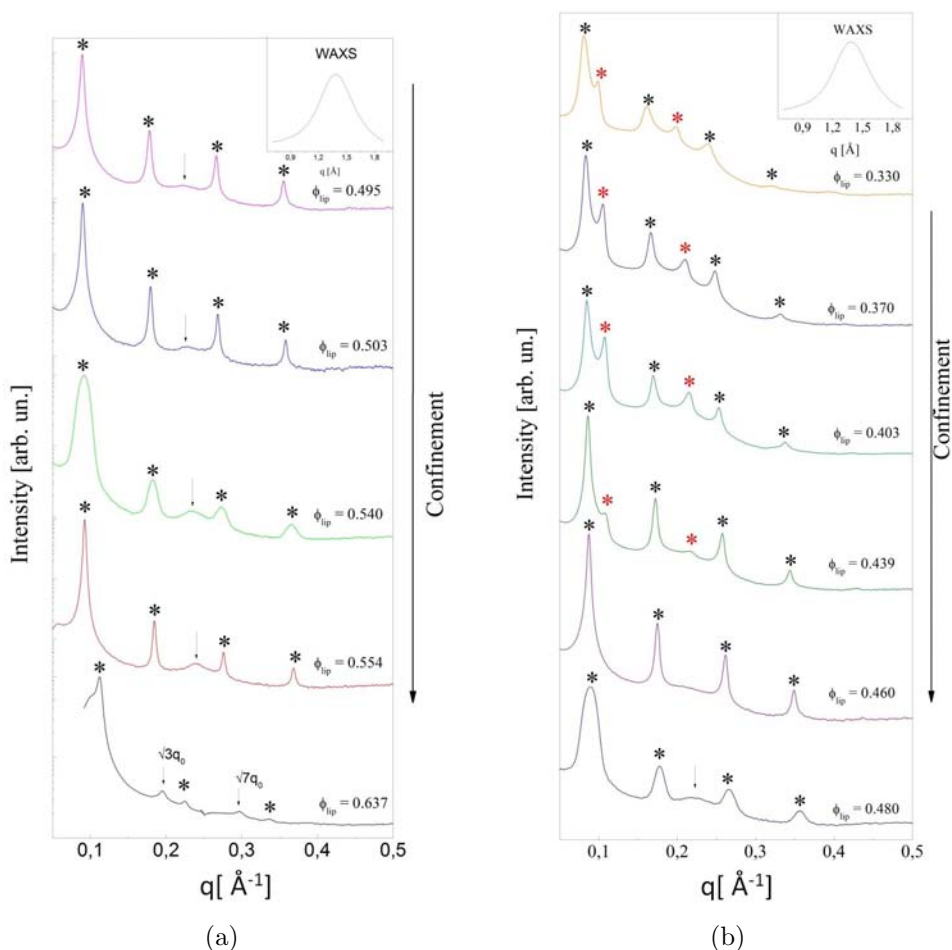


Figure 3.44: Scattered intensities from samples with $\rho = 3.1$, prepared with brine solutions of ammonium acetate at 0.25 M. Lamellar peaks are indicated by stars and reflections arising from DNA ordering are pointed by arrows.

same manner as observed before, one of these phases has a well-marked long-range order, resulting in up to four Bragg peaks. The second smectic phase, in turn, is less ordered and gives rise to only two reflections, indicated by red stars in fig. 3.44. As the system is dehydrated, a single-phase domain emerges where, for most of samples, it is possible to identify the typical nematic peak convoluted between the second and third lamellar orders. Finally, in the driest region of the line, for $\phi_{lip} > 0.56$, an hexagonal symmetry is found. At wide-angle region, the characteristic broad peak at $q \approx 1.4 \text{ \AA}^{-1}$ shows that the fluid state of carbonic chains does not change upon salt addition. Such behavior is quite similar to that one observed for samples prepared with pure water, where these domains have appeared in the very same sequence. The unique difference is that, here, the $L_{\alpha}^N \rightarrow L_{\alpha}^H$ transition occurs without an intermediate coexisting domain, perhaps too narrow to have been detected.

In fig. 3.45, the unit cell parameters are indicated as a function of lipid volume fraction. In order to allow a direct comparison, data from salt-free formulations, prepared from the same lots of sonicated DNA and lipid-Simulsol mixtures and scanned at the same synchrotron run, are also presented in 3.45. The results are found to agree, not

only qualitatively, but also quantitatively, showing that the salt addition does not change significantly the mesophase behavior. These findings reinforce and support the importance of entropic forces as major players in the interactions within the complex, since Helfrich and hydration forces are referred to in the literature as having no dependence upon ionic conditions [47, 61]. In addition, as discussed in sec. 1.4.1, the short range interactions between DNA molecules is thought to be driven by repulsive hydration forces [46], which agrees with the salt-independent behavior found above.

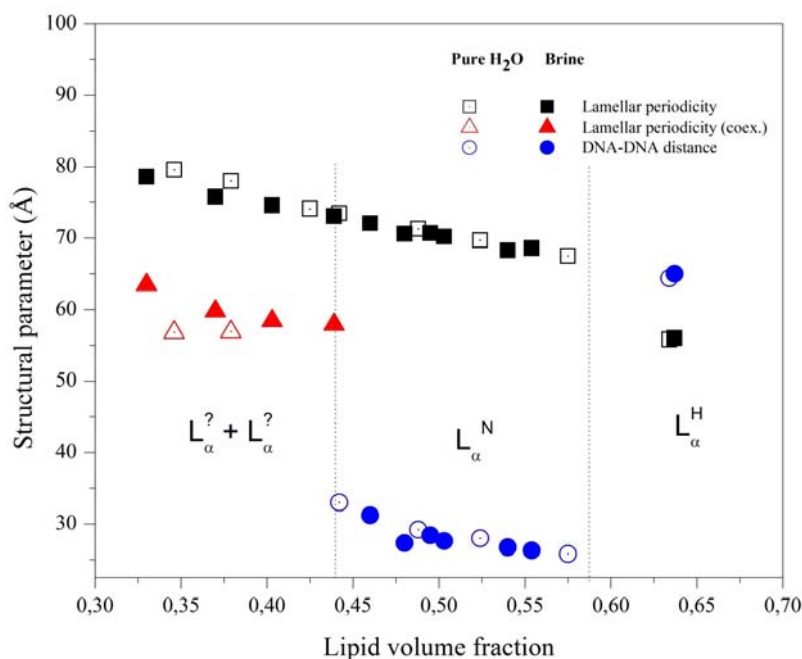


Figure 3.45: Behavior of the structural parameters as a function of the lipid volume fraction, for samples with $\rho = 3.1$. Squares represent the periodicity of the main smectic phase whereas triangles correspond to the periodicity of the coexisting lamellar phases. Circles represent the interaxial spacing between DNA rods. Full symbols indicate the parameters related to salt-containing samples and open markers correspond to salt-free preparations, examined under the same conditions. Dotted lines: guide for the eyes with the approximate borders between mesophase domains.

The samples were also analyzed by polarizing and epifluorescence microscopies. One pair of pictures from each domain is exhibited in fig. 3.46. Lamellar textures appear for all samples along the dilution series. In fluorescence, the phase separation is clearly observed for the coexisting domain represented in fig. 3.46(b), where a concentrated DNA-containing part is found surrounded by an apparently uncomplexed lamellar phase. The other two single-phase domains have homogeneous distribution of nucleotides embedded in the lipid phase.

Dilution line $\rho = 5.1$

The dilution line with lipids-to-DNA ratio $\rho = 5.1$ was scanned in the same manner as described above. The overall hydrations ranged from $\phi_{wt} = 0.127$ to $\phi_{wt} = 0.576$. The corresponding lipid volume fractions were situated in the interval $0.356 \leq \phi_{lip} \leq 0.729$. In

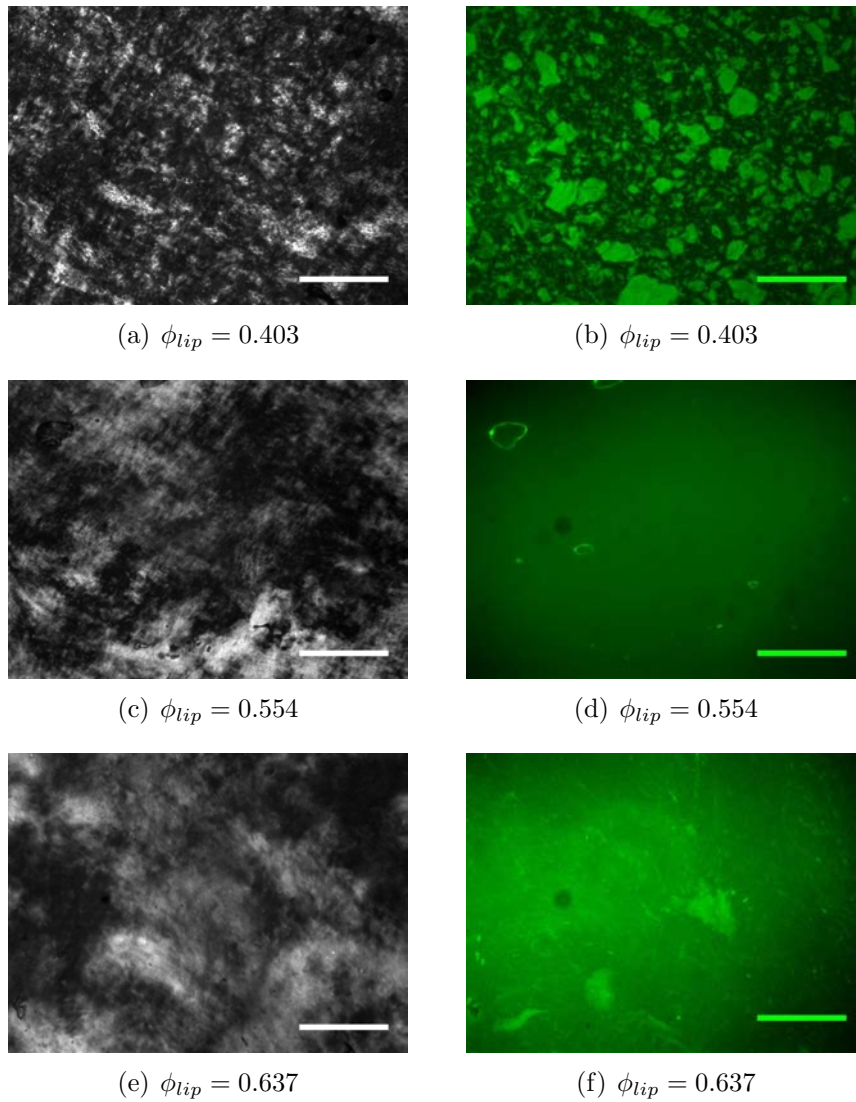


Figure 3.46: Representative polarizing and epifluorescence images from samples prepared with $\rho = 3.1$ and hydrated with brine solutions. Scale bars: $100\mu\text{m}$.

fig. 3.47, the small- and middle-angle scattering profiles are shown, $I(q)$ vs. q , for diluted samples which $\phi_{lip} \leq 0.543$.

A set of regularly spaced Bragg reflections, indicated by stars in fig. 3.47, shows the presence of a lamellar phase with a well-marked long-range order. For most of samples, it is also possible to identify a second set of peaks, pointed by black arrows, arising from a short-range ordered smectic phase. The displacement of the peaks upon hydration shows that the periodicities decrease as the lipid concentration increases, a behavior quite similar to the one observed in binary lipids-water mixtures. Only two formulations, with $\phi_{lip} = 0.421$ and $\phi_{lip} = 0.527$, are found to be monophasic. Following the same reasoning as used in analyzing the lower-order monophasic domains along the line $\rho = 3.1$, we interpret these samples as L_{α}^N points. The presence of the broad peak at $q \approx 1.38 \text{ \AA}^{-1}$ indicates the fluid state of the bilayers.

Polarizing and fluorescence microscopies (see figs. 3.48(a) and 3.48(b)) show lamellar textures together with inhomogeneity in DNA distribution. These images show zones

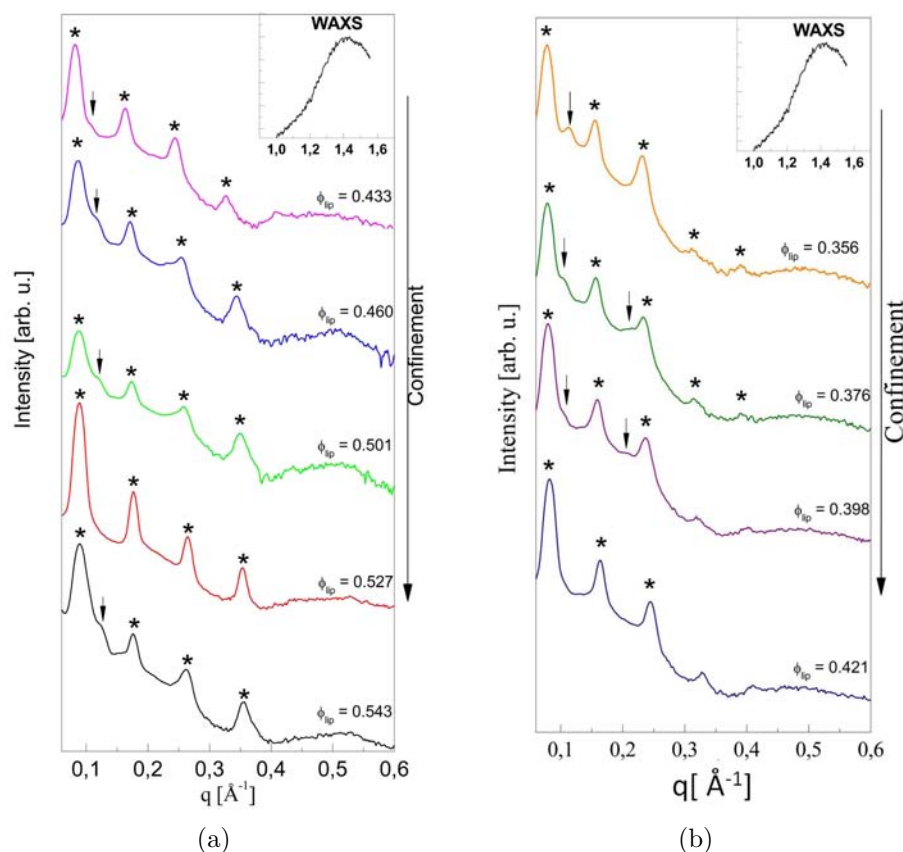


Figure 3.47: $I(q)$ vs. q plots from samples with $\rho = 5.1$ and ϕ_{lip} ranging from 0.356 to 0.543. Stars indicate peaks arising from a lamellar phase with well-marked long-range order and arrows point to those arising from a short-range order structure. Inset: WAXS shows the fluidity of the membranes.

which are bright in fluorescence and optically isotropic in polarizing microscopy, suggesting the formation of concentrated aqueous DNA phases together with two lipid lamellar phases containing nucleotides in-between bilayers.

In fig. 3.49(a), the scattering profiles for a narrow domain are shown with lipid volume fractions placed in the interval $0.564 < \phi_{lip} < 0.601$. It is a complex coexisting region wherein highly-ordered symmetries are found together with lamellar phases. The peaks associated to these accompanying lamellar phases are pointed by red and/or blue arrows. **The new feature of this domain is the sudden appearance of 2D columnar rectangular lattices** whose Bragg peaks are identified by black arrows, with the corresponding Miller indices between brackets. The sample with $\phi_{lip} = 0.601$ stands out because it is a three-phase formulation and it is possible to identify the diffuse DNA peak arising from nematic ordering into one of the lamellar phases. Under polarizing optical microscopy (see Fig. 3.48(c)), only lamellar textures are observed leading us to conclude that the lipid part is assembled into smectic-like structures and the rectangular symmetries arise from the supramolecular assembly of DNA embodied in-between bilayers. In fluorescence, the samples are inhomogeneous with DNA presenting different concentrations in the coexisting phases. The appearance of (h, k) peaks with $h + k = 2n + 1$ means that such symmetries are simple rectangular as outlined in Fig. 3.49(b). The lattice parameters a

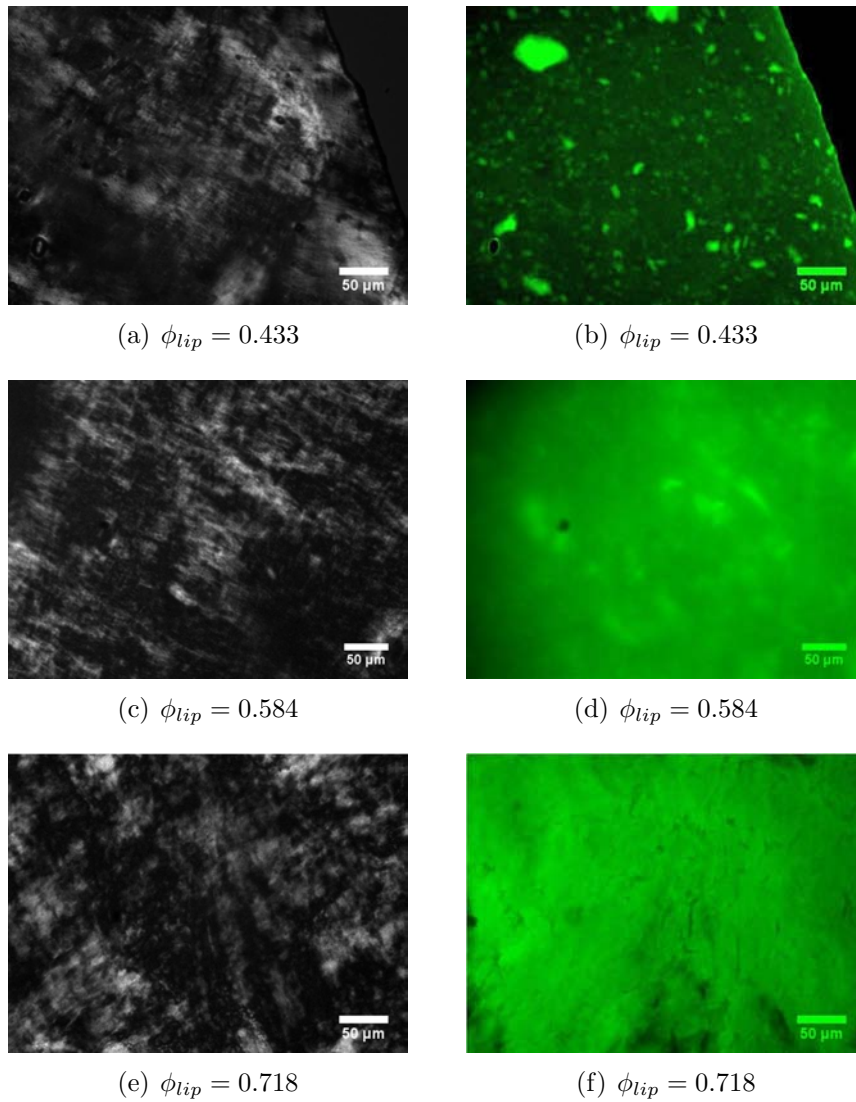


Figure 3.48: Polarizing and fluorescence optical microscopy images of representative samples from dilution line $\rho = 5.1$. All samples showed birefringent textures and an inhomogeneous fluorescence was found throughout dilution line.

and b are indicated jointly to the respective diffractograms on 3.49(a). Presumably, this rectangular lattice is an intermediate stage on DNA ordering towards the 2D hexagonal symmetry observed for driest samples.

In the driest region, that is, for ϕ_{lip} ranging from 0.612 to 0.730, X-rays show a coexisting domain of lamellar and hexagonal symmetries. The respective scattering plots, $I(q)$ vs. q , are presented in fig. 3.50. The peaks arising from smectic structures are identified by red arrows whereas those indexed to hexagonal lattices are pointed by black arrows. The broad reflection in the wide angle region attests the fluidity of membranes. The hexagonal lattice found here is quite similar to that one observed along the line $\rho = 3.1$, that is, the parameter a is nearly constant around 65 \AA which leads us to interpret this phase as L_{α}^H . On the other hand, the smectic period of the coexisting phase depends strongly on hydration. This observations means that, once formed a hexagonal structure into the complex, it is stable and changes on the overall amount of water are

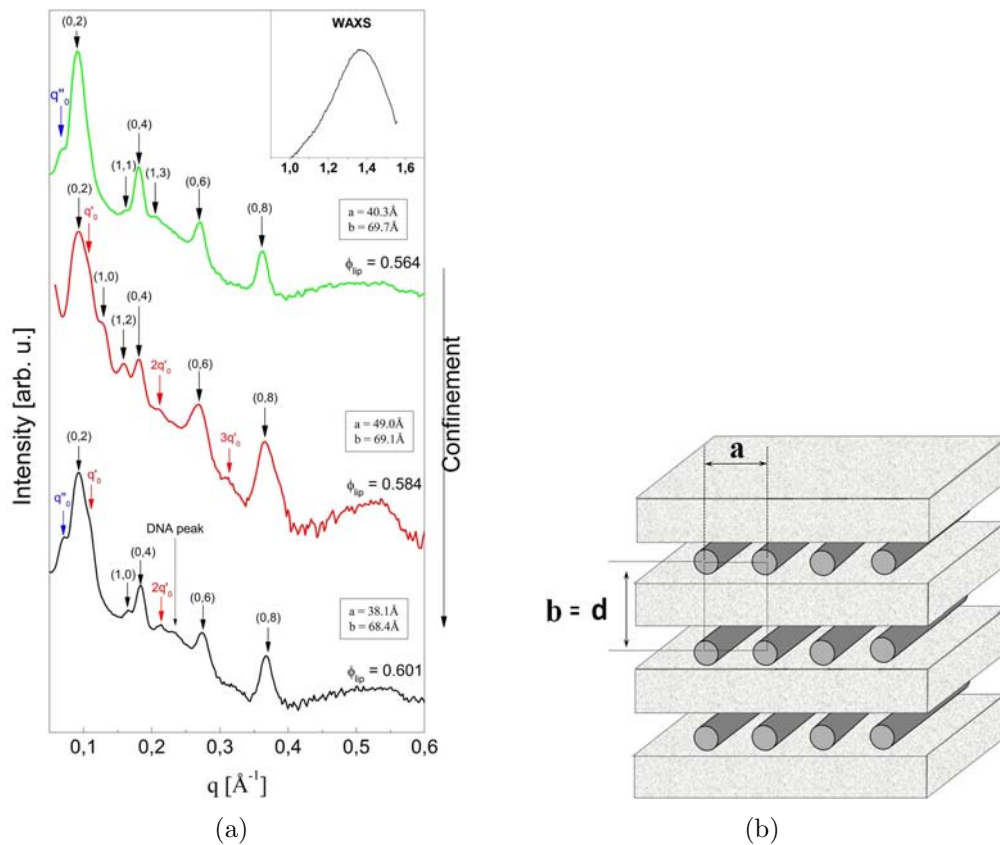


Figure 3.49: (a) Diffractograms from a narrow and complex domain wherein lamellar phases were identified together with 2D columnar rectangular lattices of DNA. Inset: WAXS showing the disordered state of carbonic tails. (b) Schematic draw of a 2D simple rectangular superlattice of nucleotides in-between bilayers.

incorporated by the coexisting lamellar phase. Polarizing microscopy reveals only lamellar textures and fluorescence shows inhomogeneities (see figures 3.48(e) and 3.48(f)).

In fig. 3.51, the behavior of the lattice parameters as a function of the volume fraction is shown. Squares indicate the lamellar periodicities of the lipid phase and circles represent the distance between DNA rods. The behavior is dominated by two biphasic domains, *I* and *II* in fig. 3.51.

The hydrated domain *I* has two lamellar phases hosting DNA with unknown ordering into aqueous layers. We observe two groups of smectic periods. The first group of periodicities ranges from 71.4 Å to 81.1 Å providing interbilayer spacing larger enough to accommodate DNA rods with a diameter equal to 20 Å. The second group ranges from 55.1 Å to 59.7 Å and, in this case, the aqueous layers are at the limiting value to host nucleotides. Therefore, we conclude that this second group is probably composed by uncomplexed lamellar phases, whereas the first one is formed by smectic lipid phases complexed with DNA. The absence of the diffuse peak between smectic orders and the lack of knowledge on the exact concentration of nucleotides in each phase make it difficult to interpret the DNA assembling in this phase. As discussed before, for very low concentrations of nucleotides ($\rho \geq 29$), the rods should be isotropically distributed in the intermembrane water channels. A possible insight to get some information about

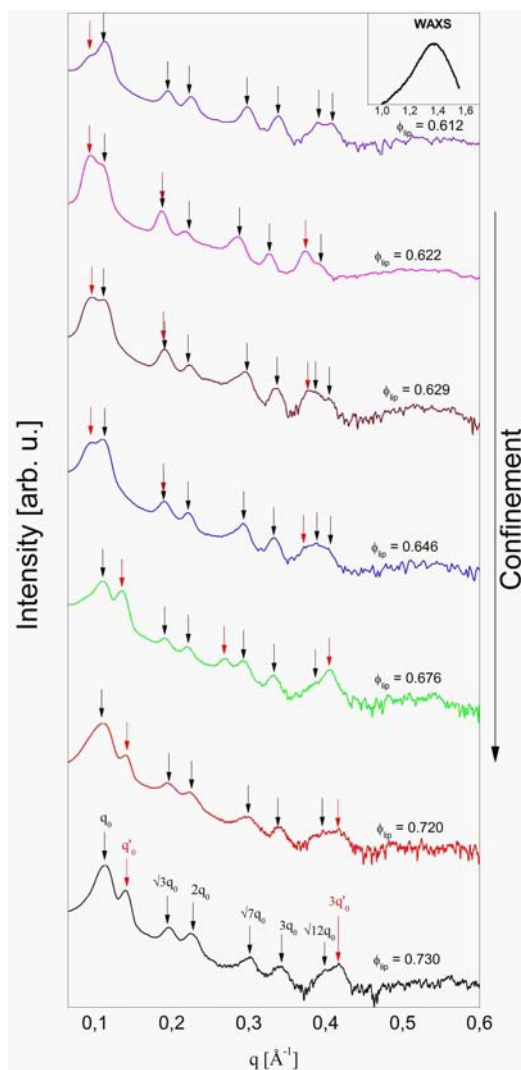


Figure 3.50: Diffractograms from samples with $\rho = 5.1$ and ϕ_{lip} between 0.612 and 0.730. Hexagonal symmetries were identified together with lamellar phases.

the amount of DNA in each phase would be to perform image analysis over fluorescence images and compare the light intensities between bright and dark zones [23]. However, since YOYO fluorescence depends closely on orientation, and we could not assure linearity of detection, we think that this approach can be used only in a roughly qualitative manner, being not meaningful to extract quantitative data. Therefore, we are not able to determine precisely the organization of nucleotides within the aqueous layers.

The dry domain *III* also presents a coexistence between two lamellar phases. One of these phases hosts a 2D hexagonal structure of nucleotides. Similarly to the behavior observed along the line $\rho = 3.1$, the lattice parameter a decreases slightly as the lipid concentration increases and reaches a minimum value of $a = 64.1 \text{ \AA}$. The organization of nucleotides within of the other lamellar phase is somewhat more complicated. Again, the lack of knowledge on the exact concentration of DNA does not allow to determine the exact assembly. For concentrations in the vicinity of $\phi_{lip} \approx 0.625$, it is observed the same characteristics of epitaxy found along the line $\rho = 3.1$, with the coexisting lamellar phase presenting periodicities around 65 \AA . This leads to the conclusion that, for these

samples, the organization of nucleotides is nematic-like. On the other hand, for samples with $\phi_{lip} > 0.650$, the repetition distance is quite lower, around 45 Å. Obviously, in this last case, there is no DNA embedded between the membranes.

The intermediate domain *II* is a region of transition. This characteristic is evidenced when one regards the behavior of the lamellar periodicity as the continuation of the hydrated domain *I* (values around 70 Å). The coexisting phase, in turn, also seems to be continued in the dry domain *III* (values around 55 Å). One of the lamellar phases hosts 2D simple rectangular DNA lattices. The ordering of nucleotides in the other lamellar phase is nematic for an overall $\phi_{lip} = 0.601$. For the other samples, it cannot be exactly determined due to the reasons described above.

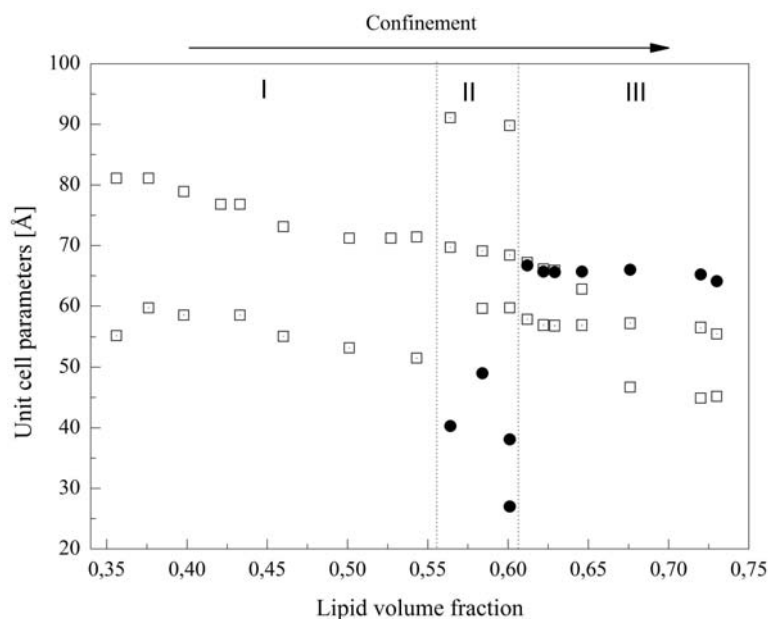
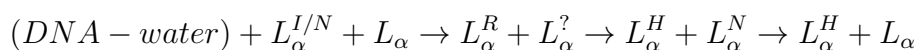


Figure 3.51: Behavior of the structural parameters for dilution line $\rho = 5.1$. Squares represent the smectic spacing of the lipid phase and circles, the separation between DNA rods. Dashed lines: guide for the eyes representing the approximate location of the boundaries between domains. Domain I: lamellar + lamellar, domain II: lamellar + rectangular, domain III: lamellar + hexagonal

At contrast to the data observed along the line $\rho = 3.1$, here single-phase domains are not found. The interpretation of the behavior of mesophases along the line $\rho = 5.1$ can be summarized as follows:



Dilution line $\rho = 8.1$

Samples with $\rho = 8.1$ were prepared with lipid volume fractions comprised between 0.382 and 0.773. The equivalent hydration range is situated in the interval $0.128 < \phi_{wt} < 0.572$.

In Fig. 3.52, it is shown the scattering profiles from diluted samples for which the

lipid amount is $\phi_{lip} < 0.535$. Similarly to the two lines described previously, we find two sets of Bragg peaks arising from lamellar phases. One of these sets, pointed by stars, corresponds to a long-range ordered structure whereas the other one, indicated by black arrows, is associated to short-range ordering. The behavior of the periodicity is also analogous to the one observed in the other lines. In the WAXS region, the typical broad peak from the fluid carbonic tails is found accompanied by the reflection related to water. Polarizing microscopy (see Fig. 3.55(a)) exhibits classical lamellar textures and fluorescence shows strong inhomogeneities. The presence of bright fluorescent zones, co-localized with optical isotropy, points to the formation of a separated (dilute) phase of DNA.

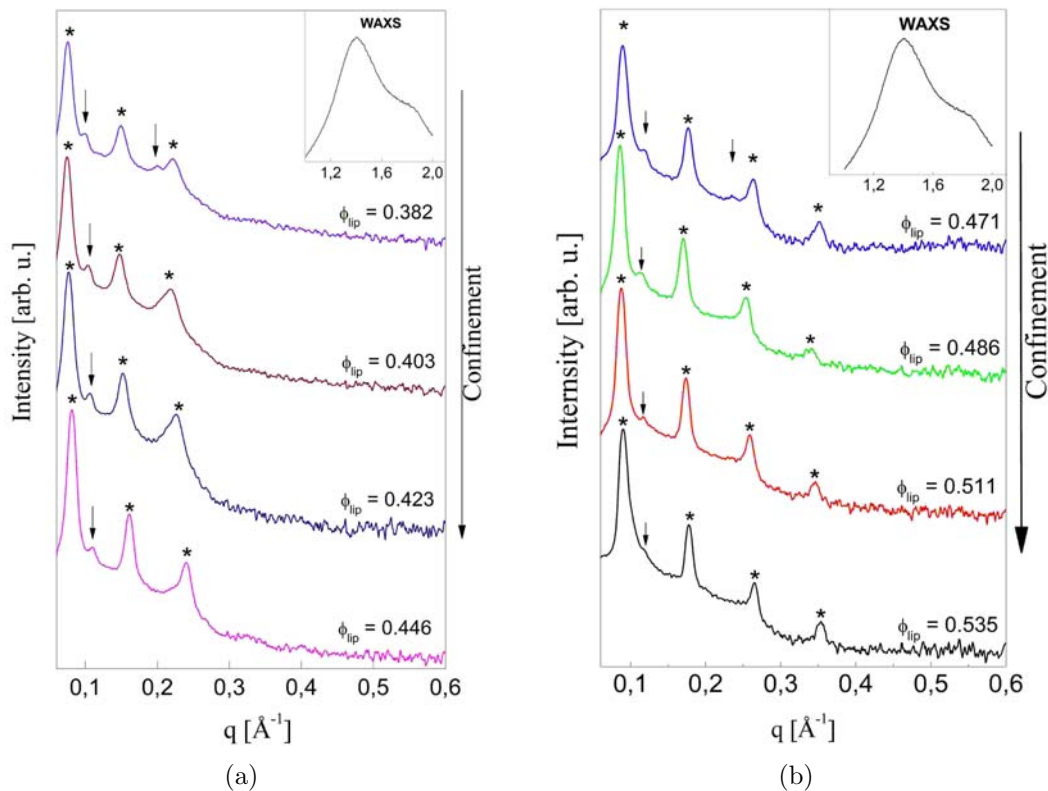


Figure 3.52: Diffractograms from samples with $\rho = 8.1$ and ϕ_{lip} between 0.382 and 0.535. Long-range ordered lamellar phases are indicated by stars whereas arrows point short-range ordered ones. Inset: WAXS shows the fluid state of membranes.

Following the dilution line towards higher amounts of lipids, a more ordered and complex domain appears. In Fig. 3.53, the plots of $I(q)$ vs. q are shown for samples in the range $0.556 < \phi_{lip} < 0.648$. X-rays reveal the presence of a two-phase region wherein lamellar assemblies are found in coexistence with 2D rectangular structures, similarly to the results observed along the line $\rho = 5.1$. The smectic peaks are indicated by red arrows and the reflections arising from the rectangular arrangements are pointed by black arrows jointly with the respective Miller indices between brackets. Wide-angle scattering reveals that the fluid state of membranes does not change.

For the samples with $\phi_{lip} = 0.623$ and $\phi_{lip} = 0.648$, the unambiguous indexation of the crystallographic symmetries is very difficult and hindrances related to the intensities of the

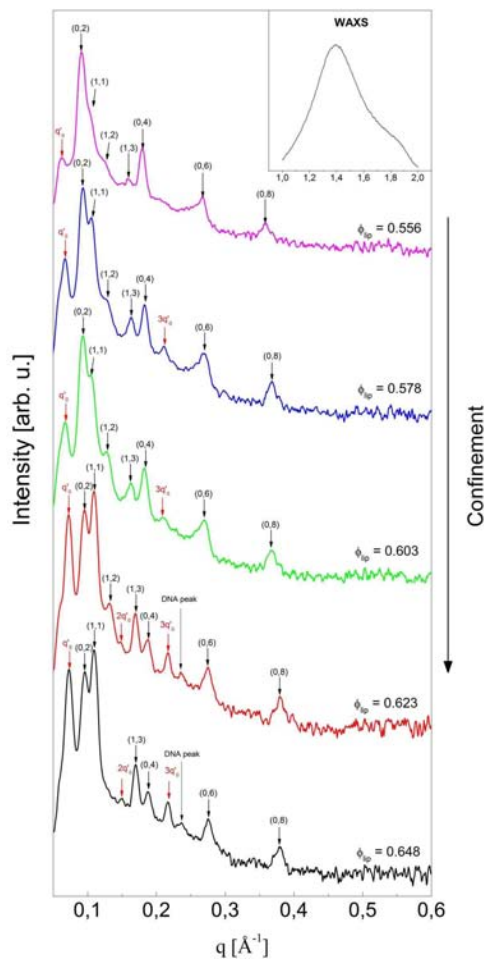


Figure 3.53: Scattering profiles from samples with $\rho = 8.1$ and ϕ_{lip} between 0.556 and 0.648. Lamellar structures are indicated by red arrows whereas indexation of 2D rectangular symmetries are pointed by black arrows with the respective Miller indices between brackets. Inset: WAXS shows the fluid state of membranes.

peaks arise. In Fig. 3.54, these formulations were indexed using a coexisting 2D rectangular lattice. As this superlattice of DNA is embedded in-between the bilayers of a lamellar phase, some peaks from the rectangular lattice appear convoluted with smectic reflections. This is the case of the peaks indexed by $hk = (02), (04), (06), \dots$. However, in principle, we would expect higher values for intensities arising from these peaks than those arising only from DNA structures, $hk = (11), (13), \dots$. In order to examine other possibilities, we tested indexations with the cubic groups $Pn3m$, $Ia3d$ and $Im3m$, traditionally found in lipoplexes and various surfactant-water systems [67, 68, 127, 128, 152]. Nevertheless, these symmetries were not able to successfully describe the peak positions. In addition, cubic phases are optically isotropic and, in polarizing microscopy, only lamellar textures are observed in these complexes (fig. 3.55(c)). Fluorescence reveals non-uniform distribution of DNA in these samples, fig. 3.55(d), a result consistent with two-phase domains. The current 2D rectangular lattice coexisting with a smectic phase is the better indexation that accommodates the set of observations although the relative intensities do not match exactly.

The degree of ordering in the system increases significantly upon the increase of lipid

concentration. For compositions situated in the range $0.668 < \phi_{lip} < 0.714$, a coexisting columnar hexagonal structure appears with lattice parameter a around 65 \AA . This is the region of highest complexity along the dilution line. The diffractograms corresponding to these samples are displayed in fig. 3.54. The formulation with overall lipid amount $\phi = 0.668$ presents a lamellar phase in coexistence with the hexagonal structure. The other two samples, in turn, have a 2D rectangular lattice together with the hexagonal symmetry. As the lipid concentration varies, changes occur only in the phase hosting the rectangular superlattice, whereas the one hosting the hexagonal arrangement remains relatively stable. WAXS confirms the L_α state of membranes and polarizing microscopy shows clearly lamellar textures. In fluorescence, inhomogeneities confirm the absence of monophasic behavior.

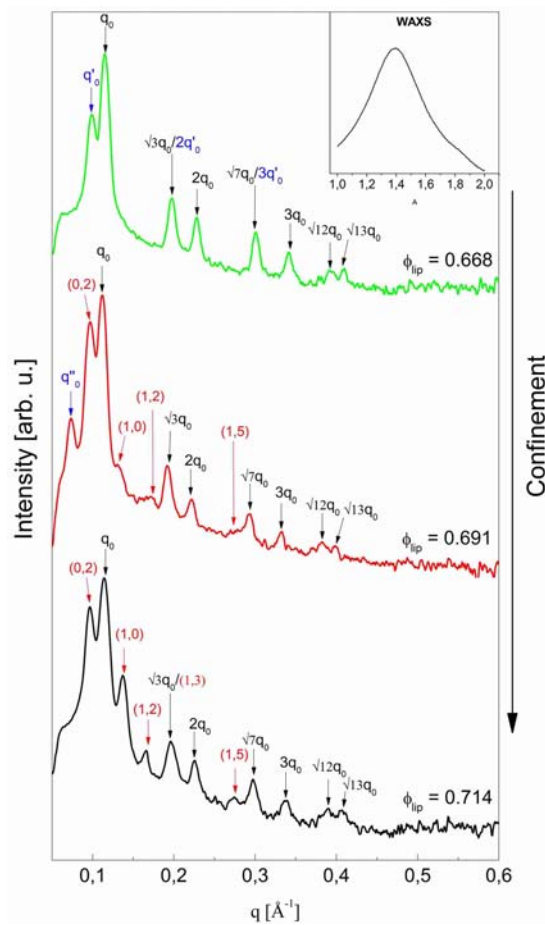


Figure 3.54: $I(q)$ vs. q plots from samples with ϕ_{lip} between 0.668 and 0.714 and $\rho = 8.1$. Black arrows point the peaks from 2D hexagonal structures whereas the red arrows indicate 2D rectangular indexing. Inset: WAXS shows the fluid state of membranes.

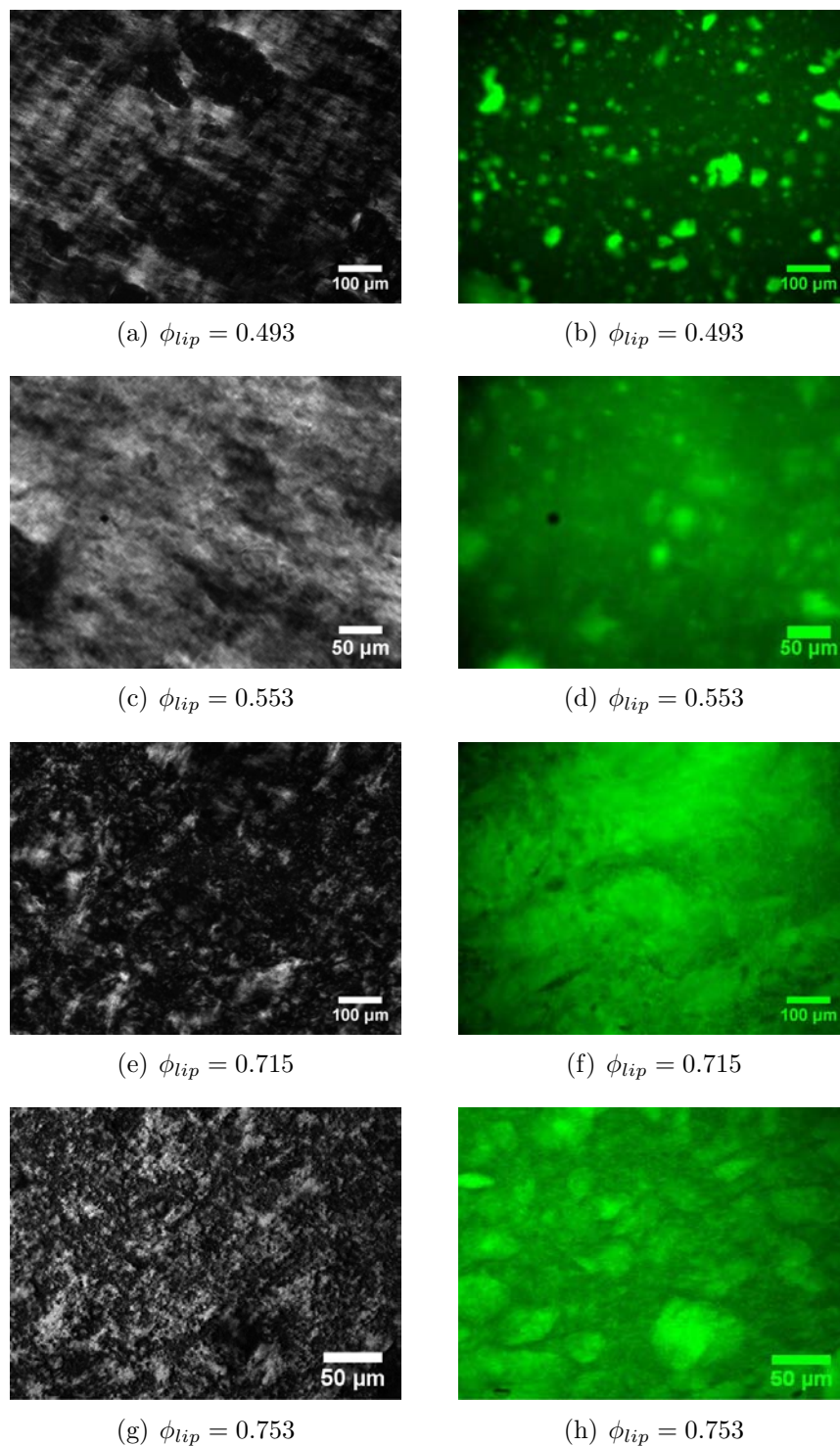


Figure 3.55: Polarizing and fluorescence microscopies of representative samples observed for $\rho = 8.1$. All samples showed birefringent textures and inhomogeneous fluorescence was found throughout this dilution line.

The more concentrated region along the line shows a coexistence between lamellar and 2D hexagonal structures. The diffractograms corresponding to this domain are presented in Fig. 3.56. The lattice parameter of the hexagonal phase remains constant around 65 Å whereas the lamellar periodicity of the associated smectic phase changes upon hydration.

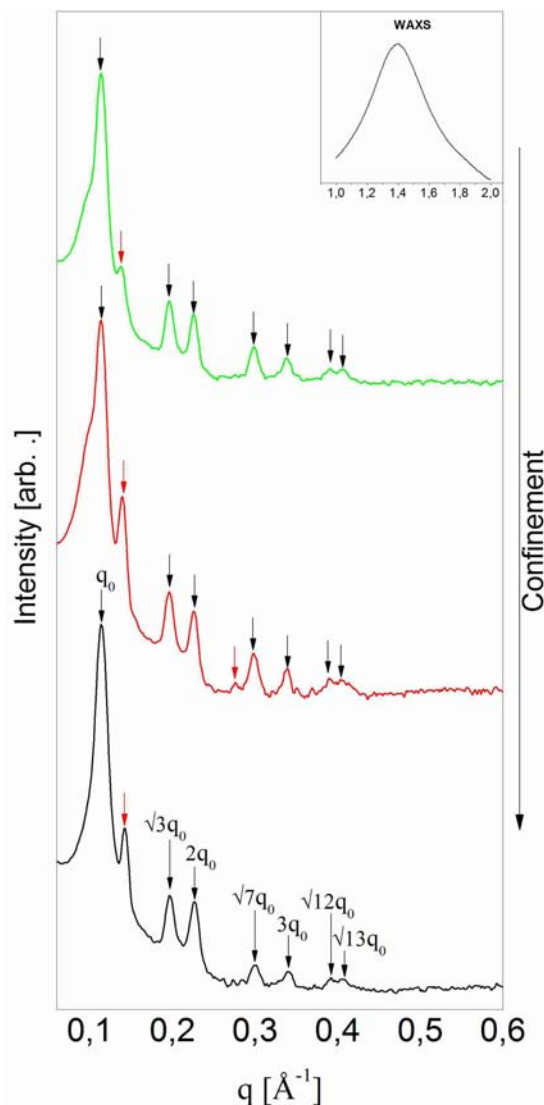


Figure 3.56: Diffractograms from the driest domain along the line $\rho = 8.1$. Hexagonal symmetries are pointed by black arrows and the coexisting lamellar peak is indicated by red pointers. Inset: WAXS shows the fluid state of membranes.

The behavior of the structural parameters arising from X-rays is summarized in Fig. 3.57. The hydrated domain *I* as well as the driest domain *IV* are easier to interpret. The former presents the coexistence between lamellar phases. Two sets of periodicities are observed. The larger periodicity ranges from 71.3 Å to 86.1 Å, close to the dilution limit of the host phase. These values lead to intermembrane spacings larger enough to accommodate DNA rods without steric hindrance: The minimum periodicity to geometrically allow the incorporation of DNA into the lipid phase is $\Phi_{DNA} + \delta_m = 56.5$ Å. The second range of periodicities is comprised between 53.7 Å and 62.9 Å. In this case, we may have either formulations containing nucleotides or uncomplexed lipid phases. The exact

assembly of molecules inside the lamellar matrix, however, remains unknown due to the same reasons as discussed for the other lines. The driest domain *IV* corresponds to the coexistence between a lamellar phase of lipids with $d \approx 45 \text{ \AA}$ and our now “traditional” hexagonal structure hosted in-between bilayers. The first lamellar phase has not sufficient spacing to accommodate DNA rods and it is, therefore, uncomplexed.

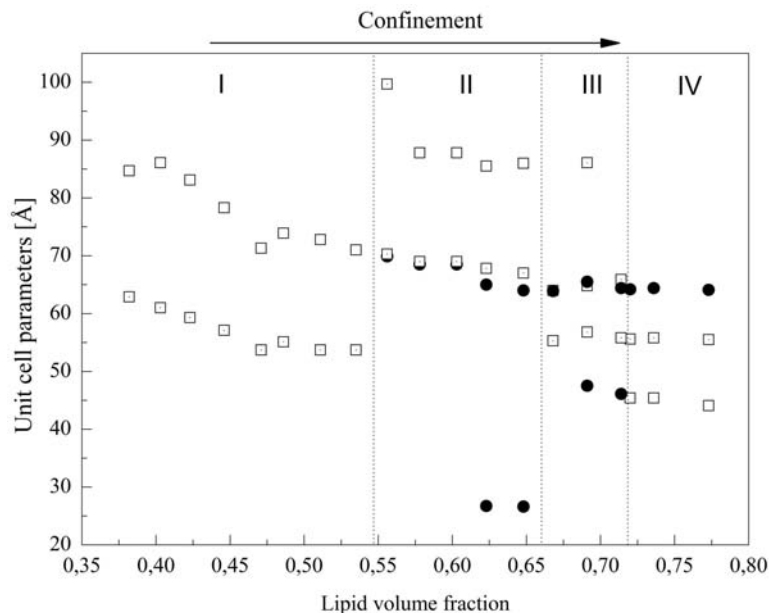
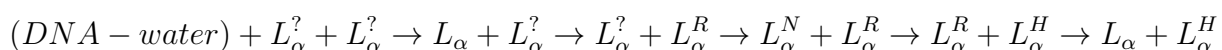


Figure 3.57: Behavior of the structural parameters along dilution line $\rho = 8.1$. Squares represent the smectic spacing of the lipid phase and circles, the separation between DNA rods. Dashed lines: guide for the eyes representing the approximate boundaries between domains.

The domains *II* and *III* are considerably more complex and proper crystallographic determinations have been found very difficult. In domain *II*, we have indexed such formulations by using a lamellar structure hosting a 2D rectangular lattice of DNA together with a second lamellar phase. The periodicity of the coexisting smectic structure is close to the dilution limit, having spacing large enough to accommodate rods with a diameter of 20 \AA . Fluorescence images indicate the presence of DNA inside both phases, however, as the concentration is unknown, the ordering of the nucleotides in this lamellar phase cannot be exactly determined. Nonetheless, for two samples, with $\phi_{lip} = 0.623$ and $\phi_{lip} = 0.648$, distances of *ca.* 26 \AA can be identified between nucleotides (circles at the bottom of the domain), which is an evidence of nematic ordering. The lattice parameters of the rectangular structures are virtually equal, with $a = b$. This means that the cylinders form a *quasi*-square 2D structure embedded in-between bilayers. In domain *III*, a remarkable feature is the presence of epitaxial matches between D_{rect} and a_{hex} . [127].

The phase behavior along the line $\rho = 8.1$ can be summarized as follows:



Phase diagram

In Fig. 3.58, we display the complete experimental phase diagram, as studied here. The very rich polymorphism of mesophases of the system as well the structural transitions between liquid-crystalline arrangements driven by confinement are evidenced. Except for two formulations along the line $\rho = 5.1$ ($\phi_{lip} = 0.53$ and $\phi_{lip} = 0.37$), which were found to be L_α^N phases, all formulations with $\rho \neq 3.1$ were found to self-assemble in coexisting phases. The phase boundary may be close to the nominal composition corresponding to the sample with $\phi_{lip} = 0.53$ at $\rho = 5.1$, and smaller steps in ρ should be investigated in order to clarify this apparent “re-entrant” behavior. Polarizing microscopy showed lamellar textures in all the investigated hydration range, pointing to the persistence of a smectic-like assembly for the lipid phases. Therefore, apart from lamellar structures observed in X-rays diffractograms, the peaks are presumably arising from the supramolecular assembly of DNA rods embedded in-between the bilayers.

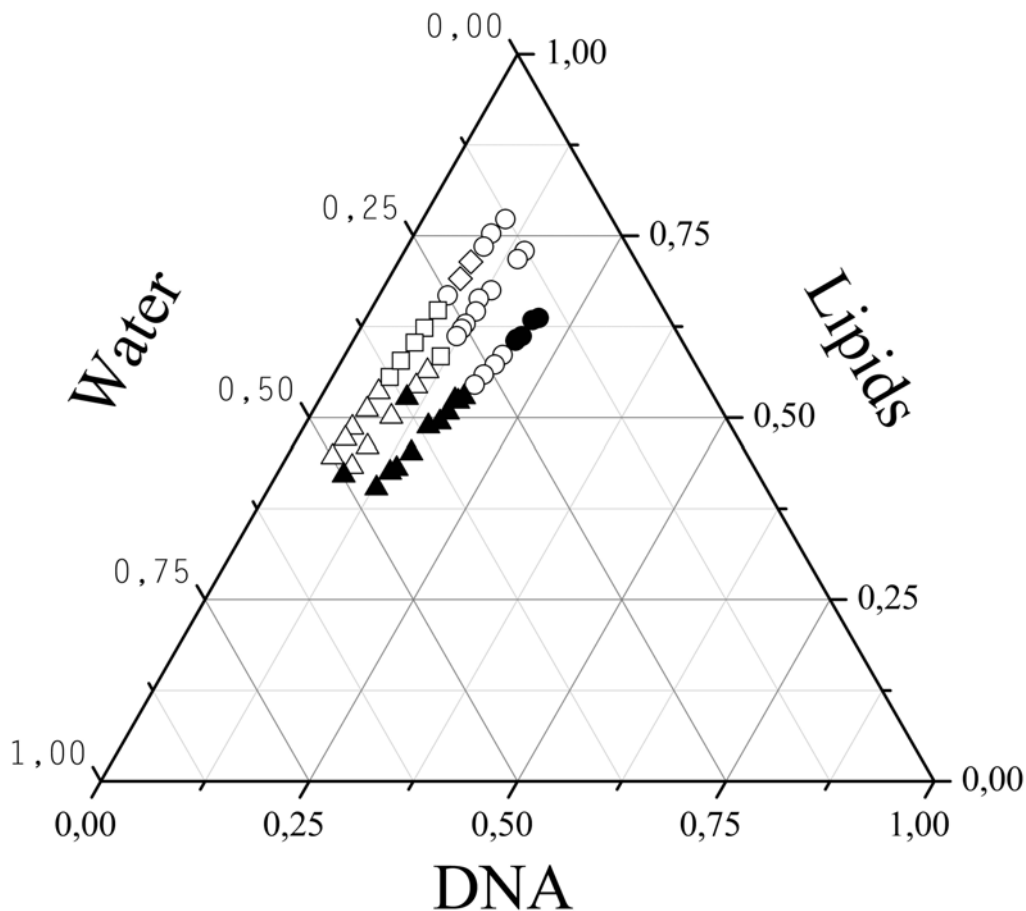


Figure 3.58: Complete phase diagram resulting from the present work. Monophasic domains were systematically observed along the line $\rho = 3.1$ only, in qualitative agreement with the theoretical predictions from reference [17]. Solid symbols indicate single-phase points: $\blacktriangle = L_\alpha^N$, $\bullet = L_\alpha^H$. Open markers represent phase coexistence: $\triangle = L_\alpha^N + L_\alpha^N$ or $L_\alpha^N + L_\alpha$, $\circ = L_\alpha^H + L_\alpha^N$ or $L_\alpha^H + L_\alpha$, $\diamond = L_\alpha^H + L_\alpha^R$, $\square = L_\alpha^N + L_\alpha^H$ or $L_\alpha + L_\alpha^H$.

The question of why the DNA is incorporated completely only for *large* amounts of

nucleotides is an interesting one because, in contrast with cationic lipid systems, here electrostatics is not an obvious candidate to drive complexation. The globally neutral charge of lecithin headgroups as well as the neutrality of the helper surfactant requires other mechanisms to explain the formation of the complex. This matter was theoretically addressed before by using a Flory approach and the authors of reference [17] managed to develop a theoretical phase diagram which is in reasonable agreement with our experiments. Unfortunately, the model does not include a description of the dry region where highly ordered superlattices are found. This difficulty in dealing with dehydrated domains is partially due to the restriction of undulations in strongly confined geometries, as well as to strong, short-range interactions other than steric repulsion becoming increasingly relevant. For strongly confined complexes, the thickness of the aqueous layers is very close indeed to the diameter of DNA rods. This proximity increases steric and other short-range interactions between bilayers and nucleotides in such a way that a model consistently describing the system must compulsorily take into account their interplay, which is beyond the Flory approach.

3.2.2 Membranes with 50:50 PC-to-Simulsol ratio

The phase behavior of DNA-lipids complexes prepared from 50:50 PC-to-Simulsol membranes was also investigated. Since in the previous studies the systematic presence of single-phases domains was found along the dilution line $\rho = 3.1$ only, this lipids-to-DNA ratio was also chosen for these last investigations. Two series of samples, scanning 19 points along the dilution line were prepared in the very same manner as described before. Ten of them were hydrated with pure water whereas the other ones were diluted with brine solutions. The X-rays experiments were carried out at the high-resolution synchrotron beam line described in Sec. 2.3.1. The reduced 1-D diffraction resulting from the “pure water” preparations are exhibited in Figs. 3.59.

The general phase behavior is very similar to the one observed for samples prepared with 70:30 PC-to-Simulsol bilayers, however some differences appear. Formulations containing very low amounts of lipids, that is, $\phi_{lip} \lesssim 0.370$, are characterized by two coexisting lamellar structures. One of these phases is a long-range ordered one, exhibiting up to three Bragg peaks. It should be noted that for samples with the same formulation, but prepared with a lecithin-richer membrane, four lamellar orders were observed in the diffractograms (see the sample with $\phi_{lip} = 0.346$ in Fig. 3.28, for instance). This observation can be interpreted as a direct consequence of the decreasing of the rigidity of bilayers. The other lamellar phase is a short-range ordered one, exhibiting no more than two peaks.

Proceeding towards lower water amounts, the formation of a single-domain, with diffractograms composed by equally-spaced peaks, is observed. Again, this region is interpreted as a nematic assembly of DNA strands intercalated in the water gaps of lipid lamellar phases. In few of these samples the presence of the diffuse peak convoluted between the second and the third lamellar orders can be noticed.

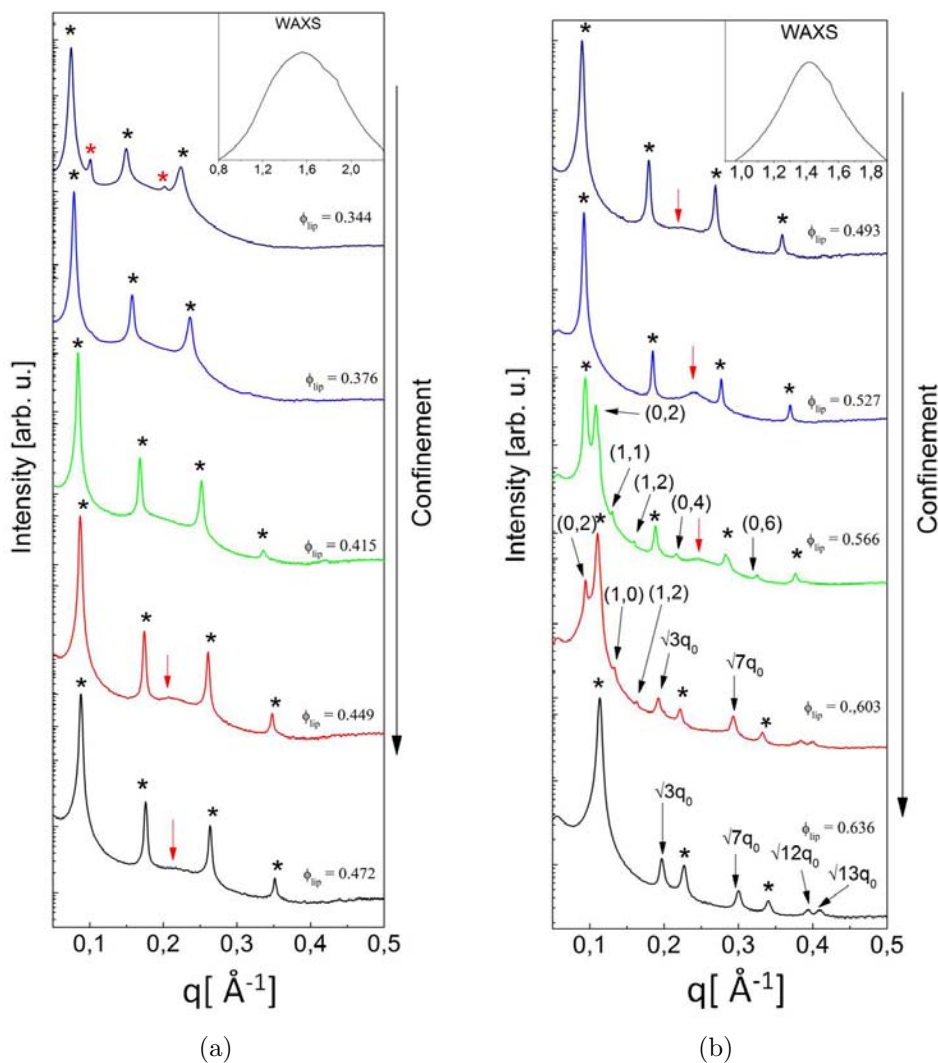


Figure 3.59: Reduced 1-D diffractograms from samples hydrated with pure water whose lipid part was composed by 50:50 PC-to-Simulsol bilayers. Lamellar peaks are indicated by stars. DNA peaks are pointed by arrows. The numbers appearing between (...) are the crystallographic (h, k) planes of a 2D rectangular symmetry. Inset: WAXS diffuse peak due to fluidity of the aliphatic tails.

For samples with $\phi_{lip} = 0.566$ and $\phi_{lip} = 0.603$, the phase behavior is very complex. The emergence of 2D rectangular symmetries is observed for both formulations. The more diluted one is indexed by a coexistence between a rectangular and a lamellar phase. In the other sample, the coexisting symmetry is indexed as being L_{α}^H . At the extremity of the dilution line, the more concentrated formulation with $\phi_{lip} = 0.636$ presents a single L_{α}^H structure.

The data from the salt-containing series are presented in Fig. 3.60. The phase behavior is found to be the same as for the salt-free samples. A notable exception is the region of transition between the L_{α}^N and the L_{α}^H domains. Here, a coexistence between two lamellar phases, one of them containing clearly a nematic peak, is observed.

Data from the WAXS region again show the fluid state of the aliphatic tails for both cases. The structural parameters of the unit cells found in these complexes are highlighted in Fig. 3.61. The dotted lines are guides for the eyes, approximately delimitating the

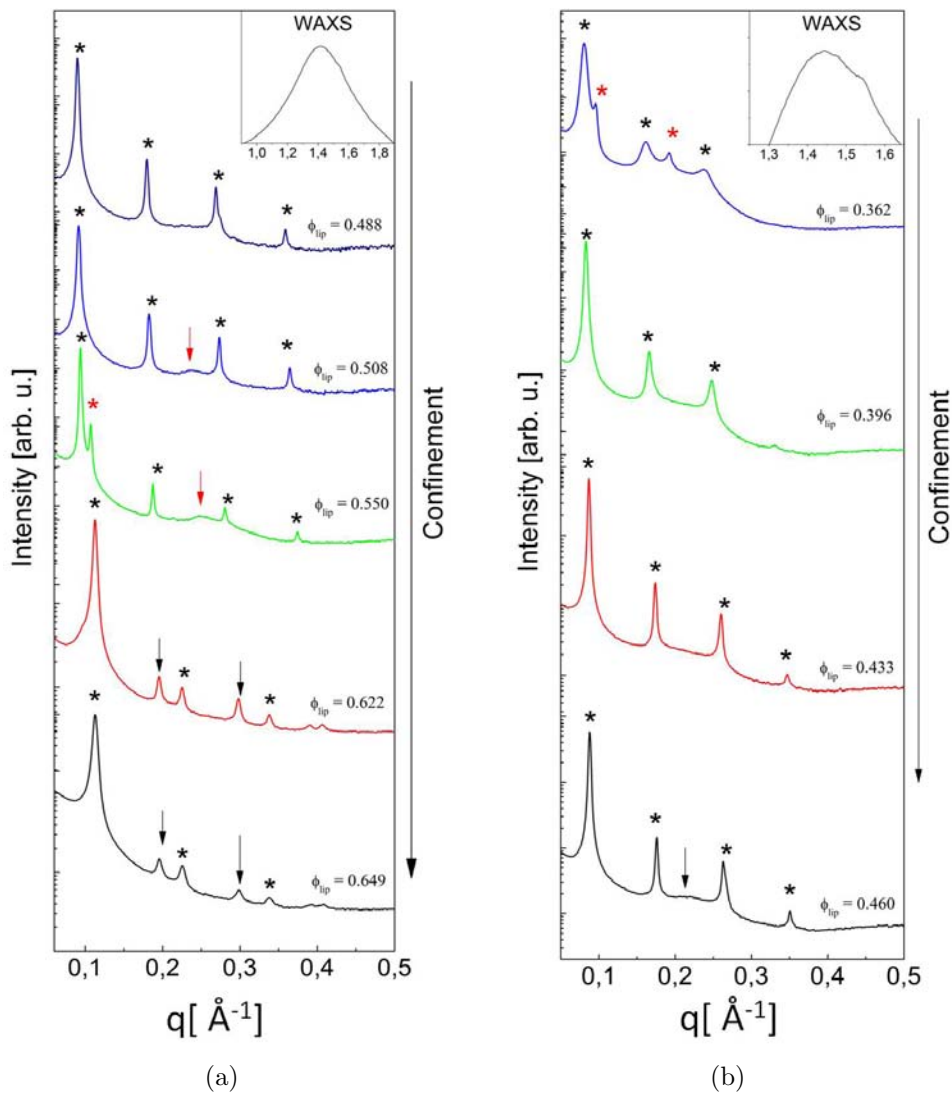
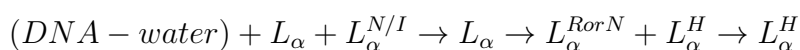


Figure 3.60: 1-D diffractograms from preparations using 0.25 M ammonium acetate solutions as solvent. The lipid part used here was obtained from mixing PC and Simulsol at the ratio of 50:50. Lamellar peaks are indicated by stars. DNA peaks are pointed by arrows. Inset: WAXS diffuse peak due to fluidity of aliphatic tails.

boundaries between the domains. Domain *I* is characterized by the coexistence between a long- and a short-range ordered lamellar phase. Domain *II* is a single-phase region where the rods have nematic orientation in the plane of the membranes of a smectic phase. Region *III* is a complex coexisting domain where rectangular phases appear. In the driest domain, one has another single-phase domain characterized by a hexagonal symmetry.

Comparing the lattice parameters presented in 3.61 with those obtained with the other composition of bilayers (Fig. 3.39), one also observes quantitative similarities. The lattice parameters of the hexagonal phases, for instance, are around 65 Å, the very same value as obtained before. The range of periodicities and the DNA-DNA distances are also very close in quantitative terms. The phase behavior described above can be summarized as follows:



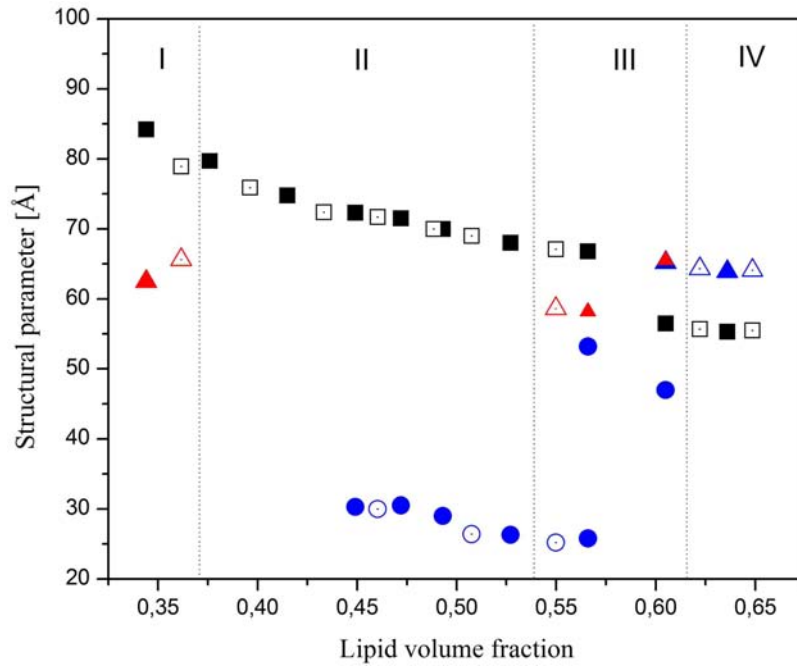


Figure 3.61: Structural parameters of unit cells as function of lipid volume fraction for samples prepared with bilayers containing 50:50 PC-to-Simulsol ratio. Squares are the lamellar periodicity and circles, the distance between DNA fragments. Solid symbols correspond to samples hydrated with pure water, while empty marks indicate preparations hydrated with brine solutions.

3.3 Discussion

3.3.1 Varying the DNA amount

In fig. 3.62 diffraction data from samples with different DNA amounts are shown together. As the hydration amount was kept constant, the resulting lamellar periodicities are approximately the same for all formulations, with $d \approx 73 \text{ \AA}$.

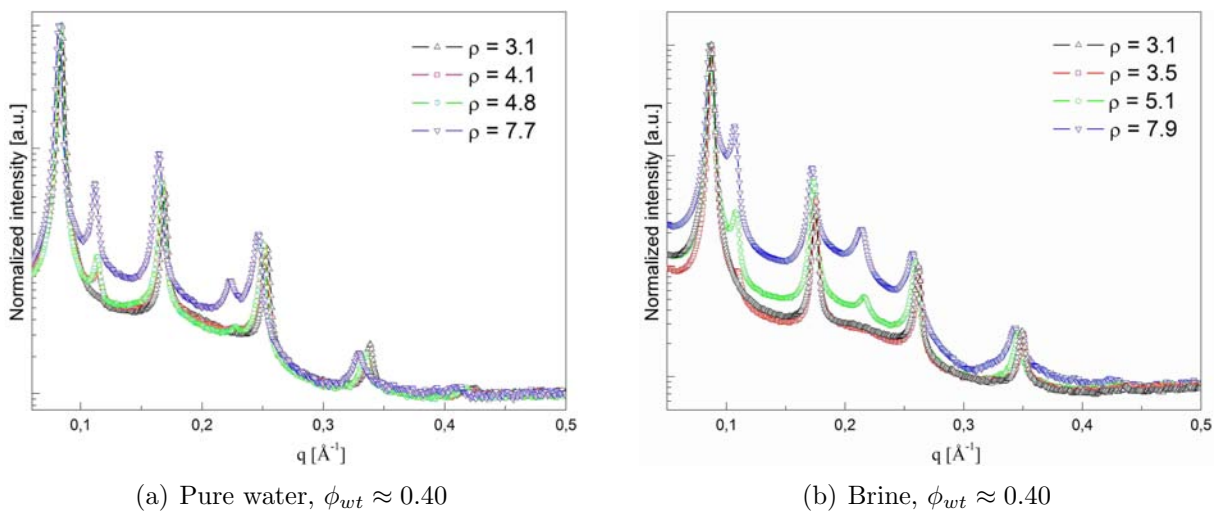


Figure 3.62: Comparison among samples with different values of ρ , prepared from membranes with 70:30 PC-to-Simulsol ratio. The lamellar periodicity is approximately the same for all formulations with $d \approx 73 \text{ \AA}$.

With this simple comparison, it is possible to notice two coexisting smectic repeating distances for $\rho > 3.1$. The second lamellar phase is presumably made with an excess of lipids forming an uncomplexed phase. As the DNA amount increases, however, the peaks associated to this second structure decrease in intensity and, for $\rho = 3.1$, only reflections from a single lamellar phase are observed. This observation is a clear illustration of the dependence on ρ for the DNA complexation in these systems formulated from neutral lipids.

In Fig. 3.63, this same comparison is done with data obtained from 50:50 membranes. This time, except for a very weak shoulder on the curve from $\rho = 8.1$ (blue curve in Fig. 3.63(b)), the samples are monophasic. This finding suggests that the elastic properties of the host phase also play a relevant role on the complexation, which reinforces the major importance of steric undulation interactions in driving the intermolecular relationships within the system studied in this work and qualitatively supports the Flory approach given by the authors of Ref. [17].

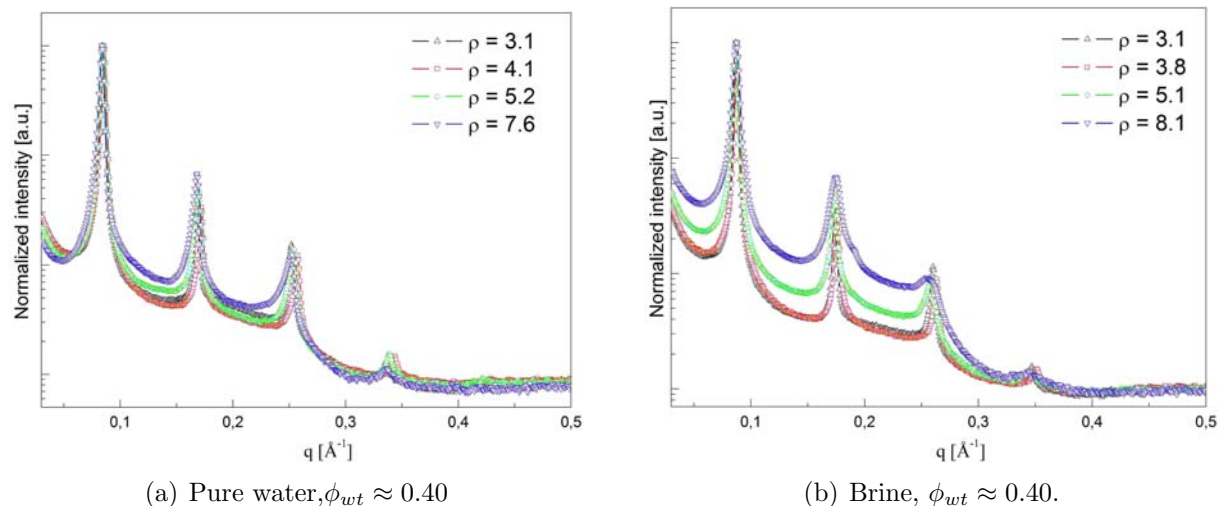


Figure 3.63: Comparison among samples with different values of ρ , prepared from membranes with 50:50 PC-to-Simulsol ratio. The lamellar periodicity is approximately the same for all formulations with $d \approx 73$ Å.

Below, we discuss some consequences of the introduction of nucleotides in-between the bilayers.

3.3.2 Effects of DNA on the smectic ordering of L_α phases

Besides the formation of polymorphic superlattices embedded between bilayers, we observed that the introduction of DNA has dramatic effects on the very ordering of the lipid phase. In Fig. 3.64, we present a comparison between three spectra from samples with and without nucleotides but with approximately the same lamellar periodicity. The membrane composition is 70:30 PC-to-Simulsol. The DNA-containing systems were evaluated under different ionic strengths, that is, with or without ammonium acetate (0.25 M) in the solvent. One can note that, in spite of the latter similarity, the DNA-containing

phases are significantly more ordered than the system without DNA. This increase in smectic ordering is clearly evidenced by the appearance of the third and fourth lamellar orders, together a narrowing of the Bragg peaks. Diffuse scattering is remarkably distinct, too. While in the binary system there is a form factor broad maximum around $q \approx 0.370 \text{ \AA}^{-1}$, in the ternary complex, this region is quite distinct with a very strong reflection on top of what appears to be rather close to a form factor *minimum* associated to the fourth lamellar order. This difference between the form factors may be associated to changes introduced by the anionic behavior of DNA into the electron density profile of the system [93]. In addition, as discussed before, the diffuse signal between the second and third lamellar orders for the DNA-containing systems arises from correlations between nucleotides, that is to say, a structure factor contribution.

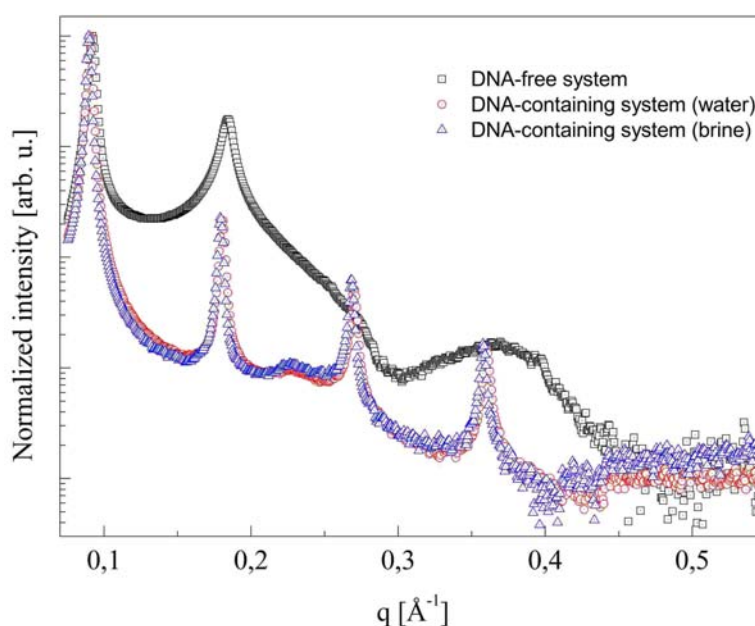


Figure 3.64: Comparison of spectra from samples with and without DNA. The lamellar periodicity is around 68 \AA . Inserting the nucleotides in-between bilayers is observed to significantly enhance the smectic ordering, with the appearance of third and fourth lamellar orders as well as the narrowing of all the previously observed peaks. Differences between salt-containing and salt-free samples are negligible.

The samples whose spectra are represented in 3.64 have lipid volume fractions around 0.51. This composition allows to place the X-rays data from these formulations in the same context of the direct space images exhibited in figs. 3.12(c) and 3.40(a), which show clearly differences of ordering between DNA-free and DNA-containing samples. In the case of the DNA-free formulation, fig. 3.12(c), it is possible to observe the corrugations on the borders of membranes whereas in the DNA-containing sample, fig. 3.40(a), they virtually disappear.

These findings show that DNA addition induces a type of “hardening” in the system, increasing the number of correlated layers and decreasing the amplitude of fluctuations. In order to tentatively explain such effect, we wish to present two conjectures. In the first one, short-range direct interactions between adjacent membrane surfaces would be mediated

by the inserted particles. The soft nature of the forces involved in the stabilization of the lamellae (van der Waals, hydration and undulations) would then be somewhat modified by the rigid structure of DNA which would act as “cement” of the complex. In the second conjecture, the rods between bilayers would restrict the space available for membrane fluctuations, resulting in an enhanced purely steric repulsion, as has been observed in lamellar phases hosting (spherical) colloidal particles [153–155]. Such a restriction would decrease disorder, allowing a growth in the number of correlated layers. Moreover, this mechanism could also be related to the formation of organized DNA lattices. Indeed, in other studies in the literature, the appearance of ordered structures embedded in multilamellar phases seems to be closely associated to the reduction of fluctuations. In references [65] and [156], centered-rectangular phases appear associated to $L_\alpha \rightarrow L_\beta$ transitions. In reference [66] a simple rectangular structure emerged by varying the temperature and, in [21], columnar hexagonal phases were obtained from steric confinement. In all these cases, a common feature is the reduction of membrane fluctuations in such a way that the latter could be a general agent driving the phase behavior.

In order to get some quantitative estimation on this effect, a typical sample from the L_α^N domain, with $\rho = 3.1$ and $\phi_{lip} = 0.508$ and smectic spacing $d = 66.4 \text{ \AA}$, was selected and fitted following the same procedure as described in section 3.1.1. It should be emphasized that Nallet’s approach was originally developed to describe scattering from pure (membrane–solvent) lyotropic lamellar phases and, therefore, it does not take into account the presence of nucleotides in-between bilayers. Nevertheless, such a model has been successfully used to describe X-rays diffraction from polymer-doped smectic phases [94, 95]. Here, for samples from the L_α^N domain, the DNA peak is well localized between the second and the third lamellar orders. Since the range of the interactions between nucleotides is short, contributions from higher orders due to DNA-DNA correlations are assumed to be negligible. Therefore, if the region containing the diffuse DNA peak is excluded from the fitting process, the structure factor of the ternary system is, in a first approximation, described by $S(q)$ as given in Eq. 1.22. On the other hand, the part related to the form factor is not correctly modeled by Nallet’s approach. Thus, for our purposes here, the parameters of $P(q)$ are left free to be adjusted and the obtained values may not have any physical meaning. The best fit obtained with the above-proposed attempt is shown in Fig. 3.65.

Comparing the diffractogram presented in Fig. 3.65 and a binary sample with equivalent periodicity (see the sample with $\phi_{lip} = 0.550$ in table 3.1 and fig. 3.17(a)), the parameter of Caillé decreases from $\eta = 0.13(1)$, in the DNA-free system, to $\eta = 0.02(1)$, when nucleotides are inserted in-between bilayers. Similarly, the amplitude of fluctuations, calculated from the root square of Eq. 3.3, decreases from $\sigma = 7.6(5) \text{ \AA}$ to $\sigma = 3.2(1.0) \text{ \AA}$. Although these results are only rough estimations, they allow to state that incorporation of DNA to the smectic phase increases the smectic ordering by a factor ≈ 6 , in terms of η , whereas the amplitude of fluctuations is reduced. It should be noted that these effects

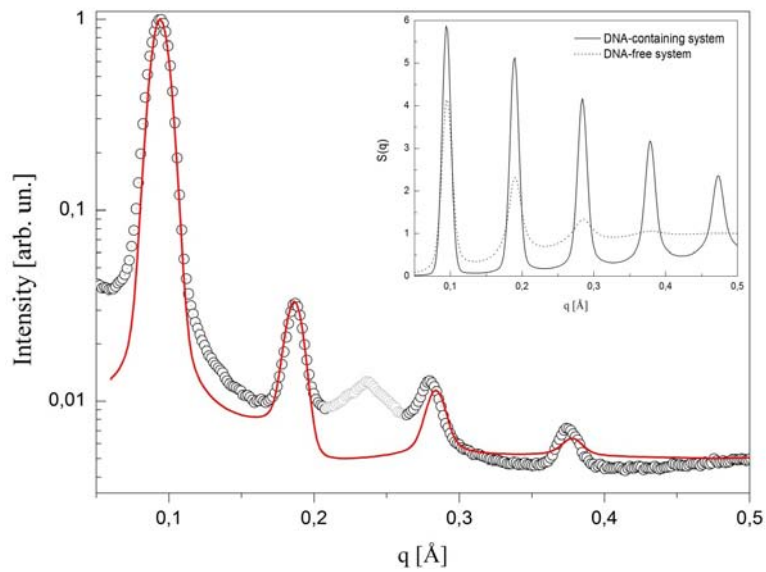


Figure 3.65: Diffractogram from a typical sample, with $\phi_{lip} = 0.508$ (70:30 PC-to-Simulsol) and $\rho = 3.1$, fitted with the model of Nallet et al. The diffuse peak arising from DNA-DNA correlations, in gray, was excluded from the fitting process which led to the following adjusted parameters: $d = 66.4 \text{ \AA}$ and $\eta = 0.02(1)$. N was estimated to be 60. Inset: structure factor from the DNA-containing system compared to a binary sample with equivalent periodicity.

are not associated to transitions in the fluidity state of the membranes, since the usual characteristic diffuse peak appears at the wide-angle region in all cases. On the other hand, it has been shown that such behavior is independent upon salt addition. Therefore, the increase in smectic ordering seems to be induced by steric interactions between DNA cylinders and bilayers.

CHAPTER 4

DYNAMICAL RESULTS

4.1 Simulations

Few simulations were carried out in order to test the concept introduced in Sec. 1.8 and evaluate the consistency of the analysis procedure. The basic idea consisted in using the equations of Brownian dynamics, 1.26, to generate FRAP images for further fit by the proposed expression 1.33.

These “virtual experiments” were performed with a MatLab routine kindly provided by the authors of Ref. [113], which has been modified to incorporate the anisotropic diffusion of DNA fragments within lamellar phases. This software allowed the simulation of diffusion inside only one aqueous layer. A second tool was specially designed, under the Java-based platform *ImageJ* [157], to process the projection of several layers and to approach the situation of membranes homeotropically aligned along the axis of the microscope. In order to make the computer images more realistic, a 2 % of random noise was introduced to the final images. The simulation parameters were the diffusion coefficients D_{\parallel} and D_{\perp} , the time interval between records, the total number of records, the bleach duration and the pixel-to-length ratio.

4.1.1 Isotropic case

The case of isotropic diffusion was studied first. A temporal sequence of FRAP images was generated with $D_{\parallel} = D_{\perp} = 0.025\mu m^2/s$ and initial Gaussian shape of variance $w_0^2 = 1\mu m^2$. The bleach duration was chosen to be 2 s and the spatial scale was kept at 0.05 pixel/ μm . The total number of images was 15, totalizing 30 seconds of diffusion. In Fig. 4.1, selected images from this series are exhibited together with the respective azimuthally averaged spatial profiles.

The time evolution of the spot is easily observed, with the increasing of the bleached width and the vanishing of its amplitude. The fluorescence profile is perfectly fitted by

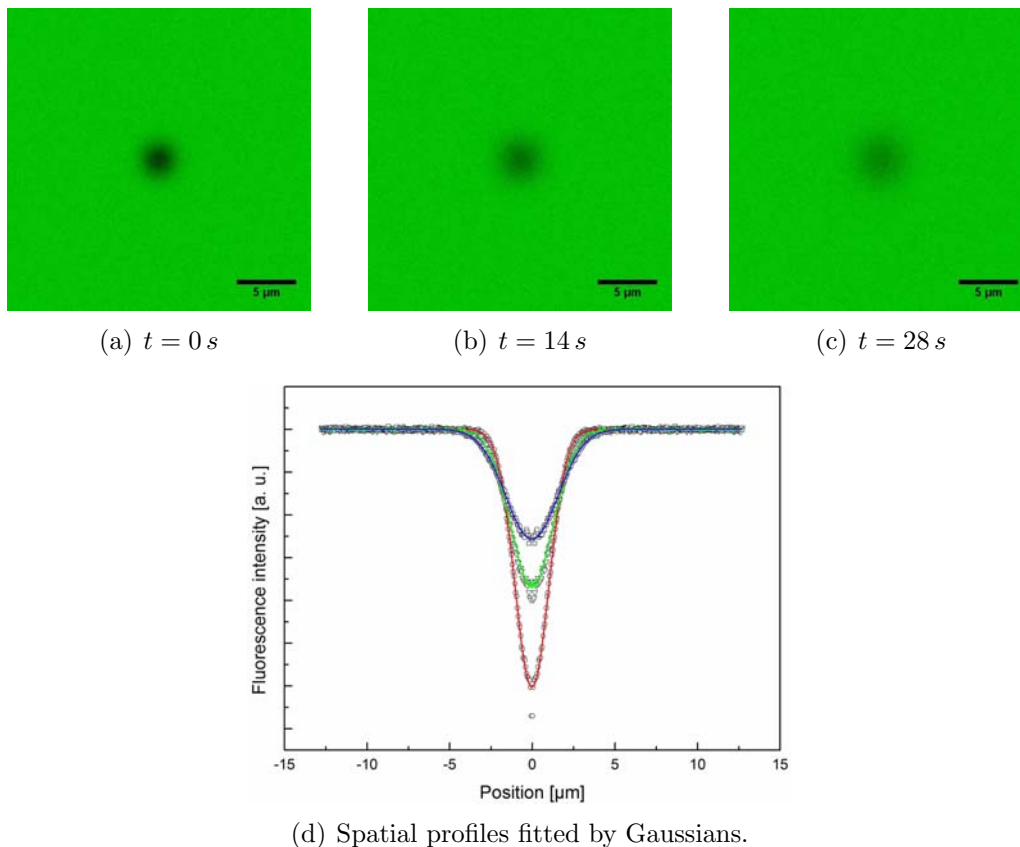


Figure 4.1: (a)-(c) Time evolution of the simulated bleached spots for an isotropic diffusion. In (d), the spatial profiles appear fitted by Gaussian functions.

Gaussian functions, attesting the isotropic behavior of diffusion. The time evolution of variances throughout the simulation are plotted in Fig. 4.2. The mobility ratio is extracted from the slope giving a value of $D = 0.0257(4)\mu\text{m}^2/\text{s}$, in close agreement with the chosen simulation parameter.

4.1.2 Anisotropic case

After the analysis of the simpler case of isotropic diffusion, attention was focused on the anisotropic case. As a preliminary step, a temporal series of FRAP images, simulating the diffusion inside ONE layer, was generated with $D_{\parallel} = 2.5 \times 10^{-2}\mu\text{m}^2/\text{s}$ and $D_{\perp} = 2.5 \times 10^{-3}\mu\text{m}^2/\text{s}$. The time interval between records was $\Delta t = 10\text{s}$, with a total number of 15 images. The pixel-to-length ratio was the same used above.

As expected, the resulting spots have elliptical shape with major and minor semi-axis parallel and perpendicular to the directions of fast and slow motions, respectively. Since the mobility is simulated on the basis of Brownian motion, the spatial profiles along each semi-axis are properly described by Gaussian functions. A typical example of these anisotropic spots is shown together with the corresponding 3D profile in Fig. 4.3. The elliptical shape is evidenced. In the 3D image, it is possible to observe a Gaussian profile along the major semi-axis.

The projection along the axis z was obtained by averaging 180 elliptical spots, rotated

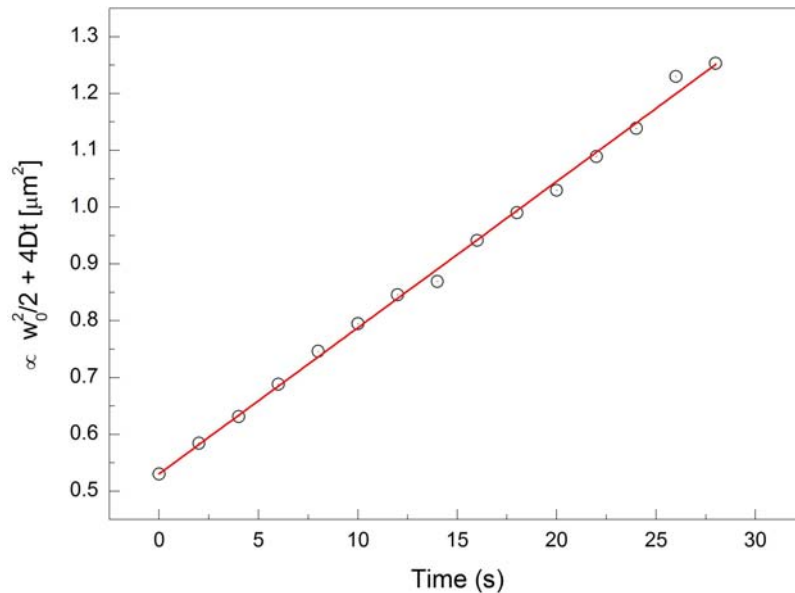


Figure 4.2: Increase in time of the variance along the series simulating isotropic diffusion. The slope of the linear fit gives a value of $D = 0.0257(4)\mu\text{m}^2/\text{s}$.

in steps of 1 degree around the image center. This procedure is equivalent to the angular averaging performed in Eq. 1.30 and corresponds to the superposition of several equivalent layers with local nematic directors sampling the interval $[0, \pi]$. The bleached spots have circular symmetry, very similar to the ones observed in the isotropic case (Fig. 4.1(b)).

The fluorescence intensity profiles along cross sections, however, are quite different from the Gaussian form observed in isotropic diffusion. In Fig. 4.4, an image arising from this process is presented together with the respective spatial profile. The lines in 4.4(b) are fits by a Gaussian function and by the modified Eq. 1.33. The non-Gaussian features are strikingly illustrated, specially regarding the region of the tails and the peak, where the data is far from the Gaussian curve. On the contrary, data is much better described by the functional form of 1.33, with now two distinct parameters extracted from the data. The broader and more slowly-decaying tails as compared to the Gaussian function are now satisfactorily accounted for in the same illustrative case.

The temporal behavior of the two adjusted variances, w_{\parallel}^2 and w_{\perp}^2 , is presented in Fig. 4.5. The diffusion coefficients are found to be $D_{\parallel} = 0.0220(7)\mu\text{m}^2/\text{s}$ and $D_{\perp} = 0.0023(1)\mu\text{m}^2/\text{s}$. These values are in good agreement with the values of the chosen simulation parameters, specially regarding the anisotropy ratio $D_{\parallel}/D_{\perp} = 9.6$, quite close to the expected one is 10.

It should be noted that the above-described simulations were made *independently* of the analysis procedure. In other words, the equation used to fit the data was not used during the creation of FRAP images. Conversely, the temporal series of spots were generated exclusively by using the bi-dimensional form of the Brownian diffusion, Eq. 1.26. The convoluted images, in turn, were obtained by simply summing numerous equivalent, but slightly rotated, layers.

The fact that the model allows to distinguish between isotropic and anisotropic cases,

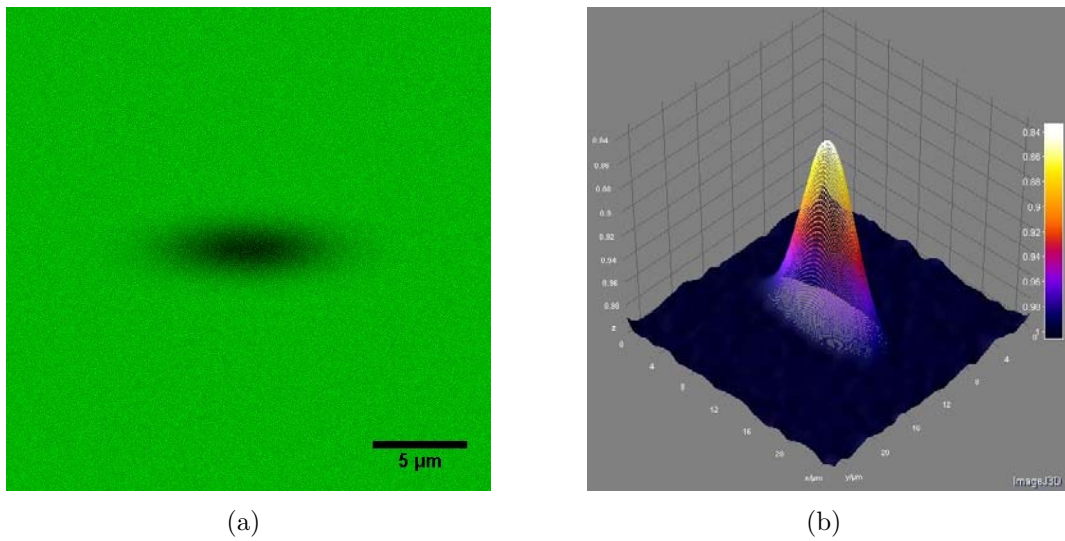


Figure 4.3: Simulated FRAP spot for anisotropic diffusion inside one layer with local nematic ordering.

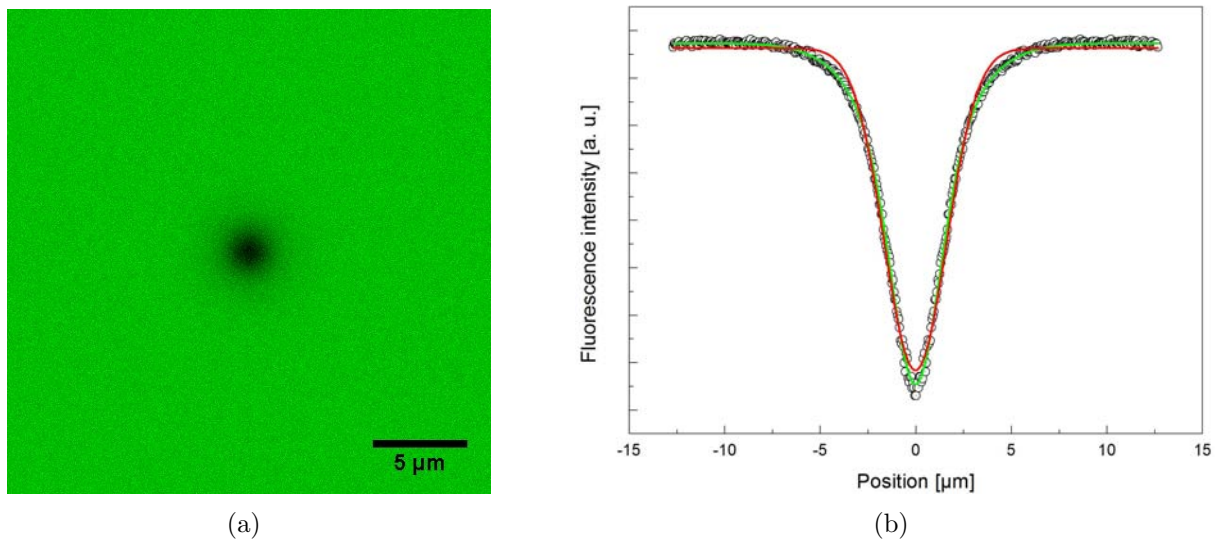


Figure 4.4: (a) FRAP image resulting from the averaging of 180 scans, uniformly rotated in the interval $[0, \pi]$. (b) Cross-section spatial profile of the fluorescence intensities. The solid lines correspond to fits by a Gaussian function (red) and by the modified form proposed in Eq. 1.33 (green).

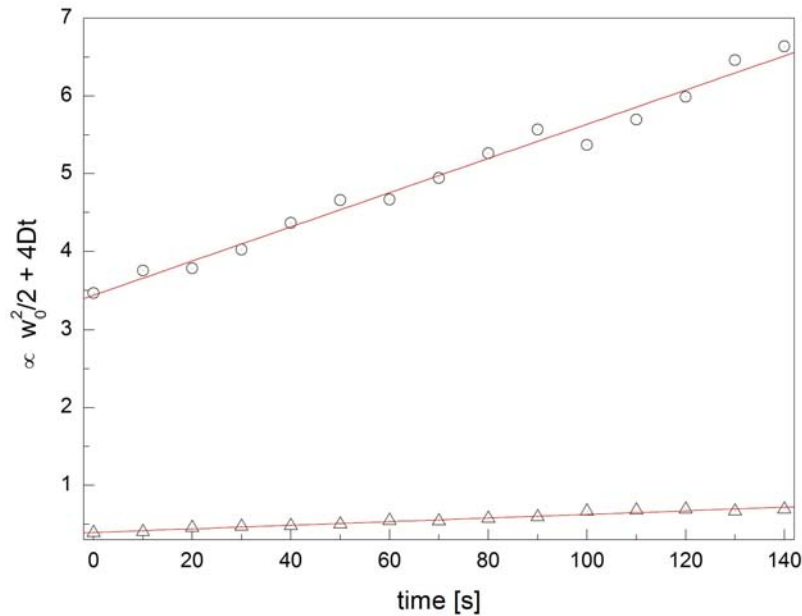


Figure 4.5: Temporal behavior of the two variances obtained from fits of Eq. 1.33 to simulated data. The obtained diffusion constants are $D_{\parallel} = 0.0220(7)\mu\text{m}^2/\text{s}$ and $D_{\perp} = 0.0023(1)\mu\text{m}^2/\text{s}$, in good agreement with the chosen parameters.

and gives quantitative mobility ratios in close agreement with the simulation parameters, illustrates the robustness of the Dobrint’s proposition. With confidence on the reliability of the model, the following stage now focuses on real experiments.

4.2 Experiments

4.2.1 Isotropic DNA-water system

Experiments on dynamics started by the analysis of diffusion in an aqueous solution of DNA fragments, without the lipid lamellar phase. The goal of this preliminary step was to probe the instrumental parameters necessary for successful FRAP investigations and to gain experience with the analysis procedure under real experimental conditions.

A systematic study of diffusion in DNA aqueous solutions, using the same analysis tool employed in this work, was conducted before in Ref. [109]. Here, only the results for a sample containing 80 mg of DNA per ml are presented¹. At such concentration, the solution is expected to be in the isotropic phase, near the boundary with the so-called *pre-cholesteric* domain [31]. A slide-cover glass sandwich was prepared and examined according to the procedure described in Sec. 2.6. The bleach duration was 500 ms, the time interval between records was 326 ms and the total number of recorded images was 13.

Three selected examples of the temporal series obtained from this sample are shown in Fig. 4.6. Despite the fact that the recovery scans are quite noisy due to the relatively low

1. The experiments on DNA aqueous solution were carried out in close collaboration with Cassio Alves, PhD. student at IFUSP.

concentration of fluorophores, Gaussian shapes give a very good description for the data. This behavior corresponds to the classical signature of Brownian diffusion in isotropic media.

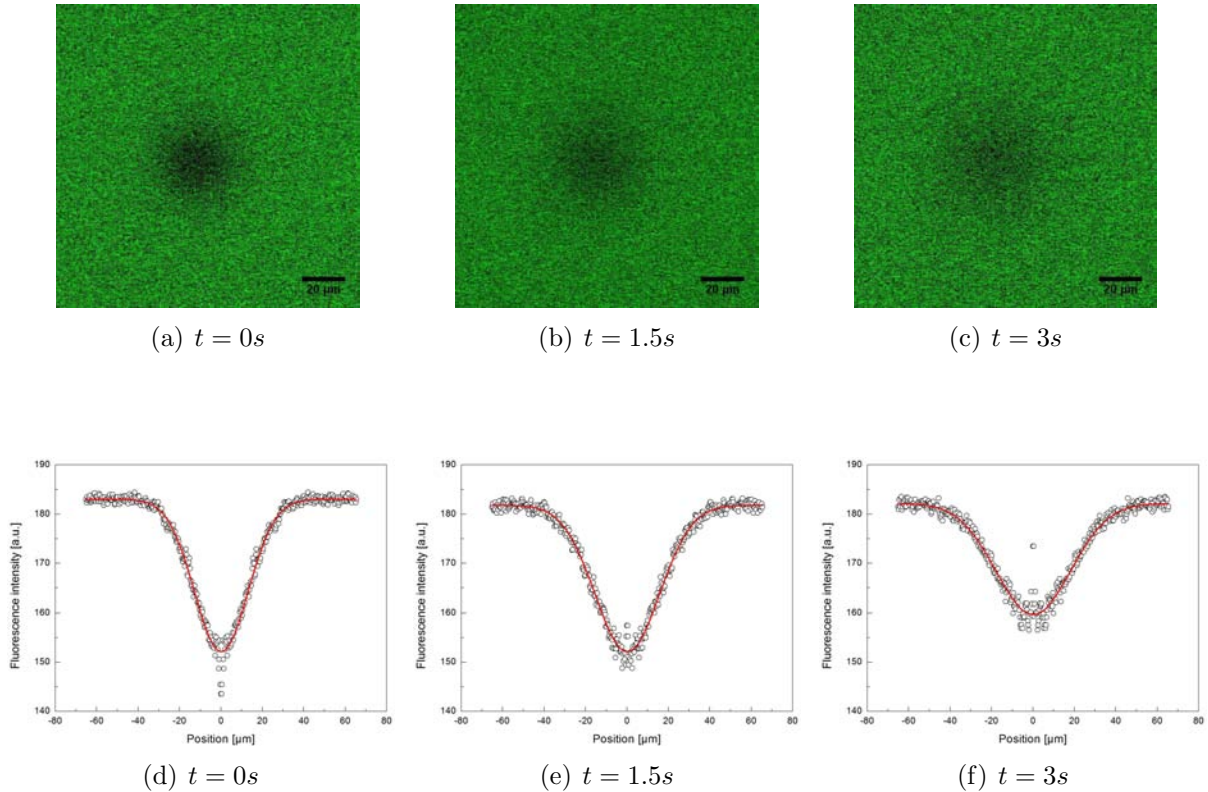


Figure 4.6: Bleaching spots during a FRAP experiment on an aqueous DNA solution with concentration of 80 mg/ml. Below each spot, the corresponding fluorescence profile is shown, properly adjusted by a Gaussian function.

The time behavior of the variance associated to the bleached zone is exhibited in Fig. 4.7. From the slope of the curve, the value of $D = 25.6(1.4)\mu m^2/s$ is obtained for the diffusion constant of the DNA fragments. This value is somewhat lower than that one predicted for non-interacting solutions of rods with the same aspect ratio of the fragments used here [103, 104, 108]. Therefore, we conclude that the particles are in a regime of weak interaction, which is consistent with an intermediate state before the isotropic/cholesteric transition observed at concentrations slightly higher ($C_{DNA} \approx 100$ mg/ml) [31, 58].

4.2.2 Ternary DNA-lipid complex

We managed to get fairly well oriented samples for two compositions in the ternary DNA-lipid-water system whose volume fractions of water, DNA and lipids are, respectively, 0.50, 0.08 and 0.42 for the most hydrated sample, with a comparatively lesser load in DNA fragments, and 0.38, 0.15 and 0.47 for the other sample, also richer in DNA. Polarising and fluorescence images from these formulations are shown in Fig. 4.8, where the regions of interest selected for the bleaching are delimited by dotted red circles. It should be noted that the FRAP zones have homeotropic anchoring, as attested by the

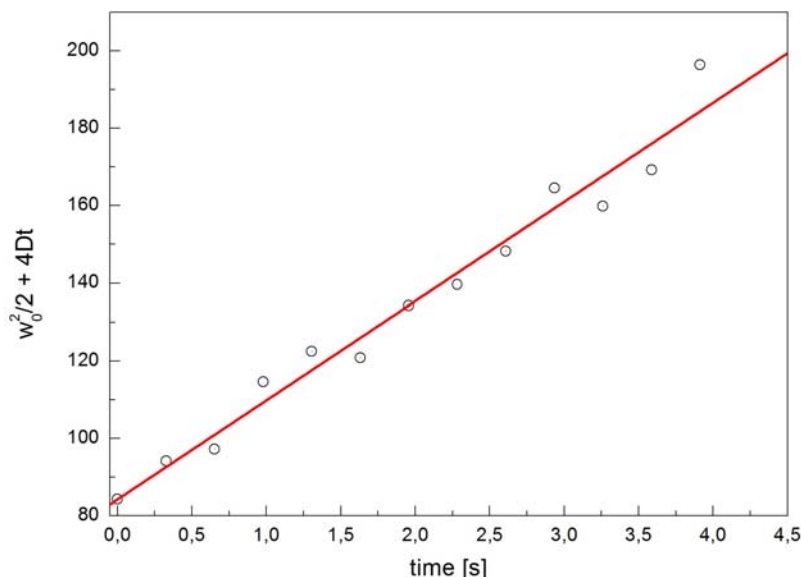


Figure 4.7: Temporal evolution of the variance, obtained from Gaussian fits, for FRAP in a DNA aqueous solution at concentration 80 mg/ml. The slope of the linear fit gives a value of $D = 25.6(1.4)\mu m^2$.

dark pattern under crossed polarizers.

Both samples are macroscopically homogeneous and their small-angle x-ray scattering spectra, shown in Fig. 4.9, with 4 sharp Bragg peaks in the ratio 1:2:3:4, are characteristic of a lamellar stacking of bilayers [20]. Though only the less hydrated sample displays the typical broad line signalling the 2D nematic order of the DNA fragments confined within the water layers, the other sample most probably exhibits the same structure. From X-rays, the water channels are 39.7 Å thick in this latter sample, implying that the rotational degrees of freedom for 500 Å long DNA rods are restricted to an almost two-dimensional space. The DNA volume fraction in water exceeds then by a fair margin the 2D overlap concentration - estimated here to be about 3% volume fraction - and a disordered DNA structure is therefore very unlikely [20, 24].

The experiments were carried out using a 40× objective and the bleach duration was 4 s for both samples. For the DNA-richer sample, the time interval between recorded images was 20 s and the total number of images was 80. For the other formulation, the time interval between images was 15 s and the total number was 40.

In Figs. 4.10, selected scans of the bleached region are exhibited together with their respective false-colored 3D profiles. The spots have circular symmetry throughout the series, with the fluorescence intensities and the widths clearly evolving in time.

The fluorescence recovery profiles depart largely from the Gaussian shape for both samples, where functions accounting for only one diffusion coefficient are not able to properly describe the tail region of the data. These deviations are clearly outlined in Fig. 4.12, where typical profiles are compared to fits to either a Gaussian function or the modified Bessel form 1.33.

As an illustrative example, the time evolution of the first 28 fluorescence profiles for

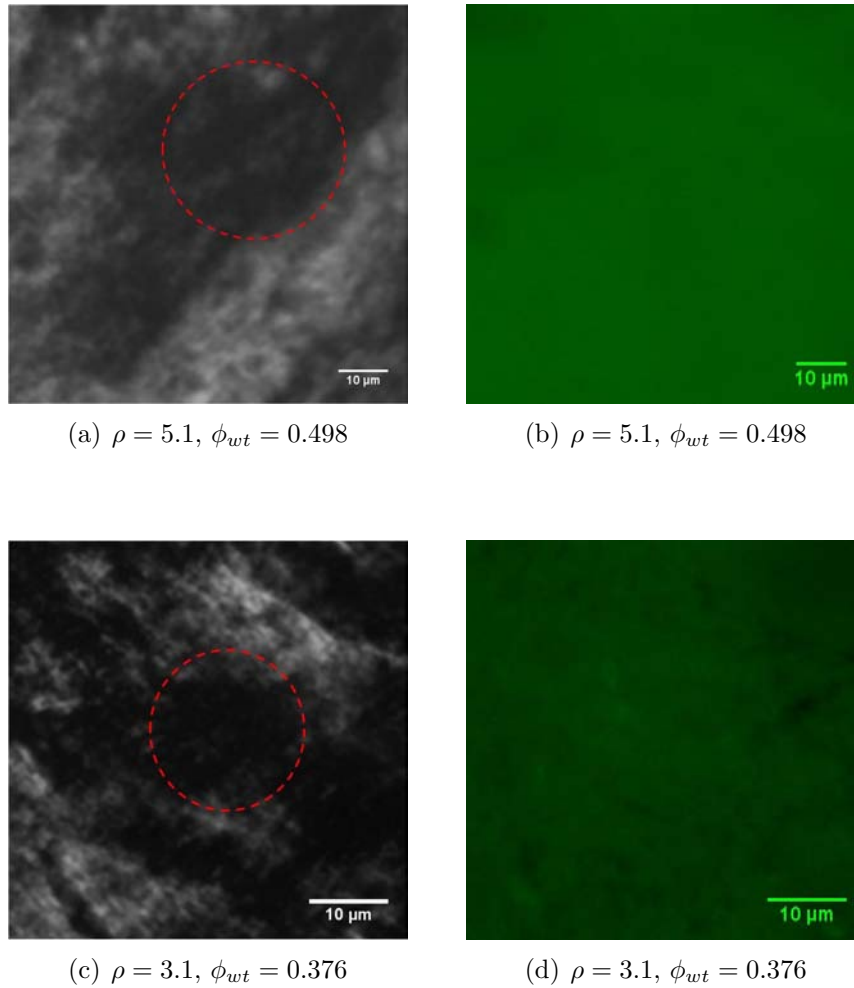


Figure 4.8: Polarising and fluorescence images from ternary samples. Homeotropically oriented regions, indicated by the red dotted circles in polarising images, were chosen to perform the bleaching. In addition, homogeneity of fluorescence ensures the presence of one-phase domain.

the sample with $\rho = 5.1$ appear in Fig. 4.13 together with fits to Gaussian or modified Bessel functions (red lines). Analyzing profiles along the time series reveals that profiles departing from the Gaussian shape at time t systematically depart from the Gaussian shape at any latter time $t' > t$. This indicates that the non-Gaussian shapes cannot be attributed to a saturation of the initial bleaching process, as this should also lead to a relaxation towards Gaussian shapes in the long-time limit.

The time behavior of the two obtained variances for the sample with $\rho = 5.1$ are exhibited in fig. 4.14. These parameters are clearly distinct at all times, which evidences, now in quantitative terms, the non-Gaussian shape of the fluorescence recovery profiles mentioned above. It should be noted that the variances are also distinct at $t = 0$, whereas the model description given by Eq. 1.33 implies an initially Gaussian shape. This deviation could be associated to the shape of the laser beam along the optical axis, which would be similar to a hyperboloid of revolution instead a cylinder. In a such situation, the projection of several slices at different heights would result in a azimuthally symmetric spot with fluorescence intensity profile diverging from the Gaussian form.

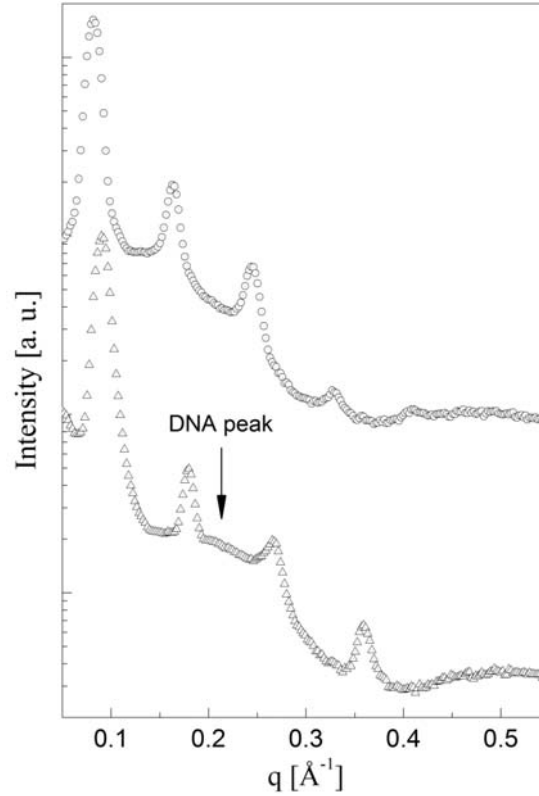


Figure 4.9: X-rays spectra from the two formulations also evaluated by FRAP experiments: \circ correspond to the sample with $\rho = 5.1$ and periodicity $d = 76.2 \text{ \AA}$. \triangle represent data from the sample with $\rho = 3.1$ and $d = 69 \text{ \AA}$.

The obtained diffusion coefficients are $D_{\parallel} = 1.3 \times 10^{-2} \mu\text{m}^2/s$ and $D_{\perp} = 2.8 \times 10^{-3} \mu\text{m}^2/s$, leading to an anisotropic ratio $D_{\parallel}/D_{\perp} \approx 4.5$. Note that the absolute values are several orders of magnitude lower than that one observed in the isotropic aqueous solutions, reflecting in part the concentration but mostly the confinement influences on the dynamics properties.

Quite similar results are obtained for the other DNA richer sample. The systematic appearance of non-Gaussian profiles was observed throughout the series and the temporal behavior of the adjusted variances is shown in Fig. 4.15. It has been observed that, at earlier times (up to $t \approx 250s$), neither the Gaussian profile, nor the modified Bessel model, were able to give a satisfactory description for the experimental data. This discrepancy may be possibly attributed to the crudeness of the approximate treatment made in deriving the model, but this should not impair its validity at least in the long-time limit. As a matter of fact, Fig. 4.15 indicates that the two variances are reasonably well fitted by laws linear in time for $t \geq 250 \text{ s}$. Notwithstanding the model failure at (and near) $t = 0$, such a behavior is the usual (and expected) signature of Brownian dynamics. We therefore confidently consider the two slopes resulting from a data analysis based upon 1.33 as directly related to the two diffusion coefficients D_{\parallel} and D_{\perp} . In terms of quantitative parameters, the obtained diffusion coefficient are $D_{\parallel} = 2.7 \times 10^{-3} \mu\text{m}^2/s$ and $D_{\perp} = 6.6 \times 10^{-5} \mu\text{m}^2/s$, with anisotropic ratio $D_{\parallel}/D_{\perp} \approx 40$.

From the above described results, the model proposed in Sec. 1.8 has proved to be

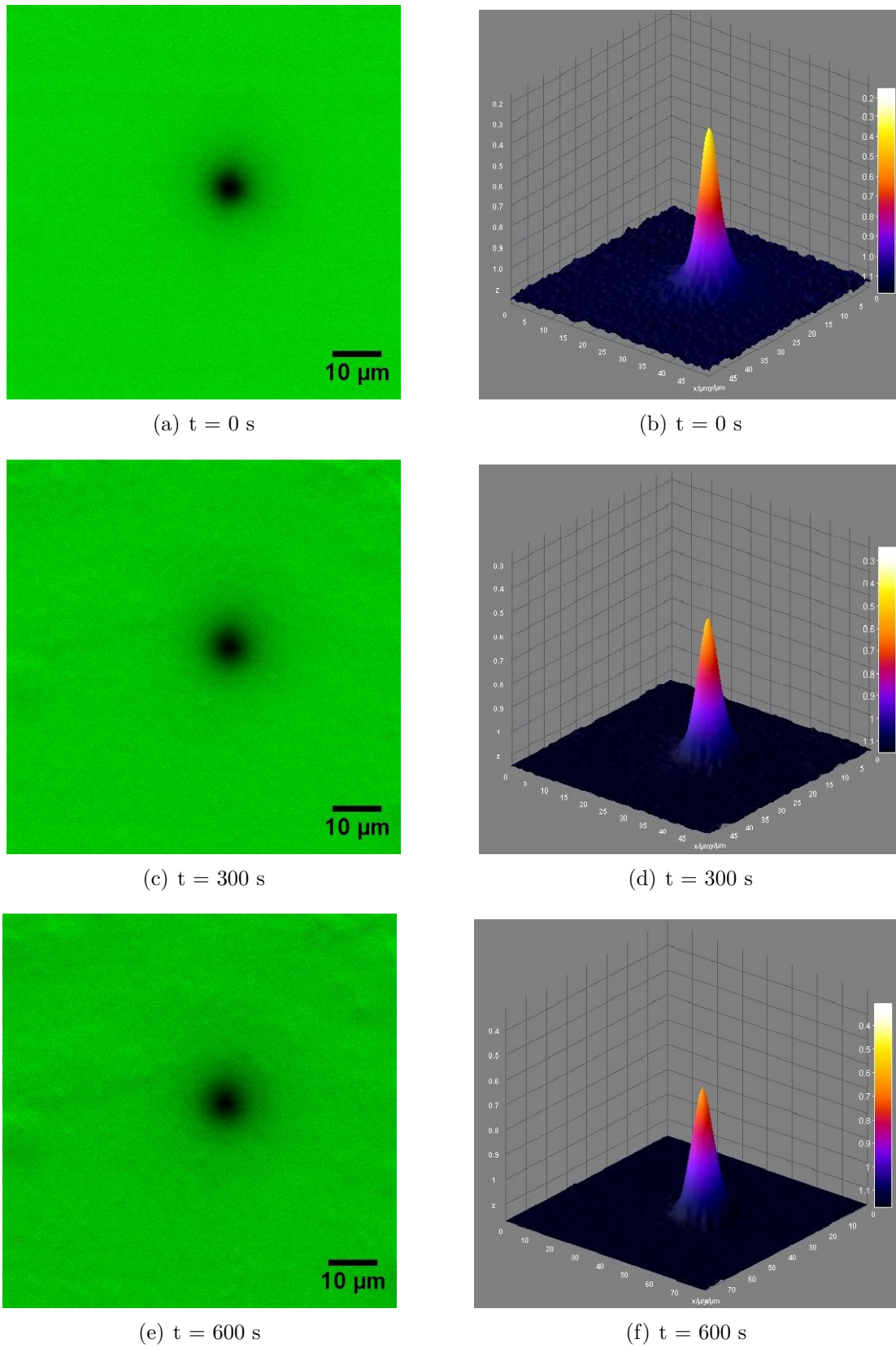


Figure 4.10: Time evolution of the bleached zone together the respective colour-coded (inverted) 3D profiles. The lipids-to-DNA ratio is $\rho = 5.1$, with water amount $\phi_{wt} = 0.498$.

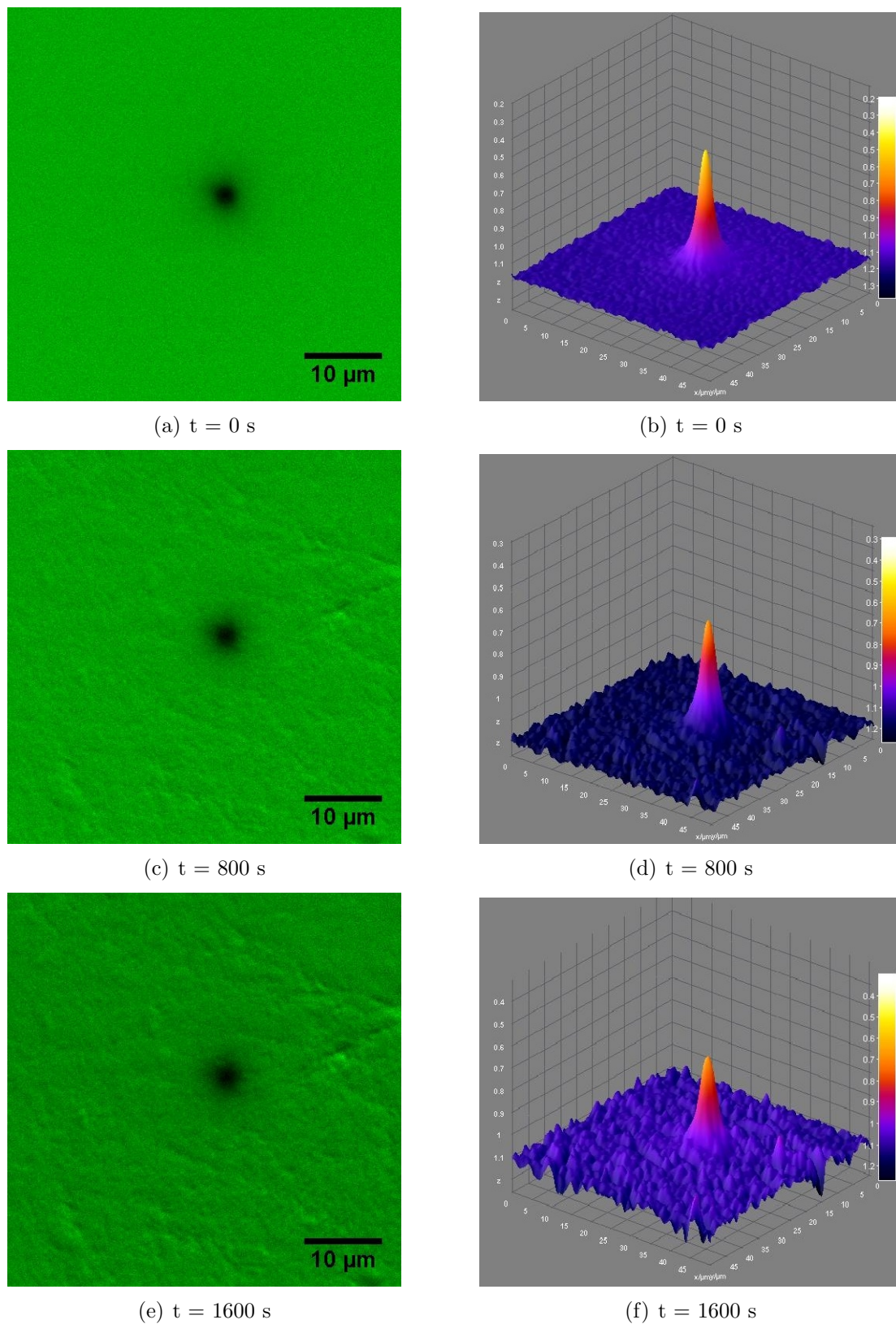


Figure 4.11: Time evolution of the bleached zone for $\rho = 3.1$ and $\phi_{wt} = 0.376$, together with the respective colour-coded (inverted) 3D profiles.

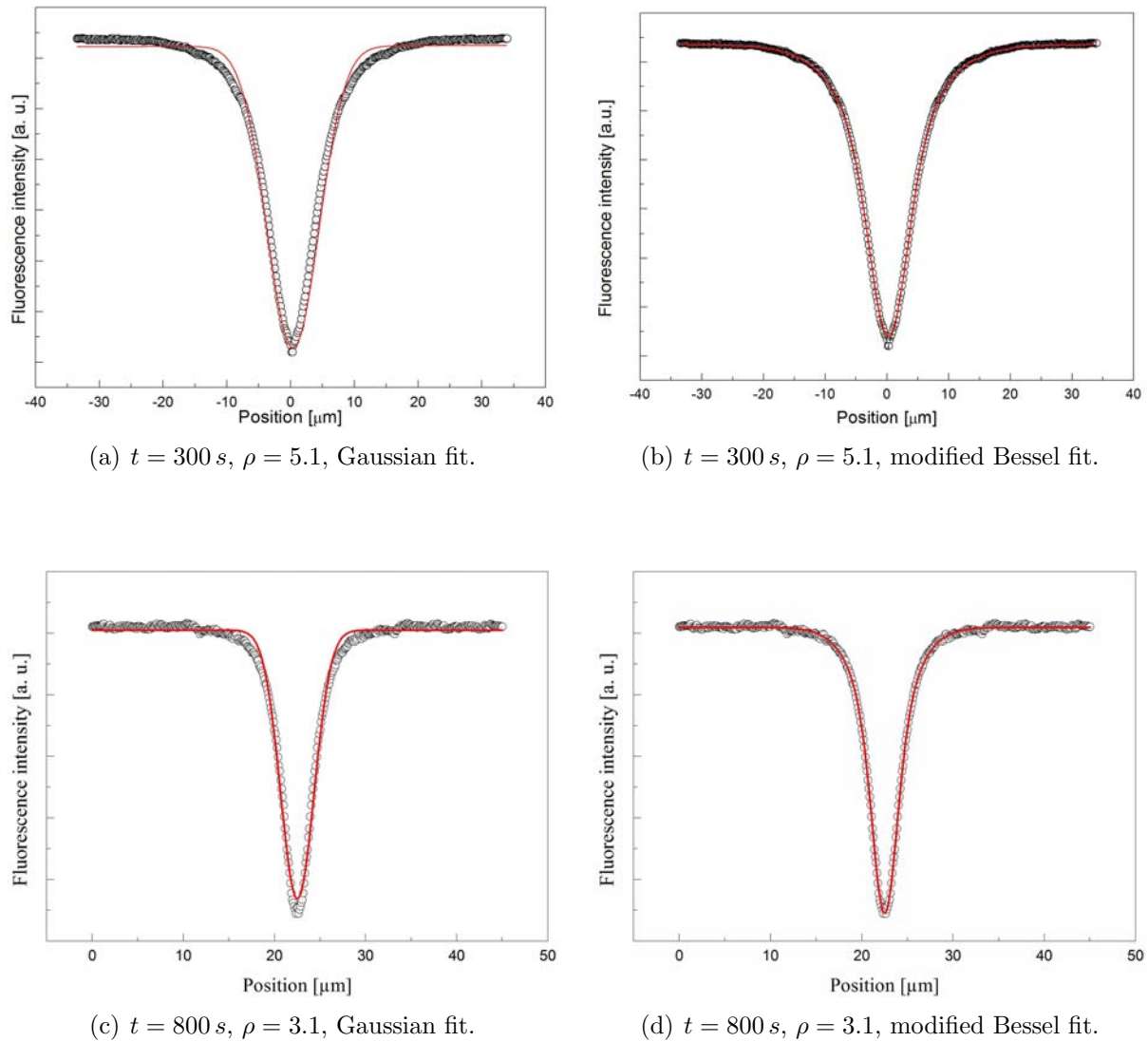


Figure 4.12: Fluorescence recovery data from homeotropically-oriented ternary samples. The solid red lines are fits to Gaussian functions or to Eq. 1.33.

adequate for analysing FRAP profiles of DNA diffusion in-between lipid bilayers. Even though the averaging led to axially symmetric fluorescence recovery profiles, diffusion coefficients parallel and perpendicular to the nematic director could be extracted from the data [24].

Both confinement and DNA concentration were simultaneously varied in the ternary complexes, with DNA volume fractions (with respect to solvent) and heights of the solvent channel, respectively, 16% and 40.0 Å for one sample, 44.7% and 32.5 Å for the other one. Since the diameter of the rods is about 20 Å, in both cases the particles are strongly confined.

The anisotropic ratio between the coefficients parallel and perpendicular appeared to be dependent upon concentration. For the sample containing a lesser DNA load, this ratio was found to be ≈ 4.5 , whereas for the DNA-richer formulation it was ≈ 40 . Such behavior is qualitatively consistent with numerical simulations [32, 158], where the anisotropy increases with the growth of the nematic ordering, which is expected to occur

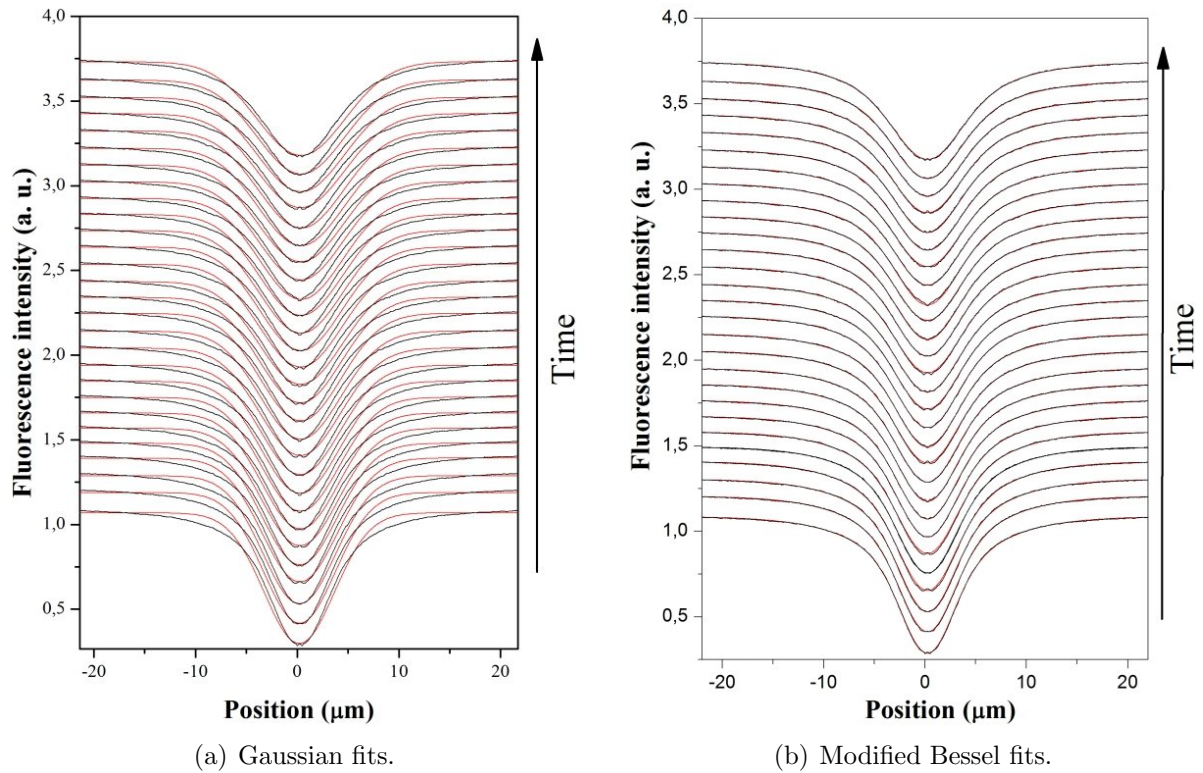


Figure 4.13: Time evolution of the first 28 fluorescence recovery profiles for samples with $\rho = 5.1$ fitted according to (a) Gaussian functions and to (b) Eq. 1.33.

upon the increasing of concentration. On the other hand, a such behavior would be also consistent with the increasing of the confinement.

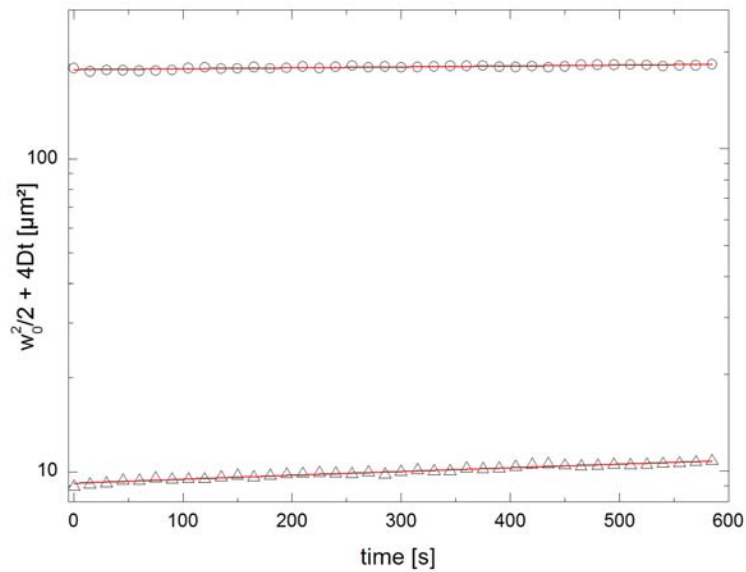


Figure 4.14: Increase in time of the two variance parameters for an oriented domain in the ternary sample with DNA content 0.08. The lines are linear fits to the data, leading to diffusion coefficients $D_{\parallel} = 1.3 \times 10^{-2} \mu m^2$ (o) and $D_{\perp} = 2.8 \times 10^{-3} \mu m^2$ (Δ).

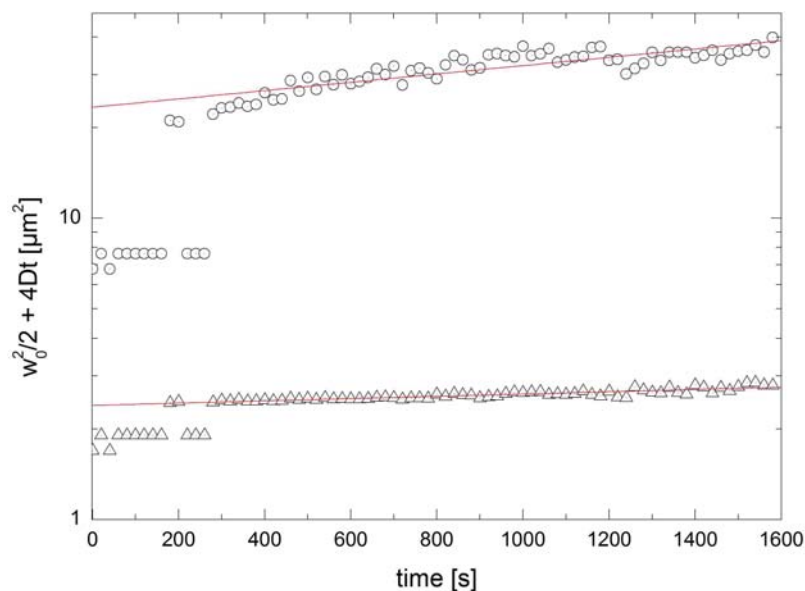


Figure 4.15: Increase in time of the two variance parameters for an oriented domain in the sample with $\rho = 3.1$. The slopes of the linear fits lead to diffusion coefficient $D_{\parallel} = 2.7 \times 10^{-3} \mu m^2/s$ (o) and $D_{\perp} = 6.6 \times 10^{-5} \mu m^2/s$ (Δ).

CONCLUSIONS AND PERSPECTIVES

Throughout this thesis, the structural and dynamical properties of a hydrated complex formed between DNA fragments (150 bp) and zwitterionic bilayers were investigated. The host phase was obtained from mixtures of zwitterionic PCs and Simulsol, a blend of electrically neutral surfactants. The nucleotides, in turn, were obtained by sonication of long chains of calf-thymus DNA. One accomplishment of the work is the systematic study of the phase diagram of this system, whose low hydration region was investigated here for the first time. The full incorporation of nucleotides to the lipid phase was observed to be strongly related to the amount of DNA in the complex, evidencing the importance of excluded volume interactions on complexation and phase behavior. In addition, analyses on the interplay of the forces within the lamellar phases suggest undulation and hydration forces as major players in the complex. Another result derived from the current study is the validation of a theoretical proposition for the extraction of anisotropic diffusion coefficients in the very particular conditions of ordered phases of DNA inserted in the water channels of homeotropically-oriented stacks of membranes.

Three special features of the complexes produced under the above-described conditions merit to be highlighted in these concluding remarks. First, the lack of net charge on membranes allows to exclude the opposite-charge attraction as a direct player in complexation. Therefore, one has a singular condition to probe the effects of other forces, especially those of entropic origin. Secondly, since the system is formulated below its hydration limit, the organization of the particles in-between the bilayers is driven by the *confinement* exerted by a fluid matrix, at nanoscopic scale. A third remarkable characteristic of the DNA-lipid system investigated in this thesis is the restriction of the solvent to the intermembrane spacing, without exchanges with a bulk solution. This attribute presumably has direct consequences on the counterion release process. Since the Na^+ ions are trapped in-between the bilayers, the entropic gain associated to the release of these cations must be limited in the comparison with a scenario where the ions are expelled from the host phase. This context requires changes in the traditional interpretation of the mechanism involved in the formation of lipoplexes, where the counterion release has

a central role. Therefore, another mechanism should be at play, possibly involving interfacial effects at both bilayer-water and DNA-bilayer interfaces. The exact mechanism that induces the correlations between DNA is not very clear and is a difficulty issue. A problem is related to the fact that, at first glance, DNA should not want to go in between bilayers since the scenario where charges appear surrounded by a low dielectric medium is not favored. A possible task in order to address this matter in the future would be the study of the adsorption of nucleotides at oil-water interfaces by preparing Langmuir films with zwitterionic surfactants and DNA solutions.

The work started by investigating the structure of the host phase, that is, the DNA-free system composed only by lipids and solvent. A careful analysis showed that this lipid matrix self-assembles into lamellar structures across a wide range of hydrations. This statement is supported by X-rays data and also by electron and optical microscopy observations. Two characteristic regimes are found in the dilution domain: the first one is driven by the usual swelling law $d = \delta_m / (1 - \phi_{wt})$, explicating the geometrical relationship between periodicity and water amount. In the second regime, excess of water appears in the system as a consequence of the full hydration of membranes. The behavior of the parameter of Caillé showed that the van der Waals attraction is balanced by a mixed repulsive interaction arising from the combination of hydration and Helfrich's forces. Applying an approach proposed by Petrache and co-workers [132], we were able to determine that the decay length of this "hybrid" interaction is about three times higher than the one typically found for lamellae formed from pure lecithins. These findings show that the addition of Simulsol to membranes enhances the importance of entropic forces in the system.

In a second stage, DNA-containing complexes were investigated. The swelling properties of the host phase were used to control the smectic stacking period and adjust the confinement imposed by the lipid walls over the nucleotides inserted within the aqueous gaps. Apart from the sodium counterions neutralizing the DNA phosphate groups, no extra ions were introduced to mediate the complexation. A rich polymorphism of DNA superlattices, embedded in multilamellar phases of lipids, was demonstrated. The formation of single-phase domains was found to be strongly dependent on the amount of nucleotides, being found only for DNA-richer formulations when the PC-to-Simulsol ratio in membranes is 70:30. This suggests a major role of packing constraints and short-range forces in complexation. Confinement was found to have dramatic effects on the supramolecular assembly of the complex. As a function of hydration, from weak DNA-DNA in-plane correlations to highly-ordered columnar rectangular and hexagonal structures were found. Simple geometric models were proposed and proved to be a fitting way to describe such organizations, especially when the separations between membranes are large enough to accommodate DNA rods without need for deformations of bilayers. It should be noted that the phase transitions on DNA superlattices do not appear associated to $L_\alpha \rightarrow L_\beta$ transitions on membranes.

When the proportion between PC and Simulsol in the system is 50:50, the full incorporation of nucleotides to lamellae is also observed for lower amounts of DNA. Nevertheless, the phase behavior upon hydration (or upon confinement) remains quite similar to the one found in complexes prepared with the other (presumably more rigid) membranes. In addition, the introduction of salt, which is thought to change the entropic gain associated to the release of sodium counterions [63] in addition to reducing the screening length of electrostatic forces, had no noticeable effect neither on the formation of the complex nor on its phase behavior. These observations reinforce the role of the elastic properties on the formation of the complex, as derived in the Flory-based model of ref. [17], whereas the confinement seems to be the predominant driver of the organization of particles in-between the bilayers.

The addition of nucleic acids appears to improve the smectic ordering of the host phase and a mechanism based on steric reduction of membrane fluctuations is suggested. The reduction of the space between membranes implies a decrease of the degree of freedom for fluctuations, allowing the organization of DNA into strongly correlated superstructures. A tentative approach using the model of Nallet et al. was implemented in this thesis in order to quantify this effect. The results show that the fluctuations fall by a factor around one order of magnitude upon insertion of DNA in the host phase. Nevertheless, since the model of Nallet et al. was not developed to take into account the scattering from the particles inserted in the water channels, the method is not able to fit the full range of the data and remains necessarily elusive. A perspective approach to properly describe the structure and form factors of such DNA-lipids-water complexes has been developed by Oliveira et al. [159]. The proposition is based on finite element techniques which are used to simulate scattering curves and decouple the form and structure factor associated to the complex. An example of such calculation is shown in fig. 4.16.

Regarding the dynamical analyses, the model proposed by Dobrindt proved to be adequate for analyzing FRAP profiles in systems with the very specific conditions of symmetry of the complexes studied in this work: local nematic symmetry for rod-like particles, averaged along an axis perpendicular to the nematic director. Even though the averaging led to axially symmetric fluorescence recovery profiles, diffusion coefficients parallel and perpendicular to the nematic director could be extracted from the data. Confinement and concentration of the DNA fragments were varied simultaneously, with lipids-to-DNA volume ratio and height of the solvent channel, respectively, $\rho = 5.1$ and 40.5 \AA for one sample, $\rho = 3.1$ and 33.1 \AA for the other one. Since the diameter of DNA plus a hydration shell is about 24 \AA , in both cases the confinement of the DNA fragments by the lipid bilayers is strong. Confinement of the DNA fragments by the lipid bilayers appears to be very effective in slowing down the Brownian motion of the particles, but the increase in dynamic anisotropy D_{\parallel}/D_{\perp} may, tentatively, be ascribed to a concentration effect mainly, though more detailed investigations that are beyond the scope of this work would be required to firmly establish this point. This also opens a perspective to study

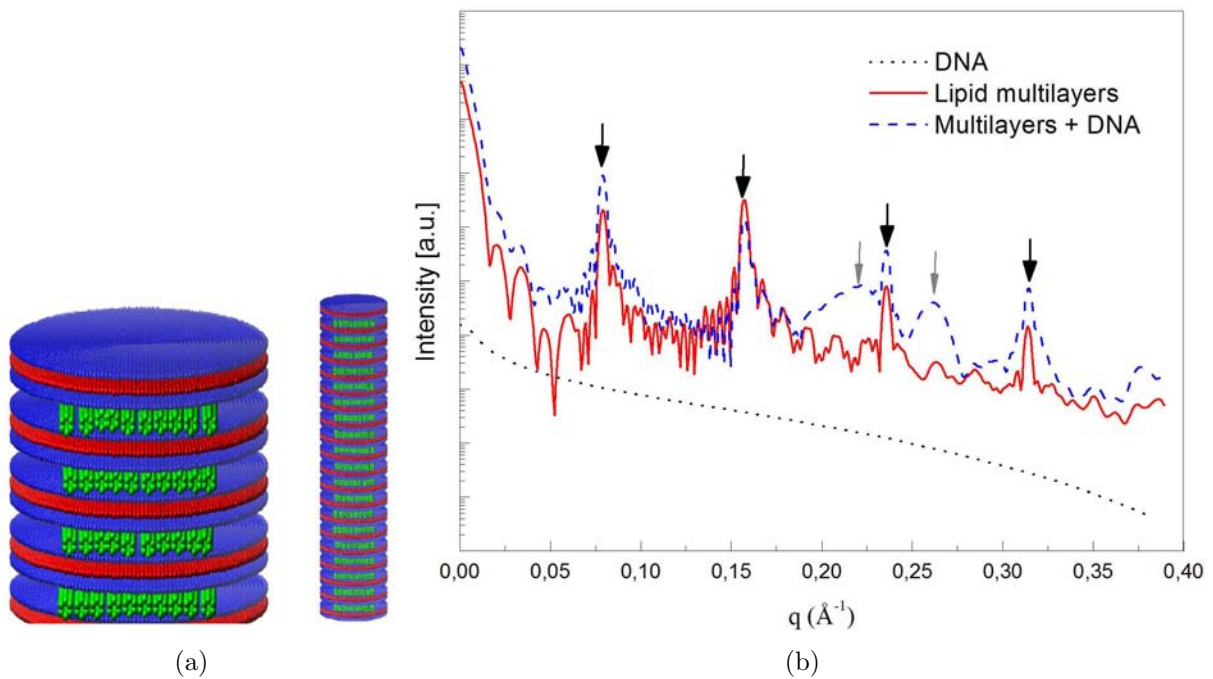


Figure 4.16: Simulation using finite element method: (a) Stacks of lipids with DNA rods in the water gaps constructed from spherical subunits with different electron density profiles. (b) Resulting scattering curves arising from the model (figures kindly provided by C.L.P. Oliveira).

interfacial effects involved in the interactions between DNA and membranes, since the friction of the particles in the plane of bilayers would be expected to be dependent on the confinement. The structural and dynamical analyses conducted in this work must be regarded in a complementary picture, since it was demonstrated that the fluorescence profile of bleach spots carries also information about structure.

Most of the results presented in this thesis were published in Refs. [20, 21, 24]. A new work, exploring the effects of membrane composition on phase behavior, is under progress and will be published soon.

APPENDIX A

PROTOCOLS

A.1 DNA desalting and sonication

- In a test tube, put 100 mg (DNA calf thymus) + 10 ml of pure water. Make shake during 1 to 2 hours then left stand overnight.
- Add 1/10 of this volume of Na acetate at 3M, pH 5.2 (sodium acetate buffer solution for molecular biology, Sigma-Aldrich. Ref. S7899-500ml).
- Then add 2.5 times the volume (25 ml) of ultra-pure ethanol 100% and shake. We see that DNA precipitates as a cotton. Freeze -20°C overnight.
- In the next day, centrifuge the tube at 5200 rpm (3500g) for 15 minutes at 4°C . The supernatant is discarded and the DNA pellet is taken up in 10 ml of 70% ethanol.
- Shake the tube manually and then left at room temperature for 1 hour. Then centrifuge in the same way, 5200 rpm, 4°C , for 15 minutes. The supernatant is discarded and the pellet is taken up in 10 ml of ethanol at 70%. This step is repeated 3 times.
- After the third time, the supernatant is discarded and then the DNA is dried in a rotary evaporator for 20 minutes in order to remove all traces of ethanol (40°C the maximum temperature to not degrade the DNA, pressure low).
- If there is non evaporated water it is not a problem, since DNA will be diluted in H₂O for sonication.
- DNA is then puted into H₂O, at 10mg/ml. Then the tubes are sonicated in an ultrasonic tank. We tried this technique instead a probe sonicator because the last one to pollution (particles of titanium that detached from the probe).
- Sonication in the tank is longer, taking 33 hours. During this time, the tubes must be kept inside a mix of water (liquid) and ice in order to control the temperature inside the tank.
- After about 30 hours of sonication, check the size of the chain by electrophoresis.
- If the size is OK, freeze the samples and make standard lyophilization.

A.2 DNA labeling

YOYO-1 (491/509) from Invitrogen is purchased in solutions of 1 mM. For preparing 150 mg of YOYO-labelled DNA:

- Put 150 mg of sonicated DNA fragments (lyophilized) in pure water ($\approx 10ml$).
- Shake for 1 hour.
- Add 49.5 μl from the YOYO-1 mother solution.
- Shake for 1 hour, **protected from the light**.
- Freeze at $-80^{\circ}C$ for 2 hours (minimum) before lyophilization.

A.3 Preparation of lipids

For preparing 1 g of premix (70:30 PC-to-Simulsol ratio):

- Put 300 mg of Simulsol in a test tube.
- Add 700 mg of PC.
- Add 15 ml of ciclohexane.
- Shake for 1 hour.
- Freeze at $-80^{\circ}C$ before lyophilization.

APPENDIX B

CORRELATION LENGTH

Consider a finite periodic chain (period d) .

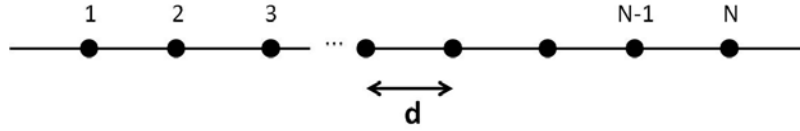


Figure B.1: Finite periodic chain.

Be an arbitrary size along the chain given by:

$$L = (N - 1) \cdot d \quad (\text{B.1})$$

The ideal structure factor:

$$\begin{aligned} S(q) &= \frac{1}{N} \sum_{k=1}^N \sum_{l=1}^N \exp[-iq(k-l)d] \\ &= \frac{1}{N} \left| \sum_{k=1}^N \exp[-iqdk] \right|^2 \\ &= \frac{1}{N} \left| \frac{1 - \exp[-iNqd]}{1 - \exp[-iqd]} \right|^2 \\ &= \frac{1}{N} \frac{\sin^2 Nqd/2}{\sin^2 qd/2} \end{aligned} \quad (\text{B.2})$$

Bragg peaks are found at:

$$q = k \times \frac{2\pi}{d} \quad (\text{B.3})$$

Near the first order peak: $q = q_0 + \epsilon$, with $q_0 = \frac{2\pi}{d}$:

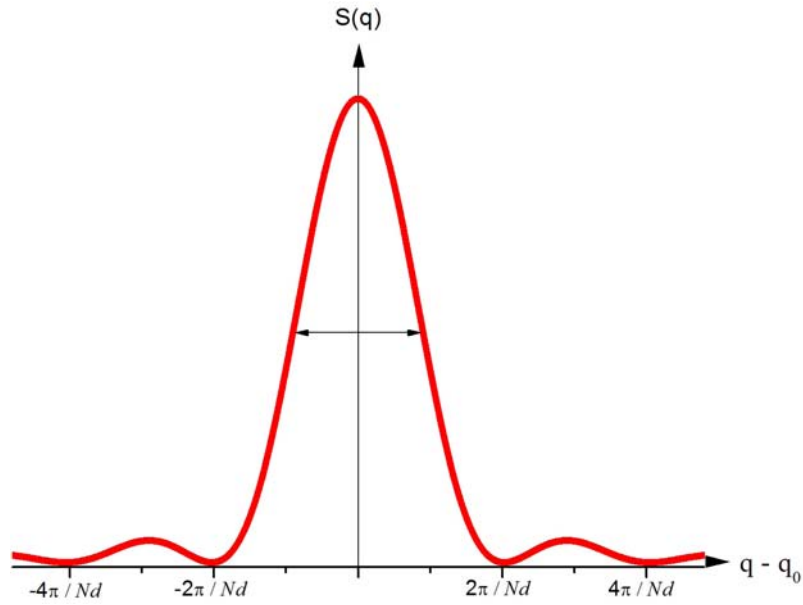


Figure B.2: Graphical form of eq. B.4. The first minima are found at $q - q_0 = \pm 2\pi/Nd$. The double arrow points the FWHM position.

$$\begin{aligned}
 S(q) &= \frac{1}{N} \frac{\sin^2 \left[\frac{Nq_0d}{2} + \frac{Nd\epsilon}{2} \right]}{\sin^2 \left[q_0 \frac{d}{2} + \frac{\epsilon d}{2} \right]} \\
 &= \frac{1}{N} \frac{\sin^2 [Nd\epsilon/2]}{\sin^2 \epsilon d/2}
 \end{aligned} \tag{B.4}$$

The second minima are found at positions:

$$\epsilon = \pm \frac{2\pi}{Nd}$$

$$S(q_0 + HWHM) = \frac{1}{N} \frac{\sin^2 \left[N \times \frac{(HWHM)d}{2} \right]}{\sin^2 \frac{(HWHM)d}{2}} = \frac{N}{2} \tag{B.5}$$

$$\Rightarrow \sin \left(N \times \frac{(HWHM)d}{2} \right) = \frac{N\sqrt{2}}{2} \sin \left(\frac{(HWHM)d}{2} \right) \tag{B.6}$$

At the limit where $N \rightarrow \infty$:

$$HWHM \times d = \frac{2.783}{N} \tag{B.7}$$

The size of the correlated domain, named ξ is $\approx Nd$, provided N is large (see eq. B.1). Therefore:

$$\xi = \frac{2.783}{HWHM} \tag{B.8}$$

Fit by Lorentzian or Gaussian function

In eq. 2.7, the parameter Δq is equal to the HWHM. Therefore, when the peak is fitted by a Lorentzian function, the correlation length is given by:

$$\xi = \frac{2.783}{\Delta q} \quad (\text{B.9})$$

When the peak is fitted by a Gaussian function:

$$\begin{aligned} \exp\left[-\frac{HWHM^2}{2\Delta q^2}\right] &= \frac{1}{2} \\ \Rightarrow \frac{HWHM}{\sqrt{2}\Delta q} &= \sqrt{\ln 2} \end{aligned}$$

leading to correlation length:

$$\xi = \frac{2.364}{\Delta q} \quad (\text{B.10})$$

This expression is deduced from the width of the structure factor of a finite chain of rods. It should be noted that the usual expression $\xi = \frac{\pi}{\Delta q}$ would be also a good approximation for the correlation length.

ANNEXE C

RÉSUMÉ EN FRANÇAIS

C.1 Motivations et objectives

L'utilisation des phases lamellaires de tensioactifs comme des vecteurs d'ADN est envisagée comme une prometteuse alternative synthétique à des méthodes virales traditionnellement utilisées en thérapie génique [1–3]. D'un point de vue de recherche fondamentale, de tels complexes sont aussi regardés comme d'excellents systèmes modèles pour l'étude de l'auto-assemblage de biomolécules dans des milieux confinés. Ces systèmes offrent donc, plusieurs défis pour les théoriciens et les expérimentateurs. Dans la littérature, il y a une grande quantité de travaux qui décrivent (ou prévoient) l'existence de plusieurs organisations pour des acides nucléiques au sein de complexes [8–10, 15, 74]. D'un autre côté, il a été reconnu une relation directe entre le type de structure présentée par le complexe et son efficacité en transfection [7]. Cela étant, ces études sont majoritairement basées sur des lipides cationiques, lesquels présentent une toxicité limitante pour les applications *in vivo*. La recherche d'alternatives basées sur des lipides neutres apparaît donc comme un développement naturel de ce processus [16, 86].

Dans ce contexte, cette thèse apporte une contribution à l'état de l'Art en présentant une étude expérimentale des mésophases de superstructures d'ADN hébergées dans des phases multi lamellaires de lipides non-cationiques. C'est un travail sur les sciences de base, qui se concentre sur les propriétés fondamentales du complexe, particulièrement l'étude de son diagramme de phase. Le complexe est composé par une membrane zwitterionique, des fragments d'ADN et de l'eau. Les bicouches sont obtenues à partir d'un mélange de phosphatidylcholine et d'acides gras éthoxylés qui agissent comme co-tensioactifs. Les particules sont obtenues par sonication de l'ADN de thymus de veau, en fragments de ≈ 150 paires de base. Notre approche consiste à varier l'hydratation du complexe de façon à changer la périodicité smectique de la phase lamellaire et, par conséquent, le *confinement* induit sur les biomolécules. La structure du complexe est suivie en utilisant un ensemble de techniques qui comprend la diffraction des rayons X, la microscopie électronique et

la microscopie optique. Une autre contribution de ce travail est relative aux propriétés dynamiques. Le mouvement brownien des nucléotides entre les bicouches est évalué par la technique de retour de fluorescence après photoblanchiment (FRAP). L'extraction des coefficients de diffusion anisotropes est faite en utilisant une approche théorique récemment développée spécifiquement pour le système évalué ici.

C.2 Bases

C.2.1 Complexes d'ADN et lipides : état de l'Art

La première description précise de la structure des lipoplexes a été réalisée par Rädler et al. en 1997 [8]. En utilisant la diffusion de rayonnement synchrotron et des techniques de microscopie optique, ces auteurs ont démontré qu'un système ADN/DOTAP-DOPC s'auto-organise dans une structure L_a^c , où les nucléotides sont insérés dans les couches aqueuses d'une phase lamellaire. Inspiré par la nomenclature donnée dans des études pionnières de microscopie électronique [11, 12], cette conformation a été bientôt appelée structure de type "sandwich". Une représentation schématique de cette organisation est montrée dans la fig. C.1(a). Dans le plan (xy) des membranes, l'ADN est condensé dans une structure bidimensionnelle où l'espacement interaxial, d_{DNA} , dépend d'un équilibre délicat entre les charges positives des lipides et les charges négatives des macromolécules hébergées. Lorsque le nombre de charges introduites par les nucléotides dépasse le nombre de charges cationiques, une phase aqueuse contenant l'ADN seul apparaît. Inversement, quand le nombre des charges positives est supérieur au nombre d'anions, une phase lipidique non complexée apparaît. La complexation est optimisée au point isoélectrique, lorsque le système est globalement neutre.

Bien que les phases lamellaires lyotropes soient les structures les plus fréquemment trouvées dans la recherche des lipoplexes, elles ne sont pas le seul type d'agrégats dans ces systèmes. Des matrices hexagonales de lipides, des structures type "nid d'abeille", sont aussi souvent observées. Dans l'étude décrite dans la Ref. [9], par exemple, des mélanges de DOPE/DOTAP ont formé une phase hexagonale inverse, H_{II}^c . Cette structure est représentée dans la fig. C.1(b). Dans un autre travail plus récent [10], les lipides ont formé une phase micellaire hexagonale, avec les nucléotides hébergés dans l'interstice de la phase, H_I^c . Cette structure est montrée dans la fig. C.1(c).

D'autres types plus rares d'organisation ont été trouvés. En particulier, les groupes cristallographiques $Im\bar{3}m$, $Ia\bar{3}d$ et $Pn\bar{3}m$, correspondant à des phases cubiques, ont été mis en évidence dans des systèmes basés sur les phosphatidylcholines [2, 67, 68].

Des études théoriques ont été également développées afin d'apporter un aperçu sur les mécanismes impliqués dans la formation des lipoplexes. Plusieurs modèles ont été proposés pour résoudre ce problème et expliquer le polymorphisme décrit ci-dessus [30, 69, 70]. Malgré la diversité des approches et plusieurs points restant encore obscurs, certains résultats consensuels ont émergé de ces études : parmi ces conclusions, on trouve que le

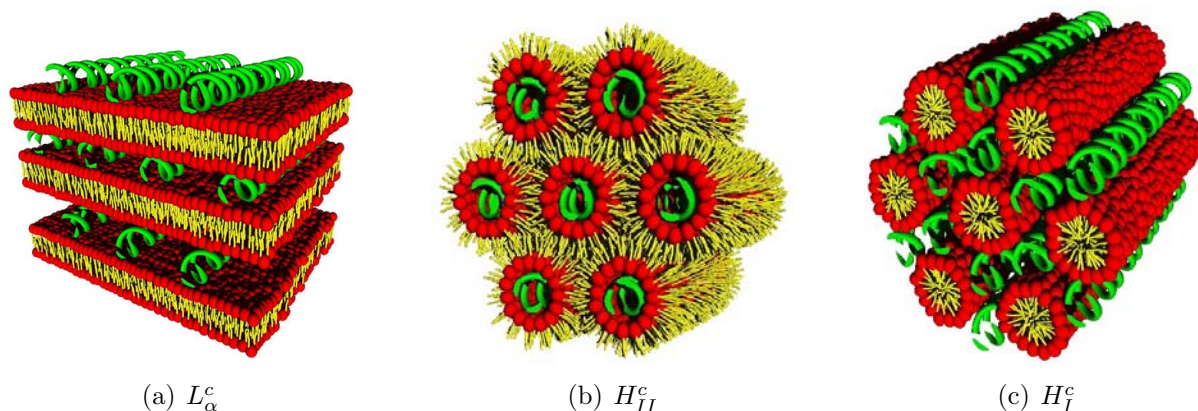


FIGURE C.1 – Schéma des structures les plus fréquemment retrouvées dans lipoplexes : (a) structure type “sandwich”, avec l’ADN inséré entre des bicouches ; (b) structure hexagonale inverse, type “nid d’abeilles”, qui contient des bâtonnets d’ADN dans des cylindres d’eau et (c) structure hexagonale micellaire avec l’ADN dans l’interstice de la phase (figures aimablement fournies par G. Tresset).

comportement de phase dépend d’un équilibre complexe entre des forces élastiques, des interactions électrostatiques et les contraintes thermodynamiques [54].

Un autre résultat dérivé de ces efforts théoriques est lié au relargage des contre-ions. Pendant la formation des lipoplexes, les deux partenaires, nucléotides et tensioactifs, sont pénalisés au niveau de l’entropie translationnelle. Sans prise en compte d’un mécanisme pour compenser cette perte, le système violerait la deuxième loi de la thermodynamique. Un tel problème est surmonté par le relargage des contre-ions : lorsque les contre-ions associés aux membranes et aux bâtonnets sont libérés dans le solvant, l’entropie globale du système monte [77], fig. C.2. À cause de ce mécanisme, la complexation ADN-lipides cationiques est souvent dite être “entropiquement dirigée” [15, 47, 72, 77].

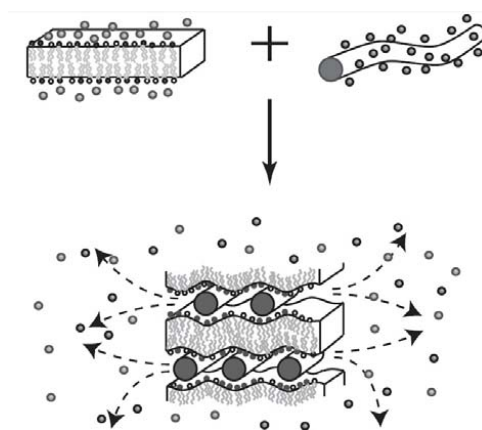


FIGURE C.2 – Mécanisme de relargage des contre-ions : lors de l’adhésion entre ADN et membranes, les contre-ions sont libérés vers le solvant et l’entropie globale du système monte. (Figure tirée de [47]).

Quand les membranes utilisées pour la formation des lipoplexes sont non-cationiques, des mécanismes théoriques différents sont requis en raison de l’absence d’interactions directes (fortes) entre les nucléotides et les tensioactifs. Roux et al. [17] ont proposé un

modèle stérique dans le contexte d'une approche de Flory. Dans ce travail, ils ont étudié la compétition entre les énergies associées à la transition isotrope/nématique de bâtonnets en solution et à leur incorporation à la phase lamellaire. La phase lamellaire a été considérée comme un réseau de sites qui pourraient être occupés (ou non) par les fragments. Les énergies libres ont été calculées pour les différentes configurations et un diagramme de phase théorique a pu être alors calculé.

Dans cette thèse, nous avons partiellement reproduit les données expérimentales de Roux et al. [17,86]. De surcroît, nous avons étendu les résultats de ces auteurs en explorant la région de basse hydratation du diagramme de phase. Nous démontrons également que l'insertion de l'ADN "durcit" l'ordre smectique de la phase lamellaire. En outre, nous évaluons le comportement du système pour des compositions différentes de la membrane et différentes conditions ioniques. Nous concluons finalement que les fluctuations et les forces d'hydratation à courte portée jouent un rôle fondamental dans le système.

C.2.2 Diffusion des rayons X par des phases lamellaires

Le modèle de Nallet et al.

Dans une courbe de diffusion des rayons X, il est facile de déterminer, à partir des positions des raies de Bragg, l'espacement lamellaire d d'un ensemble de bicouches empilées au travers de la relation $d = 2\pi/q_0$, où q_0 est le vecteur d'onde de la première raie. Toutefois, les diffractogrammes contiennent beaucoup plus d'informations que la seule distance de répétition des lamelles. La forme des raies, ainsi que le rayonnement diffus, c'est-à-dire l'intensité diffusée en dehors des raies de Bragg, permettent de sonder la structure du complexe avec plus de détails.

Plusieurs modèles ont été proposés pour décrire la diffusion du rayonnement par des phases lamellaires lyotropes [89–91]. L'objectif de ces modèles est d'obtenir des informations soit au niveau supramoléculaire, par le biais de l'extraction de paramètres tels que le paramètre de Caillé et le nombre de couches corrélées, soit au niveau de la structure fine du système, en déterminant le profil de densité électronique des bicouches de tensioactifs [42, 92].

Parmi ces modèles, nous avons utilisé dans ce travail celui proposé par Nallet et al. [93]. Selon cette proposition, les intensités des rayons X diffusés par une phase lamellaire lyotrope peuvent être décrites en fonction du vecteur d'onde q au travers de la relation :

$$I(q) = \frac{2V\pi P(q)\tilde{S}(q)}{dq^2} \quad (\text{C.1})$$

où $P(q)$ et $\tilde{S}(q)$, sont, respectivement, les facteurs de forme et de structure du système, donnés par :

$$P(q) = \frac{4\Delta\rho_H^2}{q^2} \left\{ \sin(q(\delta_H + \delta_T)) - \sin(q\delta_T) + \frac{\Delta\rho_T}{\Delta\rho_H} \sin(q\delta_T) \right\}^2 \quad (\text{C.2})$$

et

$$\begin{aligned} \tilde{S}(q_z) = 1 + 2 \sum_1^{N-1} \left(1 - \frac{n}{N}\right) \cos\left(\frac{q_z dn}{1 + 2\Delta q^2 d^2} \alpha(n)\right) \times \\ \times \exp\left\{\frac{-2q_z^2 d^2 \alpha(n) + \Delta q^2 d^2 n^2}{2(1 + 2\Delta q^2 d^2 \alpha(n))}\right\} \times \\ \times \frac{1}{\sqrt{1 + 2\Delta q^2 d^2 \alpha(n)}} \end{aligned} \quad (\text{C.3})$$

Les paramètres ajustables sur la partie relative au facteur de forme $P(q)$ sont : δ_H , qui correspond à la taille des têtes polaires des tensioactifs, δ_T , qui est la taille des queues aliphatiques et le rapport entre les contrastes électroniques des queues et des têtes, $\frac{\Delta\rho_T}{\Delta\rho_H}$.

Dans l'expression du facteur de structure, $\tilde{S}(q)$, Δq est la résolution instrumentale. Les paramètres ajustables sont : le nombre de couches corrélées, N , la périodicité des lamelles, d , et le paramètre de Caillé, η . Ce dernier se trouve intégré dans la fonction $\alpha(n)$:

$$\alpha(n) = \frac{\langle(u_n - u_0)^2\rangle}{2d^2} = \frac{\eta n^2}{16}, \quad n \text{ small} \quad (\text{C.4a})$$

$$\alpha(n) = \frac{\langle(u_n - u_0)^2\rangle}{2d^2} = \frac{\eta}{4\pi^2} [\ln(\pi n) + \gamma], \quad n \gg 1 \quad (\text{C.4b})$$

où γ est la constante d'Euler. Le paramètre de Caillé est relié aux constantes élastiques de la phase lamellaire par la relation :

$$\eta = \frac{q_0 k_B T}{8\pi \sqrt{KB}} \quad (\text{C.5})$$

Il y a donc une relation étroite entre η et les fluctuations des membranes dans une phase smectique. Pour un système idéal, où il n'y a pas d'effets de fluctuations, la valeur de η est zéro et le facteur de structure est constitué par un ensemble des raies de même intensité, dont la largeur est limitée seulement par la résolution instrumentale. Quand η est différent de zéro, les intensités des raies décroissent rapidement en fonction de q , et les largeurs des raies montent, comme il est montré dans la fig. C.3.

C.2.3 Diffusion de l'ADN dans des phases lamellaires

Modèle de Dobrindt

L'analyse des propriétés dynamiques lorsque la diffusion se produit dans des milieux anisotropes nécessite des approches spécifiques selon le type de symétrie [111, 113, 114]. Dans le cas du système évalué ici, deux difficultés doivent être surmontées : l'anisotropie imposée par la phase lamellaire et l'anisotropie liée à l'auto-assemblage de molécules d'ADN elles mêmes. Récemment, un modèle théorique portant sur les caractéristiques

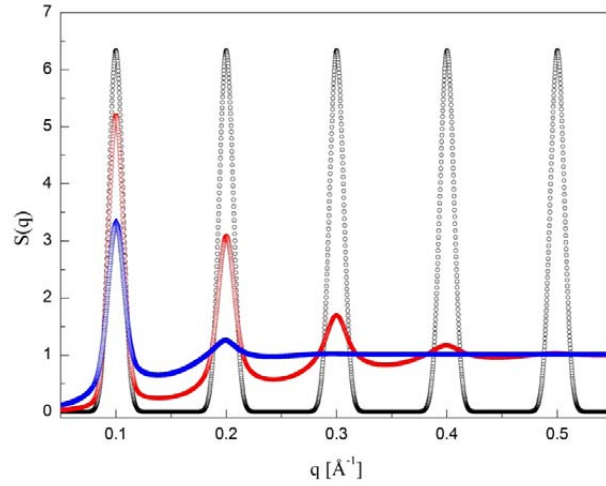


FIGURE C.3 – Facteurs de structure simulés avec trois valeurs différentes du paramètre de Caillé : $\eta = 0$ (noir), $\eta = 0.1$ (rouge) et $\eta = 0.35$ (bleu). (adaptée à partir de la figure 6 de [93]).

spécifiques de ces systèmes a été développé par Jens Dobrindt au CRPP [23]. Dans cette thèse, quelques preuves qui soutiennent la validité de cette propositions sont montrées.

Considérons une phase lamellaire orientée de façon homéotrope. Dans les couches aqueuses de cette phase, des fragments d'ADN se trouvent organisés de façon nématique, sans aucune corrélation entre les vecteurs directeurs d'une couche à l'autre. À cause de cette anisotropie, les particules se propagent plus rapidement dans la direction parallèle à l'axe des molécules d'ADN et plus lentement dans la direction perpendiculaire. Pendant une expérience de FRAP, les taches de blanchiment dans les couches adoptent une forme elliptique, avec le grand axe parallèle au directeur de la phase nématique locale. Vu que les différentes phases nématiques ne sont pas corrélées le long de l'axe optique, la tache résultante sur le plan focal image, composée à partir de la projection de plusieurs ellipses, a une forme de symétrie circulaire. Le profil de fluorescence de cette tache pendant une expérience de FRAP n'est pas adéquatement décrit par les fonctions gaussiennes, traditionnellement utilisées pour évaluer la diffusion isotrope. Dans le cas anisotrope d'intérêt, le modèle de Dobrindt propose l'expression suivante pour décrire le profil de fluorescence :

$$F_0(r, t) = F'_0(t) \exp \left[-r^2 \left(\frac{1}{w_{\parallel}^2} + \frac{1}{w_{\perp}^2} \right) \right] \times I_0 \left[r^2 \left(\frac{1}{w_{\parallel}^2} - \frac{1}{w_{\perp}^2} \right) \right] \quad (\text{C.6})$$

Les variances w_{\parallel}^2 et w_{\perp}^2 sont reliées aux coefficients de diffusion parallèle et perpendiculaire au travers des relations :

$$w_{\parallel}^2 = w_0^2 + 8D_{\parallel}t \quad (\text{C.7a})$$

$$w_{\perp}^2 = w_0^2 + 8D_{\perp}t \quad (\text{C.7b})$$

Le facteur de normalisation $F'_0(t)$ est donné par :

$$F'_0(t) = \frac{2ZC_0}{\pi\sqrt{(w_0^2 + 8D_{\parallel}t)(w_0^2 + 8D_{\perp}t)}} \quad (\text{C.8})$$

C.3 Matériaux et méthodes

C.3.1 Constituants du système

Les fragments d'ADN sont obtenus par sonication, ce qui amène à des morceaux de 150 paires de base, en moyenne. La taille des bâtonnets formés est systématiquement vérifiée par électrophorèse. Afin de permettre des observations en lumière polarisée, les bâtonnets sont marqués avec un fluorophore, le YOYO. La partie lipidique est constituée d'un mélange entre la phosphatidylcholine (lipides zwitterioniques) et le Simulsol, un mélange d'acides gras éthoxylés neutres¹. Deux compositions de membranes ont été étudiées, avec des rapports PC/Simulsol dans les proportions de 70 :30 et 50 :50. Le solvant utilisé a été de l'eau dé-ionisée pour la plupart des formulations. Pour quelques échantillons, des solutions d'acétate d'ammonium, à la concentration de 0.25M, ont été employées.

C.3.2 Expériences de rayons X

La diffraction des rayons X a été la principale technique utilisée pour les études structurales. Les expériences ont été partagées entre la ligne SWING, sur le synchrotron SOLEIL, et des sources conventionnelles. Notamment, une machine Nanostar-Bruker et une anode tournante ont été employées au Centre de recherche Paul-Pascal, à Bordeaux. La diffusion du rayonnement a été étudiée aux petits et moyens angles, pour étudier la structure à l'échelle supramoléculaire, et aux grands angles, pour évaluer l'état des queues aliphatiques des membranes dans le complexe. Les détails des configurations utilisées, avec les principales caractéristiques instrumentales, sont résumées dans le tableau C.1.

Machine	Distance échant.-dét. (mm)	Domaine en q (\AA^{-1})	$\Delta q/q$ (\AA^{-1})
SWING-SOLEIL	1575.6	$0.0600 < q < 0.7000$	1.7×10^{-3}
	608.0	$0.0300 < q < 1.7450$	3.8×10^{-3}
Nanostar-Bruker	1060	$0.0100 < q < 0.2000$	1.5×10^{-3}
	250	$0.0400 < q < 0.8250$	6.3×10^{-3}
Anode tournante	383	$0.0660 < q < 0.8200$	5.1×10^{-3}
	133	$0.190 < q < 2.200$	8.1×10^{-2}

TABLE C.1 – Principaux paramètres des configurations utilisées dans ce travail. La résolution totale $\Delta q/q$ a été estimée à la position $q = 0.215 \text{ \AA}^{-1}$.

1. La sonication de l'ADN et la préparation du mélange PC-Simulsol ont été réalisées par Annie Février, technicienne au CRPP.

C.3.3 Microscopie d'épifluorescence et à lumière polarisée

Les préparations ont été systématiquement soumises à l'inspection visuelle par microscopie en lumière polarisée et d'épifluorescence. Les objectifs principaux de ces observations ont été l'évaluation de la biréfringence optique des échantillons ainsi que de vérifier l'homogénéité de la distribution d'ADN. Les analyses ont été faites sur un microscope *Leica* modèle *CTR Mic*.

C.3.4 Microscopie électronique et cryo-fracture

Des répliques pour des observations en microscopie électronique à transmission ont été préparées selon la technique de cryofracture² [129]. Le processus de fracture et de recouvrement avec du platine et du carbone a été fait dans une machine BALTEC BAF060. Les épaisseurs de Pt et de C ont été, respectivement, 40 Å et 300 Å. Les observations ont été faites avec un microscope à transmission Hitachi H600. Pour l'extraction des informations quantitatives et le traitement des images, le logiciel ImageJ a été utilisé.

C.3.5 La technique de FRAP

La technique employée a été la retour de fluorescence après photoblanchiment. Cette technique consiste à irradier une région de l'échantillon avec une impulsion de lumière intense et de courte durée. Ce processus détruit la fluorescence locale des molécules illuminées de façon irréversible [113, 114]. Ensuite, le faisceau est atténué et la migration des molécules situées au voisinage vers la zone "blanchie" provoque un retour de la fluorescence. Les études sur les propriétés dynamiques du complexe ont été faites avec un microscope confocal *Leica DMIRE*.

L'analyse des images de FRAP et l'obtention des coefficients de diffusion anisotropes ont été faites moyennant l'utilisation de l'éq. C.6. Un logiciel a été développé sur MatLab spécialement à cette fin.

C.4 Résultats structuraux

C.4.1 Système lipides-eau : la phase hôte

Membranes avec rapport PC-Simulsol 70 :30

Les analyses structurales ont été commencées par l'étude des phases hôtes préparées à partir de membranes avec un rapport PC-Simulsol égal à 70 :30. Les échantillons ont été formulés en utilisant de l'eau pure comme solvant avec des concentrations de lipides qui ont varié dans l'intervalle $\phi_{lip} = 0,25$ à $\phi_{lip} = 0,75$. Les principaux objectifs de cette étape étaient l'évaluation du domaine de dilution et de la limite d'hydratation, ainsi

2. La préparation des répliques a été faite avec l'aide précieuse d'Isabelle Lee, technicienne au CRPP.

que la détermination de l'épaisseur des membranes formées. Par ailleurs, une autre tâche importante était la vérification de la fluidité des queues aliphatiques, L_α ou L_β' .

Des phases multilamellaires de bicouches, régulièrement espacées, sont présentes dans tout le domaine d'hydratation étudié. La diffusion aux grands angles indique que les membranes se trouvent toujours dans l'état fluide, L_α . Ces résultats présentent un excellent accord avec les observations en microscopie optique à lumière polarisée, lesquelles montrent des textures biréfringentes très caractéristiques des phases lamellaires.

Le comportement des périodicités en fonction de l'inverse de la fraction volumique des lipides est montré dans la fig. C.4. Deux domaines sont bien identifiés sur la fig. C.4. Le premier est gouverné par la loi usuelle de dilution, où la périodicité est décrite par $d = \delta_m / (\phi_{lip})$. La pente d'une ligne droite ajustée aux données permet de déterminer l'épaisseur des bicouches comme étant $\delta_m = 36.5(3) \text{ \AA}$. Le deuxième domaine est caractérisé par une saturation, quand la périodicité maximale atteint une valeur de $D_{max} = 92(5) \text{ \AA}$.

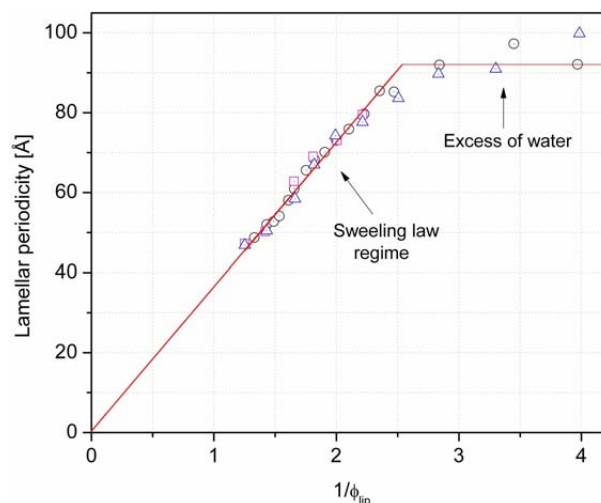


FIGURE C.4 – Comportement de la périodicité lamellaire d en fonction de $1/\phi_{lip}$. Deux domaines sont identifiés : le premier obéit à la loi de dilution usuelle, dont la pente permet déterminer l'épaisseur des membranes en $\delta_m = 36.5(3) \text{ \AA}$. Le deuxième présente un excès d'eau, avec une limite de dilution à $D_{max} = 92(5) \text{ \AA}$. Les cercles noirs correspondent aux données montrées sur la fig.3.2, les triangles bleus correspondent aux données montrées sur la fig.3.3(a) tandis que les carreaux roses sont associés aux données montrées sur la fig. 3.3(b).

Quelques-unes de ces formulations ont été aussi observées en microscopie électronique. Sur la fig. C.5, on montre deux exemples de ces images, obtenues pour un échantillon avec $\phi_{lip} = 0,752$. De vastes régions exemptes de défauts y sont trouvées, lesquelles se composent de terrasses lamellaires magnifiques, fig. C.5(a). Lorsque les fractures se produisent perpendiculairement au plan des bicouches, fig. C.5(b), il est possible de voir une forte anisotropie et, par analyse d'image en utilisant des transformées de Fourier, on détermine la périodicité lamellaire en $d = 50 \text{ \AA}$, en très bon accord avec les données des rayons X, $d = 49 \text{ \AA}$.

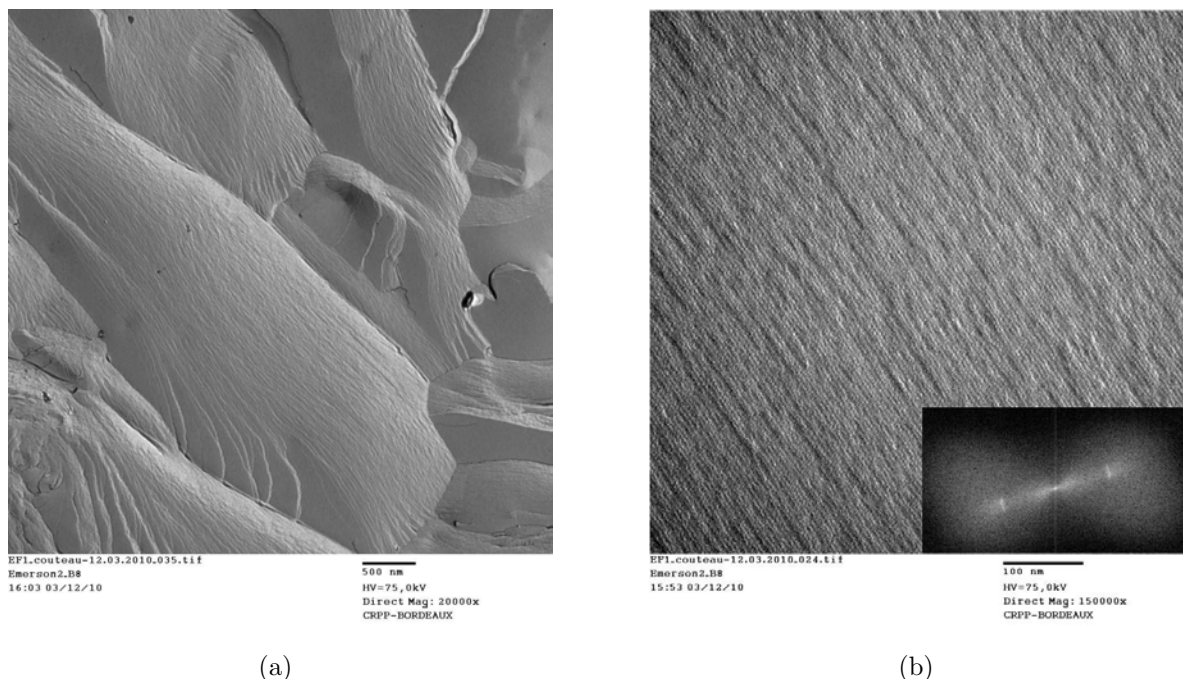


FIGURE C.5 – Images de microscopie électronique à transmission, obtenues sur un échantillon avec $\phi_{lip} = 0.752$. (a) Fractures parallèles aux plans des bicouches montrant de vastes terrasses lamellaires et (b) Fractures perpendiculaires montrant une forte anisotropie. L'analyse de Fourier a permis de mesurer la périodicité $d = 50 \text{ \AA}$, en très bon accord avec les données des rayons X, $d = 49 \text{ \AA}$.

Effets de l'addition de sel

Deux séries d'échantillons ont été préparées en utilisant des saumures comme solvant. Le sel utilisé dans les saumures a été l'acétate d'ammonium à 0,25 M. Le comportement résultant de la périodicité lamellaire, en fonction de l'inverse de la fraction volumique de lipides, est montré dans la fig. C.6. Aucune distinction notable n'est observée entre les données de formulations contenant du sel et de celles avec l'eau pure. L'épaisseur des membranes est trouvée valoir $\delta_m = 36.0(3) \text{ \AA}$ et la limite de dilution $D_{max.} = 89,3(6,5) \text{ AA}$. Ces valeurs sont très proches de celles trouvés auparavant.

Le modèle de Nallet et al. a été utilisé pour décrire les courbes de diffusion des rayons X de ces phases hôtes. Les principaux paramètres étudiés ont été le paramètre de Caillé, η , les tailles des têtes polaires, δ_H , et des queues aliphatiques, δ_T . Le comportement du paramètre de Caillé en fonction de la périodicité lamellaire est montré dans la fig. C.7(a). Tel que discuté précédemment, η est un indicateur du degré d'ordre smectique des phases lamellaire et son comportement en fonction de l'espacement intermembranaire est bien connu pour être dépendant de l'origine des interactions répulsives qui empêchent l'effondrement des membranes sous l'effets des forces de van der Waals. Les lignes sur la fig. C.7(a) correspondent à des prédictions pour des forces répulsives d'origine purement stérique (ondulations Helfrich) ou d'origine électrostatiques [34,92,94]. Comme il est possible de l'observer, aucun des deux modèles ne décrit bien le comportement de η . Cela montre la nécessité d'un autre modèle, où les forces d'hydratation soient aussi prises en compte,

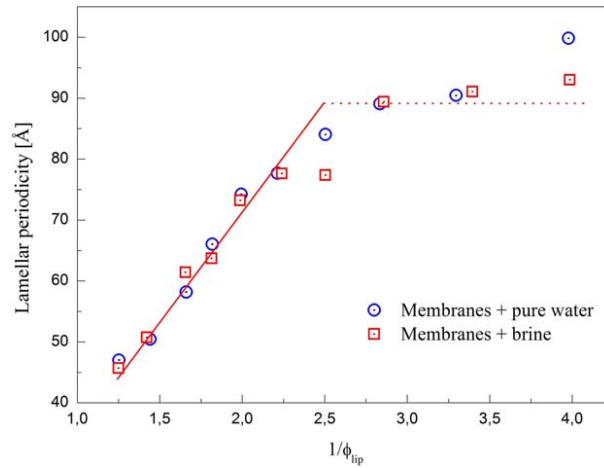


FIGURE C.6 – Périodicité lamellaire en fonction de $1/\phi_{lip}$ pour les échantillons préparés avec du sel et avec de l’eau pure. L’épaisseur des bicouches est $\delta_m = 36.0(3)$ Å tandis que la limite de dilution est $D_{max} = 89.3(6.5)$ Å.

pour faire une description appropriée des données expérimentales. Un tel modèle a été proposé par Petrache et

al. [132]. Selon ce modèle, il est possible d’extraire la moyenne quadratique de l’amplitude des fluctuations au travers de la relation :

$$\sigma^2 = \eta \frac{d^2}{\pi^2} \quad (\text{C.9})$$

Il est en outre possible de relier les amplitudes σ^2 aux séparations entre des membranes :

$$\sigma^{-2}(d'_w) = A_{fl} \exp\left(-\frac{d'_w}{\lambda_{fl}}\right) \quad (\text{C.10})$$

Dans la fig. C.7(b), le comportement de σ^{-2} en fonction de la séparation intermembranaire est montré. Comme on peut le voir, l’expression C.10 décrit bien les données observées. La longueur de décroissance des forces de fluctuation d’hydratation est trouvée être $\lambda_{fl} = 16.3(1.2)$ Å. Ce résultat est trois fois plus grand environ que les valeurs typiquement trouvées pour des membranes composées de lécithine pure. Donc, ici, on voit que l’introduction du Simulsol, en plus de faire monter la limite de dilution des lamelles formées, change la balance des interactions au sein de la phase lamellaire.

Membranes avec rapports PC-Simulsol 50 :50

Les mêmes procédures utilisées ci-dessus ont été employées dans la caractérisation des membranes avec le rapport 50 :50 entre PC et Simulsol. Avec l’addition de Simulsol, on présume que la rigidité des bicouches diminue. Seuls de petits changements ont été observés par rapport au comportement des membranes plus riches en lécithine. Un domaine d’hydratation régi par une loi de dilution usuelle a été aussi identifié et l’épaisseur des membranes a été déterminée en $\delta_m = 38,4(6)$ Å. Cette fois, il n’a pas été possible de bien identifier la limite d’hydratation des lamelles. Toutefois, il a été observé que le sys-

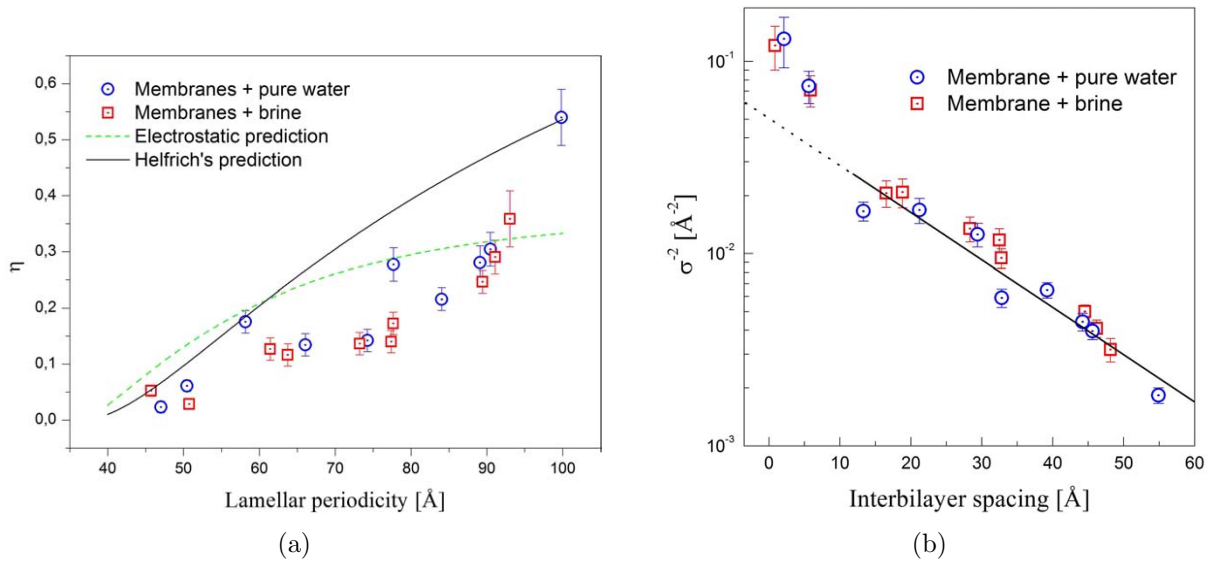


FIGURE C.7 – (a) Comportement du paramètre de Caillé en fonction de la périodicité lamellaire. Les lignes sont des prédictions théoriques pour $\eta(d)$ quand les répulsions entre lamelles sont d'origine stérique (noire) ou électrostatiques (verte). (b) Comportement de σ^{-2} en fonction de la séparation entre membranes. La ligne pleine est l'ajustement de l'expression C.10 aux données.

tème atteint des valeurs plus grandes de périodicité, ce qui a été interprété comme un changement des propriétés élastiques des phases formées.

Les modèles de Nallet et al. et de Petrache et al. ont été utilisés pour obtenir les paramètres de Caillé et étudier les fluctuations des membranes. Ici encore, il a été trouvé que les forces de van der Waals entre des bicouches sont équilibrées par un mélange de forces d'hydratation et de Helfrich.

Discussions

À partir des résultats décrits ci-dessus, on peut conclure que les phases hôtes utilisées dans ce travail s'auto-organisent dans des structures smectiques sur un domaine de dilution important. Pour les deux compositions de bicouches, il est possible d'obtenir des espacements intermembranaires plus grands que 20 Å, la séparation minimale géométriquement requise pour l'introduction de fragments d'ADN. En outre, il est également observé que le comportement de gonflement suit une relation linéaire classique, au moins dans une certaine gamme du domaine de dilution. Par conséquent, en contrôlant la concentration en lipides de la phase hôte, on peut contrôler le confinement exercé par la matrice lamellaire sur les particules insérées entre les membranes.

Pour les bicouches avec 70 :30 (PC :Simulsol), la limite d'hydratation se trouve à 92 Å environ. Pour l'autre composition de membrane, cette limite ne peut pas être déterminée avec précision. Cela témoigne de la modification introduite par l'ajout d'acides gras éthoxylés sur les propriétés des lamelles. En fait, la périodicité maximale dans les phases smectiques préparées à partir de lécithines pures (EPC, DMPC ou DPPC, par exemple)

est généralement autour de 60 Å. En soustrayant les valeurs habituelles des épaisseurs de bicouches dans ces phases, l'espacement aqueux reste à 24 Å environ [132–135]. Une telle valeur est déjà proche de l'espacement minimal requis pour accommoder des molécules d'ADN et ne permet pas une étude systématique du confinement sur l'assemblage supramoléculaire des particules hébergées. Ainsi, dans le cadre de cette thèse, l'ajout d'acides gras éthoxylés est fondamental pour élargir la gamme des espacements disponibles pour les nucléotides.

L'analyse du paramètre de Caillé a apporté quelques informations sur les interactions intermembranaires. Elle a révélé que les interactions qui préviennent l'effondrement des bicouches sous l'effet des forces attractives de van der Waals ne sont pas fondées sur la répulsion électrostatique. D'autre part, cette même analyse a montré que les interactions de Helfrich ne sont pas les seules forces de répulsion entre les membranes. Ces résultats montrent la nécessité d'un modèle hybride pour décrire l'équilibre des forces entre les bicouches. L'approche de Petrache et al. [132] s'est avérée être suffisante pour une telle analyse, en montrant qu'un mélange entre l'hydratation et les forces de fluctuations d'Helfrich est responsable de la répulsion dans les phases lamellaires. En outre, toujours selon cette méthodologie, la longueur de décroissance de cette force hybride est $\lambda_{fl} \approx 16.5$ Å, une valeur 3 fois plus élevée que celle généralement trouvée pour les bicouches de lecithines pures [134, 137, 138]. Ceci est une mesure quantitative de l'effet du Simulsol sur les propriétés élastiques des membranes utilisées ici. Ces résultats montrent que l'ajout d'acides gras éthoxylés joue un rôle clé pour agrandir l'espacement entre les membranes, ainsi que pour augmenter les effets des forces entropiques lesquelles, en l'absence d'interactions électrostatiques fortes entre ADN et membranes, sont un candidat sérieux pour induire la complexation.

C.4.2 Complexes lipides-ADN : polymorphisme structural

Membranes avec rapport PC-Simulsol 70 :30

Dans une deuxième étape, des échantillons contenant de l'ADN ont été étudiés. Contrairement à la plupart des études rapportées dans la littérature, où les complexes sont préparés dans un excès d'eau, ici, on a utilisé les propriétés de gonflement de la phase lamellaire afin de contrôler le confinement et induire l'organisation des nucléotides dans les complexes. La structure du complexe à des échelles mésoscopique et moléculaire a été suivie par SAXS et WAXS. L'addition de l'ADN n'a pas changé l'état liquide des queues aliphatiques. Un signal diffus à $q \approx 1.4$ Å⁻¹ a été observé pour toutes les formulations.

Les résultats les plus intéressants ont été observés sur la ligne $\rho = 3.1$. Deux domaines monophasiques y ont été trouvés. Le premier, placé dans une région plus diluée du diagramme ($0, 40 \lesssim \phi_{lip} \lesssim 0, 53$), est caractérisé par une symétrie nématique pour l'ADN inséré dans les couches aqueuses d'une phase lamellaire de lipides, L_{α}^N . Le deuxième domaine monophasique a été observé dans la région plus concentrée du diagramme ($\phi_{lip} \gtrsim 0, 58$).

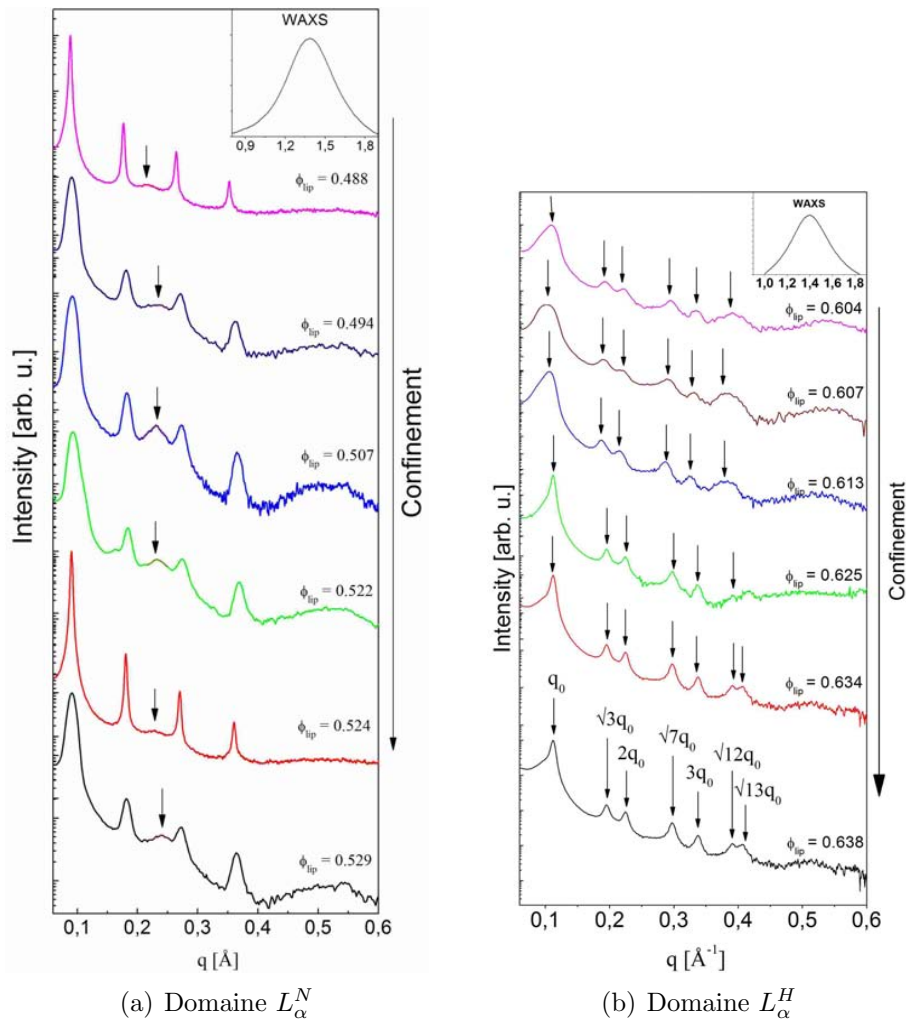


FIGURE C.8 – Diffractogrammes sélectionnés obtenus dans les deux domaines monophasiques trouvés sur la ligne $\rho = 3.1$. Les flèches indiquent le signal ayant pour origine les corrélations entre bâtonnets d’ADN. Encart : pic diffus aux grands angles montrant la fluidité des queues aliphatiques.

Les raies des diffractogrammes de cette région sont convenablement indexées par des symétries hexagonales. Les courbes de diffusion des rayons X obtenues dans ces domaines monophasiques sont montrées sur la fig. C.8.

Deux types d’organisations sont candidates pour expliquer la symétrie hexagonale observée dans le deuxième domaine : on peut avoir une phase lamellaire de lipides avec une phase hexagonale d’ADN intercalée entre ses membranes ou on peut avoir une phase hexagonale inverse de lipides contenant des bâtonnets d’ADN dans des cylindres d’eau. Les dessins schématiques de ces deux symétries sont montrés dans la fig. C.9.

Dans un travail antérieur, paru dans le contexte de la collaboration développée pendant cette thèse, des observations de microscopie optique en lumière polarisée et d’épifluorescence ont démontré que la symétrie L_α^H est le bon choix [21]. Ici, on complète ce cadre avec des observations en microscopie électronique. Dans la fig. C.10, des images de cryofracture d’un échantillon avec $\phi_{lip} = 0,634$ sont montrées. De nombreuses structures anisotropes sont visibles sur le plan des couches, fig. C.10(b). Ces structures en forme de bâtonnet

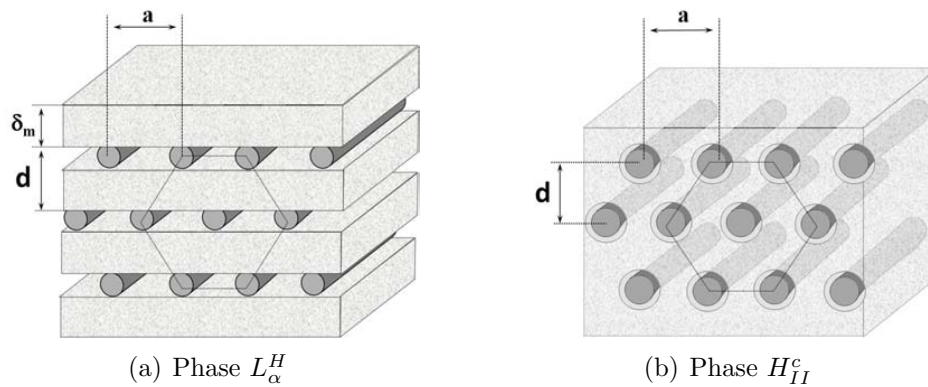


FIGURE C.9 – Représentation schématique d’une phase hexagonale colonnaire d’ADN dans une phase lamellaire de lipides, L_{α}^H (a) et d’une phase hexagonale inverse de lipides avec des bâtonnets d’ADN dans les cylindres d’eau, H_{II}^c (b).

ont en moyenne 530 \AA de long, en bon accord avec la taille attendue pour des molécules de 150 paires de bases, en tenant compte de la couche d’ombrage. La limite de résolution de la technique de cryofracture, qui est estimée à $\approx 20 \text{ \AA}$ **pour des structures périodiques** [12], ne permet pas de mesures précises du diamètre de l’ADN. Cependant, la forme des molécules peut être bien rendues comme il a été observé auparavant dans des contextes similaires [146–148]. À un grossissement plus petit, fig. C.10(a), des tiges d’ADN coexistent avec des sauts entre couches, indiqués par des flèches blanches, ce qui confirme la présence d’une stratification lamellaire. Par ailleurs, les séparations entre les branches sont mesurées à 61 \AA , en bon accord avec une séparation ADN-ADN égale à 65 \AA obtenue à partir des rayons X. L’analyse d’image, réalisée par des transformées de Fourier, fig. C.10(c), suggère la conservation d’orientation d’une couche à l’autre, en conformité avec les comportements attendus pour une structure L_{α}^H .

En plus de ces deux domaines monophasiques, deux autres domaines en coexistence sont aussi observés. Dans la région plus diluée du diagramme, on trouve la coexistence d’une phase L_{α}^N avec une phase lamellaire non complexée (sans ADN incorporé). Entre le domaine L_{α}^N et le domaine L_{α}^H , on trouve la coexistence entre ces deux domaines. L’ensemble des paramètres de cellules unitaires trouvés lors des analyses aux rayons X sur des formulations avec $\rho = 3, 1$ est synthétisé dans la fig. C.11.

Avec l’objectif d’évaluer de possibles effets de l’introduction d’ions monovalents sur les comportement du système, quelques formulations ont été préparées sur la ligne $\rho = 3, 1$, mais en utilisant des solutions d’acétate d’ammonium (0,25 M) comme solvant. Le comportement de phase des formulations préparées avec sel n’a pas présenté de changements remarquables par rapport aux formulations hydratées avec de l’eau pure.

Deux autres lignes de dilution, avec $\rho = 5, 1$ et $\rho = 8, 1$, ont été également étudiées. En général, un riche polymorphisme a été trouvé, avec un ordre plus faible à haute hydratation et l’émergence de domaines très organisés dans la région plus concentrée du diagramme. Pour ces lignes, on n’a pas retrouvé de domaines monophasiques. Exceptées deux formulations sur la ligne de $\rho = 5, 1$, avec $\phi_{lip} = 0,53$ et $\{\phi_{lip} = 0,37$, qui ont

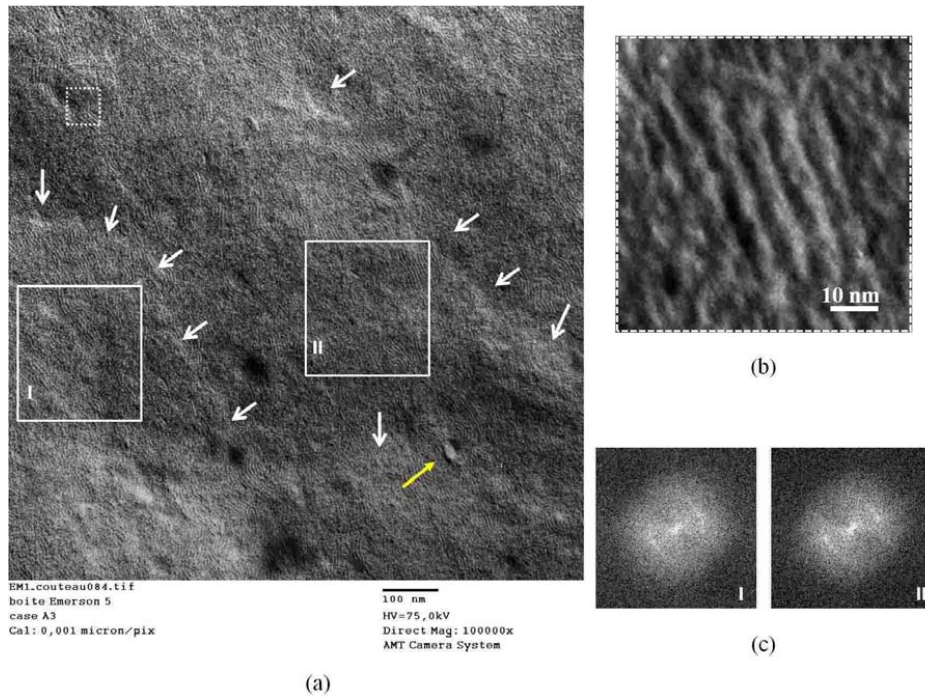


FIGURE C.10 – Clichés de microscopie électronique sur une réplique d'un échantillon du domaine L_{α}^H . (a) Flèches blanches montrant des marches smectiques qui délimitent des plans sur lesquels des structures anisotropes de forme cylindrique apparaissent. (b) Zoom du carreau pointillé sur la fig. A qui montre les bâtonnets en détail. (c) Transformée de Fourier sur les carreaux solides indiqués sur fig. A qui montre la conservation de l'orientation couche-à-couche.

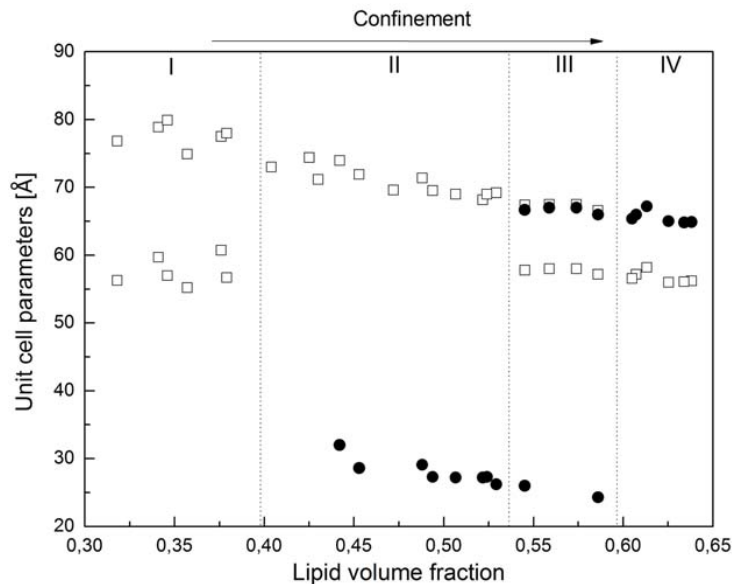


FIGURE C.11 – Comportement des paramètres structuraux en fonction de la fraction volumique des lipides le long d'une ligne de dilution avec $\rho = 3, 1$. Les carreaux représentent le pas smectique de la phase hôte tandis que les cercles, la séparation entre bâtonnets d'ADN. Les lignes pontillées sont des guides pour l'œil qui représentent les frontières approchées entre domaines.

présenté des symétries L_{α}^N monophasiques, toutes les structures ont été trouvées en co-existence. En plus, des observations de microscopie en lumière polarisée montrent des

textures lamellaires dans toute la gamme d'hydratation étudiée, soulignant la persistance d'une assemblée smectique des phases lipidiques. En microscopie de fluorescence, il a été possible d'identifier soit une coexistence entre des phases avec et sans ADN, ou la présence simultanée de nucléotides dans les deux phases lamellaires. Outre les organisations nématique et hexagonale déjà trouvées auparavant, ces lignes de dilution ont également révélé des raies de Bragg qui pourraient être indexées selon des symétries rectangulaires de l'ADN dans des phases lamellaires de lipides, L_α^R . Dans la figure C.12, le diagramme de phase expérimental complet obtenu pendant cette thèse est montré.

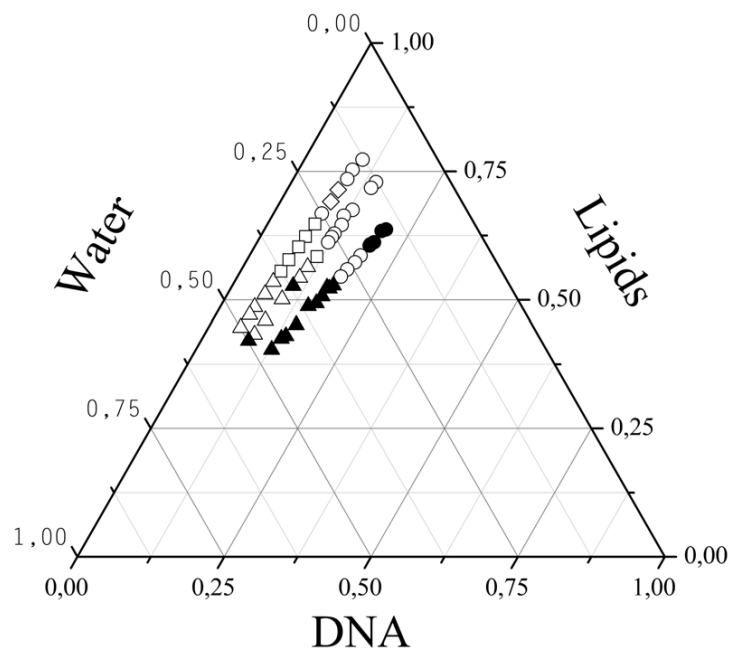


FIGURE C.12 – Diagramme de phase complet résultant de ce travail. Des domaines monophasiques sont observés de façon systématique seulement le long de la ligne $\rho = 3.1$. Les symboles pleins indiquent des points monophasiques : $\blacktriangle = L_\alpha^N$, $\bullet = L_\alpha^H$. Les symboles vides représentent une coexistence de phase : $\triangle = L_\alpha^N + L_\alpha^N$ or $L_\alpha^N + L_\alpha$, $\circ = L_\alpha^H + L_\alpha^N$ or $L_\alpha^H + L_\alpha$, $\diamond = L_\alpha^H + L_\alpha^R$, $\square = L_\alpha^N + L_\alpha^H$ ou $L_\alpha + L_\alpha^H$.

Membranes avec rapport PC-Simulsol 50 :50

Le comportement de phase des complexes ADN-lipides, préparés à partir de membranes avec le rapport 50 :50 (PC :Simulsol), a également été étudié. Vu que les études précédentes ont montré la présence systématique de domaines monophasique seulement le long de la ligne de dilution $\rho = 3,1$, les formulations ont été préparées avec ce rapport lipides :ADN. Un total de 19 échantillons a été formulé. Dix d'entre eux ont été hydratés avec de l'eau pure alors que les autres ont été dilués avec des saumures.

Le comportement de phase général est similaire à celui observé pour des échantillons préparés à partir de membranes de composition 70 :30 (PC :Simulsol). Les paramètres de cellule unitaire en fonction de la fraction volumique des lipides le long de la ligne de dilution est montré dans la fig. C.13.

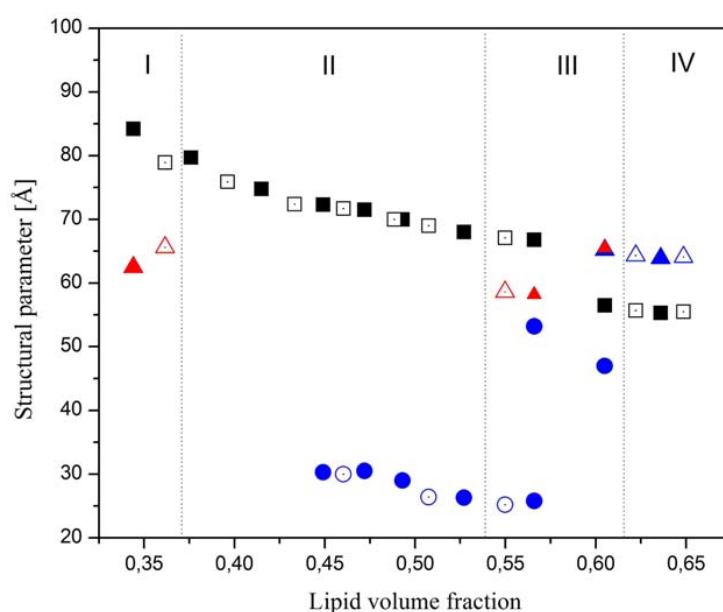


FIGURE C.13 – Paramètres structuraux en fonction de la fraction volumique des lipides pour les formulations préparées à partir de membranes 50 :50 (PC :Simulsol). Le rapport lipides :ADN est $\rho = 3,1$. Les carrés représentent les périodicités lamellaires et les cercles, les distances ADN-ADN. Les symboles pleins correspondent à des échantillons hydratés avec de l'eau pure et les symboles vides, à des échantillons hydratés avec de la saumure.

Discussions

Dans la fig. C.14, on montre des spectres de diffraction obtenus à partir d'échantillons avec ρ variable, pour des membranes de composition 70 :30 (PC :Simulsol). Comme le montant de l'hydratation est maintenu constant, les périodicités résultantes sont approximativement les mêmes pour toutes les formulations, avec $d \approx 73 \text{ \AA}$.

Avec cette simple comparaison, il est possible de vérifier la présence des phases en coexistence pour $\rho > 3,1$. La deuxième phase lamellaire est associée à un excès de lipides et forme une phase non complexée. À mesure que la quantité d'ADN augmente, les raies

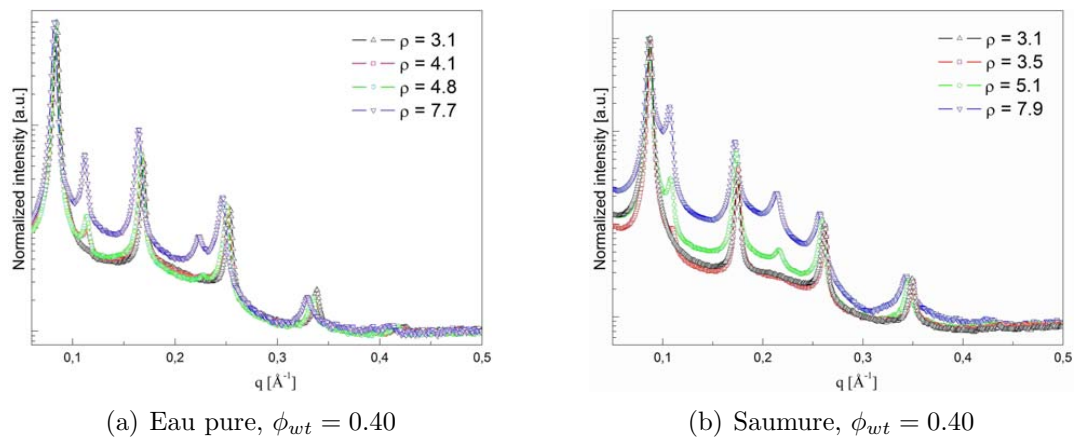


FIGURE C.14 – Comparaison entre des formulations avec différentes valeurs de ρ , préparées à partir de membranes 70 :30 (PC :Simulsol). La périodicité lamellaire $d \approx 73 \text{ \AA}$ pour les quatre échantillons.

associées à cette deuxième structure diminuent et, pour $\rho = 3, 1$, seulement les réflexions d'une unique phase lamellaire sont observées. Cette observation est un exemple clair de la dépendance de la complexation en ρ pour ces systèmes formulés à partir de lipides neutres.

Dans la fig. C.15, on montre des spectres de diffraction obtenus à partir d'échantillons à ρ variable. Comme le montant de l'hydratation est maintenu constant, les périodicités résultantes sont approximativement les mêmes pour toutes les formulations, avec $d \approx 73 \text{ \AA}$.

Dans la fig. C.15, la même chose est faite avec les données obtenues à partir des membranes 50 :50 (PC :Simulsol). La périodicité de ces échantillons est située autour de 73 \AA . Cette fois-ci les échantillons sont monophasiques, à l'exception d'un épaulement très faible sur l'échantillon à $\rho = 8, 1$, courbe bleue dans la figure C.15(b). Cette constatation suggère que les propriétés élastiques de la phase hôte jouent également un rôle significatif sur la complexation, ce qui renforce l'importance majeure des interactions stériques dans la conduite des relations intermoléculaires dans le système étudié dans ce travail. En outre, ces constats soutiennent l'approche de Flory donnée par les auteurs de la réf. [17].

Outre la formation de superstructures polymorphes d'ADN entre bicouches, on a observé que l'introduction des nucléotides a des effets dramatiques sur l'ordre smectique de la phase hôte. Dans la fig. C.16, on présente une comparaison entre des spectres obtenus à partir d'échantillons avec et sans nucléotides. On peut noter que, malgré la *quasi* égalité des périodicités, les formulations contenant de l'ADN sont significativement plus ordonnées que le complexe sans ADN. Cette augmentation de l'ordre smectique est clairement attestée par l'apparition d'un troisième et d'un quatrième ordre lamellaires, ainsi que par l'affinement des raies de Bragg.

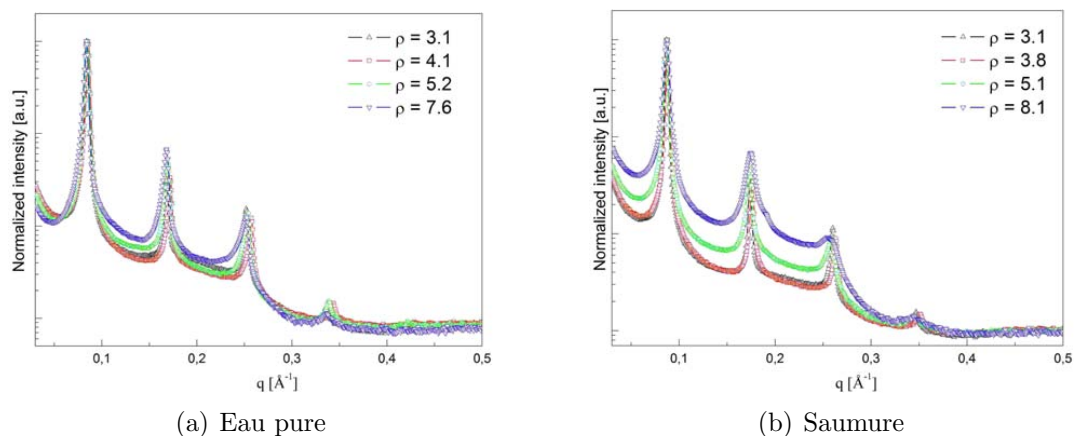


FIGURE C.15 – Comparaison entre des formulations avec différentes valeurs de ρ , préparées à partir des membranes 50 :50 (PC :Simulsol). La périodicité lamellaire $d \approx 73 \text{ \AA}$ pour les quatre échantillons.

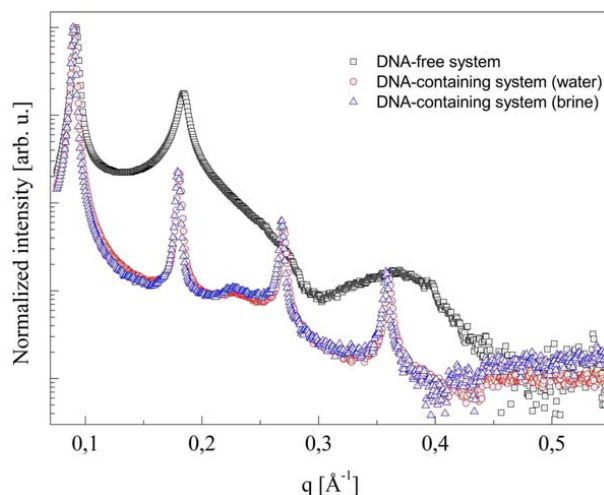


FIGURE C.16 – Comparaison entre des spectres obtenus à partir d'échantillons avec et sans ADN. La périodicité lamellaire est à peu près $d = 68 \text{ \AA}$. L'insertion d'ADN entre les bicouches augmente significativement l'ordre smectique. Les différences entre les formulations avec et sans sel sont négligeables.

C.5 Résultats dynamiques

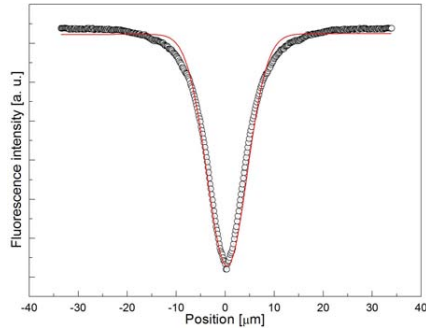
C.5.1 Expériences de FRAP

On a réussi à obtenir des échantillons assez bien orientés pour deux compositions dans le ternaire ADN-lipides-eau, dont les fractions volumiques pour l'eau, l'ADN et les lipides sont, respectivement, 0,50, 0,08 et 0,42 pour l'échantillon le plus hydraté, avec une charge relativement plus petite en fragments d'ADN ($\rho = 5.1$), et de 0,38, 0,15 et 0,47 pour l'autre échantillon ($\rho = 3.1$), également plus riche en ADN.

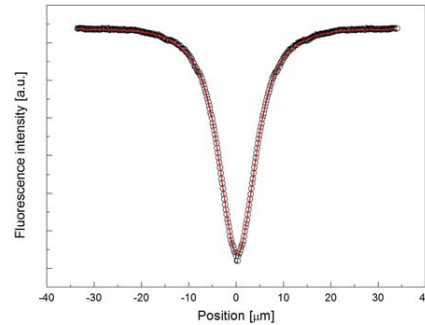
Les deux échantillons sont macroscopiquement homogènes et leurs spectres qui aux petits angles montrent 4 raies de Bragg dans les rapports 1 :2 :3 :4, sont caractéristiques d'un empilement de bicouches lamellaires [20]. Bien que seulement l'échantillon moins hydraté présente aussi une bosse diffuse typique ayant pour origine l'ordre nématique

des fragments confinés dans les couches d'eau, l'autre échantillon a probablement la même structure.

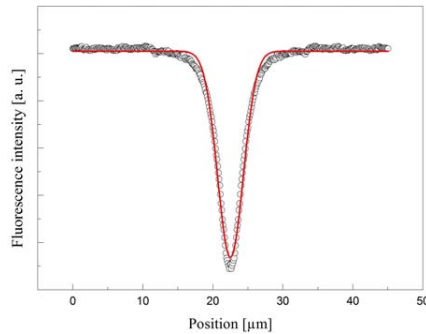
Les profils de retour de fluorescence s'écartent largement de la forme gaussienne pour les deux échantillons et les fonctions qui tiennent compte d'un seul coefficient de diffusion ne sont pas en mesure de bien décrire la région de la queue des données. Ces écarts sont clairement décrits dans la fig. C.17, où des profils typiques sont comparés et les ajustements faits soit avec une fonction de Gauss soit à partir de l'expression utilisant la fonction de Bessel modifiée, éq. C.6.



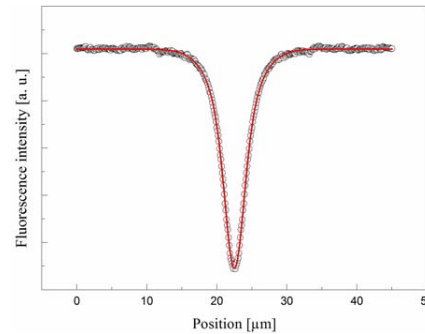
(a) $t = 300 \text{ s}$, $\rho = 5.1$, Ajustement avec une gaussienne .



(b) $t = 300 \text{ s}$, $\rho = 5.1$, Ajustement avec la fonction de Bessel modifiée.



(c) $t = 800 \text{ s}$, $\rho = 3.1$, Ajustement avec une gaussienne.



(d) $t = 800 \text{ s}$, $\rho = 3.1$, Ajustement avec la fonction de Bessel modifiée.

FIGURE C.17 – Profils de fluorescence des expériences de FRAP sur d'échantillons ADN-lipides-eau, d'orientation homéotrope. Les lignes rouges sont des ajustements par des fonctions gaussiennes ou par l'éq. C.6.

Le comportement temporel des deux variances obtenues pour l'échantillon avec $\rho = 5, 1$ sont exposées dans la fig. C.18. Ces paramètres sont clairement distincts, à tout moment, ce qui témoigne, maintenant en termes quantitatifs, de la forme non gaussienne des profils de retour de fluorescence. Les coefficients de diffusion obtenus sont $D_{\parallel} = 1, 3 \times 10^{-2} \mu\text{m}^2/\text{s}$ et $D_{\perp} = 2.8 \times 10^{-3} \mu\text{m}^2/\text{s}$, conduisant à un rapport d'anisotropie $D_{\parallel}/D_{\perp} \approx 4, 5$.

Des résultats assez similaires sont obtenus pour l'échantillon plus riche en ADN. L'écart systématique des profils à la forme gaussienne a été observé tout au long de la série. Le comportement temporel des variances ajustées est montré dans la fig. C.19. Il a été observé que, au début de la série (jusqu'à $t \approx 250 \text{ s}$), ni le profil gaussien, ni le modèle de Bessel modifié, n'ont été en mesure de donner une description satisfaisante des données

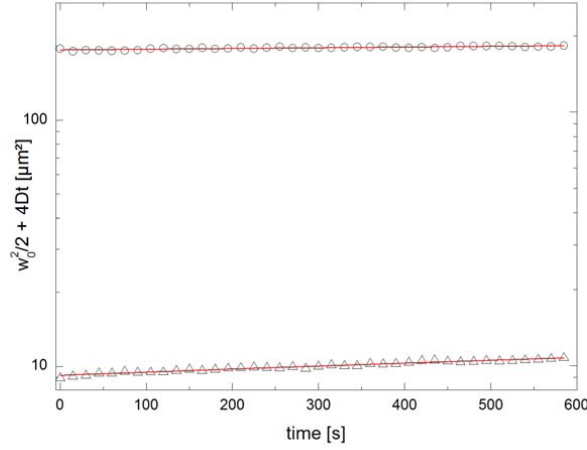


FIGURE C.18 – Variation temporelle des deux variances pour un échantillon avec $\rho = 5,1$ et $d = 77 \text{ \AA}$. Les lignes sont des ajustements linéaires qui conduisent à des coefficients de diffusion $D_{\parallel} = 1.3 \times 10^{-2} \mu\text{m}^2/\text{s}$ (\circ) et $D_{\perp} = 2.8 \times 10^{-3} \mu\text{m}^2/\text{s}$ (\triangle).

expérimentales. Cet écart peut être éventuellement attribuée à la rusticité du traitement approximatif fait en établissant le modèle, mais cela ne devrait pas nuire à sa validité, au moins dans la limite des grandes valeurs de temps. En effet, la figure C.19 indique que les deux variances sont raisonnablement bien décrites par des lois linéaires pour $t \geq 250 \text{ s}$. Malgré l'échec du modèle proche de $t = 0$, un tel comportement est la signature typique d'une dynamique brownienne. On a, donc, confiance à considérer les deux pentes résultant d'une analyse des données basées sur C.6 comme étant directement liées aux deux coefficients de diffusion D_{\parallel} et D_{\perp} . En termes quantitatifs, les coefficients de diffusion obtenus sont $D_{\parallel} = 2,7 \times 10^{-3} \mu\text{m}^2/\text{s}$ et $D_{\perp} = 6,6 \times 10^{-5} \mu\text{m}^2/\text{s}$, avec un rapport d'anisotropie $D_{\parallel}/D_{\perp} \approx 40$.

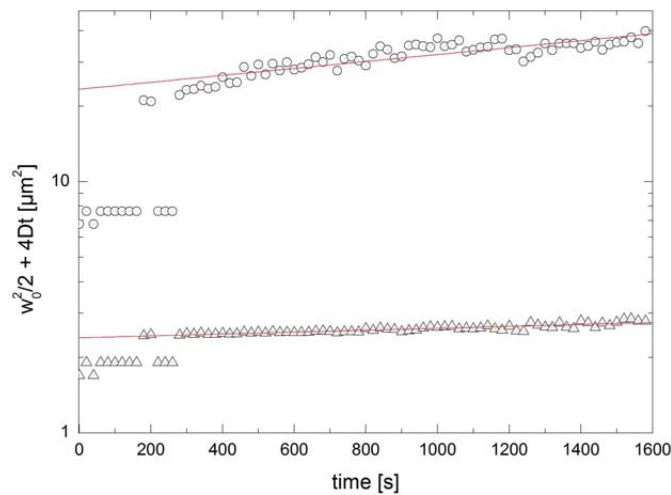


FIGURE C.19 – Variation temporelle des deux variances pour un échantillon avec $\rho = 3,1$ et $d = 69,6 \text{ \AA}$. Les lignes sont des ajustements linéaires qui conduisent à des coefficients de diffusion $D_{\parallel} = 2.7 \times 10^{-3} \mu\text{m}^2/\text{s}$ (\circ) et $D_{\perp} = 6.6 \times 10^{-5} \mu\text{m}^2/\text{s}$ (\triangle).

À partir des résultats décrits ci-dessus, le modèle proposé par Dobrindt s'est révélé

être approprié pour l'analyse par les profils de FRAP de la diffusion d'ADN entre des bicouches lipidiques. Des coefficients de diffusion parallèle et perpendiculaire à la direction nématique peuvent être extraits des données [24].

C.6 Conclusions et perspectives

Au long de cette thèse, les propriétés structurales et dynamiques d'un complexe hydraté formé à partir de fragments d'ADN (150 pb) et de bicouches non-cationiques ont été étudiés. La phase hôte a été obtenue

à partir de mélanges de phosphatidylcholines zwitterioniques et de Simulsol, un mélange de tensioactifs électriquement neutre. Les nucléotides, à leur tour, ont été obtenus par sonication de chaînes longues d'ADN de thymus de veau. Un accomplissement du travail est l'étude systématique du diagramme de phase de ce système, dont la région de faible hydratation a été étudiée ici pour la première fois. L'intégration complète des nucléotides à la phase lipidique a été observée pour être fortement liée à la quantité d'ADN dans le complexe, mettant en évidence l'importance des interactions de volume exclu sur la complexation et le comportement de phase. En outre, les analyses sur l'interaction des forces dans les phases lamellaires suggèrent que forces de fluctuation et d'hydratation sont des acteurs majeurs dans le complexe. Un autre résultat provenant de cette étude est la validation d'une proposition théorique pour l'extraction des coefficients de diffusion anisotrope dans les conditions très particulières de phases ordonnées d'ADN insérées dans les canaux d'eau d'une pile de membranes avec orientation homéotrope.

Trois caractéristiques spécifiques des complexes produits dans les conditions décrites ci-dessus méritent d'être soulignées dans ces remarques finales. En premier lieu, l'absence de charge nette sur les membranes permet d'exclure l'attraction entre des charges opposées comme acteur direct dans la complexation. Par conséquent, on a alors pour condition singulière d'étudier les effets des autres forces, en particulier celles d'origine entropique, dans l'interaction. Deuxièmement, puisque le système est formulé au dessous de sa limite d'hydratation, l'organisation des particules entre les bicouches est gouvernée par le *confinement* exercé par une matrice fluide, à l'échelle nanoscopique. Une troisième caractéristique remarquable du système est la restriction du solvant à l'espacement intermembranaire, sans la présence d'échanges avec une solution en vrac. Cet attribut a vraisemblablement des conséquences directes sur le processus de libération de contre-ions. Vu que les ions Na^+ sont piégés entre les bicouches, le gain entropique associé au relargage de ces cations doit être limité quand on compare des systèmes où les ions sont expulsés de la phase hôte. Ce contexte exige des changements dans l'interprétation traditionnelle du mécanisme impliqué dans la formation des lipoplexes, où la libération de contre-ions a un rôle central. Par conséquent, un autre mécanisme doit être en scène ce qui, éventuellement, implique des effets interfaciaux dans les interfaces bicouches-eau et ADN-bicouches.

Le travail a commencé par étudier la structure de la phase hôte, c'est-à-dire, le système

sans ADN composé uniquement par les lipides et le solvant. Une analyse détaillée montre que cette matrice lipidique s'auto-assemble dans des structures lamellaires à travers une large gamme d'hydratation. Cette affirmation est soutenue par des données des rayons X, ainsi que par des observations de microscopie électronique et optique. Deux régimes caractéristiques sont trouvés dans le domaine de dilution : le premier est régi par la loi de dilution usuelle $d = \delta_m / (1 - \phi_{wt})$. Dans le deuxième régime, un excès d'eau apparaît dans le système comme une conséquence de l'hydratation complète des membranes. Le comportement du paramètre de Caillé a montré que l'attraction de van der Waals est équilibrée par une interaction répulsive mixte résultant d'une combinaison entre forces d'hydratation et forces de Helfrich. En appliquant une approche proposée par Petrache et al. [132], on a été en mesure de déterminer la longueur de décroissance de cet interaction. La valeur trouvée est trois fois plus grande environ que celles généralement trouvées pour des lamelles formées à partir de lécithines pures. Ces résultats montrent que l'ajout de Simulsol aux membranes accroît l'importance des forces entropiques dans le système.

Dans une deuxième étape, des complexes contenant de l'ADN ont été étudiés. Les propriétés de gonflement de la phase ont été utilisées pour contrôler le pas smectique et ajuster le confinement imposé par les couches des lipides sur les nucléotides insérés au sein de la phase. À part les contre-ions de sodium qui neutralisent les groupes phosphate de l'ADN, aucun ion supplémentaire n'a été introduit pour médier la complexation. Un riche polymorphisme supramoléculaire d'ADN, inséré dans des phases lipidiques multilamelaires, a été mis en évidence. La formation de domaines monophasiques a été trouvée être fortement dépendante de la quantité de nucléotides, étant observée uniquement pour des formulations riches en ADN, lorsque le rapport PC :Simulsol est 70 :30. Ceci suggère un rôle majeur des contraintes stériques et de forces à courte portée dans la complexation. Il a été trouvé que le confinement a des effets dramatiques sur l'assemblage supramoléculaire des complexes. Des modèles géométriques simples ont été proposés et ont été capables de bien décrire les organisations observées, en particulier lorsque les séparations entre membranes sont assez grandes pour accueillir des brins d'ADN sans besoin de déformations des bicouches. Il faut noter que les transitions entre mésophases n'apparaissent pas associées à des transitions $L_\alpha \rightarrow L_{\beta'}$ dans les membranes.

Lorsque la proportion PC :Simulsol est 50 :50, l'incorporation complète des nucléotides aux lamelles est également observée pour des quantités inférieures de l'ADN. Cependant, le comportement de phase en fonction de l'hydratation (ou du confinement) reste assez similaire à celui trouvé dans les complexes préparés avec les autres membranes (probablement plus rigides). En outre, l'ajout de sel, ce dont on présume qu'il diminue le gain d'entropie associé à la libération des contre-ions sodium [63], n'a eu aucun effet notable ni sur la formation du complexe, ni sur son comportement de phase. Ces observations renforcent le rôle des propriétés élastiques sur la formation du complexe, tel que calculé dans le modèle de volume exclu décrit dans la réf. [17], alors que le confinement semble être le moteur principal de l'organisation des particules entre des bicouches.

L'ajout d'acides nucléiques semble augmenter l'ordre de la phase smectique. La réduction de l'espace entre les membranes implique une diminution du degré de liberté pour les fluctuations, ce qui permet l'organisation de l'ADN dans des superstructures fortement corrélées. Une approche utilisant le modèle de Nallet et al. a été appliquée à ce système ternaire afin de quantifier cet effet. Les résultats montrent que les fluctuations chutent par un facteur d'environ un ordre de grandeur lors de l'insertion de l'ADN dans la phase hôte. Cependant, puisque le modèle de Nallet et al. n'a pas été développé pour tenir compte des particules insérées dans les canaux d'eau, la méthode n'est pas en mesure de bien ajuster les spectres complets. Une perspective de bien décrire les facteurs de forme et de structure d'un tel complexe ADN-lipides-eau est en train de développement par Oliveira et al. [159]. La proposition est basée sur des techniques d'éléments finis qui sont utilisés pour simuler des courbes de dispersion des rayons X et découpler les facteurs de forme et de structure associés au complexe. Un exemple de ce calcul est montré dans la figure. C.20.

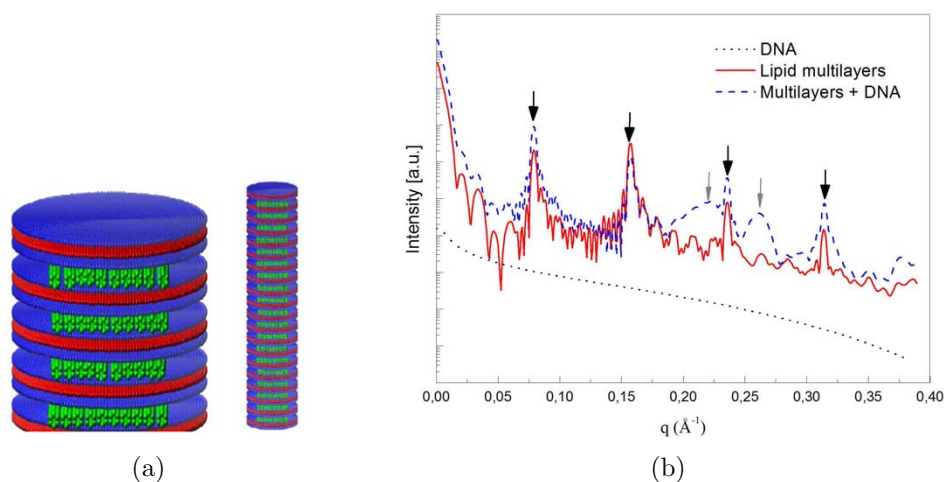


FIGURE C.20 – Simulation avec une méthode d'éléments finis : (a) Piles de lipides avec bâtonnets d'ADN entre des bicouches, construit à partir de sous-unités sphériques. (b) Diffractogrammes résultants obtenus à partir du modèle (figures aimablement fournies par C.L.P. Oliveira).

En ce qui concerne les analyses dynamiques, le modèle proposé par Dobrindt s'est avéré suffisant pour analyser les profils de FRAP dans des systèmes avec des conditions très spécifiques de symétrie pour les complexes étudiés dans ce travail : symétries locales nématiques de bâtonnets, moyennées le long d'un axe perpendiculaire aux directeurs nématiques. Même si la moyenne conduit à une symétrie axiale des profils de retour de fluorescence, les coefficients de diffusion parallèle et perpendiculaire au directeur nématique peuvent être extraits des données. Le confinement et la concentration des fragments d'ADN ont été variés simultanément, avec des rapports volumiques lipides :ADN et hauteur du canal de solvant, respectivement, $\rho = 5, 1$ et $40, 5 \text{ \AA}$ pour un échantillon, $\rho = 3, 1$ et de $33, 1 \text{ \AA}$ pour l'autre. Comme le diamètre de l'ADN, plus une couche d'hydratation, est d'environ 24 \AA , dans les deux cas, le confinement des fragments d'ADN par les bicouches lipidiques est fort.

Le confinement des fragments d'ADN par les bicouches lipidiques semble être très efficace dans le ralentissement du mouvement brownien des particules. En revanche, l'augmentation de l'anisotropie de diffusion D_{\parallel}/D_{\perp} peut, en principe, être attribuée à un effet de concentration. Cela ouvre aussi une perspective d'étude des effets interfaciaux impliqués dans les interactions entre l'ADN et les membranes, car le frottement des particules dans le plan de bicouches pourrait être dépendant du confinement. Les analyses structurales et dynamiques menées dans ce travail doivent être considérées dans un cadre de complémentarité, car il a été démontré que le profil de fluorescence des taches apporte également des informations sur la structure.

BIBLIOGRAPHY

- [1] M. Malmsten. *Soft Matter*, (2):760–769, 2006.
- [2] R. Koynova and B. Tenchov. *Soft Matter*, 5:3187–3200, 2009.
- [3] J. N. Israelachvili. *Intermolecular and Surfaces Forces*. Academic Press Limited, London, 1991.
- [4] P. L. Felgner. *Proc. Natl. Acad. Sci.*, 84:7413–7417, 1987.
- [5] P. L. Felgner and G. M. Ringold. *Nature*, 337:387–388, 1989.
- [6] P. L. Felgner and G. Rhodes. *Nature*, 349:351–352, 1991.
- [7] C. Safinya. *Curr. Opin. Struc. Biol.*, 11:440–448, 2001.
- [8] J. O. Radler; I. Koltover; T. Salditt and C. R. Safinya. *Science*, 275:810–814, 1997.
- [9] I. Koltover; T. Salditt; J. O. Radler and C. R. Safinya. *Science*, 281:78–81, 1998.
- [10] K. K. Ewert; H. M. Evans; A. Zidovska; N. F. Bouxsein; A. Ahmad and C. R. Safinya. *J. Am. Chem. Soc.*, 128:3998–4006, 2006.
- [11] J. Gustafsson; G. Arvidson; G. Karlsson and M. Almgren. *Biochim. Biophys. Acta*, 1235:305–312, 1995.
- [12] B. Sternberg; F.L. Sorgi and L. Huang. *FEBS Lett.*, 356:361–366, 1994.
- [13] B. J. Battersby; R. Grimm; S. Huebner and G. Cevc. *Biochim. Biophys. Acta*, 1372:379–383, 1998.
- [14] V. A. Rakhmanova; E. V. Pozharski and R. C. MacDonald. *J. Membr. Biol.*, 200:35–45, 2004.
- [15] D. Harries; S. May; W.M. Gelbart and A. Ben-Shaul. *Biophys. J.*, 75:159–173, 1998.
- [16] T. Pott and D. Roux. *FEBS Lett.*, 511:150–154, 2002.
- [17] A. Colin and D. Roux. *Eur. Phys. J. E*, 8:499–506, 2002.
- [18] R. Podgornik and V. Parsegian. *Langmuir*, 8:557–562, 1992.
- [19] M. Manciu and E. Ruckenstein. *Adv. Coll. Interf. Sc.*, 112:109–128, 2004.

- [20] E. R. Teixeira da Silva; E. Andreoli de Oliveira; A. Fevrier; F. Nallet and L. Navailles. *Eur. Phys. J. E*, 34:83, 2011.
- [21] E. Andreoli de Oliveira; E. R. Teixeira da Silva; E. Grelet; A. Fevrier; F. Nallet and L. Navailles. *Europhys. Lett.*, 91:28001, 2010.
- [22] C. Leal; D. Topgaard; R. W. Martin and H. Wennerstrom. *J. Phys. Chem. B*, 108:15392–15397, 2004.
- [23] J. Dobrindt. Dna diffusion in concentrated aqueous solution and confined between lipid bilayers. Master's thesis, University of Bordeaux-Centre de Recherche Paul-Pascal, 2006.
- [24] J. Dobrindt; E. R. Teixeira da Silva; C. Alves; C. L. P. Oliveira; F. Nallet; E. Andreoli de Oliveira and L. Navailles. *accepted by EPJE*, 2011.
- [25] C. R. Cantor and P. R. Schimmel. *Biophysical Chemistry part I*. W.H. Freeman and Company, 2002.
- [26] J. F. Faucon and P. Méléard. *Liposomes, aspects technologiques, biologiques et pharmacologiques*. Les Editions INSERM, 1993.
- [27] J. Seeling; H. U. Gally and R. Wohlgemuth. *Biophys. Biochim. Acta*, 467:109–119, 1977.
- [28] P. G. de Gennes and J. Prost. *The physics of liquid-crystals*. Claredon Press, Oxford, 1993.
- [29] G. Tresset. *PMC Biophysics*, (2):doi: 10.1186/1757–5036/2/3, 2009.
- [30] D. Harries. *Electrostatic interaction between macromolecules and mixed lipid bilayers*. PhD thesis, Hebrew University Senate, 2001.
- [31] F. Livolant and A. Leforestier. *Prog. Polym. Sc.*, 21:1164–1996, 1996.
- [32] H. Lowen. *Phys. Rev. E*, 59:1989–1995, 1999.
- [33] R. Podgornik; H. H. Strey and V. A. Parsegian. *Curr. Op. Coll. Int. Sc.*, 3:534–539, 1998.
- [34] D. Roux; C. Safinya and F. Nallet. *Micelles, membranes, microemulsions and monolayers*, pages 303–346. Springer-Verlag, New York, 1994.
- [35] G. S. Smith; E. B. Sirota; C. R. Safinya and N. A. Clark. *Phys. Rev. Lett.*, (60):813–816, 1988.
- [36] O. Diat; D. Roux and F. Nallet. *J. Phys. II France*, 3:1427–1452, 1993.
- [37] F. Nallet; D. Roux; C. Quiliet; P. Fabre and S. T. Milner. *J. Phys. II France*, 4:1477–1499, 1994.
- [38] F. Nallet; D. Roux and J. Prost. *Phys. Rev. Lett.*, 62:276–279, 1989.
- [39] T. Charitat and S. Lecuyer. *Biointerphases*, 3(2), 2008.
- [40] D. Sornette and N. Ostrowsky. *Micelles, membranes, microemulsions and monolayers*, pages 251–295. Springer-Verlag, New York, 1994.

- [41] W. Helfrich and R. M. Servuss. *Nuovo Cimento*, 3:137–151, 1984.
- [42] D. Roux and C. Safinya. *J. Phys. II France*, 49:307–318, 1988.
- [43] J. N. Israelachvili and H. Wennerstrom. *J. Phys. Chem.*, 96:520–531, 1992.
- [44] J. Faraudo and F. Bresme. *Phys. Rev. Lett.*, 94:07782, 2005.
- [45] D. M. LeNeveu; R. P. Rand; V. A. Parsegian and D. Gingell. *Biophys. J.*, 18:209–230, 1977.
- [46] S. Leikin; V. A. Parsegian and D. C. Rau. *Annu. Rev. Phys. Chem.*, 44:369–395, 1993.
- [47] R. Podgornik; D. Harries; J. DeRouchey; H.H. Strey and V. A. Parsegian. *Gene Therapy - therapeutic mechanisms and strategies*, chapter Interaction in macromolecular complexes used as nonviral vector for gene delivery, pages 443–478. 2003.
- [48] W. Helfrich. *Z. Naturforsch*, 28c:693–703, 1973.
- [49] W. Helfrich. *Z. Naturforsch*, 33a:305–315, 1978.
- [50] W. Gelbart; R. Bruinsma; P. Pincus and V. Parsegian. *Phys. Today*, 53:38–44, 2000.
- [51] J. D. Watson and F.H.C. Crick. *Nature*, (171):737–738, 1953.
- [52] C. R. Calladine; H. R. Drew; B. F. Luisi and A. A. Travers. *Understanding DNA*. Elsevier Academic Press, London, 2004.
- [53] A. Meyer-Koll; C. Fleck and H. von Gronberg. *J. Phys. Condens. Matter*, 16:6041–6052, 2004.
- [54] S. May and A. Ben-Shaul. *Curr. Med. Chem.*, 11:151–167, 2004.
- [55] M. Feig and B. M. Pettitt. *Biopolym.*, 48:199–209., 1998.
- [56] C. Leal; L. Wadso; G. Olofsson; M. Miguel and H. Wennerstrom. *J. Phys. Chem. B.*, 108:3044–3050, 2004.
- [57] G. S. Manning. *Biophys. Chem.*, 51:924–933, 1969.
- [58] T. E. Strzelecka and R. L. Rill. *Macromol.*, 24:5124–5133, 1991.
- [59] R. Podgornik; H. H. Strey; D. C. Rau and V. A. Parsegian. *Biophys. Chem.*, 57:111–121, 1995.
- [60] H. H. Stry; R. Podgornik; D. C. Rau and A. Parsegian. *Curr. Op. Struc. Biol.*, 8:309–313, 1998.
- [61] D.C. Rau; B. Lee and V. A. Parsegian. *Proc. Nat. Acad. Sc.*, 81:2621–2625, 1984.
- [62] G. Odriozola; F. Jimenez-Angeles and M. Lozada-Cassou. *Phys. Rev. Lett.*, 97:018102, 2006.
- [63] I. Koltover; K. Wagner and C. R. Safinya. *Proc. Nat. Acad. Sc.*, 97:14046–14051, 2000.
- [64] H. Liang; D. Harries and G. C. L. Wong. *Proc. Nat. Acad. Sc.*, 102:11173–11178, 2005.

- [65] F. Artzner; R. Zantl; G. Rapp and J. O. Radler. *Phys. Rev. Lett.*, 81:5015–5018, 1998.
- [66] G. Caracciolo; D. Pozzi; R. Caminiti; G. Mancini; P. Luciani and H. Amenitsch. *J. Am. Chem. Soc.*, 129:10092–10093, 2007.
- [67] R. Koynova; L. Wang and R. MacDonald. *Mol. Pharmaceut.*, 5:739–744, 2008.
- [68] A. Bilalov; U. Olsson and B. Lindman. *Soft Matt.*, 7:730–742, 2011.
- [69] O. Farago and N. Gronbech-Jensen. *Phys. Rev. Lett.*, 96:0181102, 2006.
- [70] L. Golubovic; T.C. Lubensky and C.S. O’Hern. *Phys. Rev. E*, 62:1069–1093, 2000.
- [71] C. S. O’Hern and T. C. Lubensky. *Phys. Rev. Lett.*, 80:4345–4348, 1998.
- [72] R. Bruinsma. *Eur. Phys. J. B*, 4:75–88, 1998.
- [73] A.G. Cherstvy. *J. Phys. Chem. B*, 111:7914–7927, 2007.
- [74] S. May; D. Harries and A. Ben-Shaul. *Biophys. J.*, 78:1681–1697, 2000.
- [75] O. Farago and N. Gronbech-Jensen. *J. Am. Chem. Soc.*, 131:2875–2881, 2009.
- [76] O. Farago and N. Gronbech-Jensen. *Soft Mat.*, 7:4302–4306, 2011.
- [77] K. Wagner; D. Harries; S. May; V. Kahl; J. O. Radler and A. Ben-Shaul. *Langmuir*, 16:303–306, 2000.
- [78] R.S. Shirazi; K. K. Ewert; C. Leal; R. N. Majzoub; N. F. Bouxein and C. R. Safinya. *Biochem. Biophys. Acta*, page DOI: 10.1016/j.bbamem.2011.04.020, 2011.
- [79] C. Leal; N.F. Bouxein; K. K. Ewert and C. R. Safinya. *J. Am. Chem. Soc.*, 132:16841–16847, 2010.
- [80] N. F. Bouxein; C. S. McAllister; K. K. Ewert; C. E. Samuel and C. R. Safinya. *Biochem.*, 46:4785–4792, 2007.
- [81] C.R. Dass. *J. Mol. Med.*, 82:579–591, 2004.
- [82] M. C. Fillion and N. C. Phillips. *Biochem. Biophys. Acta*, 1329:345–356, 1997.
- [83] J. J. McManus; J. O. Radler and K. A. Dawson. *Langmuir*, 19:9630–9637, 2003.
- [84] J. J. McManus; J. O. Radler and K. A. Dawson. *J. Phys. Chem. B*, 107:969–9873, 2003.
- [85] D. Roux; P. Chenevier; T. Pott; L. Navailles; O. Regev and O. M. Monval. *Curr. Med. Chem.*, 11:169–177, 2004.
- [86] T. Pott; A. Colin; L. Navailles and D. Roux. *Interf. Sci.*, 11:249–257, 2003.
- [87] A. Caille. *C.R. Acad. Sc. Paris*, 274:891–893, 1972.
- [88] E. Kurtisovski. *Relation structure-propriétés dans les bicouches gonflées de phases lamellaires*. PhD thesis, Université Pierre et Marie Curie, 2007.
- [89] G. Pabst; M. Rappolt; H. Amenitsch and P. Laggner. *Phys. Rev. E*, 62:4000–4009, 2000.

- [90] B. Pozo-Navas K. Lohner G. Pabst, R. Koschuch and P. Laggner. *J. App. Cryst.*, 36:1378 – 1388, 2003.
- [91] R. Zhang; R. M. Suter and J. F. Nagle. *Phys. Rev. E*, 50:5047–5060, 1994.
- [92] C. R. Safinya; D. Roux; G. S. Smith; S. K. Sinha; P. Dimon; N.A. Clark and A. M. Bellocq. *Phys. Rev. Lett.*, 57:2718–2721, 1986.
- [93] F. Nallet; R. Laversanne and D. Roux. *J. Phys. II France*, 3:487–502, 1993.
- [94] M. F. Ficheux; A. M. Bellocq and F. Nallet. *Eur. Phys. J. E*, 4:315–326, 2001.
- [95] G. Bouglet and C. Ligoure. *Eur. Phys. J. E*, 9:137–147, 1999.
- [96] B. Yang; J. Lal; P. Richetti; C. Marques; W. Russel and R. Prudhomme. *Langmuir*, 17:5834–5841, 2001.
- [97] I. Grillo; P. Levitz and Th. Zemb. *Eur. Phys. J. E*, 5:377–386, 2001.
- [98] G. Pabst. *Biophys. Rev. Lett.*, 1:57–84, 2006.
- [99] P. Moreau; D. van Effenterre; L. Navailles; F. Nallet and D. Roux. *Eur. Phys. J. E*, 26:225–234, 2008.
- [100] A. Pluen; P. A. Netti; R. K. Jain and D. A. Berk. *Biophys. J.*, 77:542–552, 1999.
- [101] S. Nehls; E. L. Snapp; N. B. Cole; K. J. M. Zaal; A.K. Kenworthy; T. H. Roberts; J. Ellenberg; J. F. Presley; E. Siggia and J. Lippincott-Schwartz. *Nature Cell Biol.*, 2:288–295, 2000.
- [102] V. Chan; D. J. Graves; P. Fortina and S.E. McKenzie. *Langmuir*, 13:320–329, 1997.
- [103] M. M. Tirado and J. Garcia de la Torre. *J. Chem. Phys.*, 71:2581–2587, 1979.
- [104] M. M. Tirado and J. Garcia de la Torre. *J. Chem. Phys.*, 81:2047–2052, 1984.
- [105] B. A. Scalettar; J. E. Hearst and M. P. Klein. *Macromol.*, 22:4550–4559, 1989.
- [106] L. Wang; M. M. Garner and H. Yu. *Macromol.*, 24:2368–2376, 1991.
- [107] K. Braeckmans; L. Peeters; N. N. Sanders; S. C. De Smedt and J. Demeester. *Biophys. J.*, 85:2240–2252, 2003.
- [108] S. A. Tartakova and D. A. Berk. *Phys. Rev. E*, 71:041913, 2005.
- [109] C. Alves. Propriedades dinâmicas de fases condensadas de dna. Master’s thesis, Universidade de São Paulo-Instituto de Física, 2010.
- [110] G. L. Lukacs; P. Haggie; O. Seksek; D. Lechardeur; N. Freedman and A. S. Verkman. *J. Biol. Chem.*, 275:1625–1629, 2000.
- [111] M.P.B. van Bruggen; H.N.W. Lekkerkerker; G. Maret and J.K.G. Dhont. *Phys. Rev. E*, 58:7668–7677, 1998.
- [112] J. Crank. *The mathematics of diffusion*. Clarendon Press, Oxford, 1975.
- [113] S. Seiffert and W. Oppermann. *J. Microsc.*, 220:20–30, 2005.
- [114] G. Hauser; S. Seiffert and W. Oppermann. *J. Microsc.*, 230:353–362, 2008.

- [115] T. K. L. Meyvis; S. C. De Smedt; P. van Oostveldt and J. Demeester. *Pharm. Res.*, 16:1153–1162, 1999.
- [116] J. Dobrindt. Dna diffusion in concentrated aqueous solution and confined between lipid bilayers. Defence talk, 2006. Centre de Recherche Paul-Pascal.
- [117] C. Carlsson; A. Larsson; M. Jonsson; B. Albinsson and B. Norden. *J. Phys. Chem.*, 98:10313–10321, 1994.
- [118] A. Larsson; C. Carlsson; M. Jonsson and B. Albinsson. *J. Am. Chem. Soc.*, 116:8459–8465, 1994.
- [119] Sigma Aldrich. Product information sheet n. p7443. Technical report, Sigma Aldrich, 2007.
- [120] D. Marsh. *Biophys. J.*, 61:1036–1040, 1992.
- [121] Seppic. Product information n. 38387a. Technical report, Seppic.
- [122] J. Perez; F. Artzner; P. Barois; C. Bourgaux; P. Davidson; O. Lyon; A. Naudon; P. Panine; P. Vachette and Th. Zemb. Proposal for a small-angle x-ray scattering instrument at soleil : scientific case and brief technical description. Technical report, Synchrotron SOLEIL, 2002.
- [123] B.D. Cullity. *Elements of X-rays diffraction*. Addison-Wesley, Massachussets, 1956.
- [124] T. C. Huang; H. Toraya; T. N. Blanton and Y. Wu. *J. Appl. Cryst.*, 26:180–184, 1993.
- [125] J. S. Pedersen; D. Posselt and K. Mortensen. *J. Appl. Cryst.*, 23:321–333, 1990.
- [126] O. Francescangeli; M. Pisani; V. Stanic; P. Bruni and T. M. Weiss. *Europhys. Lett.*, 67:669–675, 2004.
- [127] E. Shyamsunder; S. M. Gruner; M. W. Tate; D. C. Turner and P. T. C. So. *Biochem.*, 27:2332–2336, 1988.
- [128] P. Barois; S. Hyde; B. Ninham and T. Dowling. *Langmuir*, 6:1136–1140, 1990.
- [129] N. J. Servers. *Nature Protocols*, 2:547–576, 2007.
- [130] S. Seiffert and W. Oppermann. *Polym.*, 49:4115–4126, 2008.
- [131] G. I. Hauser. *Umsetzung eines Verfahrens zur Bestimmung von Diffusionskoeffizienten*. PhD thesis, Technische Universitat Clausthal, 2008.
- [132] H. I. Petrache; N. Gouliaev; S. Tristam-Nagle; R. Zhang; R. M. Suter and J. F. Nagle. *Phys. Rev. E*, 57:7014–7024, 1998.
- [133] H. I. Petrache. *Structure and interactions of fluid phospholipid bilayers measured by high resolution X-ray scattering*. PhD thesis, Carnegie Mellon University, 1998.
- [134] H. I. Petrache; S. Tristam-Nagle and J. F. Nagle. *Chem. Phys. Lip.*, 95:83–94, 1998.
- [135] J. Nagle and S. Tristam-Nagle. *Curr. Op. Struct. Biol.*, 10:474–480, 2000.
- [136] T. McIntosh. *Curr. Op. Struct. Biol.*, 10:481–485, 2000.

- [137] N. Kucerka; J. Nagle; J. Sachs; S. Feller; J. Pencer; A. Jackson and J. Katsaras. *Biophys. J.*, 95:2356–2367, 2008.
- [138] N. Kucerka; Y. Liu; N. Chu; H. I. Petrache; S. Tristram-Nagle and J. F. Nagle. *Biophys. J.*, 88:2626–2637, 2005.
- [139] S. D. Guler; D. D. Ghosh; J. Pan; J. C. Mathai; M. L. Zeidel; J. F. Nagle and Stephanie Tristram-Nagle. *Chem. Phys. Lip.*, 160:33–44, 2009.
- [140] P. Berntsen; C. Svanberg and J. Swenson. *J. Phys. Chem. B*, 115:1825–1832, 2011.
- [141] G. Pabst; N. Kucerka; M. Nieh; M. Rheinstadter and J. Katsaras. *Chem. Phys. Lip.*, 163:460–470, 2010.
- [142] J. Pan; S. Tristram-Nagle and J. F. Nagle. *Phys. Rev. E*, 80:021931, 2009.
- [143] T. Salditt; I. Koltover; J. O. Radler and C. R. Safinya. *Phys. Rev. Lett.*, 79:2582–255, 1997.
- [144] D. Durant; J. Doucet and F. Livolant. *J. Phys. II France*, 2:1769–1783, 1992.
- [145] P. Pinto da Silva and D. Branton. *J. Cell Biol.*, 45:598–605, 1970.
- [146] F. Livolant. *Physica A*, 176:117–137, 1991.
- [147] A. Leforestier and F. Livolant. *Biophys. J.*, 73:1771–1776, 1997.
- [148] F. Livolant; A. M. Levelut; J. Doucet and J. P. Benoit. *Nature*, 339:724–726, 1989.
- [149] S. Weinkauf and L. Bachmann. *Ultramicroscopy*, 46:113–134, 1992.
- [150] O. Mondain-Monval. *Curr. Op. Coll. Interf. Sc.*, 10:250–255, 2005.
- [151] M. D. Rogers. *J. Sci. Instrum.*, 43:390–391, 1966.
- [152] P. Alexandridis; U. Olsson and B. Lindman. *Langmuir*, 13:23–34, 1997.
- [153] V. Ponsinet and P. Fabre. *J. Phys. II France*, 6:955–960, 1996.
- [154] Y. Suganuma; M. Imai and K. Nakaya. *J. Appl. Crystallogr.*, 40:S303–S306, 2007.
- [155] J.P. de Silva; A.S. Poulos; B. Pansu; P. Davidson; B. Kasmi; D. Petermann; S. Asnacios; F. Meneau and M. Imp  ror. *Eur. Phys. J. E*, 34:4, 2011.
- [156] R. Koynova and R. MacDonald. *Nanoletters*, 4:1475–1479, 2004.
- [157] M. D. Abramoff; P. J. Magalhaes and S. J. Ram. *Biophot. Intern.*, 11:36–42, 2004.
- [158] M. P. Lettinga; J. K. G. Dhont; Z. Zhang; S. Messlinger and G. Gompper. *Soft Matt.*, 6:4556–4562, 2010.
- [159] C.L.P. de Oliveira. Private communication.